

**Photoinduced Excited State Processes in
Carbonylpyrenes: A Comparison between Solution
and Solid-State Properties**

A thesis submitted for the degree of

Doctor of Philosophy

in the

School of Chemistry

by

Shinaj K. R.



Indian Institute of Science Education and Research
Thiruvananthapuram
Thiruvananthapuram – 695016
Kerala, India

September 2016

Declaration

I hereby declare that the work reported in this thesis is original and was carried out by me during my tenure as a Ph. D. student at the School of Chemistry, Indian Institute of Science Education and Research Thiruvananthapuram. Such material as has been obtained from other sources has been duly acknowledged in the thesis.

Place: IISER Thiruvananthapuram

Date: 30-09-2016

Shinaj K. R.

Certified that the work incorporated in this thesis "*Photoinduced Excited State Processes in Carbonylpyrenes: A Comparison between Solution and Solid-State Properties*" submitted by Shinaj K. R. was carried out by the candidate under my supervision. This thesis has not formed the basis for the award of any degree, of any university or institution.

Place: IISER Thiruvananthapuram

Date: 30-09-2016

Dr. Mahesh Hariharan

(Thesis supervisor)

Dedicated To...

My Beloved family

ACKNOWLEDGEMENTS

The thesis dissertation marks the end of a long and eventful journey for which there are many people that I would like to acknowledge for their support along the way.

First and foremost, I would like to express my special appreciation and thanks to my advisor Dr. Mahesh Hariharan, for his constant guidance and support, and for providing excellent research environment during the six years of my doctoral study. His advice on both research as well as on my career have been invaluable. He gave me the freedom to pursue my interests, simultaneously keeping me on the research track. I am extremely thankful to him for his enormous help, discussions without any limit, constant guidance and support throughout my Ph. D. work. He has constantly encouraged me to push my limits farther and farther. It is indeed a rare privilege to work under his guidance.

My sincere thanks to Prof. V. Ramakrishnan and Prof. E. D. Jemmis, present and former Directors of IISER-TVM, for allowing me to use the facilities of IISER to carry out my research work. I am grateful to my doctoral committee members, Prof. K. George Thomas, Dr. Kana M. Sureshan, Dr. Hema Somanathan and Dr. V. Sivaranjana Reddy for their support, guidance and helpful suggestions. I extend my gratitude to all my Ph. D. course instructors. I thank all the faculty members of IISER Thiruvananthapuram for all the support and motivation.

It is my pleasure to express my sincere thanks to Dr. Suresh Das, former director, NIIST Trivandrum for allowing me to use the experimental facilities in his institute. I express my sincere gratitude to Mr. Robert, Mr. Kiran and Mr. Chandran, NIIST Trivandrum for TEM and SEM microscopic imaging at NIIST.

I am deeply indebted to all my present and past group members: Dr. Rijo T. C., Mr. Ajith R. Mallia, Mr. Kalaivanan N., Mr. Abbey M. Philip, Ms. Somadrita, Dr. Salini, Dr. Nandita G. Nair, Mr. Nagaraj, Ms. Gopika Gopan, Ms. Remya Ramakrishnan, Ms. Shubhasmin Rana, Ms. Amalu Mohan, Mr. Ebin Sebastian and Ms. Anusha Thampi for their help and fruitful discussions during my Ph. D. work. During the course of my Ph. D. work, I had the pleasure of working with several project students. Their assistance during the presented work is gratefully acknowledged.

I would like to thank several people who made this work possible, and who have made my stay at IISER-TVM enjoyable. I remember the first Ph. D. batch students of IISER-TVM: Dr. Manil, Dr. Atchuth Rao, Dr. Vidyasgar, Dr. Pratap Zalake, Dr. Priyakumari, Dr. Subila, Dr. Deepthi, Dr. Jissy and Dr. Vidya for the harmony and support. Special thanks to Mr. Baiju P.

K., Mrs. Reshmi Thomas, Dr. Anoop Thomas and Dr. Gireesh K. K., who were always there for any help and warm company. I am deeply grateful to Mr. Sandeep, Dr. Shymala, Ms. Shine K. Albert, Ms. Sabnam Kar, Ms. Jiji, Ms. Rohini, Mr. Mohan, Mr. Soumik, Mr. Purnachandra Rao, Ms. Hema, Ms. Hemna, Mr. Hari, Mr. Amol and Mr. Murali for their support and affection. I thank all my friends in Techies' park hostel especially Mr. Sankaran N., Mr. Santhosh, Mr. Haris, Mr. Febin and Mr. Sujith for their support, love and care.

I take this opportunity to express my immense gratitude towards all my teachers in St. Thomas College, Thrissur for the motivation to keep high standard in my life during my graduation studies. I am thankful to all my teachers in CUSAT for helping me to pursue my passion for research during my master's graduation. I also thank them for the continuous support and care that they have provided me since my M.Sc. days. Thanks to all my M.Sc. colleagues for their support and care during my doctoral program.

I thank to Dr. V. Sivaranjana Reddy for the TDDFT calculations. My wholehearted thanks goes to Mr. Alex Andrews for single crystal X-ray diffraction measurements and helping me with various software. I express my sincere thanks to Prof. Babu Varghese, IIT-Madras, who had helped with solving some of the crystal. I thank him for the fruitful discussions and valuable suggestions we had with him. I extend my sincere thanks to Mr. Adarsh for NMR experiments, Mr. Aneesh for SEM analysis and Mr. Nibith, Mr. Shiju, Mr. Manoj for GC-mass, elemental and IR analysis. I thank Mr. Shebin George for the graphical artworks.

I would like to thank my friends outside IISER: Dr. Jimil George, for standing by me through the good and the bad times and eternally reminding me to believe in myself; Karthika, for her immense belief in my abilities and for constantly reminding me of the greener sides of life. Without her I would have struggled to find the inspiration and motivation needed to complete this dissertation.

I am indebted to Council of Scientific and Industrial Research (CSIR) and Department of Science and Technology (DST), Government of India, and IISER-TVM for the financial assistance. I thank them for ensuring a continuous funding during my doctoral study.

Above all, I would like to acknowledge the tremendous sacrifices that my parents made to ensure that I had an excellent education. For this and much more, I am forever in their debt. It is to them that I dedicate this dissertation.

Shinaj K. R.

Preface

Understanding the electronic communication between chromophores in complex molecular architectures is a key factor for designing and construction of functional photonic devices. Such correlation is based on interchromophoric electronic coupling which mediates electron and/or excitation energy transfer. In addition to interchromophoric electron/energy transfer processes, there are intrachromophoric radiationless transitions which compete with the former. Advanced spectroscopic techniques can be employed to monitor the ultrafast molecular dynamics arising from the interplay between electronic and vibronic relaxation mechanisms in multichromophoric systems.

Investigating the influence of crystal packing on the device performance is essential to design new promising materials. Despite the advancement in experimental and theoretical methods, the structure-property correlation in molecular solids is not well understood. The solid-state packing of the organic semiconductors depends on the nature of substituents and electronic distribution in the aromatic core. However, it is extremely difficult to predict the solid-state order of the crystal engineered molecules since small chemical modifications can cause huge differences in the solid-state organization. Investigation on the influence of solid-state packing on charge transport properties should be carried out using molecules that are as similar as possible in terms of molecular formula, type of intermolecular interactions and electronic properties. Ideally, they should differ in crystal packing, in order to understand the underlying aspects of charge mobility through the crystal system.

Pyrene is the fruit fly of photochemists. Its unique properties have inspired researchers from many scientific areas, making pyrene the chromophore of choice in fundamental and applied photophysical research. Since the discovery of excimer formation by Förster and Kasper in 1954, pyrene has been used as a chromophore in various charge and energy transfer systems. Despite the vast number of pyrene based donor (D)-acceptor (A) systems reported, the study of excited state dynamics of pyrene is still a burgeoning topic of interest.

The light-emitting behaviour of molecular solids differs from that of dilute solutions because emission in the solid-state is dictated by the whole collective rather than by individual molecules. Studying molecular crystals provides essential information on how molecules are arranged with respect to their neighbours and interactions that bind them together which is required to correlate the crystal packing with emission characteristics. Polyaromatic hydrocarbons are generally characterized by herringbone packing due to C–H••• π (edge-to-face) interactions. However, a

dramatic reduction in the edge to face interaction promotes for enhanced π - π overlap through face to face geometry generating slipped stack, brickwork and cofacial packing. Various covalent and noncovalent routes have been employed to tune the solid-state luminescent properties to obtain the desired emitting characteristics. Covalent routes includes changing the number and position of alkoxy substituents and alkyl chain length while noncovalent routes involve polymorphism, phase transition, nano/microcrystal forms and multi-component systems.

A brief illustration of the i) unique photophysical properties of pyrene chromophore ii) an overview on the structure-property correlation in molecular solids and iii) investigating the influence of crystal packing on the device performance is provided in Chapter 1.

Despite of the versatility and the simplicity of the molecular structure, pyrene shows complex intramolecular photophysical properties. The intermolecular energy redistribution after excitation to higher electronic states involves strong vibronic couplings of the electronic states leading to an ultrafast internal conversion ($S_n \rightarrow S_1$) that has been measured to be within 150 fs. All these processes, ultimately lead to a fluorescence contribution originating from the excited singlet state. Hence a lot of studies were focused to understand the ultrafast internal conversion processes within first hundreds of femtoseconds after excitation. It is well-known that carbonyl functional groups exhibit a degree of spin-orbit coupling at the carbonyl oxygen that allows for intersystem crossing, generating triplet state (T_n). Albeit, widely investigated, the understanding about the photophysics of carbonylpyrenes is greatly limited to their characteristic singlet emission properties. Investigation of ultrafast excited state dynamics of this family of chromophores is significant in understanding fundamental energy/electron transfer phenomena. In Chapter 2, we present quantitative studies of the excited-state dynamics of carbonyl-functionalized pyrene derivatives by using broadband transient absorption spectroscopy.

Molecular crystal engineering of polyaromatic hydrocarbons to yield 1-2D lamellar arrangement demonstrated a pivotal role in photonic and semiconductor device applications. Extended orbital overlap through π -columnar stacks compared to a herringbone arrangement of arenes proved to be vital. Recent efforts in transforming the herringbone to the columnar arrangement of arenes through various methods such as chemical modifications, co- and solvent-crystallization, heat mode mechanical stimulation and solid seeding have proven to be effective. Achieving a diverse degree of orbital overlap between the neighbouring units in the crystalline state is still a challenging task. We modulated the extent of π - π overlap between vicinal pyrene units through successive acylation. Unprecedented heteropolar dihydrogen contacts

(sp^2 C–H...H–C sp^3) in organic crystals are established using QTAIM. Hirshfeld surface analysis is indicative of an increase in π – π interactions and a concomitant decrease in the σ – π interactions with an increase in the number of acetyl groups per pyrene unit. A combination of C–H...H–C, C–H...O and π – π interactions facilitate the transformation of sandwich herringbone packing of pyrene to the herringbone arrangement and the brickwork arrangement and finally to columnar stacks. A systematic decrease in the interplanar angle between the vicinal pyrene units could be attributed to the dramatic shift in the emission spectra (ca. 42–174 nm) of crystalline acetylpyrenes when compared to pyrene. J-like aggregation and/or aggregation induced emission (AIE) in the crystal packing of acetylpyrenes corroborates the moderately emissive blue–green–orange crystals. While in another context, the extent of orbital overlap (π – π) between vicinal pyrene units in crystalline 1–4BP was regulated by exploiting the steric hindrance offered via successive benzylation. Progressive increment in the steric hindrance causes an increase in the transverse/longitudinal displacement of the vicinal pyrene units. As a result, a 48-fold reduction in the π -stacking between pyrene units was observed in tetrabenzoylpyrene with respect to monobenzoylpyrene. Moderating the molecular stacking along with crystal induced emission (CIE) through arrested intramolecular rotations of pendent benzoyl groups may give rise to green-yellow-orange solid-state emitters. In Chapter 3, we tuned the extent of π – π overlap between vicinal pyrene and achieved diverse degree of orbital overlap between the neighbouring units in the crystalline state.

Molecular ordering in organic single crystals plays a substantial role in the performance characteristics of electronic devices, such as organic field-effect transistors (OFFTs) and organic light-emitting diodes (OLEDs). Systems that can exhibit 1D and 2D conductivity are highly desirable for the fabrication of devices. Chapter 4 explores the effects of packing on charge mobility in systematically synthesized acetylpyrene derivatives. Single crystal FETs were fabricated using the top-contact, bottom-gate geometry and at increasingly negative gate voltages, the mobility was found to monotonously increase from 0.03 to 0.18 $\text{cm}^2 \text{V}^{-1} \text{s}^{-1}$.

Contents

List of Figures	
List of Tables	
List of Schemes	
1. Solid-state organization and photophysics of pyrene	
1.1. Introduction	19
1.2. Chemical modifications of pyrene	20
1.3. Introduction to the photophysics of pyrene	22
1.3.1. Molecular dynamics revealed by transient spectroscopy	23
1.4. Solid-state organization and optical properties	24
1.4.1. π - π interactions in polynuclear aromatic hydrocarbons	25
1.4.2. Tuning solid state luminescence: Structure – optical property relationships	27
1.4.2.1. Covalent routes to tune the optical properties	28
1.4.2.2. Non-Covalent routes to tune the optical properties	29
1.4.2.2.1. Polymorphism	30
• Extent of π -overlap and conformation differences	30
• Excited state intramolecular proton transfer (ESIPT)	31
1.4.2.2.2. Stimuli responsive phase transition and fluorescence switching	32
• Temperature-responsive materials	33
• Multiple-stimuli responsive materials	34
1.4.2.2.3. Crystal to amorphous transformation and emission switching	36
• Amorphization by shear stress	36
1.4.2.2.4. Multicomponent systems to tune the emission properties	38
1.5. Overview of optical behaviour of aggregate states	39
1.6. Electronic and optoelectronic organic devices	42
1.6.1. Organic Field Effect Transistors	43
1.7. Objective of the thesis	46
2. Vibronically accelerated intersystem crossing competes with internal conversion in acetylpirenes	
2.1. Introduction	48

2.2.	Synthesis, characterization and crystallization of acetylpyrene derivatives (1-4AP)	49
2.3.	Results and Discussions	50
2.3.1.	Frontier molecular analysis and steady state absorption and emission measurements	50
2.3.2.	Nanosecond transient studies	57
2.3.3.	Femtosecond transient studies	60
2.3.4.	TDDFT calculation and Jablonski diagram	65
2.4.	Conclusion	67
2.5.	Appendix	68
3.	Engineering the solid-state packing of carbonylpyrenes via C–H•••H–C, C–H•••O and π–π interactions for tuning opto-physical properties	
3.1.	Introduction	76
3.2.	Results and Discussions	79
3.2.1.	Synthesis, crystallization and thermal analysis	79
3.2.2.	QTAIM and Hirshfeld Analyses	82
3.2.3.	Crystal structure analyses of 1-4AP	86
3.2.4.	Steady-state absorption and emission measurements	92
3.3.	Results and Discussions	98
3.2.5.	Synthesis and crystallization	98
3.2.1.	Frontier molecular analysis and steady state studies	99
3.2.2.	Crystal packing of 1-4BP	107
3.2.8.	Photophysical properties of crystalline 1-4BP	110
3.4.	Conclusion	116
3.5.	Appendix	117
4.	Solid-state ordering of pyrene based single crystalline materials for high-performance organic field-effect transistors	
4.1.	Introduction	129
4.2.	Results and Discussions	131
4.2.1.	Synthesis, characterization and crystallization of bis-haloacetyl pyrene derivatives (XPs)	132
4.2.2.	Crystal structure analyses of XPs	133
4.2.3.	Hirshfeld surface analysis	145
4.2.4.	Morphological Analysis	149
4.2.5.	Conductivity measurements and theoretical calculations	154
4.3.	Conclusion	157
4.4.	Appendix	159

6. Bibliography	168
7. List of publications	183
8. Presentations at conferences	184
9. Copyrights and permission	185

List of Figures

Figure	Title	Page
1.1.	Depiction of pyrene (A) according to Clar's sextet rule; (B) nomenclature of positions; (C) K-region and non-K-region of pyrene; (D) functionalized at the active positions (1, 3, 6, 8-positions) by single bond connection; (E) fused at the K-region and (F) fused at the non-K-region.	20
1.2.	Shows (A) mirror plane three chemically distinguishable sites; (B); (C) and (D) three main groups of chemically identical sites.	21
1.3.	(A) Absorption and emission spectra of pyrene in methanol and (B) Scheme showing the relaxation processes of pyrene after photoexcitation to the S ₂ state. IC: internal conversion, IVR: internal vibrational relaxation	22
1.4.	Pictorial representation of the A) herringbone; B) sandwichherringbone; C) gamma (γ) and D) beta (β) packing motifs.	25
1.5	Bar chart representation of the ratios of (%C...H)/(%C...C) interactions and the corresponding packing motifs of PAHs.	26
1.6.	Show (A) Molecules under investigation; (B) Normalized fluorescence spectra of thin films of MBC12 (blue spectrum), DBC12 (yellow spectrum), and TBC12 (green spectrum). $\lambda_{ex} = 360$ nm. The corresponding fluorescence as visualized on excitation with a 365 nm UV light is also shown.	28
1.7.	Shows (A) Tetramer and trimer assemblies in ANP polymorphs and photographs of corresponding crystals, excited under UV light ($\lambda_{ex} = 365$ nm); (B) Variations in extent of π -overlap and corresponding crystal emission colour in ANP derivatives.	31
1.8.	ESIPT-induced emission switching in 2-(2'-hydroxyphenyl)-imidazo[1,2-a]pyridine.	32
1.9.	(A) Herringbone to brickstone structural transformation in BC8; (B) Thermochromic transformations in AA1 and AA2.	34
1.10.	Schematic representation of (A) mechanisms for fluorescence at the cost of frustrated [2 + 2] cycloaddition in CN(L)-TrFMBE; (B) Different modes of slip-stacking in DBDCS molecular sheets; thermo/piezochromic	35

	switching between green and blue forms. SEM images show corresponding changes on the crystal surface.	
1.11.	Stimuli-induced switching of solid-state emission by (A) TPE-Py; (B) hemicyanin dye; and (C) DPATPAN.	37
1.12.	The emission switching observed in (A) 1,4-bis-p-cyanostyrylbenzene by means of co-crystallization; (B) Fluorescence switching in CDPA by means of formation of multicomponent systems using acid–base interactions.	39
1.13.	Schematic diagram showing the formation of H- and J-aggregates with their possible electronic transitions.	40
1.14.	Definition of (A) pitch (P) and roll (R) angles and associated distances and vectors. The labels x and y refer to the directions of the short and long molecular axes, respectively. (B) View along the short molecular axis of a “pitched” π -stack and along the long molecular axis of a “rolled” π -stack. Schematic representation of “pitch” and “roll” angles/distances (P/dP; R/dR) and the structural description of Herringbone as well as H- and J-aggregates in terms of relative translation of molecules. Insets A and B represent pitch and roll inclinations that lead to J-aggregate and Herringbone	41
1.15.	Common OFET configurations employed: (A) top contact and (B) bottom contact.	44
1.16.	Schematic representation of the (A) HOMO and LUMO of the organic semiconductor with respect to the source-drain metal Fermi level; (B) Theoretical transport properties from a p-type OFET.	45
2.1.	Row I: Schematic molecular structure and Row II: ORTEP diagram of the crystal structure of 1-4AP derivatives.	50
2.2.	Illustrations of the frontier molecular orbitals of i) 1AP; ii) 2AP; iii) 2'AP; iv) 2''AP; vi) 3AP and vii) 4AP evaluated at the B3LYP/6-311G*++ from crystal structure.	51
2.3.	Shows A) Cyclic voltammograms of 1-4AP derivatives in CH ₃ CN and B) Energy level diagram for 1-4AP derivatives as calculated using TD-DFT (B3LYP/6-311G*++)	52
2.4.	Shows the normalised (A) absorption and (B) fluorescence spectra of 1-4AP (0.1-1 μ M) derivatives in CHCl ₃ .	53
2.5.	Shows fluorescence decay profile of (A) 1AP; (B) 2AP; (C) 2'AP; (D) 2''AP; (E) 3AP and (F) 4AP in CHCl ₃ at the respective emission maximum (λ_{exc} =375 nm).	56
2.6.	nTA spectra of (A) 1AP; (B) 2AP; (C) 2'AP; (D) 2''AP; (E) 3AP and (F) 4AP derivatives in CHCl ₃ .	57
2.7.	SVD of nanosecond transient spectra of (A) 1AP; (B) 2AP; (C) 2'AP; (D) 2''AP; (E) 3AP and (F) 4AP derivatives in CHCl ₃ .	58

2.8.	SVD of nanosecond transient spectra of (A) 1AP; (B) 2AP; (C) 2'AP; (D) 2''AP; (E) 3AP and (F) 4AP derivatives in CHCl ₃ .	58
2.9.	Show A) Variation of triplet lifetime and B) triplet quantum yield of 1-4AP in CHCl ₃ .	59
2.10.	fTA spectra of (A) 1AP; (B) 2AP; (C) 2'AP; (D) 2''AP; (E) 3AP and (F) 4AP derivatives in CHCl ₃ .	60
2.11.	Transient absorption spectra for 4AP as plotted in the early time delay where at 3.5 ps a growth around 500 nm is observed.	61
2.12.	SVD of fTA spectra of (A) 1AP; (B) 2AP; (C) 2'AP; (D) 2''AP; (E) 3AP and (F) 4AP in CHCl ₃ .	62
2.13.	Right singular vectors obtained from global analyses for (A) 1AP; (B) 2AP; (C) 2'AP; (D) 2''AP; (E) 3AP and (F) 4AP in CHCl ₃ .	62
2.14.	(A) Representative phosphorescence spectrum of 4AP in CHCl ₃ recorded at 77 K ($\lambda_{\text{ex}} = 380$ nm; dotted graph represents the fluorescence spectrum of 4AP); (B) Phosphorescence decay of 1-4AP derivatives in CHCl ₃ recorded at 77 K ($\lambda_{\text{ex}} = 380$ nm).	64
2.15.	Overlay of nTA spectra (blue trace) and fTA spectra (red trace) of (A) 1AP; (B) 2AP; (C) 2'AP; (D) 2''AP; (E) 3AP and (F) 4AP in CHCl ₃ .	65
2.16.	Decay profile of S ₄ state of 2''AP and 4AP; Potential energy cuts along C=O symmetric stretch vibrational mode of singlet excited states and triplet excited state of B) 2''AP and C) 4AP.	66
2.17.	Jablonski diagram depicting the photophysics of acetylpyrene.	66
3.1.	Volume calculated for (A) pyrene and (B) benzoyl unit in 1BP from Crystal Explorer 3.0.	78
3.2.	Row I: molecular structure of 1-4AP; Row II: corresponding single crystal X-ray structure. Photographic image of the crystals Row III: in daylight; and row IV: under UV illumination. X-ray structure of P is taken from the literature.	79
3.3.	Shows (A) DSC melting temperature (T _m); (B) near-linear increment in the melting temperature (T _m) and (C) linear increment in the ΔH values of crystalline 1-4AP derivatives.	81
3.4.	Shows QTAIM electron density map of (A) 2AP; (B) 3AP and (C) 4AP, arrows indicate the existence of intermolecular C-H...H-C contacts.	84
3.5.	Hirshfeld 2D fingerprint plot of 4AP with the region of the plots corresponding to (A) C...C and (B) H...H interactions; Hirshfeld surface of 4AP mapped with d_{norm} depicting (C) C...C and (D) H...H interactions; (E) percentage contribution of edge-to-face (C...H) and face-to-face (C...C) interactions in 1-4AP.	85

- 3.6. Close packing arrangement in 1-4AP indicating the values of $\rho = [(\%C\cdots H)/(\%C\cdots C)]$. Herringbone ($\rho > 4.5$), sandwich herringbone ($3.2 < \rho < 4.0$), γ ($1.2 < \rho < 2.7$), β ($0.46 < \rho < 1.0$). 87
- 3.7. Shows (A) the gradual decrease in the interplanar angle between the nearest molecules; (B) the decreasing angle and the consequent increase in stacking of the pyrene units in the crystalline 1-4AP. 87
- 3.8. Shows the torsional angle between adjacent pyrene units in crystal packing of (A) 1AP; (B) 2AP; (C) 2'AP; (D) 2''AP; (E) 3AP and (F) 4AP. 89
- 3.9. Shows the aerial overlap between adjacent pyrene units in close packing of (A) 1AP; (B) 2AP; (C) 2'AP; (D) 2''AP; (E) 3AP and (F) 4AP. 90
- 3.10. Shows the C-H \cdots O interactions in the crystal packing of (A) 2AP; (B) 2'AP; (C) 2''AP; (D) 3AP and (E) 4AP. 91
- 3.11. Shows fluorescence decay profile of (A) 1AP; (B) 2AP; (C) 2'AP; (D) 2''AP; (E) 3AP and (F) 4AP in CHCl₃ solution on exciting at 375 nm and collected at different wavelengths. 93
- 3.12. Shows the fluorescence excitation spectra of (A) 1AP; (B) 2AP; (C) 2'AP; (D) 2''AP; (E) 3AP and (F) 4AP in CHCl₃ as compared to absorption spectrum. 93
- 3.13. Concentration dependent emission spectra of (A) 1AP; (B) 2AP; (C) 2'AP; (D) 2''AP; (E) 3AP and (F) 4AP in CHCl₃ solution on exciting at 350 nm. 95
- 3.14. Concentration dependent excitation spectra of (A) 1AP; (B) 2AP; (C) 2'AP; (D) 2''AP; (E) 3AP and (F) 4AP in CHCl₃ solution while monitoring at 500 nm (for 1AP and 2''AP) and 550 nm (for 2AP, 2'AP, 3AP and 4AP). 95
- 3.15. Shows the normalised (A) Absorption and (B) fluorescence emission spectra of crystalline 1-4AP derivatives; excitation wavelength is 350 nm; (C) fluorescence decay profile of crystalline 2-4AP derivatives and the corresponding inset shows fluorescence decay profile of crystalline 1AP, excitation wavelength is 375 nm and emission monitored at 518 nm (1AP); 602 nm (2AP); 567 nm (2'AP); 631 nm (2''AP); 645 nm (3AP) and 646 nm (4AP) and (D) CIE colour diagram of fluorescence emission for crystalline 1-4AP derivatives. 96
- 3.16. Shows fluorescence excitation spectra of crystalline (A) 1AP; (B) 2AP; (C) 2'AP; (D) 2''AP; (E) 3AP and (F) 4AP as compared to absorption spectra. Absorption spectra of crystalline 1-4AP derivative are reproduced for comparison with excitation spectra. Emission maxima, where the excitation spectra are monitored, are indicated in the bracket. 97
- 3.17. Row I: Molecular structure of 1-4BP; Row II: close packing arrangement in the crystal (a) 1BP; (b) 2BP; (c) 2'BP; (d) 2''BP; (e) 3BP and (f) 4BP; Row 99

- III: photographic image of the crystals in daylight (above) and under UV illumination (below).
- 3.18. (A) Frontier molecular orbital (FMO) analysis of 1-4BP calculated from the B3LYP/6-311G**+ level of theory. Lower and upper plots represent the HOMOs and LUMOs, respectively (B) Cyclic voltammograms of 1-4BP in acetonitrile; (C) Absorption spectra of 1-4BP; the area filled spectrum (grey) represents the absorption spectrum of pyrene and (D) Nanosecond transient absorption spectrum of 4BP in chloroform. 101
- 3.19. Shows the (A) fluorescence spectra; $\lambda_{ex} = 380$ nm, area filled graph (grey colour) represent the emission spectrum of pyrene in $CHCl_3$ (B) fluorescence decay; $\lambda_{ex} = 375$ nm and (C) phosphorescence spectra; $\lambda_{ex} = 380$ nm of 1-4BP derivatives in ethanol. 106
- 3.20. Shows the gradual increase in the traverse/longitudinal shift between nearest pyrene molecules in the crystalline 1-4BP derivatives. 108
- 3.21. Shows the aerial overlap between adjacent pyrene units in close packing of (A) 1BP; (B) 2BP; (C) 2'BP; (D) 2''BP; (E) 3BP and (F) 4BP. 108
- 3.22. Shows the C-H...O interactions in the crystal packing of (A) 1BP; (B) 2BP; (C) 2'BP; (D) 2''BP; (E) 3BP and (F) 4BP. 110
- 3.23. (A) Absorption; (B) fluorescence spectra of crystalline 1-4BP derivatives; $\lambda_{exc} = 380$ nm.; the area filled spectrum (grey) represents the absorption and emission spectra of crystalline pyrene (C) fluorescence decay profile of crystalline 1-4BP; $\lambda_{exc} = 375$ nm and emission wavelength monitored (D) CIE colour diagram of fluorescence emission for crystalline 1-4BP derivatives. 111
- 3.24. Shows fluorescence excitation spectra of crystalline (A) 1BP; (B) 2BP; (C) 2'BP; (D) 2''BP; (E) 3BP and (F) 4BP as compared to absorption spectra. Emission maxima, where the excitation spectra are monitored, are indicated in the bracket. 113
- 3.25. (A) Indicates τ_F (major component; \square); Φ_F (\bullet) of 1-4BP in the crystalline state; Φ_F ($*$) of 1-4BP in solution state and % C...C interaction ($\pi-\pi$; Δ) obtained from Hirshfeld analysis (Table 3.13) and (B) Jablonski diagram depicting energy levels in solution (monomeric) and aggregated (crystalline) state in 1BP. 114
- 3.26. Energy levels diagram of monomer and dimer of 1BP and 4BP calculated from B3LYP/6-311G**++ level of theory. 115
- 4.1. Single crystal X-ray structure of XPs. 133
- 4.2. (A) Decrease in the intramolecular dihydrogen distance in 1,3-XP compared to 1,3-AP and (B) QTAIM electron density map of 1,3-BP indicating intramolecular dihydrogen and C-H...O interactions. 135

4.3.	Close packing arrangement in (A) 1,3-XPs and (B) 1,8-XPs indicating the values of ρ [$(\%C\cdots H)/(\%C\cdots C)$]. Herringbone ($\rho > 4.5$), sandwich herringbone ($3.2 < \rho < 4.0$), γ ($1.2 < \rho < 2.7$), β ($0.46 < \rho < 1.0$) and (C) schematic representation showing the decrease in the interplanar distance between pyrene units in 1, 3-XPs.	137
4.4.	Shows the decrease in the interplanar distance between pyrene units in 1,3-XP.	137
4.5.	Calculated ESP maps of representative monomers of A) 1,3-XP and B) 1,8-XP from crystal structure. All maps used consistent surface potential ranges [$-4.75e-2$ au (red) to $4.75e-2$ au (blue)] and an isovalue of 0.000400 au.	139
4.6.	Intermolecular interactions in 1,3-XPs. (A) Intermolecular C-H \cdots F and C-H \cdots O interactions in 1,3-FP; (B) C-H \cdots O and C-H \cdots Cl interactions in 1,3-CP; (C) C-H \cdots Br and C-H \cdots O interactions in 1,3-BP and (D) C-H \cdots I, C-I $\cdots\pi$ C-H \cdots O and π - π interactions in 1,3-IP.	140
4.7.	Shows QTAIM electron density map of 1,3-IP, arrows indicate the existence of intermolecular I $\cdots\pi$ contacts.	141
4.8.	Intermolecular interactions in 1,8-XPs. (A) Intermolecular C-F \cdots C, C-H $\cdots\pi$ and C-H \cdots F interactions in 1,8-FP; (B) C-H \cdots Cl and C-H \cdots O interactions in 1,8-CP; (C) C-H \cdots H-C, and C-H \cdots O interactions in 1,8-C'P and (D) C-H \cdots H-C and C-Br $\cdots\pi$ interactions in 1,8-BP.	142
4.9.	Shows the decrease in the interplanar distance between pyrene units in 1,8-XP.	142
4.10.	Shows QTAIM electron density map of 1,8-FP, arrows indicate the existence of intermolecular C \cdots F interactions.	143
4.11.	QTAIM electron density map of (A) 1,8-C'P and (B) 1,8-BP indicating intermolecular interactions.	144
4.12.	Hirshfeld 2D fingerprint plot of 1,3 and 1,8-XPs.	145
4.13.	Row I: chemical structure of 1-4 AP; Row II: stereo microscopic images of corresponding single crystal Row III: schematic drawing that depicts the possible crystal packing pattern and the range of $\rho = (\%C\cdots H)/(\%C\cdots C)$ contact ratio for each packing.	148
4.14.	SEM images of A) 1AP; B) 2AP; C) 2'AP; D) 2''AP; E) 3AP and F) 4AP, drop casted in benzene.	149
4.15.	Show the AFM images of A) 1AP; B) 2AP; C) 2'AP; D) 2''AP; E) 3AP and F) 4AP, drop casted in benzene.	151
4.16.	Show the laser confocal images of a) 1AP; b) 2AP; c) 2'AP; d) 2''AP; e) 3AP and f) 4AP, drop casted in benzene.	152

- 4.17. Show the TEM images of a) 1AP; b) 2AP; c) 2'AP; d) 2''AP; e) 3AP and f) 4AP, drop casted in benzene. 153
- 4.18. I-V profile determination by A) drop-casting the derivatives in benzene; B) single crystal and C) single crystal organic field-effect transistor (OFET) measurement on 4AP. 154

List of Tables

Table	Title	Page
2.1.	Electrochemical experimental and calculated energy levels of 1-4AP derivatives.	52
2.2.	Photophysical properties of 1-4AP derivatives in CHCl ₃ .	53
2.3.	Excitation energy, oscillator strength, main transition orbital, and their contribution calculated for 1-4AP derivatives using TD-DFT (B3LYP/6-311G ⁺⁺).	54
2.4.	Lifetimes of 1-4AP obtained from global analyses of fTA spectra ($\lambda_{exc}=400$ nm).	63
3.1.	Shows crystallographic data and refinement parameters for crystalline 1-4AP derivatives.	80
3.2.	Shows melting temperature (T_m) and change in enthalpy (ΔH) values for crystalline 1-4AP derivatives.	81
3.3.	Shows intramolecular (CH ₃) H•••H (aryl) (Å) distance (d) in crystalline 1-4AP derivatives that is less than the sum of van der Waals radii of two hydrogen atoms (2.4 Å).	82
3.4.	Shows calculated topological properties of the electron density for the intra- and intermolecular interaction in 2, 3 and 4AP derivatives.	83
3.5.	Percentage of intermolecular contacts of a molecule in crystalline 1-4AP.	86
3.6.	Interplanar angle between nearest pyrene molecules in crystalline 1-4AP.	88
3.7.	Shows the photophysical properties of 1-4AP derivatives.	94
3.8.	Shows crystallographic data and refinement parameters for crystalline 1-4BP derivatives.	100
3.9.	Experimental (electrochemical) and calculated energy levels of 1-4BP.	102
3.10.	Excitation energy, oscillator strength, main transition orbitals and their contribution calculated for 1-4BP using TDDFT (B3LYP/6-311G ^{**++}).	103
3.11.	Shows the photophysical properties of 1-4BP derivatives.	105
3.12.	Geometries in the face-to-face π -stacked arrangements in crystalline 1-4BP.	109
3.13.	Percentage of intermolecular contacts of a molecule in crystalline 1-4AP.	114
4.1.	Crystal data and structure refinement for 1,3 and 1,8-XP.	134

4.2.	Shows the intramolecular interactions in 1,3-XP and 1,8-XP as visualised through Mercury CSD 3.8.	136
4.3.	Calculated topological properties of the electron density for the intermolecular interaction in XPs.	141
4.4.	Shows the percentage of intermolecular contacts of a molecule in crystalline XPs.	146

List of Schemes

Scheme	Title	Page
2.1.	Shows the synthesis of acetylpyrene (1-4AP) derivatives.	72
3.1.	Shows the synthesis of benzoylpyrene (1-4BP) derivatives.	123
4.1.	Synthesis of 1,3- and 1,8-Bis(chloroacetyl)pyrene (1,3-CP and 1,8-CP).	163
4.2.	Synthesis of 1,3- and 1,8-Bis(bromoacetyl)pyrene (1,3-BP and 1,8-BP).	164
4.3.	Synthesis of 1,3- and 1,8-Bis(fluroacetyl)pyrene (1,3-FP and 1,8-FP).	165
4.4.	Synthesis of 1,3- and 1,8-Bis(iodoacetyl)pyrene (1,3- and 1,8-IP).	166

Chapter 1

Solid-state organization and photophysics of pyrene

1.1. Introduction

Pyrene has been discovered by the french chemist Auguste Laurent in 1837 by extraction from coal tar[1] but the correct chemical formula has been determined later by Gräbe (1871)[2] and the structure by Bamberger and Philip in 1887[3]. Withal, the found molecular formula remains still valid whereupon pyrene consists of 16 carbon atoms within four rings forming the polycyclic aromatic hydrocarbon (PAH). The view offered through Clar's model claims pyrene can be drawn with two circles that are cylindrically localized and two double bonds (Figure 1.1 A). Arising from this description, pyrene appears as biphenyl annulated with two further rings in the armchairs. Indeed, these double bonds at the centre exhibit increased reactivity towards oxidation due to less stabilization although still being aromatic. The position 1, 3, 6, and 8 (non K-region) have been heavily exploited for syntheses of new extended π -systems (Figure 1.1C, D&F)[4]. Recently, a few pyrene derivatives fused at the K-region were developed (Figure 1E), and they exhibited interesting properties.

Since its discovery pyrene has predominantly attracted attention for its outstanding photophysical properties, which is why pyrene is called "the fruit fly of photochemists"[5]. Pyrene is well known for its long lifetime of the excited state of the monomer in solution, high fluorescence quantum yields and the concentration dependent shift of the emission spectrum upon excimer formation[6]. Monomeric

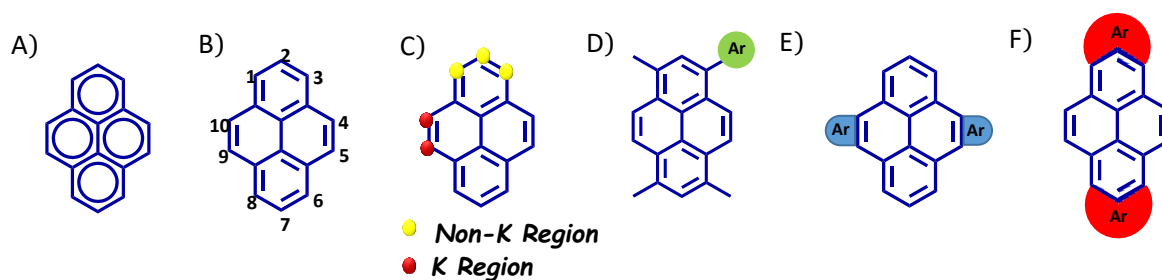


Figure 1.1. Depiction of pyrene (A) according to Clar's sextet rule; (B) nomenclature of positions; (C) K-region and non-K-region of pyrene; (D) functionalized at the active positions (1, 3, 6, 8-positions) by single bond connection; (E) fused at the K-region and (F) fused at the non-K-region (Adapted with permission from ref. 4. Copyright © 2013, American Chemical Society).

pyrene emits between 370 nm and 400 nm whereas emission of the excimer appears red-shifted[7, 8]. These properties make pyrene one of the most frequently applied fluorescence markers to monitor dynamics of polymer chains and protein structures[9-12]. After selective cysteine labelling of proteins with N-(1-pyrenyl)maleimide the appearance or absence of the excimer signal provides information about the spatial distance of labelled residues. The latter example shows that no sophisticated chemistry is required for this application and the introduction of functional groups at position 1 is already known for more than 70 years. Nevertheless, chemists have greatly extended the variety of available protocols in the meantime to functionalize pyrene for respective applications. Especially in the last decade a large number of novel methods have been reported for making new classes of pyrene compounds accessible for material applications.

1.2. Chemical modifications of pyrene

Pyrene has two mirror planes (one lies in the plane of the molecule) which divide the molecule into four quarters with three types of positions which exhibit strong difference in chemical reactivity (Figure 1.2A). Therefore, the overview about reported chemical methods to substitute pyrene is grouped into “1,3,6,8”, “2,7” and “4,5,9,10” regions. Reactivity of pyrene at 1, 3, 6 and 8 positions toward electrophiles arise from the large orbital coefficients at these carbon atoms (Figure 1.2C). First protocols are reported in 1937 by Vollmann et al. for the synthesis of mono-, di-, tri and tetra-substituted pyrene derivatives[13]. Additionally, chemists have invented multistep syntheses starting from benzene derivatives to achieve otherwise impossible substitution of pyrene. 1-substituted and 1,3,6,8-tetrasubstituted pyrenes can be easily accessible by direct electrophilic substitution of pyrene. The ease of preparation of mono- and tetrasubstituted pyrenes combined with the relatively simple purification gives the possibility to straightforwardly introduce pyrene into different molecular architectures. On the other hand, the selective preparation of pyrenes is challenging but simultaneously

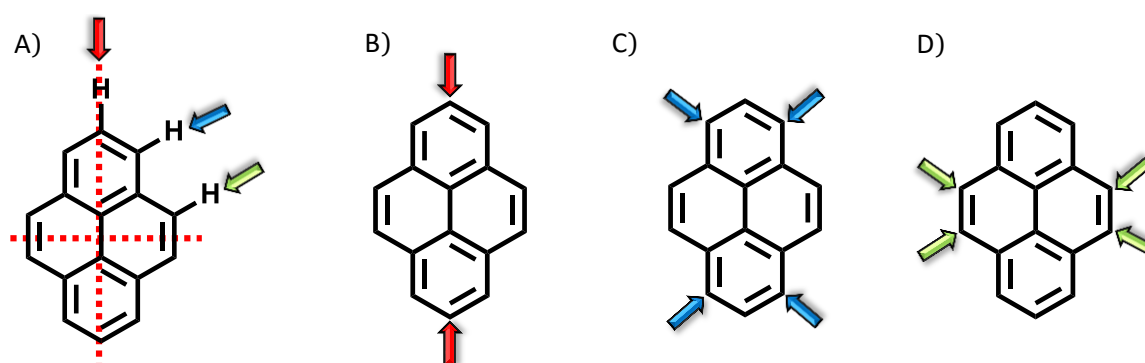


Figure 1.2. Shows (A) mirror plane three chemically distinguishable sites; (B); (C) and (D) three main groups of chemically identical sites.

highly required. It is crucial to obtain well-defined disubstituted pyrene building blocks for the controlled synthesis of linear or cyclic oligomers as well as polymers (Figure 1.2B&D).

1.3. Introduction to the photophysics of pyrene

Pyrene is an important polycyclic aromatic hydrocarbon[14, 15]. In 1954 Förster and Kasper reported the first observation of intermolecular excimers in a pyrene solution[16]. This excimer formation, combined with long-lived excited states, high fluorescence quantum yield[17], exceptional distinction of the fluorescence bands for monomer and excimer, and the sensitivity of its excitation spectra to microenvironmental changes (Ham effect)[18] brought pyrene to the most explored and well-studied organic molecule in terms of its photophysical properties.

Pyrene has its absorption in the UV spectral domain and shows distinct electronic absorption bands (Figure 1.3A). Each electronic absorption band consists of

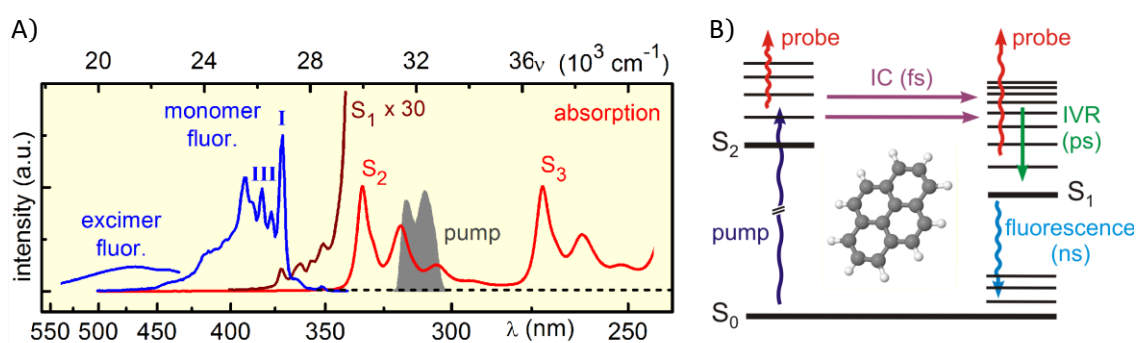


Figure 1.3. (A) Absorption and emission spectra of pyrene in methanol and (B) Scheme showing the relaxation processes of pyrene after photoexcitation to the S_2 state. IC: internal conversion, IVR: internal vibrational relaxation (Adapted with permission from ref. 20. Copyright © 2016 Elsevier).

a variety of vibrational modes that give rise to the structure in the absorption spectra [19]. The S_1 (${}^1B_{3u}$) \leftarrow S_0 (1A_g) absorption is weak compared to the absorption into higher lying electronic states [e.g., S_2 (${}^1B_{2u}$) \leftarrow S_0 (1A_g)] because this transition is forbidden due to the symmetry of the states. When pyrene is excited to higher electronic states (S_n , $n>2$) a fast (85 fs for the S_2 state) internal conversion to the S_1 state occurs mediated by vibronic coupling of the electronic states (Figure 1.3B)[20]. Starting from the excited electronic S_1 state multiple processes happen. They give rise to signals detected in ultrafast spectroscopy. From the S_1 state intersystem crossing (ISC), internal conversion (IC), and fluorescence are the pathways for the molecule to relax to the ground state.

1.3.1. Molecular dynamics revealed by transient spectroscopy

The S_1 excited state lifetime of pyrene dissolved in methanol for a concentration of about 10^{-2} mM was measured to 339 ns and the fluorescence quantum yield to 0.75[21]. These values are observed to be concentration dependent. This means that the non-radiative relaxation processes or intersystem crossing to the T_1 state are slow compared to the fluorescence. All these processes are fairly slow compared to internal conversion from the S_2 state or vibrational relaxation in the S_1 state and only give rise to negligible constant contributions on the ps time scale of the measurements. Foggi and co-workers [22] directly observed that the S_2 to S_1 internal conversion which occurs within 150 fs measured by femtosecond transient spectroscopy in solution. They found that the rate of formation of the S_1 state is a function of the electronic state excited. For excitation of higher electronic states, the formation of the S_1 state had a

longer time constant (about 400 fs when excitation of the S_4 state). The time constant of the internal vibrational excess energy redistribution after formation of the S_1 state was found to be about 4 ps for all measurements exciting different electronic states.

1.4. Solid-state organization and optical properties

Light-emitting molecular solids and their potential utility in optical devices, sensors and biological imaging has catalysed its emergence as an area of topical research with a spectrum of prolific activities. The light emitting behaviour molecular solid differ from that of dilute solution because emission of the solid-state is dictated by the whole collective rather than by individual molecules. Studying molecular crystals provides essential information on a) how molecules are arranged with respect to their neighbours in solid-state, b) weak interactions that bind them together and c) conformational preferences required to correlate the structural facts with several macroscopic properties, including their emission characteristics. Such systematic knowledge pertaining to how complex properties emerge from collections of molecules and how sensitive these properties are to specific molecular ordering in solids, could be translated to deriving new strategies to control molecular arrangement, to tune solid-state luminescent properties and also to obtain multi-colour emission[23]. Noncovalent routes inclusive of polymorphism, phase transition, nano/microcrystal forms and multi-component systems, have evolved as an efficient method to draw such correlations with a minimum number of variables[24-26]. Also it provides an opportunity to enhance the utility of a molecule of interest by

generating a wide range of solid forms and with added scope for tailoring the emission characteristics.

1.4.1. π - π interactions in polynuclear aromatic hydrocarbons

Polynuclear aromatic hydrocarbons (PAHs) are well-known to crystallise in four possible structural motifs: herringbone, sandwichherringbone, γ - and β -structures (Figure 1.4)[27-29]. Each motif is associated with a particular π -interaction geometry. The herringbone motif is constructed from edge-to-face interactions while offset stacking, as well as edge-to-face interactions, are observed in the sandwich herringbone motif where molecules stack in pairs. In the γ -motif, molecules form infinite stacks (offset and/or face-to-face) along one axis and a form of herringbone (edge-to-face) along another axis. The graphitic type layering assembly that arises in the β -motif is promoted primarily by face-to-face or offset stacking of the molecules. Because PAHs consist exclusively of carbon and hydrogen atoms, there are only three

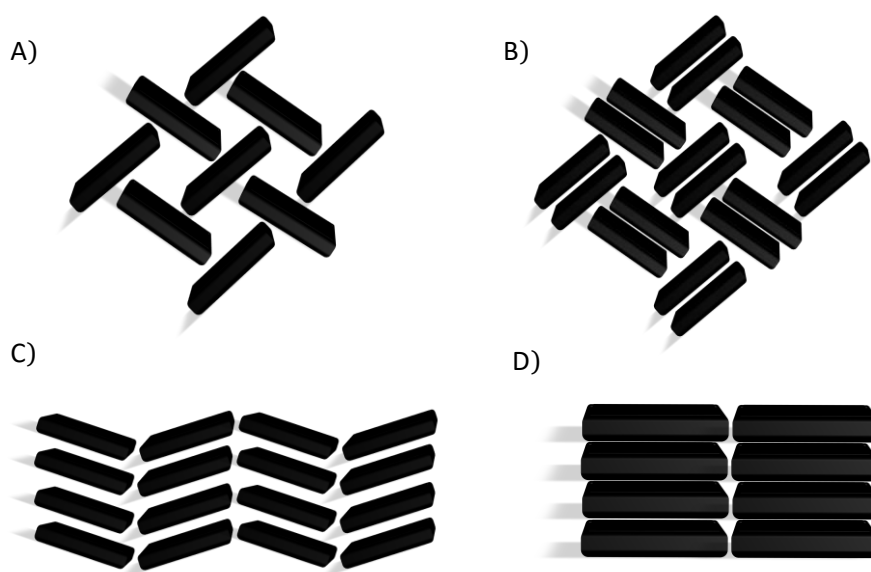


Figure 1.4. Pictorial representation of the A) herringbone; B) sandwichherringbone; C) gamma (γ) and D) beta (β) packing motifs.

possible types of interatomic interactions: C...C, H...H and C...H. The C...C interactions are optimised between parallel molecules stacked at van der Waals separation distances, whereas the C...H interactions are more effective between inclined molecules[28]. It therefore follows that the β - and γ -structures are rich in C...C interactions, C...H interactions are more prevalent in the herringbone motif, and both types of interactions are observed to a similar extent in the sandwich herringbone arrangement[28]. These observations prompted Desiraju and Gavezzotti[27-29] to investigate the molecular free surfaces of such molecules and the contributions of molecular areas to the final packing arrangement; atoms located at the core of the molecule, as well as a few peripheral carbon atoms, promote stacking (layering) while the remaining atoms facilitate glide (herringbone) packing.

In order to evaluate the packing motifs of aromatic molecules in crystals, Barbour and co-workers[30] proposed a quantitative analysis to classify the crystal structure to a particular packing motif. In order to assess the packing motif of the crystal structure, the relative contribution of each intermolecular interaction were determined and finally calculate ratios of these interactions ($\%C...H / \%C...C$). The herringbone structures all have ($\%C...H/\%C...C$) ratios greater than 4.5, sandwich motifs are in the

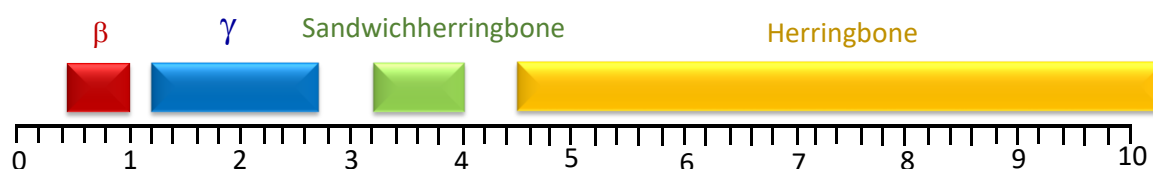


Figure 1.5. Bar chart representation of the ratios of ($\%C...H$)/($\%C...C$) interactions and the corresponding packing motifs of PAHs.

range of 3.2–4.0; γ -motifs in the range 1.2–2.7 and β -motifs fall in the range between 0.46–1.0 (Figure 1.5).

1.4.2. Tuning solid-state luminescence: Structure – optical property relationships

Several approaches are being sought to modify the fluorescence wavelength and intensity in the solid-state (state in which compounds are intended to be used) aggregate suspensions, thin films or crystalline materials. Though our molecular level awareness on the structure–property relationship in terms of optical properties is fairly well established, the perception on factors that precisely control bulk or supramolecular properties is still hazy. In organic materials, modification or alteration of chemical structures is a common approach to tune solid-state luminescence properties. For example, number and position of alkoxy substituents and alkyl chain length direct the molecular packing and consequently their fluorescence properties in diphenylbutadienes[31]. However, several limitations inherent to covalent synthesis and solid-state reactions make dynamic tuning or switching of solid-state luminescence a formidable target. Also because solid-state luminescence depends strongly on the intermolecular dipole coupling, resulting from the relative arrangements of neighbouring molecules and orientations of their dipole moments, it is difficult to expect similar properties in related molecules. Looking beyond the covalent routes that involve chemical modifications (synthetic tailoring of fluorophore cores), recent developments in the modulation of materials properties via non-covalent routes such as polymorphism (through conformational/packing changes), phase transition (structural changes while maintaining the molecular integrity),

amorphization (disrupting the long-range molecular ordering) and preparation of multi-component systems (controlling fluorophore aggregation) look promising.

1.4.2.1. Covalent routes to tune the optical properties

Several design strategies have been developed to alter the packing of organic molecules, such as extension of π conjugation to enhance the π - π interactions between adjacent molecules through chemical modification which includes incorporation of heteroatoms into the conjugated backbone to provide more non-covalent interactions (e.g., $S\cdots S$ and $N-H\cdots\pi$ interactions), and substitution with bulky groups. A detailed study on the photophysical properties of a series of alkoxy substituted diphenylbutadienes in solution and in the solid-state providing a molecular level understanding of the factors controlling their solid-state luminescence behaviour is reported by Suresh Das and co-workers[31](Figure 1.6A). The role of the number of

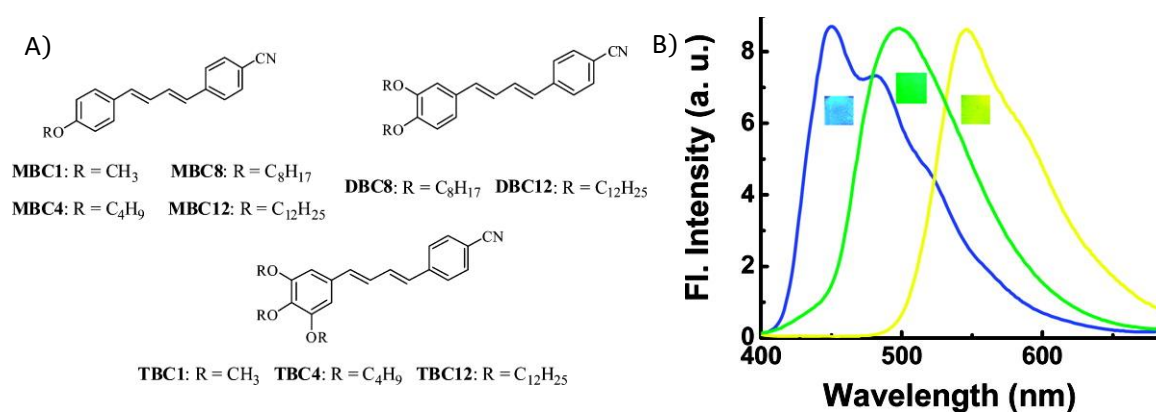


Figure 1.6. Shows (A) Molecules under investigation and (B) Normalized fluorescence spectra of thin films of MBC12 (blue spectrum), DBC12 (yellow spectrum), and TBC12 (green spectrum). λ_{ex} = 360 nm. The corresponding fluorescence as visualized on excitation with a 365 nm UV light is also shown (Adapted with permission from ref. 31. Copyright © 2008, American Chemical Society).

alkoxy substituents and the alkyl chain length in controlling the nature of the molecular packing and consequently their fluorescence properties has been elucidated. Whereas in the di- and tri-alkoxy substituted derivatives, the solid-state fluorescence was independent of the length of the alkyl chains, in the monoalkoxy substituted derivatives, increasing the length of the alkyl chain resulted in a visual change in fluorescence from green to blue. On the basis of the analysis of the molecular packing in the single crystals, this difference could be attributed to fluorescence arising from aggregates with an edge-to-face alignment in the molecules possessing short alkyl chains (methyl and butyl) to monomer fluorescence in the long alkyl chain containing derivatives (Figure 1.6B).

1.4.2.2. Non-Covalent routes to tune the optical properties

The utility in attaining the desired compounds through covalent synthesis is a tedious task which makes it as an inefficient technique to tune the solid-state properties. The solid-state luminescence within the chemically related molecules will vary depending on the intermolecular dipole coupling, resulting from the relative arrangements of neighbouring molecules and orientations of their dipole moments therefore it is difficult to expect similar properties. Looking beyond the synthetic tailoring of fluorophore cores (covalent routes) that involve chemical modifications, recent developments in the modulation of materials properties via non-covalent routes such as polymorphism (through conformational/ packing changes), phase transition (structural changes while maintaining the molecular integrity),

amorphization (disrupting the long-range molecular ordering) and preparation of multi-component systems (controlling fluorophore aggregation) look promising.

1.4.2.2.1. Polymorphism

McCrone defined a polymorph as “a solid crystalline phase of a given compound resulting from the possibility of at least two different arrangements of the molecules of that compound in the solid-state”[32]. This indicates that there are many ways in which molecules can arrange[33], while confining near-optimal packing. However, regardless of the degree of unpredictability, polymorphism offers an incomparable multitude of opportunities in material modifications and property modulations, without changing the molecular integrity[34]. Polymorphs often differ in their physico-chemical properties such as melting point, crystal shape, colour, chemical reactivity, dissolution rate, and solubility[35].

- **Extent of π -overlap and conformation differences**

In organic functional materials varied molecular arrangements based on the collective interactions, π -overlap geometries and co-planarity of adjacent π -planes could lead to different extent of electronic conjugation and solid-state emission characteristics[36, 37]. For example, five luminescent polymorphic form of 3(5)-(9-anthryl)pyrazole (ANP) exhibit distinct crystal packing by tuning the intermolecular interactions and hence the molecular assembly in the crystal structure (Figure 1.7A) [38]. Further to the hydrogen bond types, the emission colours of the crystal forms were correlated with the extent of π - π interactions: that with no interaction i.e. anthryl rings are well outside their van der Waals distance from each other (blue emission);

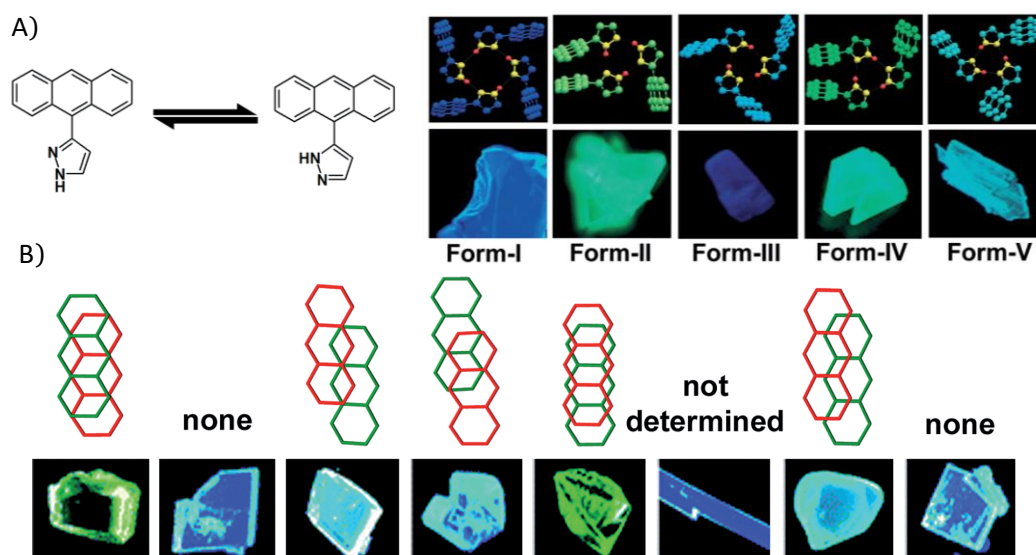


Figure 1.7. Shows (A) Tetramer and trimer assemblies in ANP polymorphs and photographs of corresponding crystals, excited under UV light ($\lambda_{ex} = 365 \text{ nm}$) (Adapted with permission from ref. 38. Copyright © 2006, John Wiley and Sons) and (B) Variations in extent of π -overlap and corresponding crystal emission colour in ANP derivatives (Adapted with permission from ref. 39. Copyright © 2009, American Chemical Society).

with strong interaction i.e. close face-to-face contacts between anthryl rings exist in their crystals (green emission), and with weak interaction i.e. characterized by weak π - π interactions between anthryl rings (blue-green emission). A series of 9-anthrylpyrazole derivatives were designed and synthesized and depending on the varying π -overlap of anthracene-arrangement, different emission colors were produced (Figure 1.7B)[39]. The emission colors of crystalline samples are strictly related to the intermolecular packing degree of the anthracene moieties: the larger overlapping area, the greater red shift of emission peak.

- **Excited state intramolecular proton transfer (ESIPT)**

A novel and effective mechanism of switching organic solid-state luminescence

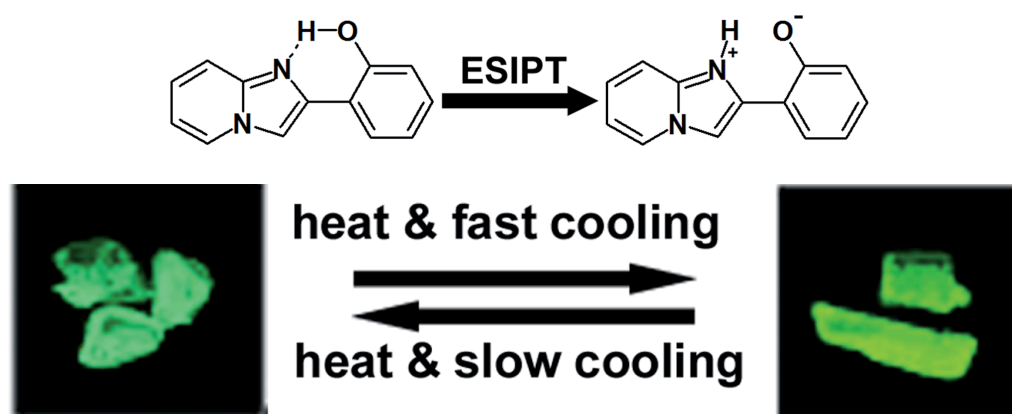


Figure 1.8. ESIPT-induced emission switching in 2-(2'-hydroxyphenyl)-imidazo[1,2-a]pyridine (Adapted with permission from ref. 41. Copyright © 2008, John Wiley and Sons).

based on an excited-state intramolecular proton-transfer (ESIPT) process[40] with resultant changes in dipole moment are a good route to achieve switchable emission colour and intensity. Interconversion of the crystal forms of 2-(2'-hydroxyphenyl)imidazo[1,2-a]pyridine by a thermal dry process realized switching of ESIPT luminescence between blue-green and yellow emission and also leads to differences in molecular conformations and modes of packing (Figure 1.8)[41]. Similarly, 2-(2-hydroxyphenyl)-4(3H)-quinazolinone (HPQ) exhibits emission by ESIPT to form dimorphs with different conformational twist[42]. The conformational twist between the phenyl and quinazolinone rings of HPQ leads to different molecular packing in the solid-state, giving structures that show solid-state fluorescence at 497 and 511 nm.

1.4.2.2.2. Stimuli responsive phase transition and fluorescence switching

Stimuli responsive phase transition and the resultant changes in fluorophore arrangements has been actively investigated and is saturated with opportunity to

obtain multi-colour emission by fluorescence switching[43]. However, the design and synthesis of organic materials that display efficient and reversible switching between two luminescent states in the solid-state still remain a challenge. This can be mainly attributed to the fact that the conversion of molecular structures in the solid-state is often very difficult, making the controlled and reversible switching of solid-state luminescence between polymorphs rather exceptional[44]. Based on the type of stimuli, the materials are broadly classified as mechanochromic or piezochromic (mechanical shock)[45], thermochromic (temperature)[46], solvatochromic (solvent)[47] and vapochromic (vapour) materials[48].

- **Temperature-responsive materials**

Phase transition induced by temperature modulation provides an excellent method to switch the solid-state emission of molecular materials. Structural modulation brought through thermally reversible transformation between two polymorphic states of octyloxy cyano substituted diphenylbutadiene (BC8) possessing visually distinguishable fluorescence (Figure 1.9A)[49]. Melting results in disruption of the weak hydrogen bonds causing the molecule to move out of its interdigitated array and form separate layers of unidirectionally oriented molecular stacks. As a result, the π -stacks move closer to each other resulting in the formation of J-aggregates which exhibit green fluorescence. The slow recovery of the stable blue fluorescing state can then be attributed to a movement of the molecules within the crystal lattice to regain the original crystal structure, causing the interdigitation of the alkyl chains possibly due to the reformation of the weak hydrogen bonds.

Diethyl-2,5-bis(4-(trifluoromethyl)phenylamino)terephthalate (AA1) and diethyl-2,5-bis(3,5-bis(trifluoromethyl)phenylamino)terephthalate (AA2) exhibit (Figure 1.9B) thermally induced reversible phase transformations accompanied by emission switching[44]. When heated below the melting point at (144 °C), red emitting crystals of AA1 (Form-I; $\lambda^{\max}_{\text{em}} = 581 \text{ nm}$) exhibit thermochromic transformation to a yellow solid (Form-II; $\lambda^{\max}_{\text{em}} = 545 \text{ nm}$); similarly AA2 crystals transform from red (Form-I; $\lambda^{\max}_{\text{em}} = 610 \text{ nm}$) to green emitting form (Form-II; $\lambda^{\max}_{\text{em}} = 503 \text{ nm}$) at 124 °C. In both cases the emission switching involves the change from the H-aggregation state, which can lead to the red shifts of emissions spectra due to exciton delocalization, to the J-aggregation state. The reverse transitions occur, however, only after the compounds melt.

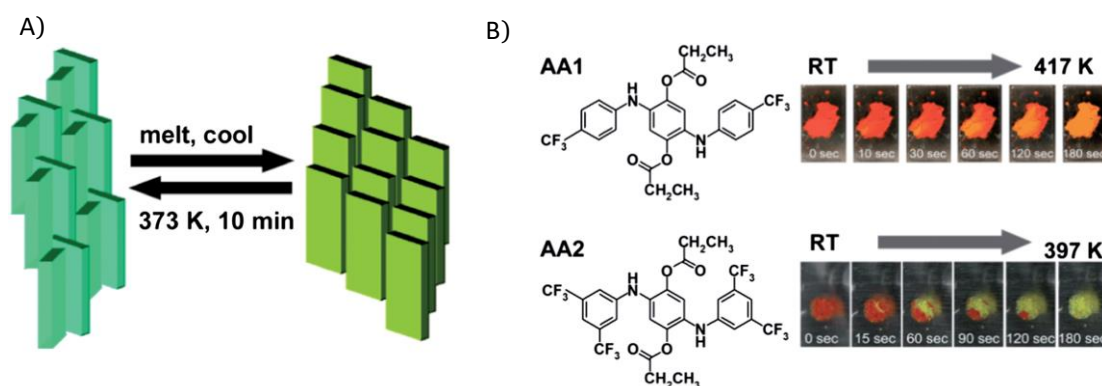


Figure 1.9. (A) Herringbone to brickstone structural transformation in BC8 (Adapted with permission from ref. 49. Copyright © 2004, Royal Chemical Society) and (B) Thermochromic transformations in AA1 and AA2 (Adapted with permission from ref. 44. Copyright © 2009, John Wiley and Sons)

- **Multiple-stimuli responsive materials**

Molecular compounds that undergo phase transition in response to multiple

stimuli with associated changes in emission characteristics are suitable for developing stimuli-responsive light emitting materials that have potential for various applications. The type of stimuli possible for ensuing emission switching are temperature, pressure and solvent vapour induced transformations[50-52].

Non-fluorescent asymmetric crystalline cyanostilbene derivative (Z)-3-(3',5' bis(trifluoromethyl)biphenyl-4-yl)-2-((4'-trifluoromethyl)biphenyl-4-yl)acrylonitrile [CN(L)-TrFMBE] produces tightly packed π -dimer systems exhibiting reversible [2 + 2] cycloaddition with characteristic fluorescence modulation (Figure 1.10A)[53]. The CN(L)-TrFMBE π dimer crystals are not at all fluorescent initially but switch to a highly fluorescent state ($\Phi_{\text{PL}}=24\%$) when an external shear-strain and/or prolonged UV

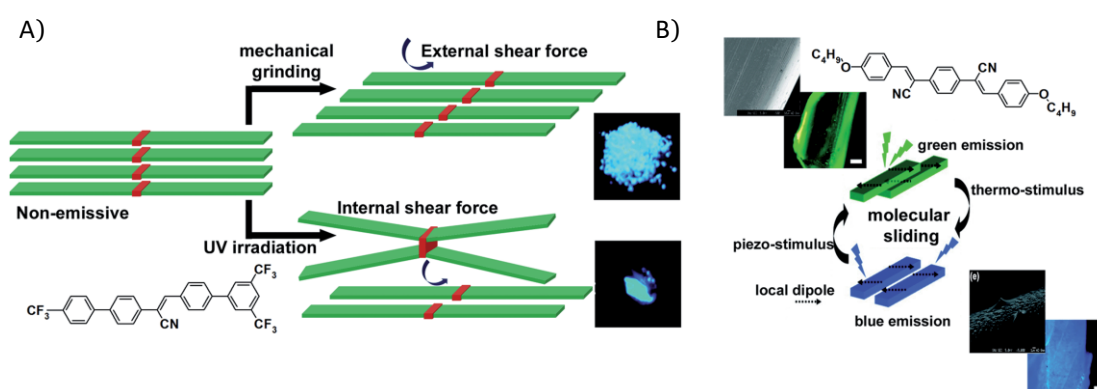


Figure 1.10. Schematic representation of (A) mechanisms for fluorescence at the cost of frustrated [2 + 2] cycloaddition in CN(L)-TrFMBE (Adapted with permission from ref. 53. Copyright © 2009, American Chemical Society) and (B) Different modes of slip-stacking in DBDCS molecular sheets; thermo/piezochromic switching between green and blue forms. SEM images show corresponding changes on the crystal surface (Adapted with permission from ref. 54. Copyright © 2010, American Chemical Society).

(365 nm) irradiation is applied. The close pairs of stilbenic (C=C) bonds (~ 3.8 Å) due to the antiparallel π dimers in the pristine crystal become perturbed under applied stimuli hence fluoresce with strong sky-blue emission at the cost of frustrated [2+2] cycloaddition. Similarly, cyanostilbene-based [(2Z,2'Z)-2,2'-(1,4-phenylene)bis(3-(4-butoxyphenyl)acrylonitrile (DBDCS))] highly luminescent molecular sheets which exhibit two-color fluorescence switching in response to pressure, temperature, and solvent vapor were reported (Figure 1.10B)[54]. Thermal annealing at 125 °C leads to sliding of molecular sheets along the shorter axis of DBDCS to initiate a phase transition with resulting shift in solid-state emission from green light ($\lambda^{\text{max}}_{\text{em}} = 533$ nm) to blue ($\lambda^{\text{max}}_{\text{em}} = 458$ nm). Rough and sheet-like regular surface projections on the transformed crystals further validates the layer-sliding mechanism. Form-II solid reverts to Form-I under shear stress and this two-colour fluorescence switching allows the fabrication of a poly(methyl methacrylate)–DBDCS blend film for rewritable fluorescent optical recording.

1.4.2.2.3. Crystal to amorphous transformation and emission switching

Crystal to amorphous conversion involves the transformation of a stable phase to one less stable. Amorphous phase being a high energy phase, amorphization requires the free energy of the crystal to be raised above to that of the amorphous phase and also involves destruction of the regular lattice arrangement by means of mechanical energy input or quench melting[55-58].

- **Amorphization by shear stress**

A heteroatom-containing luminogen (TPE-Py) obtained by melding a pyridinium

unit with tetraphenylethene through vinyl functionality under the shear stress caused transformation of crystalline phase to a non-ordered amorphous phase. The solid-state emission of TPE-Py can be reversibly switched between green and red color by grinding–fuming and grinding–heating processes with a high contrast due to the transformation from the crystalline to the amorphous state and vice versa (Figure 1.11A) [59]. Melding a benzothiazolium unit with tetraphenylethene generates a new hemicyanine luminogen, exhibiting crstochromism and its solid-state emission can be repeatedly tuned from yellow or orange to red by grinding–fuming or grinding–heating processes due to the transformation from the crystalline to the

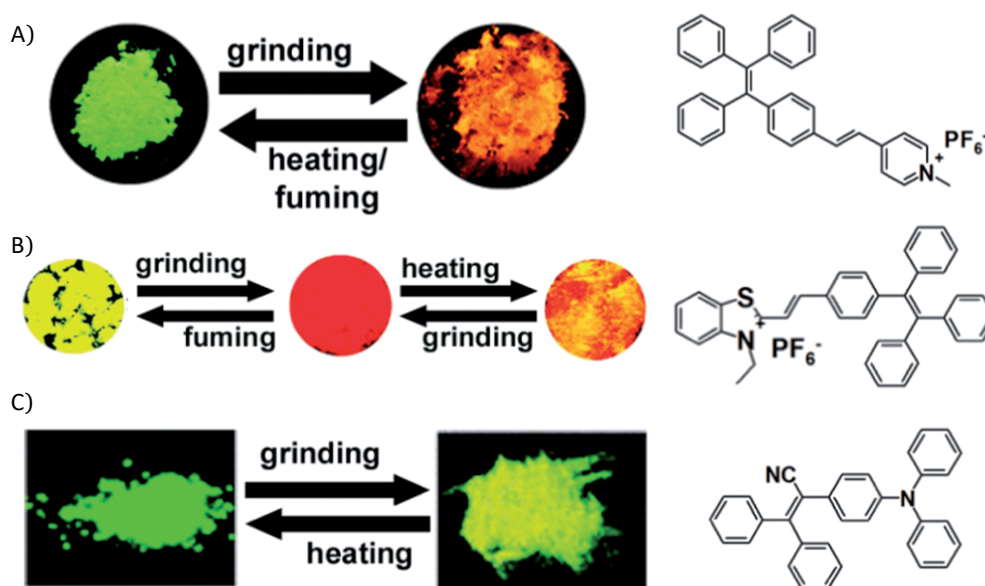


Figure 1.11. Stimuli-induced switching of solid-state emission by (A) TPE-Py (Adapted with permission from ref. 59. Copyright © 2013, Royal Society of Chemistry); (B) hemicyanine dye (Adapted with permission from ref. 60. Copyright © 2012, Royal Society of Chemistry) and (C) DPATPAN (Adapted with permission from ref. 61. Copyright © 2013, Royal Society of Chemistry).

amorphous state and vice versa (Figure 1.11B)[60]. Switching of emission colour from green ($\lambda^{\max}_{\text{em}} = 500 \text{ nm}$) to yellow ($\lambda^{\max}_{\text{em}} = 551 \text{ nm}$) with amorphization in DPATPAN, is an illustrative example in the context of tuning the solid-state emission by amorphization through shear stress (Figure 1.11C)[61].

1.4.2.2.4. Multicomponent systems to tune the emission properties

Supramolecular luminescent systems composed of two or more organic components provides a versatile approach to tuning and switching solid-state luminescence by controlling the molecular organization through weak interactions[62]. When compared to the synthetic point of view, this supramolecular approach is an easy method and highly desirable technique, and offers a wealth of opportunity for simple variation (by modifying one of the co-crystallization components) and excellent scope for tuning the solid-state luminescence by control of the solid-state structure[63].

The optical properties (such as UV-Vis absorption, luminescence emission, color, lifetime, quantum yield) in an organic solid chromophore, stilbene derivative, 1,4-bis-p-cyanostyrylbenzene (A) can be finely modified by supramolecular cocrystal formation (Figure 1.12A)[64]. By selecting the co-formers with different potential halogen or hydrogen bond interaction modes with the cyano group in A, six cocrystal systems have been synthesized, providing multi-color fluorescent organic materials. Effect of the nature of interactions and the molecular reorganization in the crystal lattice by cocrystallization is further evident from the large solid-state emission

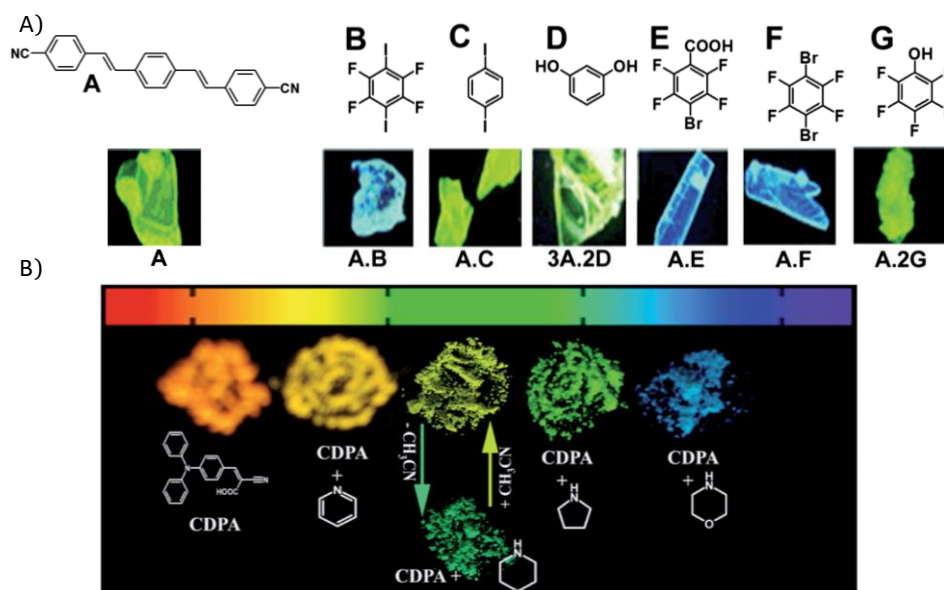


Figure 1.12. The emission switching observed in (A) 1,4-bis-*p*-cyanostyrylbenzene by means of co-crystallization (adapted with permission from ref. 64. Copyright © 2011, John Wiley and Sons) and (B) Fluorescence switching in CDPA by means of formation of multicomponent systems using acid–base interactions (adapted with permission from ref. 65. Royal Society of Chemistry).

switching observed in the molecular complexes of 2-cyano-3(4-(diphenylamino)phenyl)acrylic acid (CDPA) with organic amines (Figure 1.12B)[65]. Tuning and switching of the luminescence is demonstrated by exposing powdered CDPA to amine vapor (pyrrolidine, morpholine) and HCl solution.

1.5. Overview of optical behaviour of aggregate states

The π -conjugated molecules in solution or amorphous or crystalline solid-state exhibit two distinct types of aggregate namely J- and H-aggregates. The J-aggregates (J for Jelly who discovered the phenomenon of J-aggregates) show bathochromic shift (red shift) and H-aggregate show hypochromic shift (blue shift) in absorption spectra

in comparison to the monomer spectra. The exciton theory is developed by Micheal Kasha[66], describes the correlation between structure of aggregates and their absorption spectra. According to exciton theory, dye molecules are considered as point dipoles and upon aggregation the excited state split into two levels one being higher in energy and the other being lower in energy compared to the monomeric excited state (Figure 1.13). The allowed and forbidden transitions of the electron are governed by the tilt or slip angle (α) which is the angle between the transition dipole moments and the line joining the centres of the molecule. In the case of J-aggregates having head to tail arrangement of molecules ($\alpha < 54^\circ$), the allowed transition is to the lowest excited state which results narrow red shifted emission (Figure 1.13). But in the case of H-aggregate having face to face or sandwich type of molecular arrangement ($\alpha > 54^\circ$), the allowed transition is to the upper excited state level which results blue shifted emission (Figure 1.13)[67].

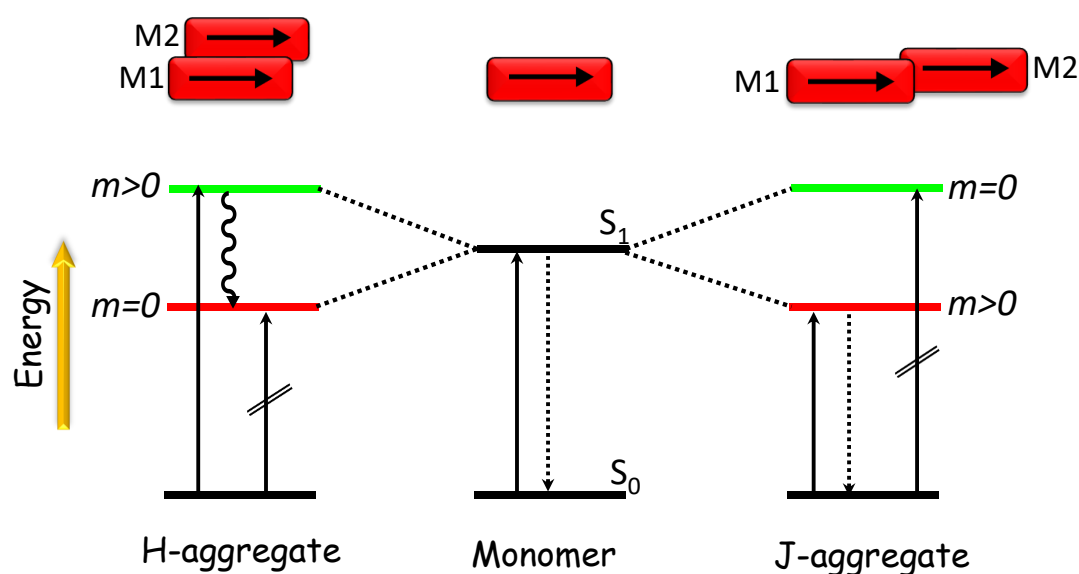


Figure 1.13. Schematic diagram showing the formation of H- and J-aggregates with their possible electronic transitions.

Curtis and co-workers[68] analyzed solid-state packing through the inclinations in given π -stack describing the inclination by two angles, called “pitch (P) and roll (R)” from an “ideal” cofacial π -stack (H-aggregate). The “pitch” inclinations describe translation of adjacent molecules relative to one another in the direction of the long molecular axis, while the “roll” inclinations that along the short molecular axis. Figure

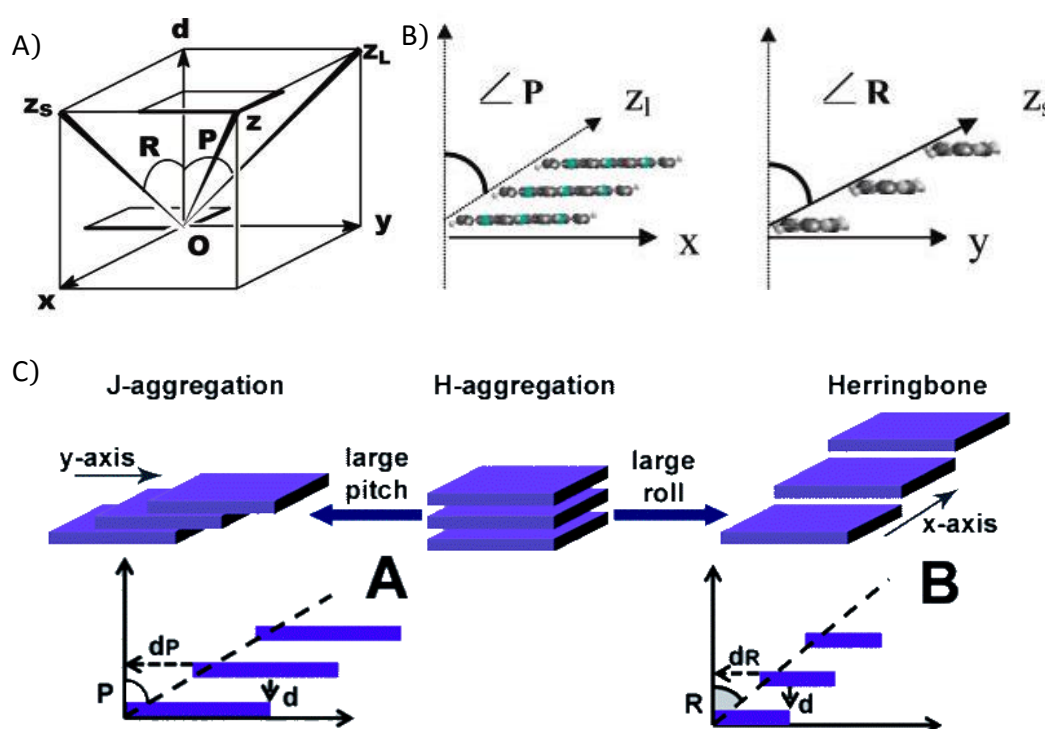


Figure 1.14. Definition of (A) pitch (P) and roll (R) angles and associated distances and vectors. The labels x and y refer to the directions of the short and long molecular axes, respectively; (B) View along the short molecular axis of a “pitched” π -stack and along the long molecular axis of a “rolled” π -stack and (C) Schematic representation of “pitch” and “roll” angles/distances (P/dP; R/dR) and the structural description of Herringbone as well as H- and J-aggregates in terms of relative translation of molecules. Insets A and B represent pitch and roll inclinations that lead to J-aggregate and Herringbone (Adapted with permission from ref. 68. Copyright © 2004, American Chemical Society).

1.14A shows the definitions of the pitch and roll angles. Let the x-y plane be parallel to the molecular plane of a molecule in a π -stack. The vectors, x and y , represent the short and long axes of the molecule, respectively, and they are perpendicular to each other. The shortest distance between the planes of the two adjacent molecules in the π -stack is defined by a vector, d , which is perpendicular to the molecular plane (Figure 1.14B). Moderately large pitch distortions preserve π - π interactions between adjacent molecules (J-aggregation), whereas roll translations greater than 2.5 Å lead to minimum π -overlap (Herringbone-type) (Figure 1.14C). Compared to the cofacial π -stacked structure in H-aggregates, translation of molecules along the long molecular axis leads to a head-to-tail arrangement with an enhanced delocalization of electronic excitation over several molecules due to a significant retention of π -overlap between neighbouring molecules. Such structural variations in molecular aggregates have profound influence on their fluorescence properties such as emission wavelength and efficiency.

1.6. Electronic and optoelectronic organic devices

The study of the influence of the crystal packing on the device performance is essential to design new promising materials. The structure-property correlation is still not well understood, although currently great efforts are being devoted in this direction, both theoretically and with experiments. The solid-state packing of the organic semiconductors depends on the nature of their conjugated electronically delocalized core together with the substituents that they might bear. However, it is

extremely difficult to predict the solid-state order of the crystal engineered molecules since small chemical modifications can cause a huge difference in the solid-state organization. Ideally, the investigation of the influence of the solid-state packing on the transport should be carried out in materials that are as similar as possible (i.e., molecular formula, type of intermolecular interactions, and electronic properties) and that only differ in crystal structure.

1.6.1. Organic field effect transistors

The first germanium based device, the transistor invented by John Bardeen, William Shockley and Walter Brattain (1947) is regarded as one of the greatest discoveries of the 20th century since it is the basic component in modern electronics. However, due to the fact that inorganic electronics have some technological limitations associated with them, organic-based devices have recently emerged in the market, beginning to replace amorphous silicon in some applications, and also have great possibility to find their place in a wide range of new applications. One of their main advantages is solution-processability, and thus, organic materials offer the possibility to fabricate low-cost and flexible devices and are also suitable for large area applications. This has been the motivation for why this field has been labeled “organic and large area electronics (OLAE)”. In addition, the versatility of organic synthesis allows for the preparation of materials according to promising properties. That is, since by chemically modifying their molecular structure and functionality the solid-state structure and the resulting macroscopic properties are altered, it is feasible to synthesize tailored materials for specific uses.

The operation principle of an organic field-effect transistor (OFET) relies on the application of an electric field that causes the formation of a conducting channel in the dielectric/semiconductor interface. The two main configurations employed in OFETs are depicted in Figure 1.15 and are known as top contact and bottom contact. In both cases, the organic semiconductor deposited on a dielectric is contacted with two metal contacts, namely, the source and drain, and on the other side of the dielectric a third contact, the gate, is placed. Thus, the source-drain current (I_{SD}) flowing along the

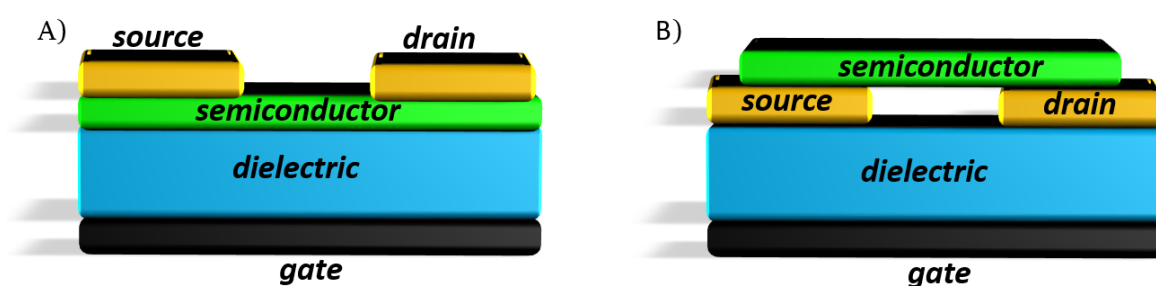


Figure 1.15. Common OFET configurations employed: (A) top contact and (B) bottom contact.

organic material can be modulated by application of a gate voltage (V_G) between the source and the gate, which creates an electric field responsible for the formation of an accumulation layer of charges at the semiconductor/dielectric interface. Also, depending on the V_G applied, the nature of the charge carriers accumulated at the interface can be controlled, that is, holes (in p-type semiconductors) or electrons (in n-type semiconductors). The voltage applied to the gate shifts the highest occupied molecular orbital (HOMO) and lowest unoccupied molecular orbital (LUMO) energy levels with respect to the metal Fermi level (E_F) of the source-drain contacts, which

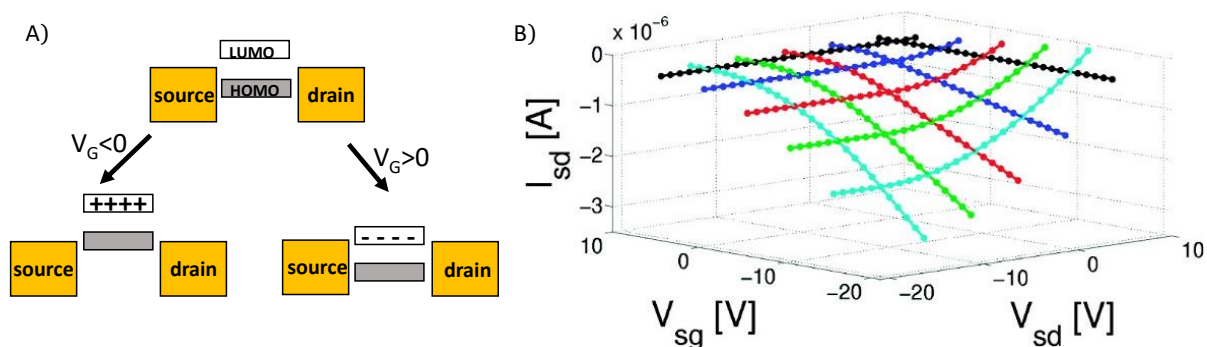


Figure 1.16. (A) Schematic representation of the HOMO and LUMO of the organic semiconductor with respect to the source-drain metal Fermi level and (B) theoretical transport properties from a p-type OFET.

allows for the formation of the conducting channel (Figure 1.16A). Hence, a negative gate voltage shifts the orbitals up and might result in the alignment of the HOMO with E_F , making it possible to have hole conduction. Otherwise, if a positive gate voltage is applied, the HOMO and LUMO will shift down, and if the LUMO becomes resonant with E_F , electrons will flow from the metal to the LUMO. However, one should bear in mind that the orbital shifting induces bending of the bands near the source-drain electrodes and, thus, there is an energy barrier at these contacts. The calculated electrical characteristics obtained in an OFET are shown in Figure 1.16B. In general, the OFET transport properties are described with two types of graphs. The output characteristics correspond to the representation of the I_{SD} versus the V_{SD} at fixed V_G . In this plot, it is clearly observable that there are two regimes, the linear regime, where the current is described by a parabola, and the saturation regime, where the source-drain current is independent of the source-drain voltage. Additional information can be extracted from the transfer characteristics, which plots the I_{SD} with

the V_G at fixed V_{SD} . Here, the on/off ratio, which is the ratio of current in the accumulation mode to the current in the depletion mode, and the threshold voltage (V_T), that is, the gate voltage from which the conduction channel starts to form, can be easily visualized.

1.7. Objective of the thesis

Pyrene is considered to be the most intriguing polyaromatic hydrocarbons (PAHs), due to its diverse photophysical properties. Upon photoexcitation, the energy redistribution to lower electronic states involves strong vibronic couplings leading to an ultrafast internal conversion (< 150 fs). All these processes, ultimately lead to fluorescence originating from the lowest excited singlet state. As a result, most of the studies were focused to understand the ultrafast internal conversion process in the first hundreds of femtoseconds after excitation. The photoexcited ultrafast properties in aromatic carbonyl compounds is generally rationalized by intersystem crossing, internal conversion, and charge transfer processes. However, much less is known, regarding the excited-state dynamics and relaxation mechanisms of carbonylpyrenes. In Chapter 2, we try to decipher the excited state dynamics of a series of carbonylpyrenes using ultrafast transient absorption studies. In Chapter 3, we emphasize on the peripheral substitution of pyrene core through successive acylation/benzoylation which cause a structure driven ordering in the crystalline state. Such structurally driven approach hold promise for a detail understanding of the intermolecular interactions which helps to regulate the arene-arene interactions in fluorescent pyrene crystals. The recent interests in pyrene based semiconductors is due to control over molecular architecture that can be achieved by modifying the structure by varying the position of substitution on the pyrene ring. Conductivity

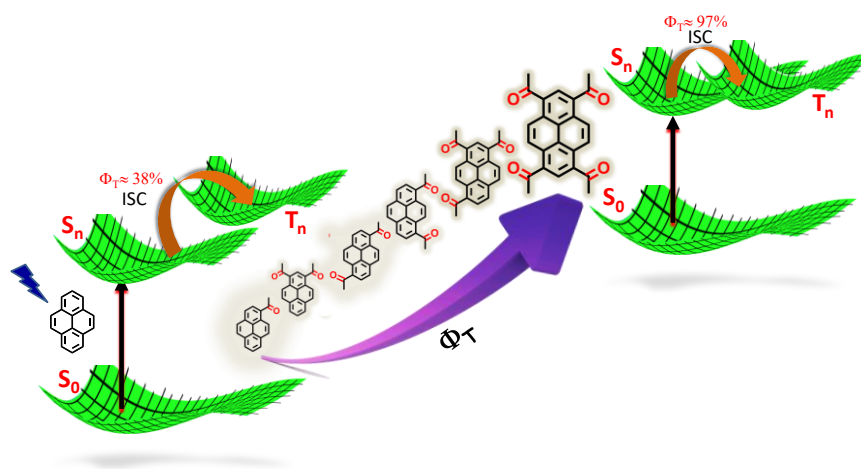
measurements in acetylpyrene crystals reveal that π -stacked packing (brickwork and columnar) is better than herringbone packing for enhanced conductance. In Chapter 4, emphasis the control over morphology that can be achieved in acetylpyrene to form microscale conducting materials and their potential application in optoelectronic devices.

Chapter 2

Vibronically accelerated intersystem crossing competes with internal conversion in acetylpyrenes

Abstract

Amongst polyaromatic hydrocarbons (PAHs), pyrene (P) is considered to be most intriguing molecule, due to its diverse photophysical properties. The pyrenyl class of chromophores has gained widespread attention from long-time owing to their robust nature, high molar absorptivity, extensive derivatization possibilities and their applications as long-lasting laser dyes, biological sensors and light harvesters for solar energy conversion. Despite this versatility and the simplicity of the molecular structure, pyrene shows complex intramolecular photophysical properties. The intermolecular energy redistribution after excitation to higher electronic states involves strong vibronic couplings of the electronic states leading to an ultrafast internal conversion ($S_1 \leftarrow S_n$) that has been measured to be within 150 fs. All these processes, ultimately lead to a fluorescence contribution originating from the excited singlet state. Hence a lot of studies were focused to understand the ultrafast internal conversion processes within first hundreds of femtoseconds after excitation. It is well-known that carbonyl functional groups exhibit a degree of spin-orbit coupling at the carbonyl oxygen that allows for intersystem crossing, generating triplet state (T_n). Albeit, widely investigated, the understanding about the photophysics of carbonylpyrenes is greatly limited to their characteristic singlet emission properties. Investigation of ultrafast excited state dynamics of this family of chromophores is trivial in understanding fundamental energy/electron transfer phenomena similar to that associated with excited state structural changes. In this chapter, we present quantitative studies of the excited-state dynamics of carbonyl-functionalized pyrene derivatives by using broadband transient absorption spectroscopy.



2.1. Introduction

Amongst polyaromatic hydrocarbons (PAHs), pyrene (P) is considered to be most intriguing molecule, due to diverse photophysical properties[69, 70]. The pyrenyl class of chromophores has gained widespread attention from the long-time owing to their robust nature[71], high molar absorptivities, extensive derivatization possibilities[4, 5, 72] and their applications as long-lasting laser dyes[73], biological sensors[74, 75] and light harvesters for solar energy conversion[76]. Despite this versatility and the simplicity of the molecular structure, pyrene shows a complex intramolecular photophysical properties. The intermolecular energy redistribution after excitation to higher electronic states involves strong vibronic couplings of the electronics states leading to an ultrafast internal conversion ($S_n \leftarrow S_1$) that has been measured to be 150 fs. All these processes, leading ultimately leads to a fluorescence contribution originating from the excited singlet state (S_2). Hence a lot of studies were focused to understand the ultrafast internal conversion process in the first hundreds of femtoseconds after excitation. The photophysical properties of most aromatic carbonyl compounds have been generally rationalized by intersystem crossing[77], internal conversion[78] and charge transfer[79]. However, much less is known, regarding the excited-state dynamics and relaxation mechanisms of pyrene chromophores functionalized with carbonyl groups.

It is well-known that carbonyls functional groups exhibit a degree of spin-orbit coupling at the carbonyl oxygen that allows for intersystem crossing generating triplet

state (T_n). In particular, pyrene chromophore is associated with singlet state photophysics. However, through the establishment of a gold(I)–carbon σ bond in (phosphine)gold(I) pyrene derivatives, the singlet state photophysics normally associated with the pyrene has been transformed to triplet state[80]. Similarly, substitution of pyrene with a nitro group similarly leads to remarkable ISC rates[81]. Though pyrene carbonyls are widely investigated, but limits in understanding the characteristic singlet emission properties ($S_n \leftarrow S_1$). Konishi and co-workers have reviewed the photophysical properties of carbonyl-functionalized pyrene derivatives [i.e., pyrene with aldehyde (1-formylpyrene), ketone (1-acetylpyrene), carboxylic acid (1-pyrenecarboxylic acid), and ester groups (1-methoxycarbonylpyrene)] using a measurement of absolute fluorescence quantum yield in various solvents and time-dependent density functional theory (TD-DFT) calculations[82-84]. Investigation of ultrafast excited state dynamics of this family of chromophores is trivial in understanding fundamental energy/electron transfer phenomena like associated with involving excited state structural changes. Here, we try to decipher the ultrafast excited state dynamics of carbonylated pyrene derivatives. In this letter, we present quantitative studies of the excited-state dynamics of carbonyl-functionalized pyrene derivatives by using broadband transient absorption spectroscopy and an in-depth global analysis of the observed kinetics. The observed ultrafast dynamics are rationalize with time-dependent density functional theory calculations.

2.2. Synthesis, characterization and crystallization of acetylpyrene derivatives (1-4AP)

Lewis acid-catalyzed (AlCl_3) electrophilic aromatic substitution of acetyl group on pyrene (P) in carbon disulfide (CS_2) affords acetylpyrene derivatives (1–4AP) in low to moderate yields (Scheme 1a, Row I)[13]. Adding a stoichiometric quantity of acetyl chloride to a solution of pyrene and AlCl_3 in CS_2 at ambient temperature rendered the desired acetylpyrene derivatives (1–4AP) (Figure 2.1, Row I)[85]. The molecular structures were further confirmed through single crystal X-ray analysis (Figure 2.1, Row II). Single crystals 1-3AP suitable for X-ray analysis were obtained by slow evaporation from varying composition of chloroform:hexane mixture while 4AP was obtained by temperature gradient cooling in chloroform.

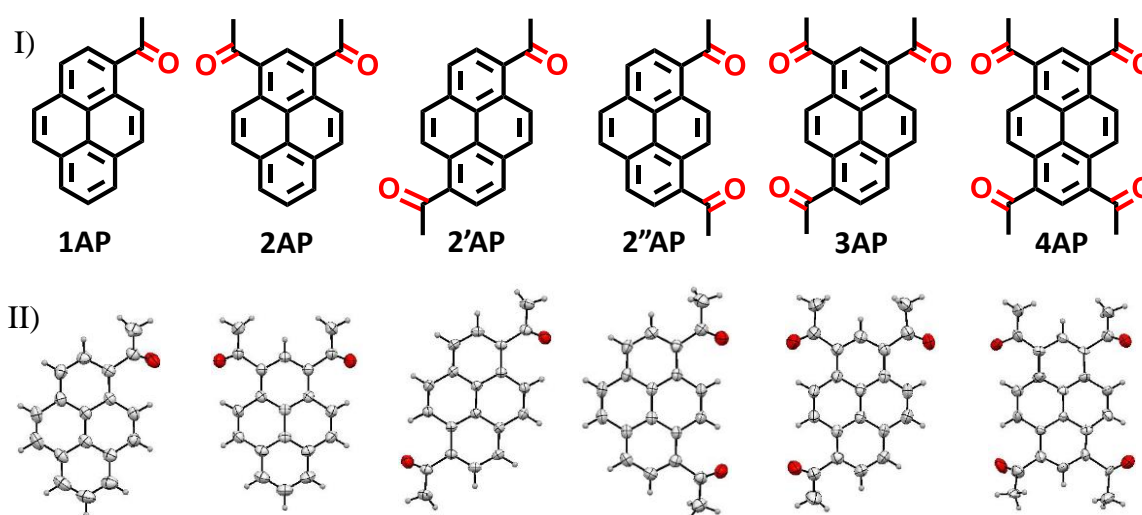


Figure 2.1. Row I: Schematic molecular structure and Row II: ORTEP diagram of the crystal structure of 1-4AP derivatives.

2.3. Results and Discussions

2.3.1. Frontier molecular analysis and steady-state absorption and emission measurements

Frontier molecular orbital (FMO) analysis, cyclic voltammetric, UV-Vis absorption and emission measurements were employed to investigate the extent of

electronic perturbations in P imparted by incremental acetyl groups. FMO analyses of 1–4AP shows that the electron density of HOMO is distributed in the P unit while the electron density of LUMO is more delocalized with a considerable extension to the carbonyl group(s) (Figure 2.2). Cyclic voltammetry was performed to investigate the variations in the HOMO-LUMO gap due to incremental carbonyl groups on the pyrene unit (Figure 2.3A). 1AP [0.1 M nBu₄NPF₆ in acetonitrile (ACN)], shows a reversible reduction peak (E_{red}) at -1.562 V *vs.* SCE corresponding to one electron reduction while oxidation peak appears at 1.483 V. The AP derivatives in ACN displayed a systematic decrease in the reduction potential, from $E_{\text{red}} = -1.562$ V *vs.* SCE for 1AP to $E_{\text{red}} = -1.0$ V *vs.* SCE for 4AP. Decrease in the electrochemical gap (HOMO - LUMO) of AP (3.045 eV for 1AP; 2.80 eV for 4AP; Table 2.1) in comparison to P (3.37 eV)[86] is in good agreement with the trend observed in the FMO analysis (Table 2.1).

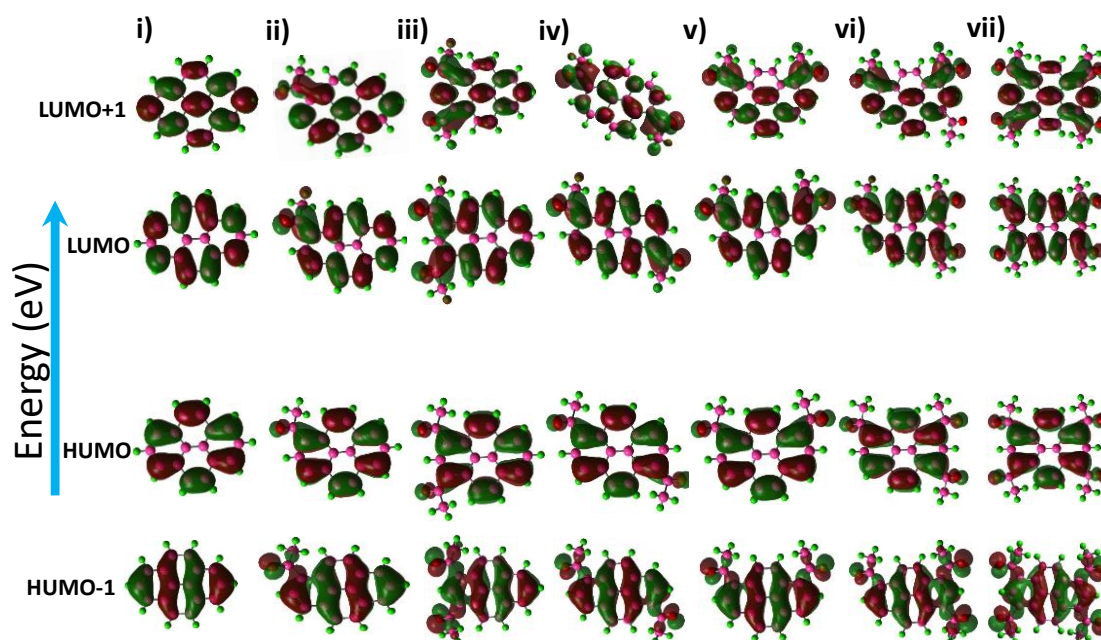


Figure 2.2. Illustrations of the frontier molecular orbitals of i) 1AP; ii) 2AP; iii) 2'AP; iv) 2''AP; vi) 3AP and vii) 4AP evaluated at the B3LYP/6-311G^{**++} from crystal structure.

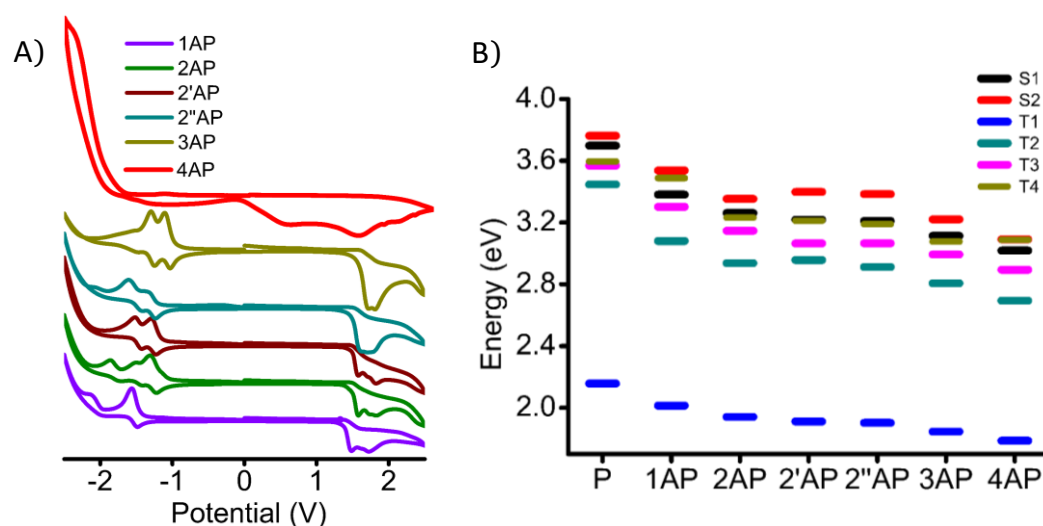


Figure 2.3. Shows A) cyclic voltammograms of 1-4AP derivatives in CH_3CN and B) energy level diagram for 1-4AP derivatives as calculated using TD-DFT (B3LYP/6-311G^{***})

UV-Vis absorption spectra of spectra of 1–4AP in chloroform exhibit bands centered around 286-298 and 359-407 nm respectively (Figure 2.4, Table 2.2)[85]. Successive addition of acetyl groups on P core afforded a systematic spectral change with a progressive red-shift (ca. 70 nm) in the absorption maximum of 4AP when compared to P. Time-dependent density functional theory (TDDFT)[87, 88] calculations were performed to examine the electronic transitions in 1–4AP derivatives (Table 2.3).

Table 2.1. Electrochemical experimental and calculated energy levels of 1-4AP derivatives.

	Energy levels (eV)				Energy levels (eV)			
	$E_{\text{on}}^{\text{ox}}$ (eV) ^a	$E_{\text{on}}^{\text{red}}$ (eV) ^a	E_{HOMO} (eV) ^a	E_{LUMO} (eV) ^a	E (eV) ^a	E_{HOMO} (eV) ^b	E_{LUMO} (eV) ^b	E (eV) ^b
1AP	1.483	-1.562	-6.283	-3.238	3.045	-5.834	-2.278	3.555
2AP	1.579	-1.306	-6.379	-3.494	2.885	-6.044	-2.611	3.432
2'AP	1.578	-1.290	-6.378	-3.51	2.868	-6.064	-2.676	3.387
2''AP	1.612	-1.344	-6.412	-3.456	2.956	-6.076	-2.704	3.372
3AP	1.724	-1.107	-6.524	-3.693	2.831	-6.260	-2.977	3.283
4AP	1.8	-1.0	-6.60	-3.80	2.80	-6.436	-3.241	3.194

^a experimental data; ^b computational data

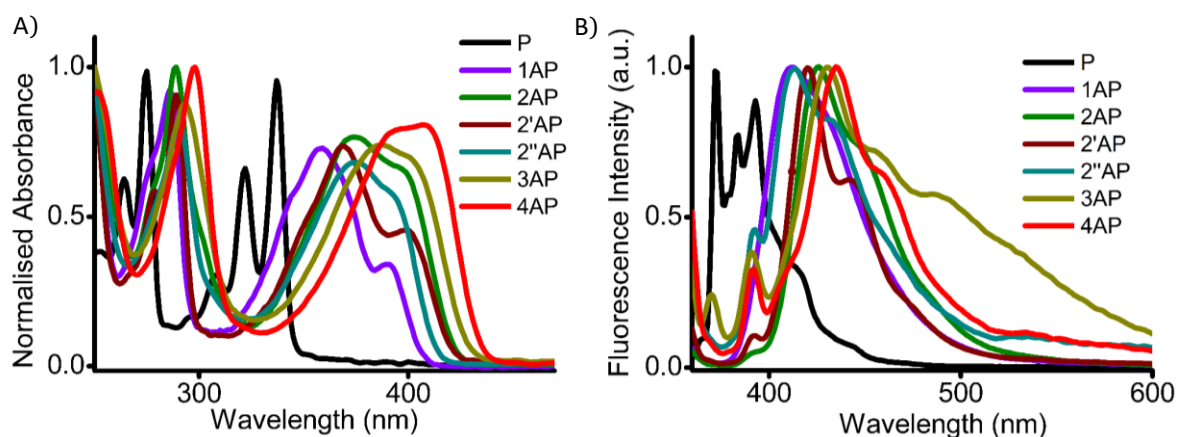


Figure 2.4. Shows the normalised (A) absorption and (B) fluorescence spectra of 1-4AP (0.1-1 μM) derivatives in CHCl_3 .

Low-lying excited electronic states mainly result from well-described $\pi-\pi^*$ transitions with a significant contribution from $n-\pi^*$ character. Figure 2.3B illustrates the plot of the vertical excitation energies where the energy level ordering in the singlet (S) and triplet (T) manifolds is shown. When compared to P, more delocalization of the excited singlet (S_2) is observed in 1-4AP with a decrease in the

Table 2.2. Photophysical properties of 1-4AP derivatives in CHCl_3 .

	$^a\lambda_{\text{abs}}$ (nm)	$^a\lambda_{\text{f}}$ (nm)	$^a\lambda_{\text{P}}$ (nm)	$^a\Phi_{\text{f}}$	$^a\tau_{\text{f}}$ (ns) [Amplitude] (%)	$^a\tau_{\text{P}}$ (ns)	$^a\lambda_{\text{T}}$ (nm)	$^a\tau_{\text{T}}$ (μs)	$^a\Phi_{\text{T}}$
P	337	393	-	0.75	150.1 [100]	-	415	11.0	38.0
1AP	359	412	520	0.004	1.39 [93] 0.98 [7]	12.7	450	4.85	52.30
2AP	373	426	520	0.008	1.39 [93] 0.65 [7]	9.8	450	5.76	90.09
2'AP	369	420	515	0.002	1.3 [80] 1.62 [20]	9.5	450	7.04	96.06
2''AP	375	413	520	0.008	1.4 [97] 0.6 [3]	11.3	490	10.13	94.53
3AP	388	431	525	0.003	1.2	9.4	490	11.08	96.45
4AP	407	435	520	0.002	0.98	11.4	500	12.16	97.03

^achloroform solution; abs – absorption; f – fluorescence; Φ - quantum yield; T- triplet

energy gap between S₂-T₄, bringing T₄ triplet state nearly isoenergetic to S₂ in 4AP.

Upon excitation at 350 nm, 1-4AP in chloroform shows bathochromic shift in the emission maximum which is in accordance with observed redshift in the absorption

Table 2.3. Excitation energy, oscillator strength, main transition orbital, and their contribution calculated for 1-4AP derivatives using TD-DFT (B3LYP/6-311G⁺⁺).

AP derivatives	State	Excitation Energy (eV)	Oscillator strength (f)	Main transition orbital	Contribution
P	T4	3.5953		HOMO-1→LUMO	0.57309
	T3	3.5686		HOMO→LUMO+2	0.51608
	T2	3.4472		HOMO→LUMO+1	0.57142
	T1	2.1566		HOMO→LUMO	0.68533
	S4	4.6312	0.0000	HOMO-2→LUMO	0.68233
	S3	4.3758	0.0000	HOMO→LUMO+2	0.68393
	S2	3.7618	0.0003	HOMO→LUMO+1	0.52179
	S1	3.6976	0.2523	HOMO→LUMO	0.66986
1AP	T4			HOMO→LUMO+1	0.50967
	T3			HOMO-2→LUMO	0.47969
	T2			HOMO-1→LUMO	0.50416
	T1			HOMO→LUMO	0.68261
	S4	4.2526	0.0189	HOMO-3→LUMO	0.53272
	S3	3.6842	0.0250	HOMO-2→LUMO	0.47754
	S2	3.5368	0.0042	HOMO-1→LUMO	0.48744
	S1	3.3811	0.3305	HOMO→LUMO	0.66907
2AP	T4	3.2322		HOMO-2→LUMO	0.61257
	T3	3.1466		HOMO-3→LUMO	0.55422
	T2	2.9366		HOMO-1→LUMO	0.62909
	T1	1.9407		HOMO→LUMO	0.68630
	S4	3.5789	0.0014	HOMO-2→LUMO	0.55139
	S3	3.5775	0.0175	HOMO-3→LUMO	0.63612
	S2	3.3534	0.0103	HOMO-1→LUMO	0.60578
	S1	3.2621	0.3659	HOMO→LUMO	0.67578

2'AP	T4	3.2122		HOMO-3→LUMO	0.58217
	T3	3.0649		HOMO-2→LUMO	0.56224
	T2	2.9569		HOMO-1→LUMO	0.63426
	T1	1.9112		HOMO→LUMO	0.68667
	S4	3.6180	0.0440	HOMO-3→LUMO	0.55533
	S3	3.5039	0.0000	HOMO-2→LUMO	0.64427
	S2	3.3982	0.0121	HOMO-1→LUMO	0.58073
	S1	3.2178	0.4263	HOMO→LUMO	0.67433
2''AP	T4	3.1900		HOMO-3→LUMO	0.57896
	T3	3.0655		HOMO-2→LUMO	0.58915
	T2	2.9120		HOMO-1→LUMO	0.61645
	T1	1.9024		HOMO→LUMO	0.68751
	S4	3.5600	0.0023	HOMO-3→LUMO	0.64141
	S3	3.4762	0.0186	HOMO-2→LUMO	0.54376
	S2	3.3842	0.0122	HOMO-1→LUMO	0.56911
	S1	3.2101	0.4039	HOMO→LUMO	0.67743
3AP	T4	3.0768		HOMO-3→LUMO	0.53675
	T3	2.9932		HOMO-2→LUMO	0.53079
	T2	2.8060		HOMO-1→LUMO	0.65503
	T1	1.8452		HOMO→LUMO	0.68923
	S4	3.4711	0.0127	HOMO-3→LUMO	0.58851
	S3	3.3850	0.0091	HOMO-2→LUMO	0.58001
	S2	3.2210	0.0174	HOMO-1→LUMO	0.62544
	S1	3.1141	0.4384	HOMO→LUMO	0.67619
4AP	T4	3.0880		HOMO-3→LUMO	0.64605
	T3	2.8940		HOMO-2→LUMO	0.60853
	T2	2.6939		HOMO-1→LUMO	0.66586
	T1	1.7869		HOMO→LUMO	0.69059
	S4	3.3928	0.0000	HOMO-5→LUMO	0.65801
	S3	3.2238	0.0000	HOMO-2→LUMO	0.67264
	S2	3.0911	0.0234	HOMO-1→LUMO	0.65083
	S1	3.0184	0.4624	HOMO→LUMO	0.67757

spectrum (Figures 2.4B). Low fluorescence quantum yield was observed for 1–4AP ($\Phi_f < 0.9\%$, Table S3; SI) in chloroform when compared with P ($\Phi_f = 75\%$)[89]. Pioneering work by Foggi et al [22] on P have established that the excitation at 340 nm populates the S_2 state which undergoes ultrafast internal conversion (τ_{IC}) to S_1 state at a rate constant of 150 ± 50 fs. Subsequently, fluorescence is observed from S_1 which forms the primary decay pathway of the S_2 with the remnants of excited singlet state (S_1) undergoing intersystem crossing to a triplet state. However in 1–4AP, strong mixing of nearly-degenerate singlet and triplet states as elucidated from the relative energies obtained from TDDFT calculations, brings efficient intersystem crossing (ISC) thereby forming a competitive pathway for internal conversion (IC). Picosecond time-resolved fluorescence measurement of 1–4AP in chloroform exhibits short singlet excited state lifetime (τ_f) in the range of 1–2 ns. (Figure 2.5, Table 2.2).

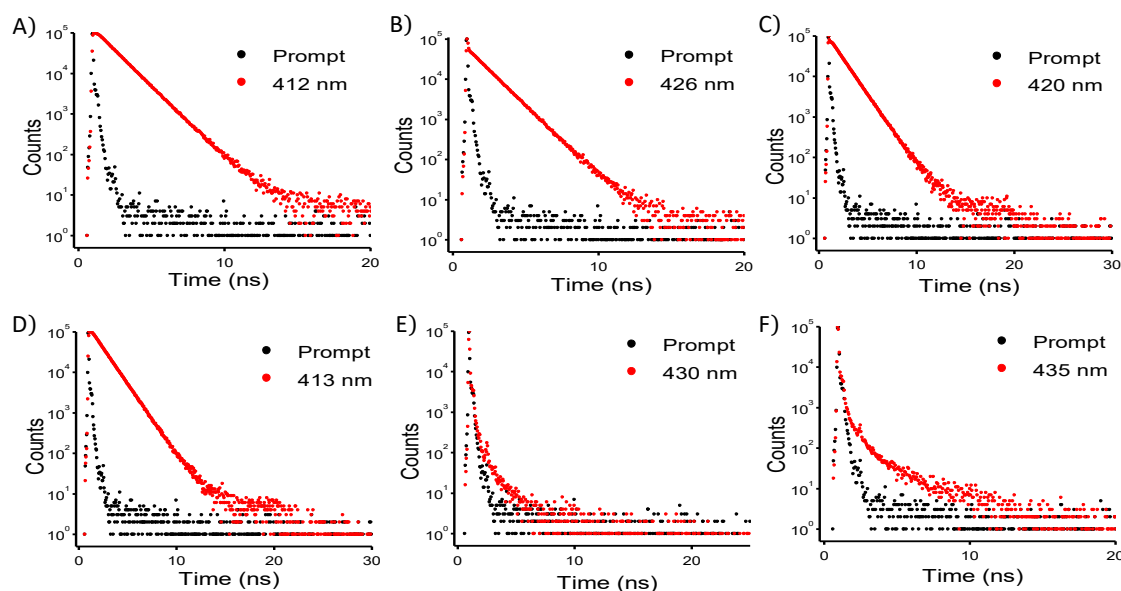


Figure 2.5. Shows fluorescence decay profile of (A) 1AP; (B) 2AP; (C) 2'AP; (D) 2''AP; (E) 3AP and (F) 4AP in $CHCl_3$ at the respective emission maximum ($\lambda_{exc}=375$ nm).

2.3.2. Nanosecond transient studies

In order to explore the excited-state dynamics, nanosecond and femtosecond transient absorption (nTA and fTA) techniques were employed to probe the events after the photoexcitation of 1–4AP in chloroform. Figure 2.6 shows the nTA spectra of 1-4AP after laser excitation (355 nm, 40 mJ per pulse). Upon excitation at 355 nm, nTA spectra for 1, 2 and 2'AP exhibit a transient absorption band centered at 450 nm with a bleach in the region that corresponds to the ground state absorption. 2'' and 3AP features a transient absorption band centered at 490 nm whereas 4AP shows transient absorption band at 500 nm. The transient absorption peak observed for 1–4AP derivatives in chloroform were readily quenched by the dissolved oxygen which strongly suggest that the transient species so formed after the nanosecond flash are due to the triplet excited state of P ($^3P^*$; Figure S5; SI)[90]. Singular value decomposition (SVD) of three dimensional ΔA versus time and wavelength spectral

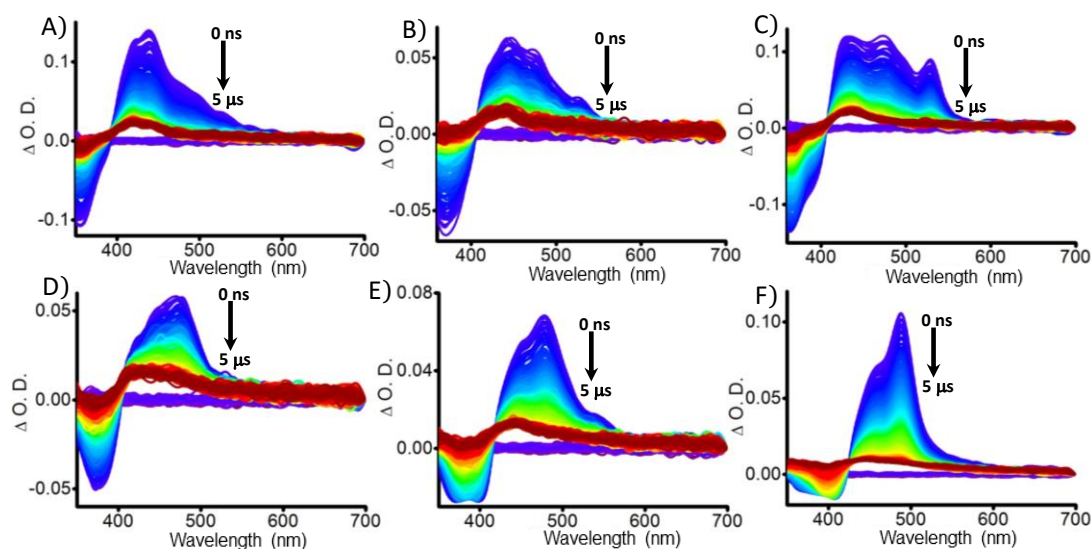


Figure 2.6. nTA spectra of (A) 1AP; (B) 2AP; (C) 2'AP; (D) 2''AP; (E) 3AP and (F) 4AP derivatives in $CHCl_3$.

data followed by global analyses were carried out to understand the principle components responsible for the respective transient absorption spectra for 1–4AP derivatives (Figure 2.7 and 2.8, Table S4; SI). SVD analyses of 1-4AP show only one

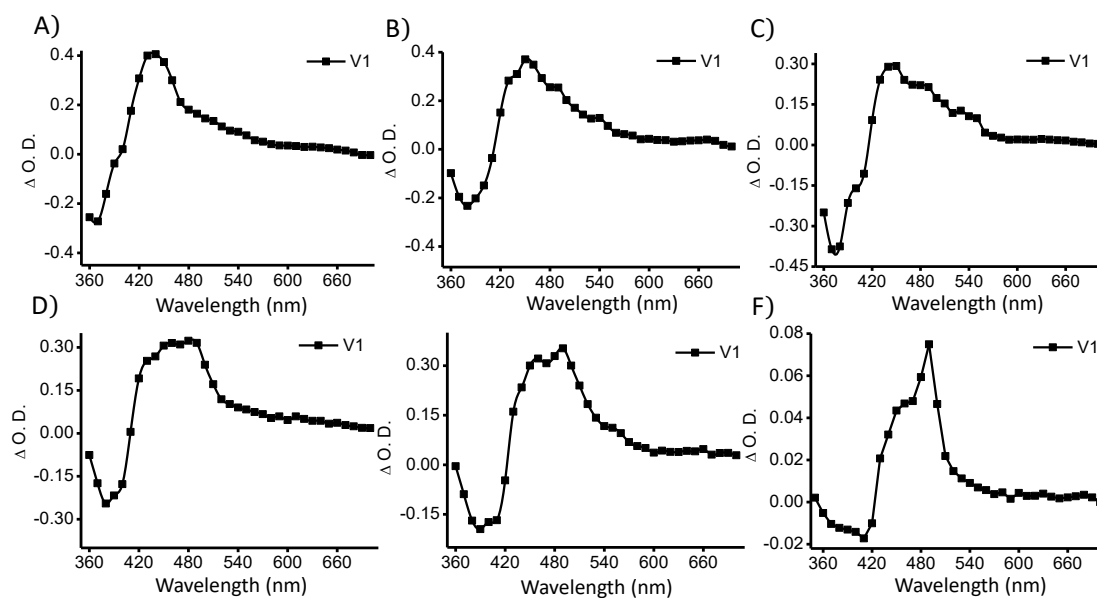


Figure 2.7. SVD of nanosecond transient spectra of (A) 1AP; (B) 2AP; (C) 2'AP; (D) 2''AP; (E) 3AP and (F) 4AP derivatives in CHCl_3 .

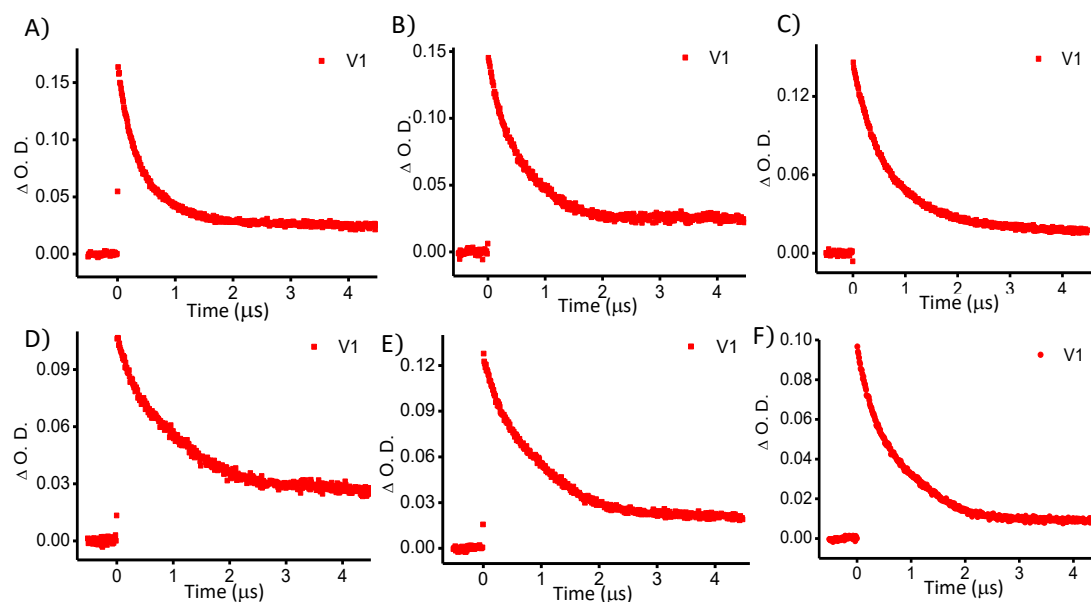


Figure 2.8. SVD of nanosecond transient spectra of (A) 1AP; (B) 2AP; (C) 2'AP; (D) 2''AP; (E) 3AP and (F) 4AP derivatives in CHCl_3 .

component with the right singular vector at the respective transient absorption spectrum, corresponding to $T_n \leftarrow T_1$ transition. Right singular vector at 450 nm for 1, 2 and 2''AP, exhibits triplet lifetime (τ_T) of 4.85, 5.76 and 7.04 μs , respectively, while right singular vector at 490 nm for 2'' and 3AP decay with a τ_T of 10.13 and 11.8 μs , respectively. A 2.5-fold increase in the τ_T was observed for 4AP in comparison with 1AP, which shows a triplet lifetime of 12.16 μs for the observed transient peak at 500 nm. Thus, a linear dependence on the rate of decay of the triplet excited state is observed on increasing the number of carbonyl substitution in the pyrene unit (Figure 2.9A, Table 2.2). Triplet quantum yield (Φ_T) of 1–4AP derivatives were determined by using triplet–triplet energy transfer to β -carotene with a tris(bipyridyl)ruthenium(II) complex ($[\text{Ru}(\text{bpy})_3]^{2+}$) as a reference[91]. Φ_T was determined by initially preparing optically matched (355 nm) solutions of $[\text{Ru}(\text{bpy})_3]^{2+}$ or 1–4AP derivatives in methanol and chloroform respectively, and were mixed with a known volume of β -carotene solution. The transient absorbance (ΔA) of the β -carotene triplet, which was formed

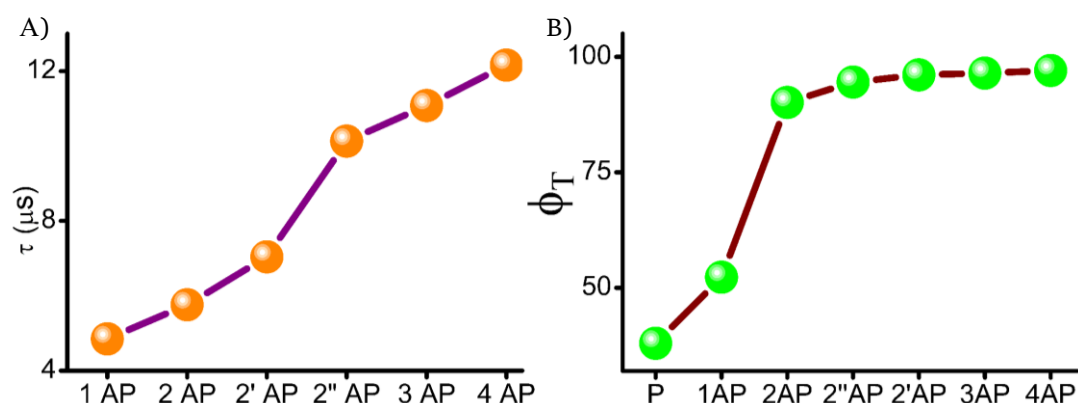


Figure 2.9. Shows A) Variation of triplet lifetime and B) triplet quantum yield of 1-4AP in CHCl_3 .

by energy transfer from $[\text{Ru}(\text{bpy})_3]^{2+}$ or 1–4AP triplet to β -carotene was monitored at 510 nm. Φ_T of AP derivatives are calculated to be 52.30% (1AP), 90.09% (2AP), 96.06% (2'AP), 94.53% (2''AP), 96.43% (3AP) and 97.03% (4AP). An remarkable enhancement in the Φ_T of AP derivatives with increase in the number of acetyl group(s) when compared to P (38.0%)[92] suggest the dominant role of carbonyl group in facilitating efficient ISC for triplet generation (Figure 2.9B, Table 2.2).

2.3.3. Femtosecond transient studies

*f*TA measurements were performed on 1–4AP in chloroform to investigate the photo-processes that occur in subnano/pico seconds (Figure 2.10). Upon excitation at 400 nm, using 110 fs laser pulse, 1–4AP exhibits transient absorption band initially evolved at 534 nm (1AP), 570 nm (2AP), 520 nm (2'AP), 520 nm (2''AP), 580 nm (3AP) and 595 nm (4AP). Foggi and co-workers have observed a similar spectral feature in the transient absorption spectra of P, after 340 nm excitation, populating higher

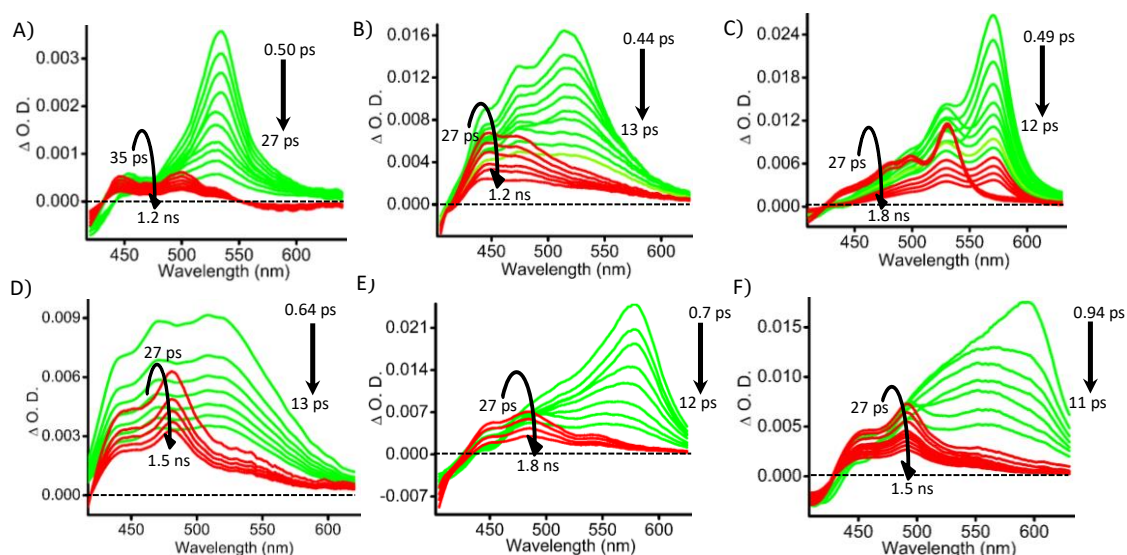


Figure 2.10. *f*TA spectra of (A) 1AP; (B) 2AP; (C) 2'AP; (D) 2''AP; (E) 3AP and (F) 4AP derivatives in CHCl_3 .

energy singlet (S_p) state ($S_n \leftarrow S_p$ transitions, where $p > n$). The singlet excited state (S_p) with an absorption maximum at 580 nm undergoes an ultrafast internal conversion within the singlet manifolds with a rate constant of 150 fs. This result supports the observed transient peak for 1–4AP monitored around 534–595 nm which undergoes ultrafast decay in subpicosecond time scale. It is pertinent to note that while the peak around 534–595 nm decays, concomitant appearance of another peak at 450 nm (1AP), 450 nm (2AP), 480 nm (2'AP), 480 nm (2''AP), 490 nm (3AP) and 500 nm (4AP) is observed within a time scale less than 10 ps (Figure 2.11). The observed peak at 450–500 nm, then decays within a time delay of 2 ns creating a long-lived absorption band. SVD followed by global analysis was employed to extract the lifetimes and decay associated spectra (DAS) from the multidimensional time-resolved absorption data. Data analysis offered two principle components around 534–595 nm and 450–500 nm

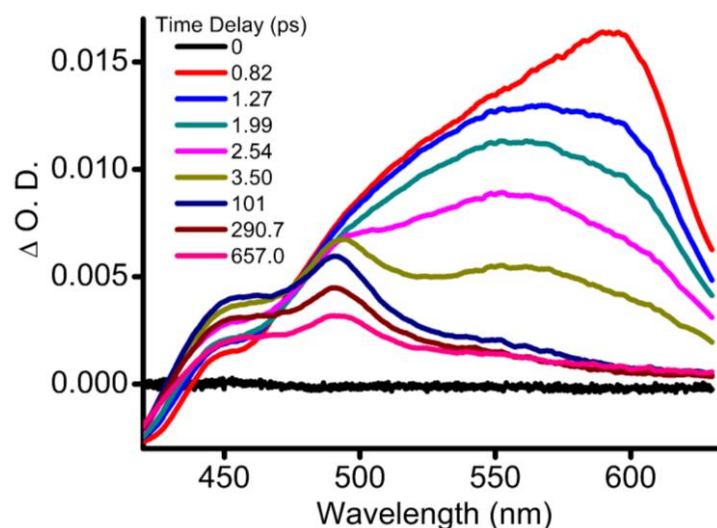


Figure 2.11. Transient absorption spectra for 4AP as plotted in the early time delay where at 3.5 ps a growth around 500 nm is observed.

respectively (Figure 2.12&2.13; Table 2.4). Two lifetimes are needed to fit the kinetic profile of the first principle component (V1), whereas V2 decays mono exponentially.

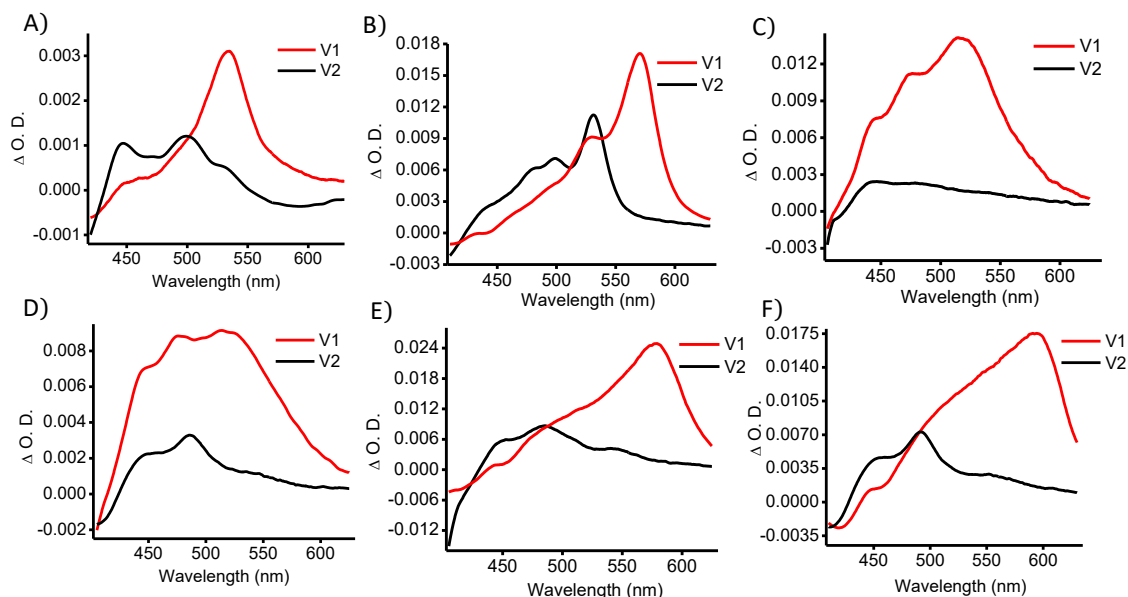


Figure 2.12. SVD of fTA spectra of (A) 1AP; (B) 2AP; (C) 2'AP; (D) 2''AP; (E) 3AP and (F) 4AP in $CHCl_3$.

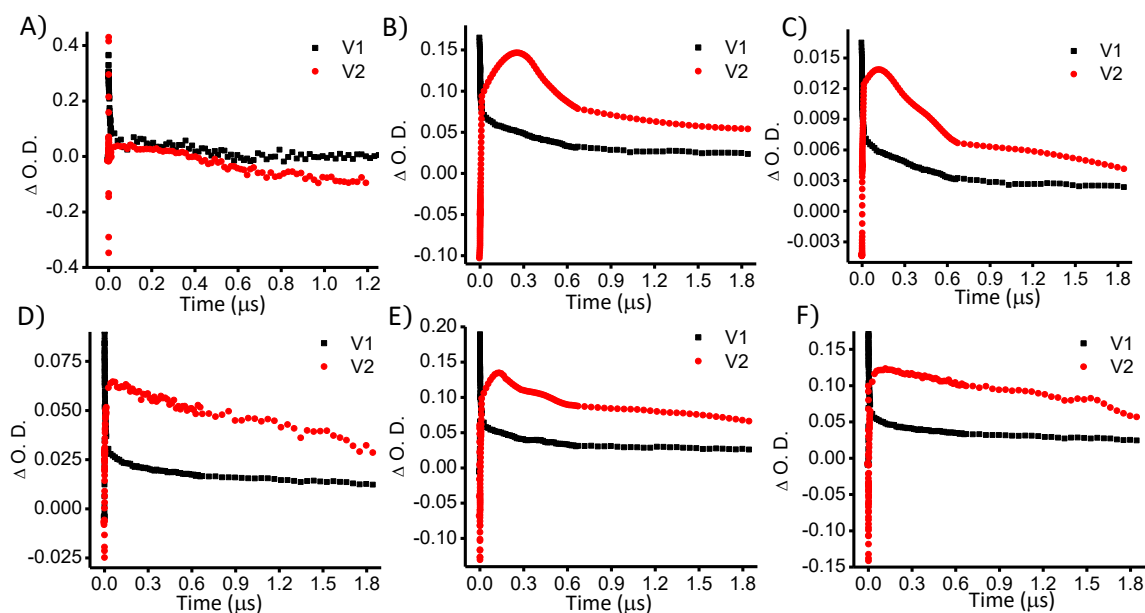


Figure 2.13. Right singular vectors obtained from global analyses for (A) 1AP; (B) 2AP; (C) 2'AP; (D) 2''AP; (E) 3AP and (F) 4AP in $CHCl_3$.

Table 2.4. Lifetimes of 1-4AP obtained from global analyses of fTA spectra ($\lambda_{exc}=400$ nm).

	V1 (ps)		V2 (ns)
	τ_1 ($S_p \rightarrow S_n$)*	τ_2 ($S_n \rightarrow T_m$)*	τ_3 ($T_m \rightarrow T_n$)*
1 AP	0.54 (76%)	9.08 (24%)	0.12
2 AP	0.70 (65%)	7.45 (35%)	0.27
2' AP	0.92 (54%)	10.28 (46%)	0.42
2'' AP	0.43 (80%)	5.42 (12%)	0.48
3 AP	0.58 (78%)	11.27 (22%)	0.54
4 AP	1.40 (61%)	7.9 (39%)	1.96

* $p>n$; * $m>n$

The DAS are shown in Figure 2.12 and the lifetime corresponding to the kinetic profiles are tabulated in Table 2.4. The short-lifetime component ($\tau_1 \leq 150$ fs) affiliated with the DAS centered around 534-595 nm attributes to the relaxation pathway from a higher excited state (S_p) state to a lower singlet excited state (S_n) through internal conversion (Table 2.4). The second lifetime (τ_2) is assigned to intersystem crossing (ISC) from the singlet excited state to a receiving triplet state (T_n) (Table 2.4). This assignment is supported by an isobestic point in the transient absorption spectra of 1-4AP which suggests the state-to-state relaxation dynamics (Figure 2.11). Crespo-Hernández and co-workers have observed a similar characteristics in the femtosecond broadband transient absorption of excited dynamics of (tricyclohexylphosphine)gold(I) pyrenyl complexes that showed IC in the singlet manifold followed by 11-100 ps ISC to a receiver triplet state. Consequently, time-gated emission measurements of 1-4AP in chloroform at 77 K show phosphorescence in the spectral 480-650 nm when excited at 350 nm (Figure 2.14A&B Table 2.2). Thus,

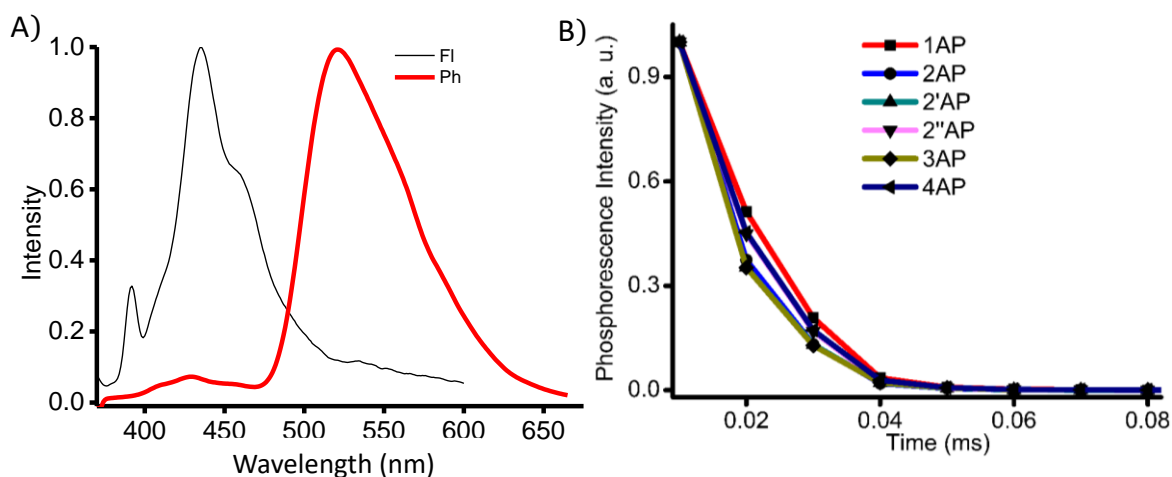


Figure 2.14. (A) Representative phosphorescence spectrum of 4AP in CHCl_3 recorded at 77 K ($\lambda_{\text{ex}} = 380 \text{ nm}$; dotted graph represents the fluorescence spectrum of 4AP) and (B) phosphorescence decay of 1-4AP derivatives in CHCl_3 recorded at 77 K ($\lambda_{\text{ex}} = 380 \text{ nm}$).

photoexcitation of 1–4AP creates a higher singlet excited state that undergo rapid intersystem crossing to a triplet state (T_n), effectively competing with the internal conversion to S_1 . The long-lived component (τ_3) exhibited a lifetime of 0.12 ns (1AP), 0.27 ns (2AP), 0.42 ns (2'AP) 0.48 ns (2''AP), 0.54 ns (3AP) and 1.96 ns (4AP) (Table 2.4) which can be assigned as relaxation within the triplet manifold resulting in the T_n state ($T_n \leftarrow T_m$ transition, $m > n$). The transient peak observed from fTA measurements around 450-500 nm decays within 2 ns and is in good agreement with the triplet-triplet (T-T) absorption spectrum obtained from the nanosecond laser experiments (Figure 2.15). Considering the exceedingly high quantum yield ($\Phi_T \sim 100\%$) for ISC to the triplet manifold of 1–4AP in chloroform, suggests plausible small energy gap resulting in significant spin-orbit coupling between the singlet ($\pi\pi^*$) and triplet ($n\pi^*$) excited states, which explains the ultrafast ISC.

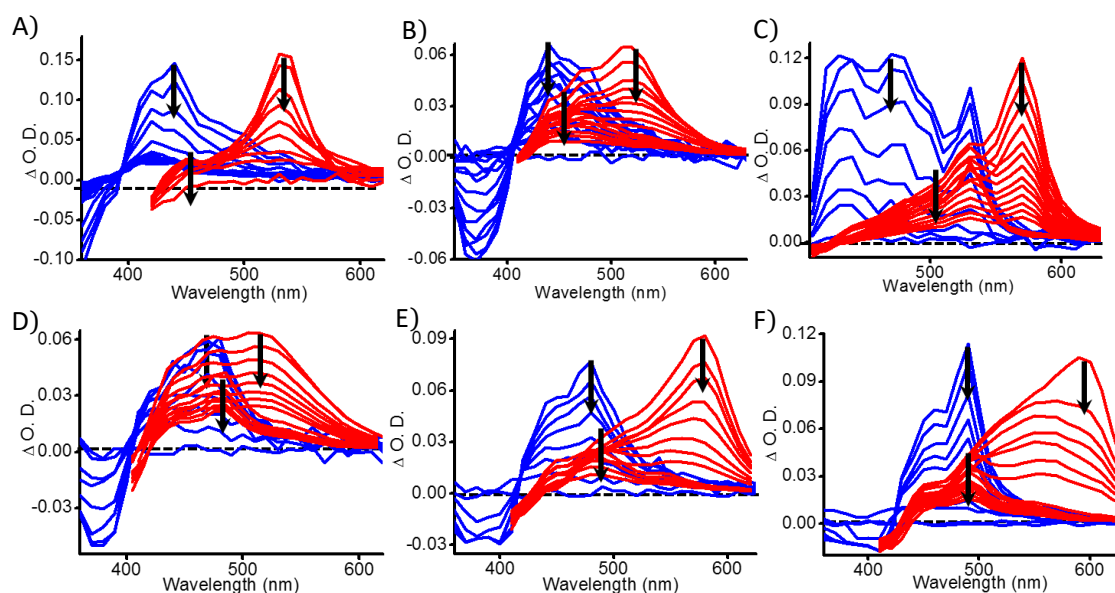


Figure 2.15. Overlay of *nTA* spectra (blue trace) and *fTA* spectra (red trace) of (A) 1AP; (B) 2AP; (C) 2'AP; (D) 2''AP; (E) 3AP and (F) 4AP in CHCl_3 .

2.3.4. TDDFT calculation and Jablonski diagram

Quantum nuclear dynamics simulations within the linear vibronic coupling theory were carried out for 2''AP and 4AP to elucidate the experimental $S_n \leftarrow S_p$ decay. A vibronic Hamiltonian consisting four low-lying singlet excited states (S_4 - S_1) and relevant vibrational modes corresponding to intrastate and interstate coupling parameters has been employed. Although the observed IC decay is difficult to assign for a particular excited singlet state, it is assumed that the S_4 state is populated upon electronic excitation in the pump-probe spectroscopy. And, hence the quantum wave packet dynamics simulations on S_4 state are carried out for a meaningful comparison with the experiment. Figure 2.16A depicts the S_4 population decay of 2''AP and 4AP. Upon vertical excitation to S_4 , ~90 % of the population was transferred to lower singlet states within 20 fs in 2''AP. The decay of S_4 is slower in 4AP compared to 2''AP. For

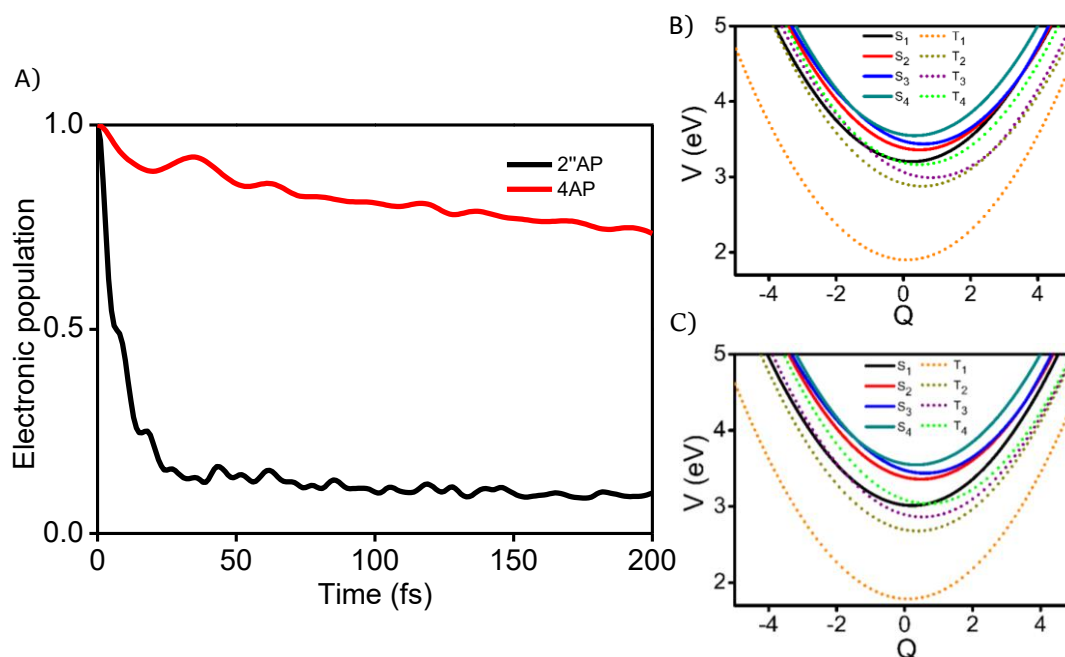


Figure 2.16. A) Decay profile of S_4 state of 2''AP and 4AP; Potential energy cuts along C=O symmetric stretch vibrational mode of singlet excited states and triplet excited state of B) 2''AP and C) 4AP.

further insight on IC and ISC lifetimes and quantum yields, potential energy cuts of singlet and triplet excited electronic states along the C=O symmetric stretching vibrations are plotted in Figure 2.16B&C. Based on the near-degenerate energy levels

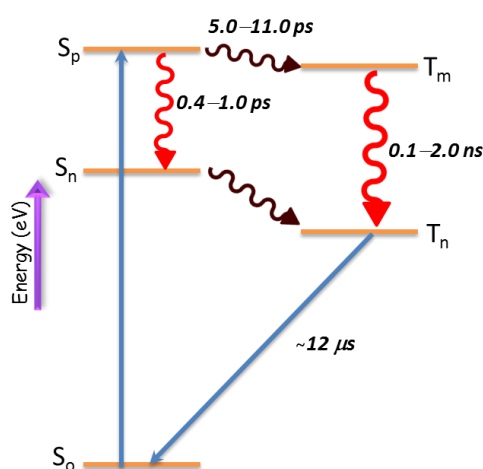


Figure 2.17. Jablonski diagram depicting the photophysics of acetylpyrene.

of singlet-triplet manifold and quantum dynamics simulations, it is proposed that the ISC occurring via two pathways, i) $S_p \rightarrow S_n \rightarrow T_n$ and ii) $S_p \rightarrow T_m$ without involvement of lower singlet excited states, responsible for the observed higher triplet quantum yields of acetylpyrenes (Figure 2.17).

2.5. Conclusion

In conclusion, we present a comprehensive excited-state dynamical study of acetylpyrene derivatives using pump-probe transient absorption. Photo-excitation of acetylpyrene at 400 nm, populates the excited singlet state (S_p) which undergoes rapid ISC efficiently competing with IC to the lowest excited singlet state (S_n). A near unity Φ_T for tetraacetylpyrene (4AP; $\Phi_T \sim 100\%$) suggest the dominant role of carbonyl group in facilitating efficient ISC for triplet generation. Ultrafast internal conversion in the triplet manifold leads to the emitting triplet T_n , which decays radiatively by phosphorescence with a time scale of 12 μ s. Our observation will also give further insight into the utilization of acetylpyrene based molecular systems in molecular electronics since characterization of triplet excited states is essential for research on organic photovoltaics and singlet fission.

2.6. Appendix

Experimental section

- **Materials and Methods**

Pyrene (98%), acetyl chloride (98%) and aluminum chloride (99.99%) were purchased from Sigma Aldrich and used as such without further purification. Carbon disulfide used as a solvent for the reaction was dried and distilled by standard procedure. TLC analysis were performed on precoated aluminum plates of silica gel 60 F254 plates (0.25 mm, Merck) and developed TLC plates were visualized under short and long wavelength UV lamps. Flash column chromatography was performed using silica gel of 200-400 mesh employing a solvent polarity correlated with the TLC mobility observed for the substance of interest. Yields refer to chromatographically and spectroscopically homogenous substances.

Melting points (mp) were obtained using a capillary melting point apparatus and are reported without correction. IR spectra were recorded on a Shimadzu IRPrestige-21 FT-IR spectrometer as neat KBr pellets for all the derivatives. ^1H and ^{13}C NMR spectra were measured on a 500 MHz and 125 MHz Bruker advanced DPX spectrometer respectively and 1,1,1,1-tetramethylsilane (TMS) is used as the internal standard for ^1H and ^{13}C NMR measurements. CHN analyses were carried out on an Elementar vario MICRO cube Elemental Analyzer. All values recorded in elemental analyses are given in percentages. High Resolution Mass Spectra (HRMS) were recorded on Agilent 6538 Ultra High Definition (UHD) Accurate-Mass Q-TOF-LC/MS system using either atmospheric pressure chemical ionization (APCI) or electrospray ionization (ESI) mode.

Spectral Measurements:

Absorption spectra were recorded on Shimadzu UV-3600 UV-VIS-NIR while fluorescence and excitation spectra were performed on Horiba Jobin Yvon Fluorolog spectrometers respectively. The excitation wavelength used is 350 nm unless otherwise mentioned. Fluorescence lifetime measurements were carried out in an IBH

picosecond single photon counting system. The fluorescence decay profiles were deconvoluted using IBH data station software version 2.1, and fitted with exponential decay, minimizing the χ^2 values of the fit to 1 ± 0.05 . All spectroscopic experiments were performed by using standard quartz cuvettes of path length 1cm for solution in dried and distilled solvents. The excitation laser used is 375 nm with a pulse width of less than 100 ps. 1-4AP derivatives in chloroform were found to have lifetime significantly shorter than the excitation pulse width. The solution state fluorescence quantum yields were determined by using optically matched solutions. Quinine sulfate dissolved in 0.5 M H_2SO_4 ($\Phi_f = 0.546$) is used as the standard for 1-4AP derivatives.

Nanosecond transient absorption measurements. Nanosecond laser flash photolysis experiments of the argon purged solutions were carried out in an Applied Photophysics Model LKS-60 laser kinetic spectrometer using the third harmonic (355 nm, pulse duration ≈ 10 ns) of a Quanta Ray INDI-40-10 series pulsed Nd:YAG laser as the excitation source. Triplet states of 1-4AP in CHCl_3 were confirmed performing the experiments with oxygen purged solutions.

Femtosecond pump-probe transient absorption technique. Spectra-physics Tsunami Oscillator (80 MHz, 800 nm) was used as seed for a Spectra-Physics Spitfire Regenerative amplifier (1 KHz, 4 mJ). A fraction of the amplified output was used to generate 400 nm pump pulse. Residual 800 nm pulse was sent through a delay line inside an Excipro pump-probe spectrometer from CDP Systems. A rotating CaF_2 plate (2 mm thickness) was used to generate continuum of white light from the delayed 800 nm pulses. The continuum of white light was split into two and the streams were used as probe and pump pulses. Transient absorption spectra were recorded using a dual diode array detector with a 200 nm detection window with an optical delay of 1.6 fs. Near infrared measurements were performed using a multichannel infrared detector that scans from 900 to 1600 nm. Sample solutions were prepared in a rotating sample cell with 4 mm path length. IRF was determined by solvent (10% benzene in methanol) two photon absorption and was found to be approximately 110 fs at about 530 nm.

Energy per pulse incident on the sample is attenuated employing 80% neutral density filter when required.

fTA measurements of 1-4AP derivatives in CHCl_3 were carried out by exciting the respective sample at 400 nm, 200 nJ, ~110 fs pulses, allowing excitation of pyrene unit.

Cyclic Voltammetry (CV): Electrochemical measurements were performed on a BASi (Bioanalytical Systems, Inc.) C-3 cell stand controlled by Epsilon electrochemical workstation. A three electrode system is then constructed constituting a glassy carbon as the working electrode, a platinum-wire as the counter electrode, and an Ag/Ag^+ (3 M NaCl) as the reference electrode. The electrochemical measurements were conducted under nitrogen atmosphere (5 psi, 10 minutes) in a deoxygenated anhydrous acetonitrile of tetra-n-butylammonium hexafluorophosphate (supporting electrolyte, 0.1 M) for AP derivatives, in CHCl_3 with a scan rate of 50–100 mVs^{-1} . Calibration of the instrument was performed using the ferrocene/ferrocenium (Fc/Fc^+) redox couple as an internal standard and measured under same condition before and after the measurement of samples. The energy level of Fc/Fc^+ was assumed to be -4.8 eV with respect to vacuum. The half-wave potential of Fc/Fc^+ was estimated to be 0.5 V with reference to the Ag/Ag^+ electrode.

HOMO and LUMO energy levels were calculated from the following equations:

$$E_{\text{HOMO}} = -(E_{\text{ox}}^{\text{onset}} + 4.8) \text{ eV} \quad \text{and} \quad (1)$$

$$E_{\text{LUMO}} = -(E_{\text{red}}^{\text{onset}} + 4.8) \text{ eV} \quad (2)$$

respectively, where $E_{\text{ox}}^{\text{onset}}$ and $E_{\text{red}}^{\text{onset}}$ are the onset oxidation and reduction potentials relative to the Ag/Ag^+ reference electrode.

The electrochemical energy gap (E_g) is estimated as follows:

$$E_g = (E_{\text{LUMO}} - E_{\text{HOMO}}) \text{ eV} \quad (3)$$

where E_{LUMO} and E_{HOMO} are the corresponding to HOMO and LUMO energy levels calculated after converting the values in Ag/Ag^+ with respect to the standard calomel electrode (SCE) convention.

Determination of fluorescence quantum yield and radiative and non-radiative rate constants: Solution state fluorescence quantum yields of AP derivatives were

calculated by relative quantum yield method as follows,

$$\Phi_s = \Phi_{\text{ref}} \left(\frac{I_s}{I_{\text{ref}}} \right) \left(\frac{OD_{\text{ref}}}{OD_s} \right) \left(\frac{n_s}{n_{\text{ref}}} \right)^2 \quad (4)$$

wherein, Φ_s and Φ_{ref} are the quantum yields of sample and reference respectively, I_s and I_{ref} are the area under the emission spectrum for sample and reference respectively. OD_s and OD_{ref} are the absorbances of sample and reference respectively at the excitation wavelength. n_s and n_{ref} are the refractive index of the solvent in which sample and reference are taken.

Radiative (k_r) and non-radiative (k_{nr}) rate constants from the singlet excited states are calculated from the fluorescence quantum yields, Φ_f .

$$\Phi_f = \frac{k_r}{k_r + k_{\text{nr}}} \quad (5)$$

The rate constants k_r and k_{nr} can be evaluated by measuring fluorescence lifetimes (τ_f) from TCSPC measurements. The following equations depict relation between Φ_f , τ_f , k_r and k_{nr} .

$$k_r = \frac{\Phi_f}{\tau_f} \quad \text{and} \quad (6)$$

$$k_{\text{nr}} = \frac{1 - \Phi_f}{\tau_f} \quad (7)$$

a change in Φ_f could be attributed to the changes in either k_r/k_{nr} . The enhancement in the quantum yield (Φ_f) with increased solvent polarity is due to the stabilization of the excited states by virtue of interaction with the solvent dipoles and decrease in the non-radiative (k_{nr}) rate constant.

X-ray Crystallography

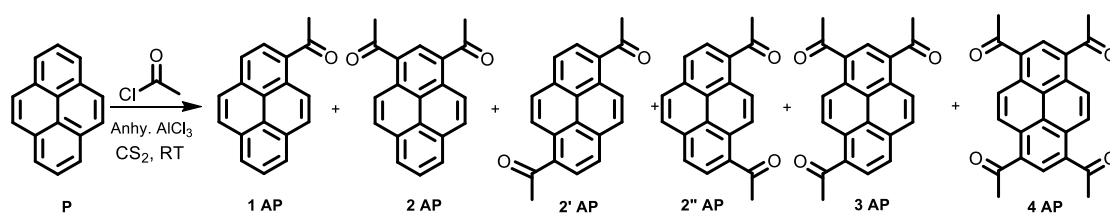
X-ray Crystallography: High-quality specimens of appropriate dimensions were selected for the X-ray diffraction experiments. Crystallographic data collected are presented in the supplementary information. Single crystals were mounted using oil (Infinite V8512) on a glass fibre. All measurements were made on a CCD area detector with graphite monochromated Mo $K\alpha$ radiation. The data was collected using Bruker APEXII detector and processed using APEX2 from Bruker. All structures were solved by direct methods and expanded using Fourier techniques. The non-hydrogen atoms were refined anisotropically. Hydrogen atoms were included in

idealized positions, but not refined. Their positions were constrained relative to their parent atom using the appropriate HFIX command in SHELXL-97. The full validation of CIFs and structure factors of 1-4AP derivatives were performed using the CheckCIF utility and found to be free of major alert level. 3D structure visualization and the exploration of the crystal packing of 1–4AP were carried out using Mercury 3.1.

Computational Methods

Geometry optimization and single point energy calculations for 1-4AP performed at B3LYP/6-311G**++ level of theory using the crystal structure data, for Frontier molecular orbital (FMO) analyses. Energy gap is determined as the difference between energies of LUMO and HOMO as described in equation 3. Energy level diagram is plotted using the energies obtained from FMO analyses. All computations were performed with the Gaussian 09 program suite.

Synthesis Details



Scheme 2.1. Shows the synthesis of acetylpyrene (1-4AP) derivatives.

Preparation of acetylpyrene (1-4AP) derivatives: Pyrene dissolved in CS₂ (yellow solution) was maintained at ambient temperature and subsequently anhydrous AlCl₃ was added. Acetyl chloride was then slowly syringed to the suspension. Subsequently, hydrogen chloride was liberated. After 3 hrs the mixture was added slowly to a vigorously stirred mixture of ice and concentrated HCl. The resulting suspension was filtered and vacuum dried and purified through column chromatography (silica gel) to give acetylpyrene (1-4AP) derivatives.

1AP (yield= 5.1%). M.p. 90.4-91.8°C. ¹H NMR [500 MHz, C₂D₂Cl₄, δ]: 9.09 (d, J= 9.35 Hz, 1H), 8.43 (d, J = 8.05 Hz, 1H), 8.33 (d, J = 2.9 Hz, 1H), 8.32 (d, J = 2.9 Hz, 1H), 8.29 (d, J = 9.4 Hz, 1H), 8.24 (d, J = 1.35 Hz, 1H), 8.22 (s, 1H), 8.13 (m, 2H), 2.96 (s, 3H). ¹³C NMR [125 MHz, C₂D₂Cl₄, δ]: 202.57, 134.08, 131.96, 131.11, 130.47, 129.91, 129.86,

129.40, 127.37, 127.31, 126.72, 126.67, 126.34, 125.06, 124.97, 124.30, 124.26, 30.74. IR (KBr, cm^{-1}): 3041, 1675, 1249. Elemental analysis: calcd. value for $\text{C}_{18}\text{H}_{12}\text{O}$: 88.50% C, 4.95% H; found: 88.78% C, 4.88% H. HRMS (EI) m/z calculated for $\text{C}_{18}\text{H}_{12}\text{O}$ $[\text{M}]^+$: 244.0888, found: 244.0872.

2AP (yield= 9.4%). M.p. 179.0-181.1°C. ^1H NMR [500 MHz, DMSO (d_6), δ]: 8.87 (s, 1H), 8.78 (d, $J = 9.30$ Hz, 2H), 8.38 (d, $J = 7.65$ Hz, 2H), 8.35 (d, $J = 9.35$ Hz, 2H), 8.13 (t, $J = 7.60$ Hz, 1H), 2.88 (s, 6H). ^{13}C NMR [125 MHz, DMSO (d_6), δ]: 201.94, 131.41, 131.21, 130.37, 129.87, 128.03, 127.43, 127.20, 124.39, 124.18, 123.19, 30.71. IR (KBr, cm^{-1}): 3048, 1681, 1249. Elemental analysis: calcd. value for $\text{C}_{20}\text{H}_{14}\text{O}_2$: 83.90% C, 4.93% H; found: 84.07% C, 4.93% H. HRMS (EI) m/z calculated for $\text{C}_{20}\text{H}_{14}\text{O}_2$ $[\text{M}]^+$: 286.0994, found: 286.0991.

2'AP (yield= 9.6%) M.p. 205.7-206.9°C. ^1H NMR [500 MHz, DMSO (d_6), δ]: 8.86 (d, $J = 9.35$ Hz, 2H), 8.55 (d, $J = 8.05$ Hz, 2H), 8.35 (d, $J = 8.05$ Hz, 2H), 8.28 (d, $J = 9.40$ Hz, 2H), 2.83 (s, 6H). ^{13}C NMR [125 MHz, DMSO (d_6), δ]: 202.20, 133.33, 132.31, 129.07, 128.20, 127.73, 126.39, 125.35, 123.73, 30.64. IR (KBr, cm^{-1}): 3028, 1676, 1251. Elemental analysis: calcd. value for $\text{C}_{20}\text{H}_{14}\text{O}_2$: 83.90% C, 4.93% H; found: 83.96% C, 4.90 % H. HRMS (EI) m/z calculated for $\text{C}_{20}\text{H}_{14}\text{O}_2$ $[\text{M}]^+$: 286.0994, found: 286.0986.

2''AP (yield= 37.5%) M.p. 161.6-163°C. ^1H NMR [500 MHz, DMSO (d_6), δ]: 8.87 (s, 2H), 8.55 (d, $J = 8.0$ Hz, 2H), 8.37 (d, $J = 8.0$ Hz, 2H), 8.27 (s, 2H), 2.82 (s, 6H). ^{13}C NMR [125 MHz, DMSO (d_6), δ]: 202.02, 133.21, 132.81, 129.14, 127.83, 127.43, 126.40, 125.78, 123.75, 30.58. IR (KBr, cm^{-1}) 3000, 1659, 1231. Elemental analysis: calcd. value for $\text{C}_{20}\text{H}_{14}\text{O}_2$: 83.90% C, 4.93% H; found: 83.96% C, 4.89% H. HRMS (EI) m/z calculated for $\text{C}_{20}\text{H}_{14}\text{O}_2$ $[\text{M}]^+$: 286.0994, found: 286.0981.

3AP (yield= 18.9%) M.p. 178.8-179.3°C. ^1H NMR [500 MHz, CDCl_3 , δ]: 9.13 (d, $J = 9.5$ Hz, 1H), 9.02 (d, $J = 9.0$ Hz, 1H), 9.0 (d, $J = 9.5$ Hz, 1H), 8.70 (s, 1H), 8.47 (d, $J = 8.0$ Hz, 1H), 8.34 (d, $J = 8.0$ Hz, 1H), 8.29 (d, $J = 9.5$ Hz, 1H), 2.97 (s, 6H), 2.95 (s, 3H). ^{13}C NMR [125 MHz, CDCl_3 , δ]: 201.72, 201.19, 201.15, 133.87, 132.46, 131.96, 131.91, 131.18, 130.66, 130.32, 128.51, 128.09, 127.66, 127.31, 126.17, 126.08, 126.04, 124.67, 123.90, 30.52, 30.51,

30.46. IR (KBr, cm^{-1}): 3020, 1664, 1255. Elemental analysis: calcd. value for $\text{C}_{22}\text{H}_{16}\text{O}_3$: 80.47% C, 4.91% H; found: 80.63% C, 4.87% H. HRMS (EI) m/z calculated for $\text{C}_{22}\text{H}_{16}\text{O}_3$ $[\text{M}]^+$: 328.1099, found: 328.1086.

4AP (yield= 4.6%) M.p. 295.6-297.0°C. ^1H NMR [500 MHz, $\text{C}_2\text{D}_2\text{Cl}_4$, δ]: 9.04 (s, 4H), 8.70 (s, 2H), 2.99 (s, 12H). ^{13}C NMR [125 MHz, $\text{C}_2\text{D}_2\text{Cl}_4$, δ]: 201.80, 134.01, 133.96, 130.47, 128.21, 127.25, 125.25, 30.97. IR (KBr, cm^{-1}): 3004, 1685, 1270. Elemental analysis: calcd. value for $\text{C}_{24}\text{H}_{18}\text{O}_4$: 77.82% C, 4.90% H; found: 77.61% C, 4.85% H. HRMS (EI) m/z calculated for $\text{C}_{24}\text{H}_{18}\text{O}_4$ $[\text{M}]^+$: 370.1205, found: 370.1210.

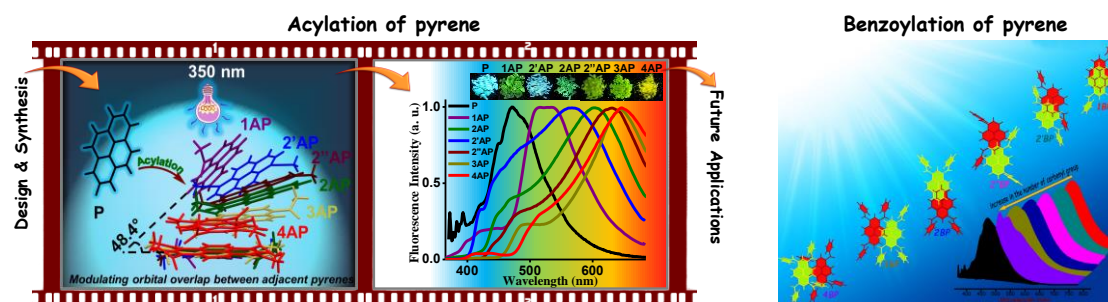
Chapter 3

Engineering the solid-state packing of carbonylpyrenes via C–H···H–C, C–H···O and π – π interactions for tuning opto-physical properties

Abstract

Molecular crystal engineering of polyaromatic hydrocarbons to yield 1–2D lamellar arrangement demonstrated a pivotal role in photonic and semiconductor device applications. In this report, we modulated the extent of π – π overlap between vicinal pyrene units through successive acylation. Quantum theory of atoms in molecules (QTAIM) and Hirshfeld surface analyses were employed to understand the close packing interactions which indicates an increase in π – π interactions and a concomitant decrease in the σ – π interactions with an increase in the number of acetyl groups per pyrene unit. A combination of C–H···H–C, C–H···O and π – π interactions facilitate the transformation of sandwich herringbone packing of P to the herringbone arrangement in 1 and 2'AP, the brickwork arrangement in 2 and 2''AP and columnar stacks in 3–4AP. A systematic decrease in the interplanar angle between the vicinal pyrene units could be attributed to the dramatic shift in the emission spectra (ca. 42–174 nm) of crystalline 1–4AP when compared to pyrene. J-like aggregation and/or aggregation induced emission (AIE) in the crystal packing of 1–4AP corroborates the moderately emissive blue–green–orange crystals.

While in another context, the extent of orbital overlap (π – π) between vicinal pyrene units in crystalline 1–4BP was regulated by exploiting the steric hindrance offered via successive benzylation. Steric hindrance due to incremental benzoyl groups causes a systematic reduction in the orbital overlap (π – π) between vicinal pyrene units affording green–yellow–orange solid-state emitters. Crystallization induced emission could arise from: i) electronic (dipolar/excitonic) interactions, ii) arrested bond rotations, and/or iii) lack of solvation in crystalline 1–4BP ($\Phi_{\text{Fl}} \sim 2$ –26%) when compared to that in solution ($\Phi_{\text{Fl}} \leq 1\%$).



- 1) Rajagopal, S. K.; Philip, A. M.; Nagarajan, K.; Hariharan, M. *Chem. Commun.* 2014, **50**, 8644–8647.
- 2) Rajagopal, S. K.; Reddy, V. S. Hariharan, M. *CrystEngComm* 2016, **18**, 5089–5094.

3.1. Introduction

Molecular crystal engineering[93] of polyaromatic hydrocarbons to yield 1–2D lamellar arrangement demonstrated a pivotal role in photonic[94-96] and semiconductor device applications[97-100]. Extended orbital overlap through π -columnar stacks compared to a herringbone arrangement of arenes proved to be vital[101-103]. Recent efforts in transforming the herringbone to the columnar arrangement of arenes through various methods such as chemical modifications[104], co-[105, 106] and solvent-crystallization[107], heat-mode[108], mechanical stimulation[109, 110] and solid seeding[111] have proven to be effective. Achieving a diverse degree of orbital overlap between the neighboring units in the crystalline state is still a challenging task. Monitoring the effect of subtle orientation differences and thereby the orbital overlap between the neighboring units in arenes is even more challenging. The extent of orbital overlap through π - π interactions between the vicinal arenes could be reflected in the optical properties of the crystals[23]. Extremely high sensitivity of pyrene fluorescence towards environmental effects can amplify the consequence of orientation factor/orbital overlap between the adjacent units[112].

Our ongoing interest to regulate the arene-arene interactions in fluorescent crystals[113, 114], vesicular gels[115] and thin films prompted us to explore the correlation between optical properties *vs.* peripheral substitution of pyrene. We employed a simple and convenient Friedel-Crafts reaction, invented 137 years ago[116], to increase the number of carbonyl groups in pyrene. Carbonyl conjugated

arenes in solution exhibit diverse excited state processes[82] depending on the adjacent functionality such as (i) low fluorescent ($\Phi_f \leq 0.002$) aryl aldehydes/ketones dominated by intersystem crossing (ISC); (ii) moderate fluorescent secondary/tertiary carboxamides[117] dominated by internal conversion and (iii) high fluorescent aryl acids/esters[118] dominated by radiative processes. Extremely low Φ_f in solution hampered the efforts to explore the optical properties of aryl ketones/aldehydes in the crystalline state though a plethora of pyrene derivatives have been explored for optoelectronic applications[5, 119].

Furthermore, heteropolar C-H...H-C interactions are rarely found to be an integral force in organic crystals when compared to C-H...O[120], C-H... π [121], homopolar C-H...H-C[122] interactions, etc. Heteropolar C-H...H-C interactions could arise from the dipolar/quadrupolar nature of sp^2 C-H bond that could induce a dipole on the vicinal sp^3 C-H unit. Highly electronegative substituents/groups adjacent, either geminal or vicinal, to a sp^2 C-H unit may polarize the bond allowing for extended interactions[123]. We herein report for the first time a systematic control on the organization of adjacent pyrene units through the progressive addition of acetyl groups that transform the sandwich herringbone structure of pyrene to a columnar arrangement in tri/tetraacetylpyrene. Distinct packing arrangements, through C-H...H-C, C-H...O and π - π interactions, in acetylpyrene derivatives offer diverse solid-state colouring and fluorescent properties.

Crystalline pyrene based blue organic light emitting devices (OLED) suffer from strong excimer contributions[124]. Disruption of nearest neighbour interactions in

crystalline pyrene is expected to enhance the performance of OLEDs[125]. A variety of chemical[126-130] and physical approaches[98, 107] have been utilized to regulate pyrene-pyrene interactions. Efforts to tune the interchromophoric interactions in molecular crystals using π - π [85, 115], C-H... π [113, 131], C-H...O[132] and C-H...H-C[133] contacts for favourable photophysical properties allowed us to employ the combination of steric and conjugation effects of benzoyl units of pyrene based systems. The significant dimension of the benzoyl unit (105.2 \AA^3)[134] as compared to pyrene (237.5 \AA^3) could potentially perturb strong π - π interactions ($-13.8 \text{ kcal mol}^{-1}$) [135] between the nearest pyrene units (center-to-center distance of 3.53 \AA) (Figure 3.1).

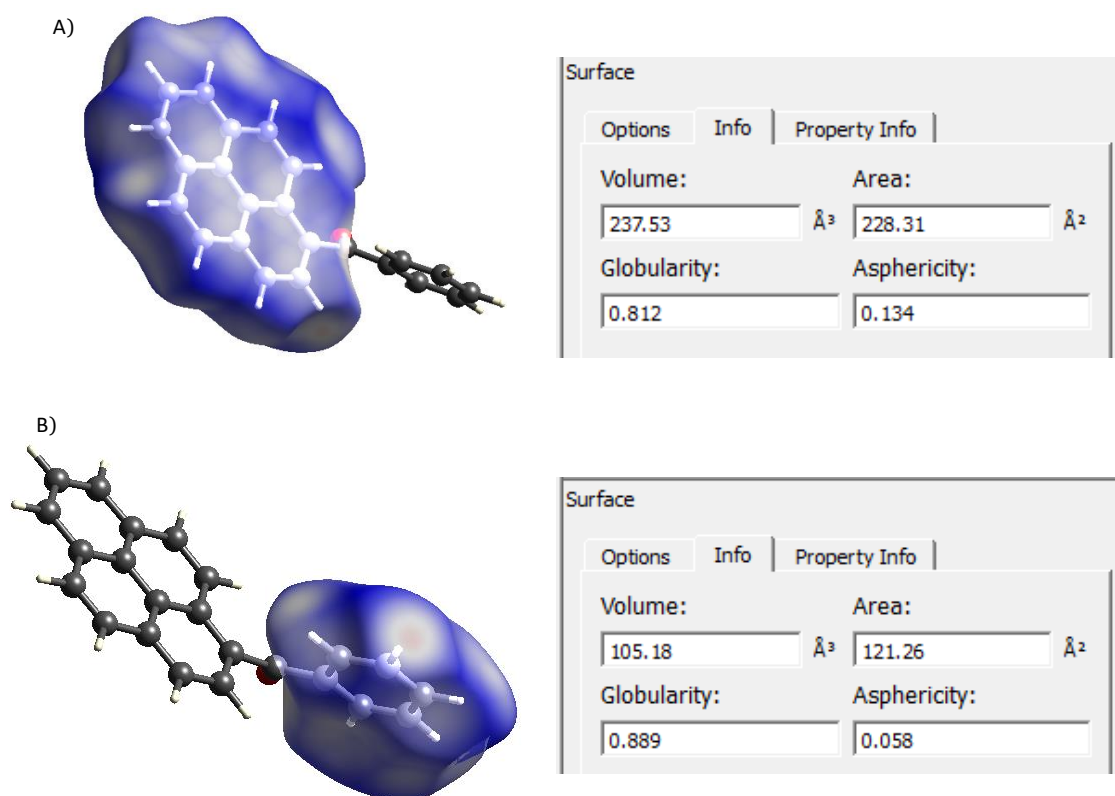


Figure 3.1. Volume calculated for (A) pyrene and (B) benzoyl unit in 1BP from Crystal Explorer 3.0.

3.2. Results and Discussions

3.2.1. Synthesis, crystallization and thermal analysis

Adding a stoichiometric quantity of acetyl chloride to a solution of pyrene and AlCl_3 in carbon disulfide (CS_2) at ambient temperature rendered the desired acetyl derivatives (1–4AP) with moderate yield (Figure 3.2, Row I)[13]. Compounds (1, 2, 2', 2'', 3AP) were crystallized by varying the acetone:hexane composition, whereas 4AP was obtained by temperature gradient cooling in chloroform. Acetyl derivatives (1, 2', 2'', 3, 4AP) yielded solvent free monoclinic crystal system except for 2AP which exhibits a solvent free orthorhombic crystal system (Figure 3.2, Row II; Table 3.1). Differential scanning calorimetric (DSC) analysis of 1-acetylpyrene (1AP) exhibited a sharp melting transition (T_m) at 90.4 1C (Figure 3.3A). A significant decrease (ca. 63

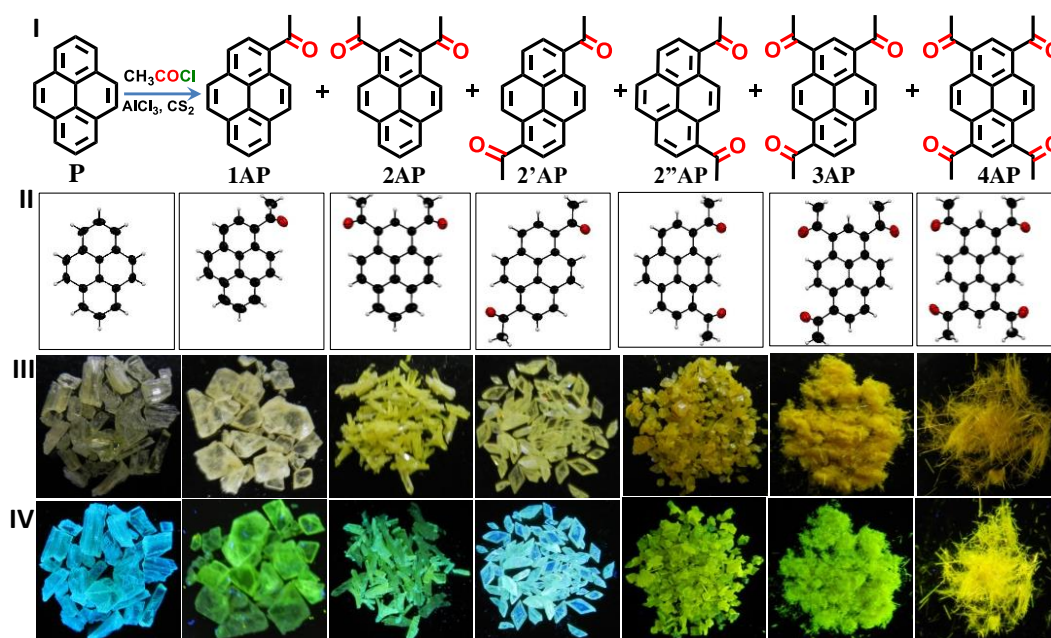


Figure 3.2. Row I: molecular structure of 1–4AP; Row II: corresponding single crystal X-ray structure. Photographic image of the crystals Row III: in daylight; and Row IV: under UV illumination. X-ray structure of P is taken from the literature[136].

Table 3.1. Shows crystallographic data and refinement parameters for crystalline 1-4AP derivatives.

	1AP	2AP	2'AP	2''AP	3AP	4AP
formula	C ₁₈ H ₁₂ O	C ₂₀ H ₁₄ O ₂	C ₂₀ H ₁₄ O ₂	C ₂₀ H ₁₄ O ₂	C ₂₂ H ₁₆ O ₃	C ₂₄ H ₁₈ O ₄
formula wt	244.28	286.31	286.31	286.31	328.35	370.38
colour, shape	Pale Yellow	Yellow	Yellow	Yellow	Yellow	Orange
dimens, mm	0.20x0.15x0.10	0.20x0.15x0.10	0.25x0.20x0.15	0.20x0.15x0.10	0.20x0.15x0.10	0.20x0.10x0.10
crystal system	Monoclinic	Orthorhombic	Monoclinic	Monoclinic	Monoclinic	Monoclinic
space group, Z	<i>Cc</i>	<i>Pnma</i>	<i>P</i> ₂ (1)/ <i>n</i>	<i>P</i> ₂ (1)/ <i>c</i>	<i>P</i> ₂ (1)/ <i>c</i>	<i>C</i> ₂
<i>a</i> , Å	34.4472	7.3519	9.243	8.1941	11.0402	20.1864
<i>b</i> , Å	7.3598	16.6654	7.463	23.0417	20.0564	39.6060
<i>c</i> , Å	9.8621	11.3344	10.095	7.4020	7.2682	7.0261
α , deg	90.00	90.00	90.000	90.00	90	90.00
β , deg	98.492	90.00	98.880	93.824	96.682	109.988
γ , deg	90.00	90.00	90.000	90.00	90	90.00
<i>V</i> , Å ³	2472.87	1388.72	688.0	1394.43	1598.44	5279.0
temp, K	296	296	296	296	296	293
<i>d</i> calcd, g/cm ⁻³	1.312	1.369	1.382	1.364	1.364	1.398
no. of reflections collected	9183	5744	4832	10022	12353	15979
no. of unique reflections	3756	1269	1200	2408	2825	8235
$2\theta_{\max}$, deg	50	50	50	50	50	50
no. of parameters	343	106	128	201	226	1023
<i>R</i> 1, <i>wR</i> 2 (<i>I</i> > 2 σ (<i>I</i>))	0.0418, 0.1111	0.0427, 0.1126	0.0416, 0.1148	0.0764, 0.1157	0.0612, 0.1756	0.0893, 0.2275
<i>R</i> 1, <i>wR</i> 2 (all data)	0.0489, 0.1268	0.0601, 0.1277	0.0562, 0.1229	0.1201, 0.1314	0.1276, 0.2316	0.1412, 0.2631
goodness of fit	1.053	1.036	1.069	1.068	1.061	1.069
CCDC number	CCDC 984436	CCDC 984437	CCDC 984438	CCDC 984439	CCDC 984440	CCDC 984441

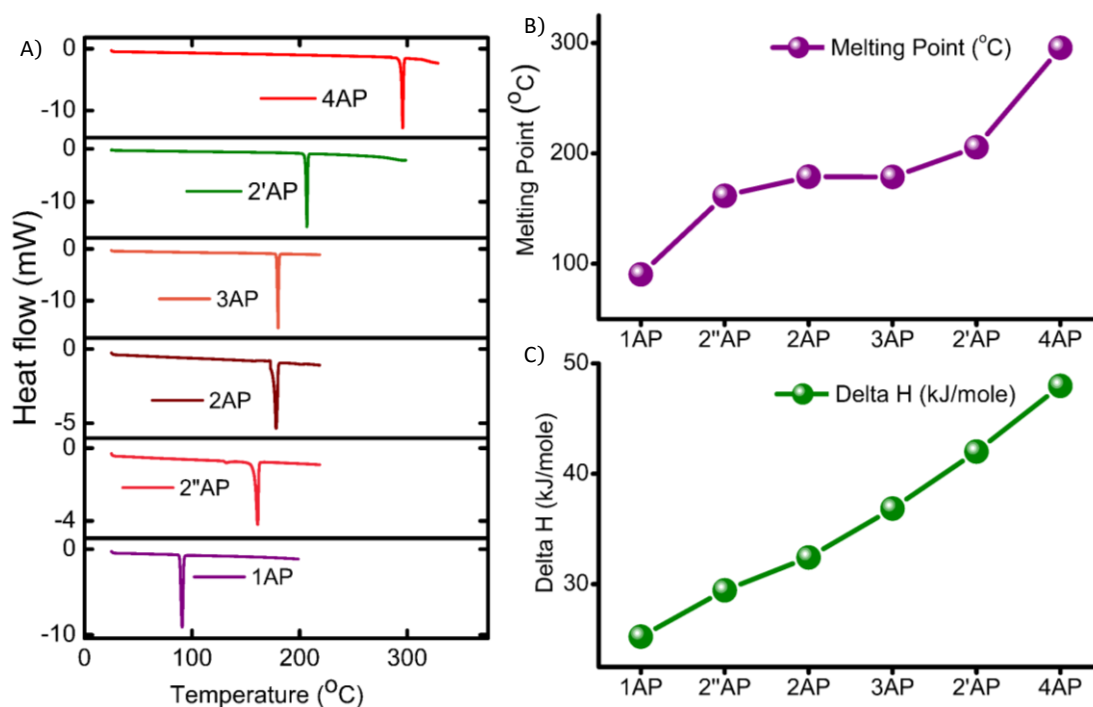


Figure 3.3. Shows (A) DSC melting temperature (T_m); (B) near-linear increment in the melting temperature (T_m) and (C) linear increment in the ΔH values of crystalline 1-4AP derivatives.

°C) in the T_m of 1AP when compared to the T_m of the model compound pyrene (P)[137] is indicative of attenuation in the ordered arrangement of the crystalline 1AP. However, further increase in the number of acetyl groups in the pyrene core resulted

Table 3.2. Shows melting temperature (T_m) and change in enthalpy (ΔH) values for crystalline 1-4AP derivatives.

	^a T_m (°C)	^b ΔH (kJ/mole)
1AP	90.4	25.24
2''AP	161.7	29.45
2AP	179.0	32.41
3AP	178.8	36.86
2'AP	205.7	42.00
4AP	295.6	47.96

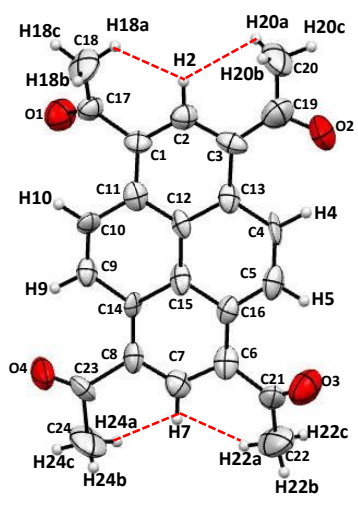
^aMelting temperature; ^bChange in enthalpy during melting

in a near-linear increase (Figure 3.3B) in the T_m having a maximum of 295.6 °C as in the symmetric 4AP derivative. A similar trend was observed for the change in enthalpy during the melting process for 1-4AP (Figure 3.3C and Table 3.2).

2.3.2. QTAIM and Hirshfeld analyses

Qualitative analyses of the single crystal X-ray structure of 1-4AP indicate intra- and intermolecular distances between the methyl and aryl hydrogens in the range of 2.098–2.4 Å (Tables 3.3 and Figure 3.4). Distances appearing at less than the double of van der Waal's radius of hydrogen atom (2.4 Å) could indicate the existence of dihydrogen (H...H) bonding[138]. Quantum theory of atoms in molecules analyses (QTAIM)[139, 140] of the crystalline 1-4AP offered no characteristics supporting the intramolecular dihydrogen interactions at distances less than 2.4 Å. Intermolecular C-H...H-C interactions in crystalline 2, 3 and 4AP (Figure 3.4) are exemplified through the values of electron density at the (3, -1) bond critical point (BCP; $\rho_b(r)$), its Laplacian

Table 3.3. Shows intramolecular (CH_3) H...H (aryl) (Å) distance (d) in crystalline 1-4AP derivatives that is less than the sum of van der Waals radii of two hydrogen atoms (2.4 Å).



	Interaction	d , (Å)
1AP	H18a...H2	2.183
	H20a...H2	2.098
2AP	H18a...H2	2.098
	H20a...H2	2.098
2'AP	H18a...H2	2.350
	H22a...H7	2.350
2''AP	H18a...H2	2.315
	H24a...H7	2.356
3AP	H18a...H2	2.186
	H20a...H2	2.146
	H22a...H7	2.144
4AP	H18a...H2	2.078
	H20a...H2	2.186
	H22a...H7	2.055
	H24a...H7	2.139

($\nabla^2\rho_b(r)$), the interaction distance (d) as indicated in Table 3.4, a bond and virial path in the potential energy density map. A closed-shell intermolecular C–H...H–C interaction possessing considerable bond path between a pair of similar hydrogens

Table 3.4. Shows calculated topological properties of the electron density for the intra- and intermolecular interaction in 2, 3 and 4AP derivatives.

Description	Interaction	^a d, (Å)	^b $\rho_b(r)$, eÅ ⁻³	^c $\nabla^2\rho_b(r)$, eÅ ⁻⁵	^d DE (kJ mol ⁻¹)
2AP	H18c...H'18c	2.230	0.036	0.520	3.46
	O1...H10	2.325	0.093	1.354	
	O2...H4	2.335	0.093	1.354	
	O'1...H'10	2.335	0.093	1.356	
	O'2...H'4	2.335	0.093	1.355	
3AP	H20c...H'8	2.246	0.041	0.471	4.29
	H20c...H'9	2.579*	0.019	0.249	1.87
	O1...H10	2.185	0.127	1.892	
	O2...H4	2.199	0.123	1.838	
	O3...H5	2.298	0.101	1.474	
	O'2...H'4	2.199	0.123	1.836	
	O2...H'9	3.242	0.013	0.182	
	O'3...H'5	2.299	0.101	1.473	
4AP	O'1...H'10	2.185	0.127	1.892	
	H'18c...H''22c	2.239	0.040	0.514	4.32
	H'4...H18a	2.394	0.034	0.450	3.50
	H'5...H18c	2.577*	0.023	0.300	2.29
	O2...H4	2.186	0.128	1.897	
	O4...H9	2.210	0.121	1.785	
	O1...H10	2.322	0.096	1.411	
	O3...H5	2.354	0.091	1.314	
	O'1...H''22c	2.490	0.062	0.708	
	O''3...H'18c	2.490	0.062	0.708	
	O'3...H'5	2.186	0.127	1.897	
	O'1...H'10	2.210	0.121	1.786	
	O'4...H'9	2.322	0.095	1.412	
	O'2...H'4	2.354	0.091	1.313	
	O''4...H9	2.354	0.091	1.312	
O''3...H''5	2.210	0.120	1.785		
O'2...H20b	3.309	0.013	0.175		
O''1...H''10	2.186	0.127	1.898		
O''2...H''4	2.322	0.096	1.411		

^ad = distance ^b $\rho_b(r)$ = electron density at the BCP. ^c $\nabla^2\rho_b(r)$ = Laplacian of ^b $\rho_b(r)$. ^dDE = dissociation energy. *Though H...H distance is >2.4 Å, QTAIM exhibited electron density at (3, -1) BCP.

(CH₃) is seen in 2AP (Figure 3.4A). Non polar C-H...H-C interaction evaluated accumulation of electron density, $\rho_b(r)$, 0.036 eÅ⁻³ and the positive value of the Laplacian at the BCP (0.52 eÅ⁻⁵), to form extended chain-like C-H...H-C contacts along the *b*-axis in 2AP. Derivatives 1, 2' and 2'' AP lack intermolecular C-H...H-C interaction as confirmed through QTAIM calculations. Similar electronegativity differences between involved sp³C-H bonds could only arise from electrically neutral hydrogens in the vicinity. The influence of the adjacent carbonyl group may impart repulsive C-H...H-C interactions from the first order electrostatic contribution. C-H...H-C contacts could be due to second-order mutual polarization of distorted charge clouds of the C-H bonds due to the vicinal carbonyl group. Carbonyl groups

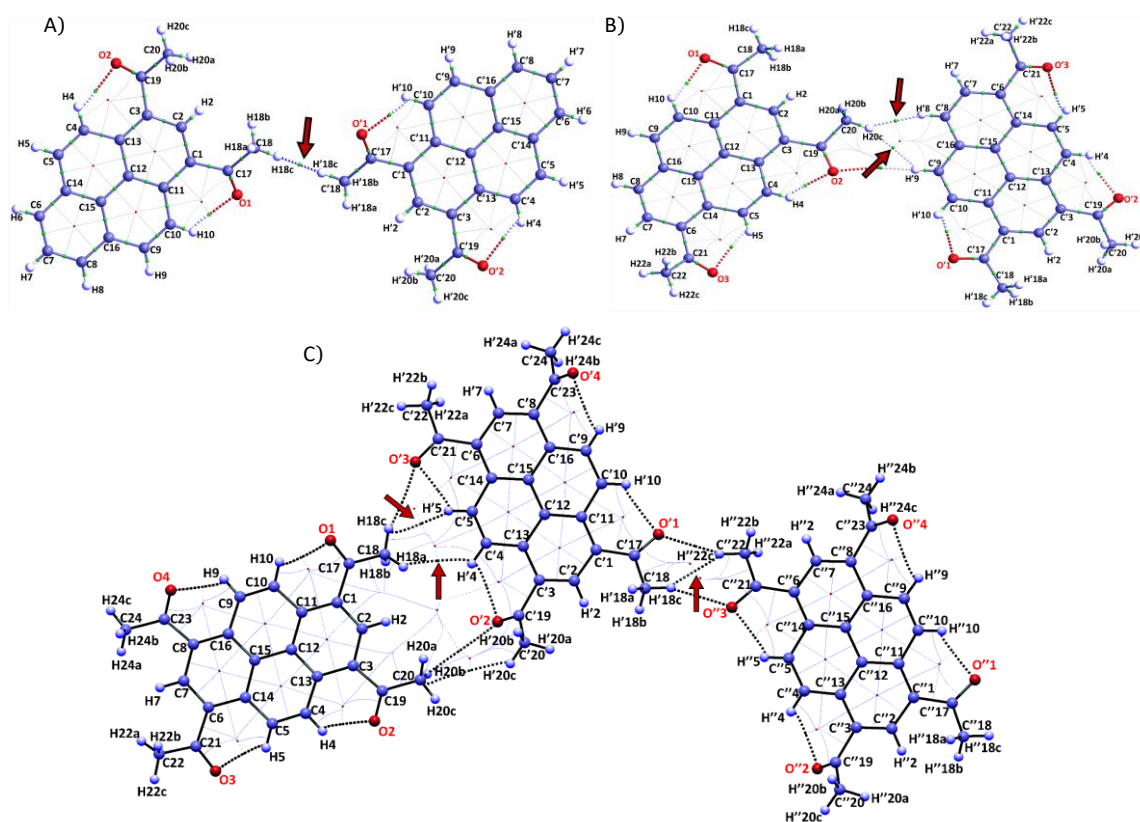


Figure 3.4. Shows QTAIM electron density map of (A) 2AP; (B) 3AP and (C) 4AP, arrows indicate the existence of intermolecular C-H...H-C contacts.

adjacent to the interacting sp^3 methyl groups could make the C-H bonds both polarizable and polarizing with respect to each other, as observed for B-H bonds[141].

3AP exhibits $(CH_3)H \cdots H(\text{aryl})$ interactions whereas 4AP shows a bond path for $(CH_3)H \cdots H(CH_3)$ and $(CH_3)H \cdots H(\text{aryl})$ interactions (Figure 3.4B&C). QTAIM calculations also confirmed the existence of C-H...O and C-H...C interactions in the derivatives 2-4AP, apart from the C-H...H-C contacts (Table 3.4).

Hirshfeld surface analyses[134] of 1-4AP (Figure 3.5 and Table 3.5) exhibit systematic trends in the weak interactions with an increase in the number of

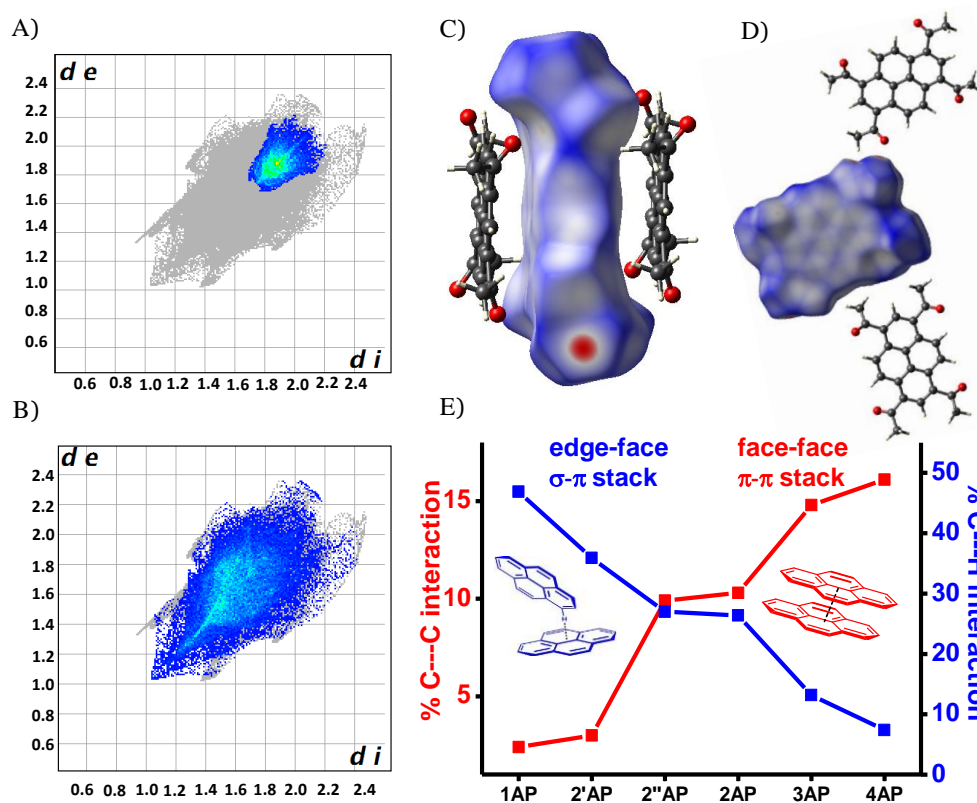


Figure 3.5. Hirshfeld 2D fingerprint plot of 4AP with the region of the plots corresponding to (A) C...C and (B) H...H interactions; Hirshfeld surface of 4AP mapped with d_{norm} depicting; (C) C...C and (D) H...H interactions and (E) percentage contribution of edge-to-face (C...H) and face-to-face (C...C) interactions in 1-4AP.

Table 3.5. Percentage of intermolecular contacts of a molecule in crystalline 1-4AP.

Interaction	1AP	2AP	2'AP	2''AP	3AP	4AP
H...H %	38.8	42.3	40.8	42.7	45.8	45.3
C...H %	46.9	26.4	35.9	27.0	13.2	7.4
O...H %	11.3	19.0	15.0	18.5	21.4	25.8
C...C %	2.4	10.3	3	9.9	14.8	16.1
C...O %	0.5	1.9	5.3	1.8	4.2	4.7

^atotal percentage of intermolecular contacts ca. 99.9% (1AP), 99.9% (2AP), 100% (2'AP), 99.9% (2''AP), 99.4% (3AP), 99.3% (4AP).

substituted acetyl groups per pyrene unit as the following (i) decrease in the C...H contacts that corresponds to σ - π (edge-to-face) interactions; (ii) increase in the contacts that corresponds to π - π (face-to-face) interactions; (iii) increase in the O...H contacts that corresponds to C-H...O interactions; (iv) increase in the H...H contacts that corresponds to dihydrogen interactions and (v) increase in the O...C contacts that corresponds to dipolar interactions between the carbonyl groups.

2.3.3. Crystal structure analyses of 1-4AP

Concurrence of such weak intermolecular interactions dictates the molecular packing that results in ideal columnar 2D stacks in 4AP having $\rho = 0.46$ (Figure 3.6). A value of $\rho = 19.5$ in 1AP indicates the formation of a herringbone structure in the crystalline lattice when compared to the sandwich herringbone structure in the P ($\rho = 3.4$). Efficient reduction in the ρ value from 1-4AP is a consequence of simultaneous (i) decrease in the percentage of C...H contacts (σ - π stacking) from 46.9% (1AP) to 7.4% (4AP) and (ii) increase in the C...C contacts (π - π stacking) from 2.4% (1AP) to

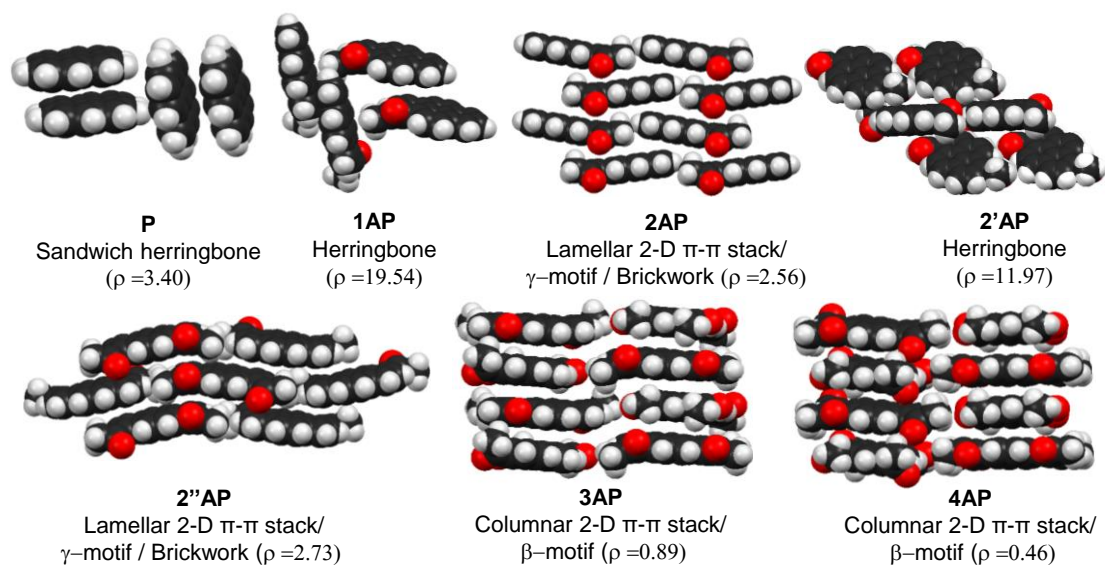


Figure 3.6. Close packing arrangement in 1–4AP indicating the values of $\rho = [(\%C\cdots H)/(\%C\cdots C)]$ [30]. Herringbone ($\rho > 4.5$), sandwich herringbone ($3.2 < \rho < 4.0$), γ ($1.2 < \rho < 2.7$), β ($0.46 < \rho < 1.0$).

16.1% (4AP). With increase in the number of acetyl groups in pyrene core, crystal packing of 1–4AP shows distinct patterns through a gradual decrease in the interplanar angle between adjacent pyrene units ($\gamma = 48.4^\circ$ for 1AP and $\gamma = 0^\circ$ for 4AP; Figure 3.7A and B and Table 3.6). Decrease in the interplanar angle was accompanied

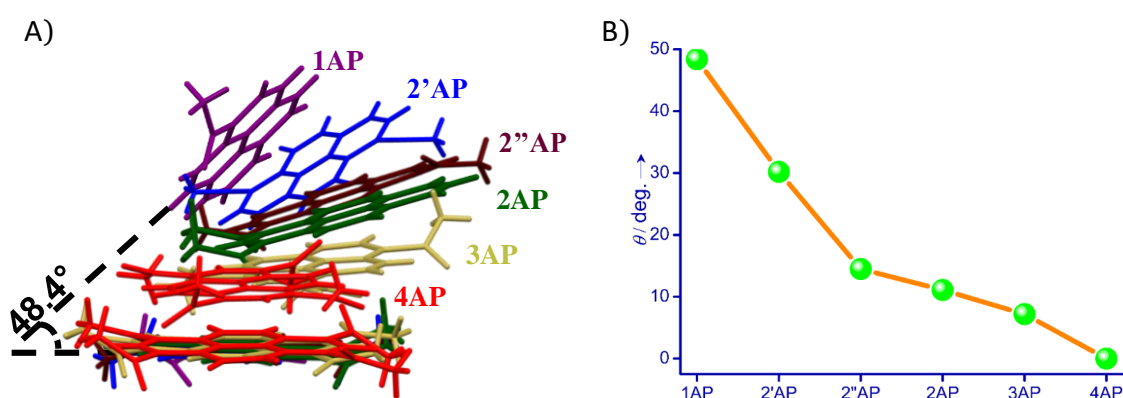


Figure 3.7. Shows (A) the gradual decrease in the interplanar angle between the nearest molecules and (B) the decreasing angle and the consequent increase in stacking of the pyrene units in the crystalline 1-4AP.

Table 3.6. Interplanar angle between nearest pyrene molecules in crystalline 1-4AP.

	Angle, deg
1AP	48.4, 50.5, 51.1
2AP	11.1
2'AP	30.2
2''AP	14.5
3AP	7.2
4AP	0, 3.9, 5.9

by transformation of the herringbone structure of 1AP to the columnar structure of 4AP. 2'AP shows herringbone packing without π - π overlap between adjacent pyrene units while the crystal structure of 2, 2''AP shows a lamellar motif with 2D π - π stacking (brickwork/ γ -motif). The torsional angles between the planes of adjacent pyrene units in 2, 2''AP were found to be 0° and 1° , respectively (Figure 3.8 and 3.9). 3AP shows columnar stacks with extended 2D π - π stacking (β -motif), consistent with 4AP. While 3AP exhibited a torsional angle of 67.8° between the planes of adjacent pyrene units, a near-orthogonal (80.4°) arrangement of pyrene units was observed for 4AP, consistent with the 1,3,6,8-tetraphenylpyrene derivatives reported by Geerts, Bredas and co-workers[142]. We observed a π - π stacking distance of 3.4–3.5 Å in 4AP when compared to 4.8 Å in 1,3,6,8-tetrakis(4-methoxyphenyl)-pyrene reported earlier. By virtue of the smaller size of the acetyl vs. phenyl substituents, we observed a shorter π - π stacking distance in 4AP. In 2AP, carbonyl oxygen interacts with the aryl hydrogen (C-H...O; Figure 3.10) forming a zig-zag arrangement along the *b*-axis (out-of-plane; 1D), while 2'AP favors a linear arrangement along the *c*-axis possessing C-H...O interactions. An interplanar angle of 14.51 between the pyrene units in 2''AP

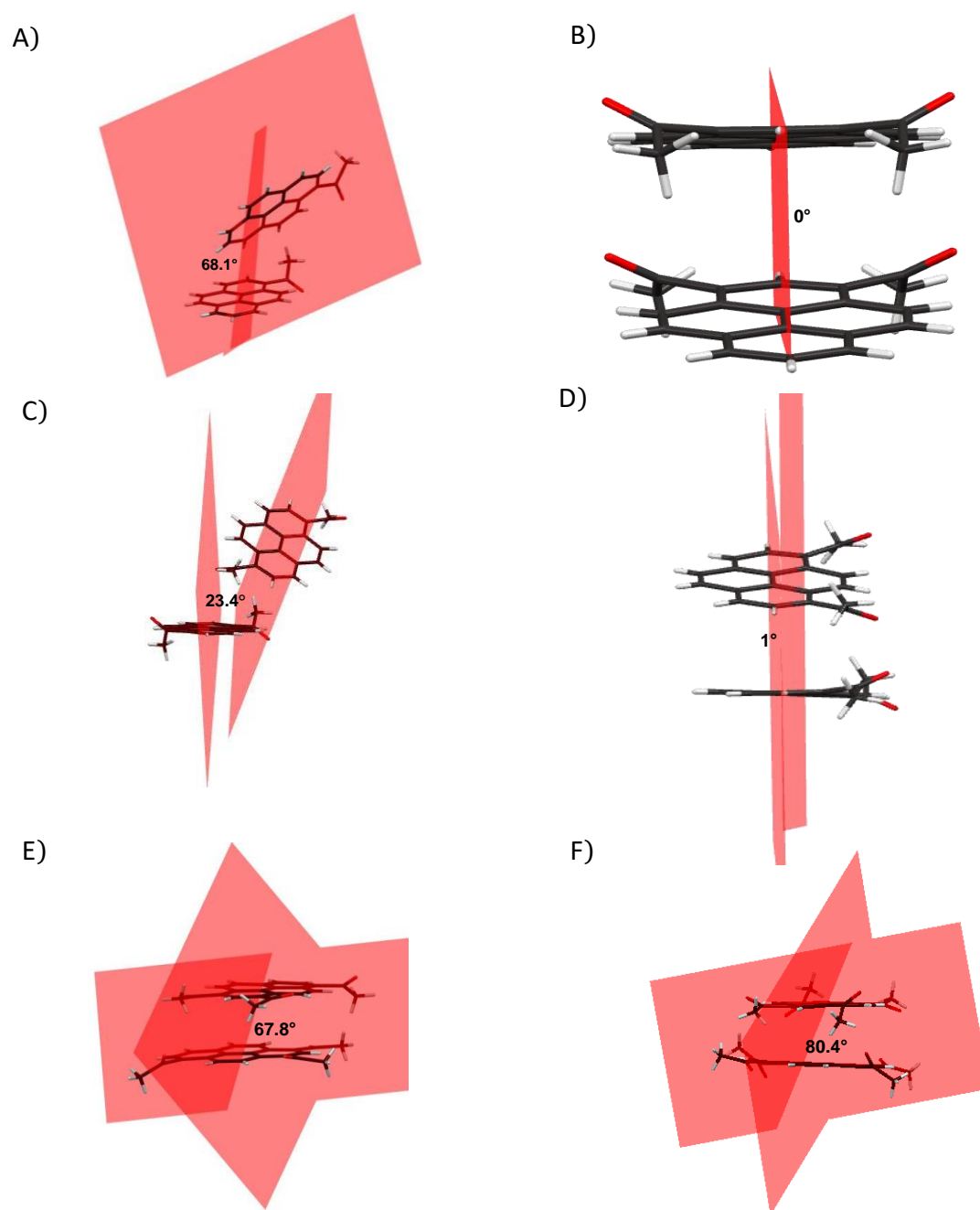


Figure 3.8. Shows the torsional angle between adjacent pyrene units in crystal packing of (A) 1AP; (B) 2AP; (C) 2'AP; (D) 2''AP; (E) 3AP and (F) 4AP.

arises from C-H...O contacts. Extended C-H...O interactions in 3-4AP across the ab-plane promotes a sheet-like arrangement of pyrene units (Figure 3.10) in combination with interplanar C-H...O interactions that support the pyrene (β -structure) stacks along the *c*-axis. In addition to C-H...O interactions, we observed C-H...H-C contacts

(3.46–4.32 kJ mol⁻¹; Table 3.4) in crystalline 2–4AP. C-H...H-C contacts in 2AP (*b*-axis; in-plane; 1D) and 3AP (*a*-axis; in-plane; 1D) promote a linear arrangement of the

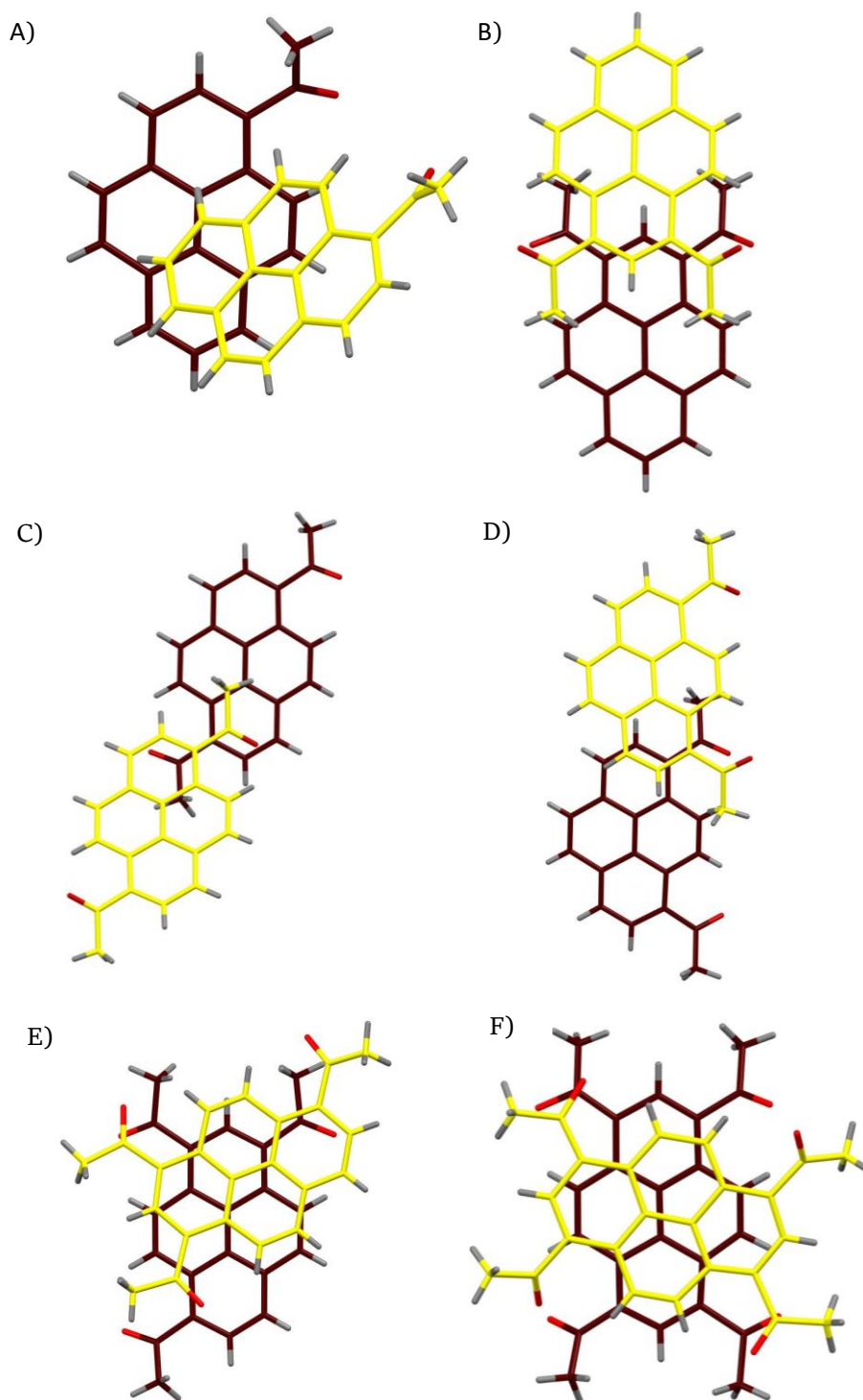


Figure 3.9. Shows the aerial overlap between adjacent pyrene units in close packing of (A) 1AP; (B) 2AP; (C) 2'AP; (D) 2''AP; (E) 3AP and (F) 4AP.

pyrene units. In 4AP, C-H...O interactions promote stacks along the *c*-axis which is reinforced by C-H...H-C contacts across the *ab*-plane.

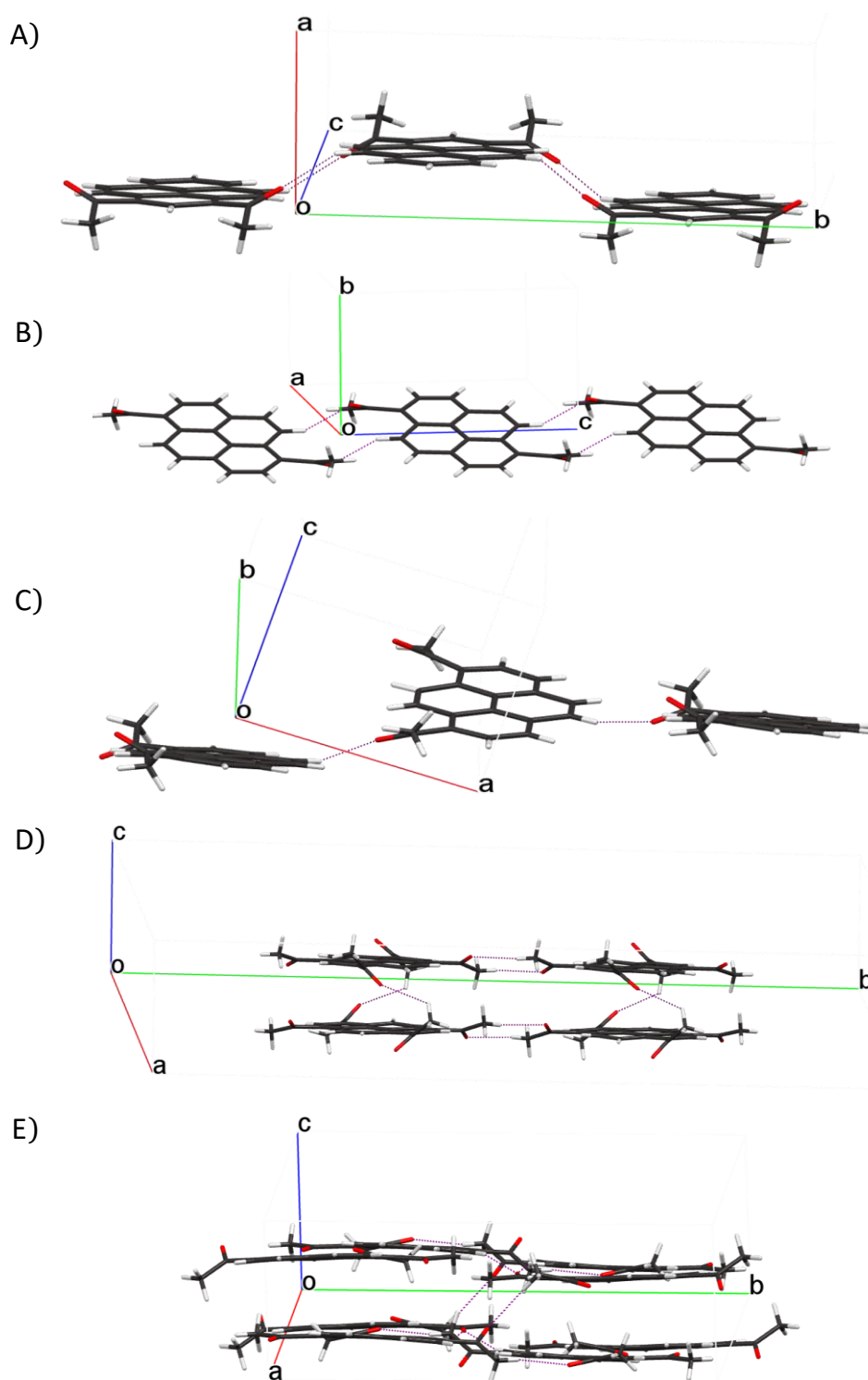


Figure 3.10. Shows the C-H...O interactions in the crystal packing of (A) 2AP; (B) 2'AP; (C) 2''AP; (D) 3AP and (E) 4AP.

2.3.4. Steady-state absorption and emission measurements

We performed steady-state and time-resolved photophysical measurements to correlate the extent of overlap between adjacent pyrene units *vs.* colour properties in crystalline 1–4AP. Experiments were also carried out in dilute solutions of chloroform to understand the photophysical properties of 1–4AP. Increasing the number of acetyl groups resulted in progressive red-shift in the UV-Vis absorption maximum of 1–4AP in chloroform, for example 22 nm (1AP) and 70 nm (4AP), when compared to P (Figure 2.4A and Table 3.7). Upon excitation at 350 nm, the emission maximum of 1–4AP in chloroform exhibited a similar trend indicating the role of extended conjugation

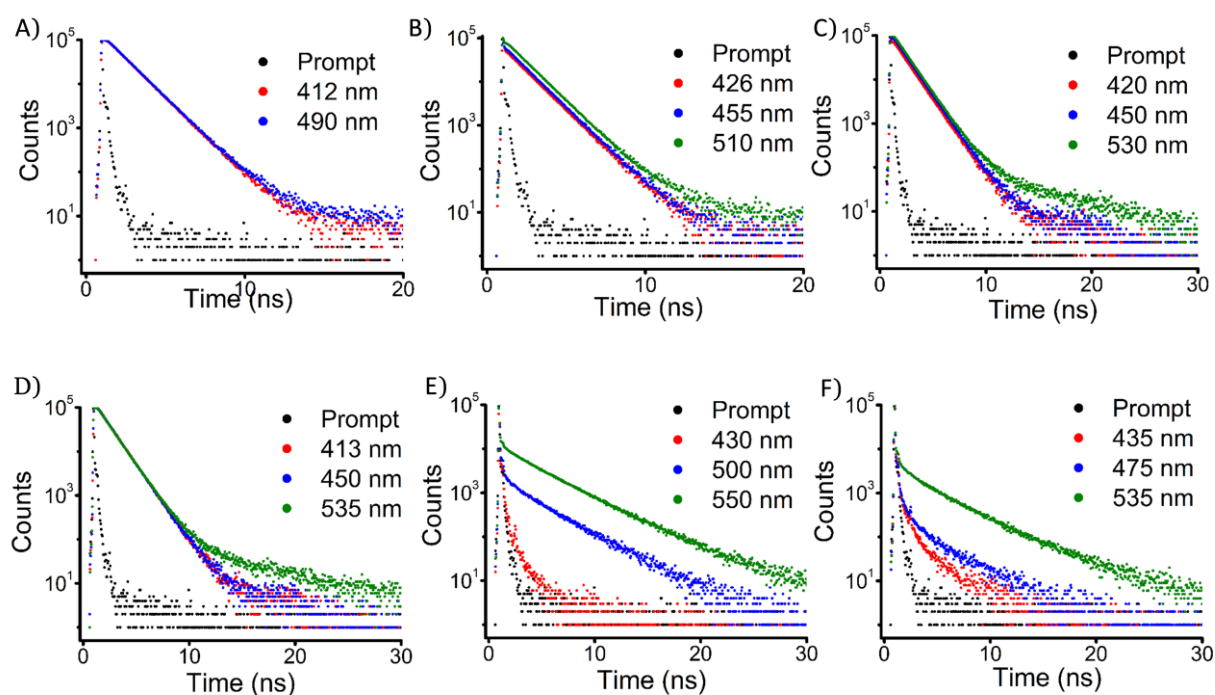


Figure 3.11. Shows fluorescence decay profile of (A) 1AP; (B) 2AP; (C) 2'AP; (D) 2''AP; (E) 3AP and (F) 4AP in CHCl_3 solution on exciting at 375 nm and collected at different wavelengths.

arising from carbonyl group(s) in the electronic transitions in the pyrene unit (Figure 2.4B and Table 3.7). We observed a significant decrease in the fluorescence quantum yield of 1-4AP ($\Phi_f \geq 0.9\%$, Table 3.7) in chloroform when compared to P ($\Phi_f = 75\%$)[89]. Observed low Φ_f of 1-4AP in chloroform could be attributed to alternate excited state decay pathways ($k_{nr} \approx k_{ISC} \gg k_r$) due to the incorporation of acetyl group(s)[82]. Picosecond time-resolved fluorescence measurements of 1-4AP in chloroform exhibit a short lifetime ($\tau_f = 1-2$ ns) when monitored at respective emission maximum upon excitation at 375 nm (Figure 3.11). While 2-4AP in chloroform shows a longer lifetime (ca. 3-5 ns) when monitored at a longer wavelength (500-550 nm) indicating the

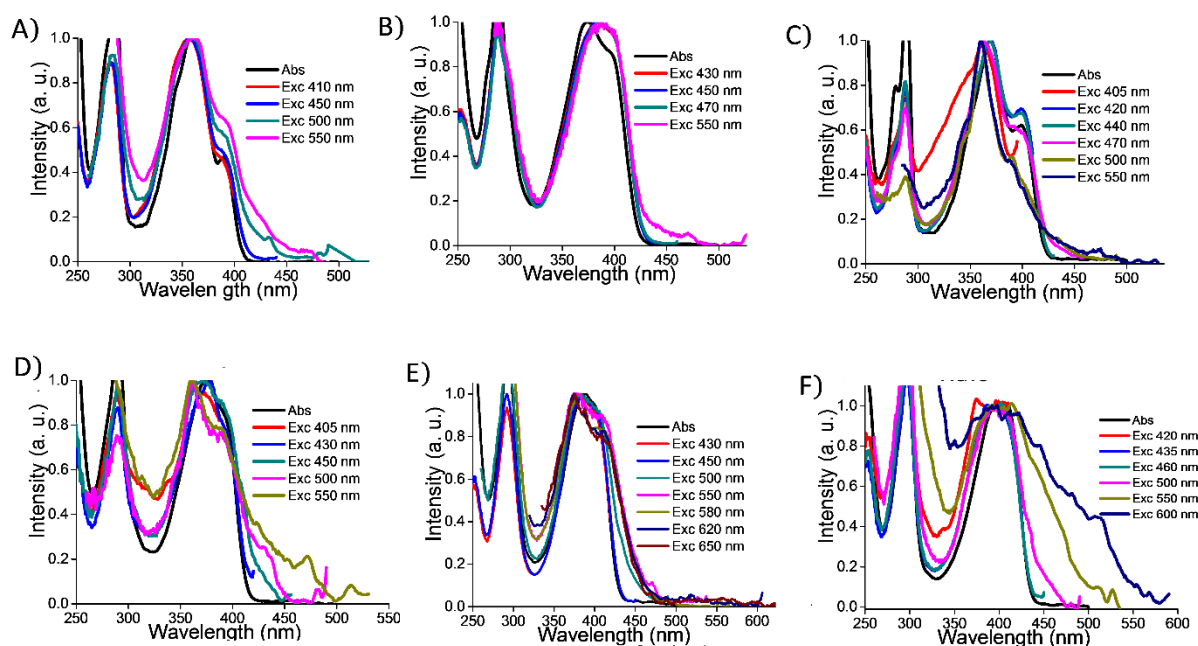


Figure 3.12. Shows the fluorescence excitation spectra of (A) 1AP; (B) 2AP; (C) 2'AP; (D) 2''AP; (E) 3AP and (F) 4AP in $CHCl_3$ as compared to absorption spectrum.

Table 3.7. Shows the photophysical properties of 1-4AP derivatives.

	^a λ_{abs} (nm)	^a λ_{f} (nm)	^a Φ_{f}	^a τ_{f} (ns) [Amplitude](%)	^a k_{r}	^a k_{nr}	^b λ_{abs} (nm)	^b λ_{f} (nm)	^b τ_{f} (ns) [Amplitude](%)	^b Φ_{f}	^b k_{r}	^b k_{nr}
P	337	393	0.75[143]	150.1 [100][144]	5×10^6	1.6×10^6	386	472	22.97 [100]	0.67[89]	2.9×10^7	1.4×10^7
1AP	359	412	0.004	1.39 [93] 0.98 [7]	2.9×10^6	7.3×10^8	414	518	574.6 [15.7], 54.43 [68.5], 2873 [15.8]	0.006	2.6×10^3	4.3×10^2
2AP	373	426	0.008 ^c	1.39 [93] 0.65 [7]	5.8×10^6	7.3×10^8	426	602	9.68 [46.5], 23.19 [30.9], 2.94 [22.6]	0.325	1.9×10^7	4.0×10^7
		510		0.7[3] 1.35 [96] 3.0 [1]								
2'AP	369	420	0.002 ^c	1.3 [80] 1.62 [20]	1.5×10^6	7.3×10^8	430	567	3.95 [38.6], 19.55 [39.2], 1.07 [22.2]	0.030	1.8×10^6	5.0×10^7
		530		0.8 [1] 1.36 [98] 4.22 [1]								
2''AP	375	413	0.008 ^c	1.4 [97] 0.6 [3]	5.8×10^6	7.2×10^8	441	631	3.47 [34.9], 11.57 [65.1]	0.063	6.0×10^6	8.0×10^7
		535		0.8 [1] 1.4 [98] 4.9 [1]								
3AP	388	431	0.003 ^c	1.2	2.5×10^6	8.3×10^8	471	645	22.48 [8.4], 4.57 [91.6]	0.277	2.7×10^7	7.0×10^7
		550		4.1 [67] 1.5 [33]								
4AP	407	435	0.002 ^c	0.98	2.0×10^6	1.0×10^9	486	646	1.17 [10.3], 2.78 [46.9], 6.11 [63.4]	0.071	1.4×10^7	1.8×10^8
		535		0.85 [55] 3.8 [45]								

^achloroform solution; ^bcrystalline state; abs – absorption; f – fluorescence; ^coverall quantum yield. Observed increase in the rate of radiative decay for crystalline 2, 2' and 2''AP when compared to 2, 2' and 2''AP in solution is indicative of the formation of 'J' type aggregate.

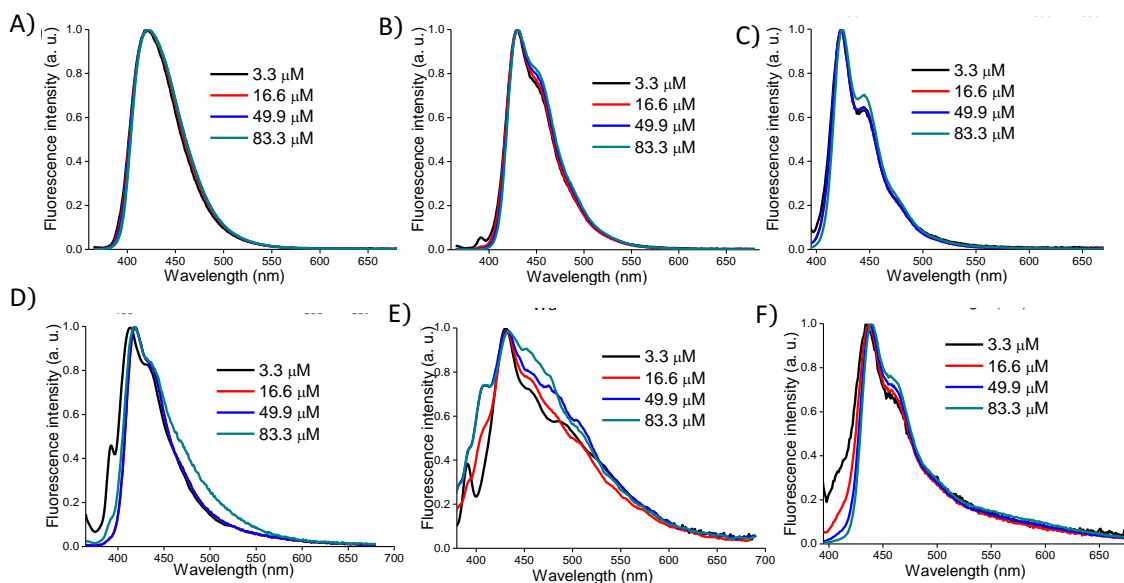


Figure 3.13. Concentration dependent emission spectra of (A) 1AP; (B) 2AP; (C) 2'AP; (D) 2''AP; (E) 3AP and (F) 4AP in CHCl₃ solution on exciting at 350 nm.

possibility of aggregation. Emission wavelength dependent excitation (Figure 3.12) in combination with concentration dependent emission (Figure 3.13) and excitation (Figure 3.14) spectra confirms the existence of ground state aggregate in 2-4AP in

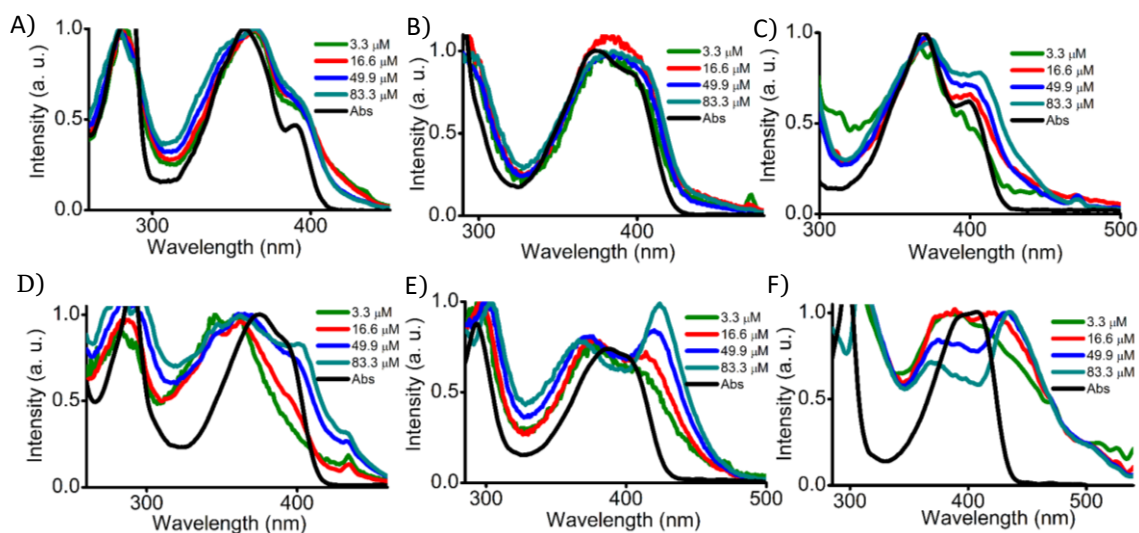


Figure 3.14. Concentration dependent excitation spectra of (A) 1AP; (B) 2AP; (C) 2'AP; (D) 2''AP; (E) 3AP and (F) 4AP in CHCl₃ solution while monitoring at 500 nm (for 1AP and 2''AP) and 550 nm (for 2AP, 2'AP, 3AP and 4AP).

CHCl₃.

In the crystalline state, 1–4AP exhibited diverse colours ranging (Figure 3.2, Row III) from pale yellow–yellow–orange resulting in a red-shift of 100 nm in the absorption maximum of 4AP when compared to P (Figure 3.15A). Upon excitation at 350 nm, 1–4AP exhibited a remarkable red-shift, for example 174 nm in the case of 4AP, in the emission maximum when compared to P (Figure 3.2, Row IV and Figure 3.15B&D). Red-shift in the excimer-like fluorescence of 1–4AP could be attributed

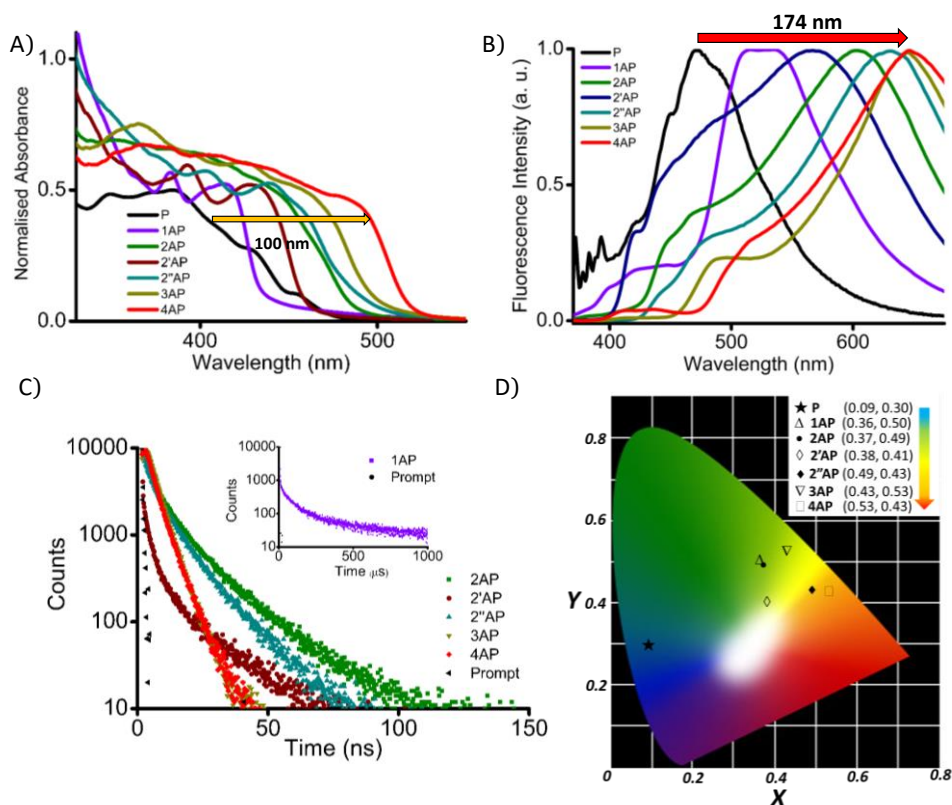


Figure 3.15. Shows the normalised (A) absorption; (B) fluorescence emission spectra of crystalline 1-4AP derivatives; excitation wavelength is 350 nm and (C) fluorescence decay profile of crystalline 2-4AP derivatives and the corresponding inset shows fluorescence decay profile of crystalline 1AP, excitation wavelength is 375 nm and emission monitored at 518 nm (1AP); 602 nm (2AP); 567 nm (2'AP); 631 nm (2''AP); 645 nm (3AP) and 646 nm (4AP) and (D) CIE colour diagram of fluorescence emission for crystalline 1-4AP derivatives.

to a combination of additional conjugation from acetyl groups and an increase in the extent of overlap between the adjacent pyrene moieties[107]. A significant red-shift in the excitation spectra of 1-4AP when compared to the corresponding absorption spectra is indicative of ground state interaction between the vicinal pyrene units (Figure 3.16). A slip-stacked arrangement between the adjacent pyrene units in the crystalline 2, 2' and 2'' AP in combination with enhanced Φ_f , τ_f and k_f when compared to that in solution indicate the possibility of J-like aggregates and/or excimers of pyrene (Figure 3.15C and Table 3.7)[145-147]. Aggregate induced enhanced emission (AIEE) due to restricted motion of the flanking acetyl groups could also result in the enhanced fluorescence of the crystalline 2, 2' and 2'' AP[148, 149]. Enhanced Φ_f in 3-4AP could be attributed to a combination of AIE, ground state aggregation and cross-

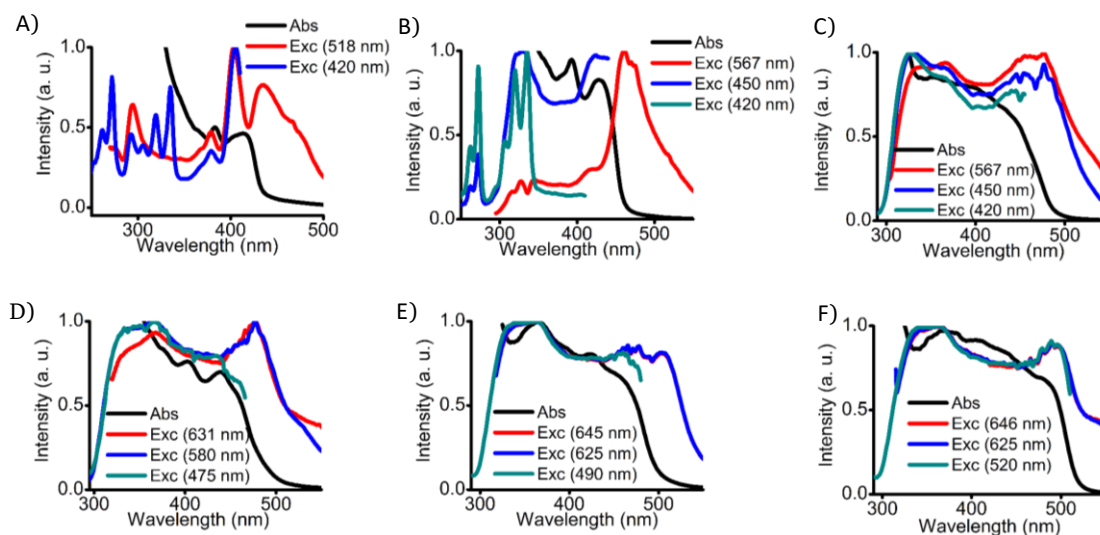


Figure 3.16. Shows fluorescence excitation spectra of crystalline (A) 1AP; (B) 2AP; (C) 2'AP; (D) 2''AP; (E) 3AP and (F) 4AP as compared to absorption spectra. Absorption spectra of crystalline 1-4AP derivative are reproduced for comparison with excitation spectra. Emission maxima, where the excitation spectra are monitored, are indicated in the bracket.

dipole arrangement of the adjacent pyrene moieties as reported earlier[67, 142, 150]. Among all the crystalline derivatives 1–4AP, nonlinear increase in the emission maximum of 3–4AP could be a consequence of orbital overlap between the adjacent pyrene units from near-orthogonal arrangement.

Thus in this effort, progressive acylation of pyrene resulted in a remarkable decrease in the interplanar angle between two neighbouring units causing significant red-shift in the solid-state fluorescence. This allowed us to employ the combination of steric and conjugation effects of benzoyl units of pyrene based systems. The significant dimension of the benzoyl unit could potentially perturb strong π - π interactions between the nearest pyrene units.

3.2.5. Synthesis and crystallization

Adding stoichiometric quantity of benzoyl chloride to a solution of pyrene (P) and AlCl₃ in carbon disulfide (CS₂) at ambient temperature rendered the benzoyl derivatives (1–4BP) in low-moderate yields (Figure 3.17, Row1). Though Harvey and co-workers[151] reported 1BP, 2BP and 2'BP, the synthesis of 2''BP, 3BP and 4BP are yet to be explored. Single crystal X-ray analyses (SCXRD) of 1–4BP were not reported earlier. SCXRD analyses were performed on 0.20 x 0.20 x 0.15 mm crystalline samples obtained through slow evaporation of 1–4BP from a varying composition of chloroform:acetone mixtures. Benzoyl derivatives 1BP (*P*-1), 2BP (*P*-1) and 3BP (*P*-1) yield solvent free triclinic crystal system while 2'BP (*P*₂₁/*n*), 2''BP (*C*2/*c*) and 4BP (*P*₂₁/*n*) exhibit solvent free monoclinic crystal system (Figure 3.17, Row III, Table 3.8).

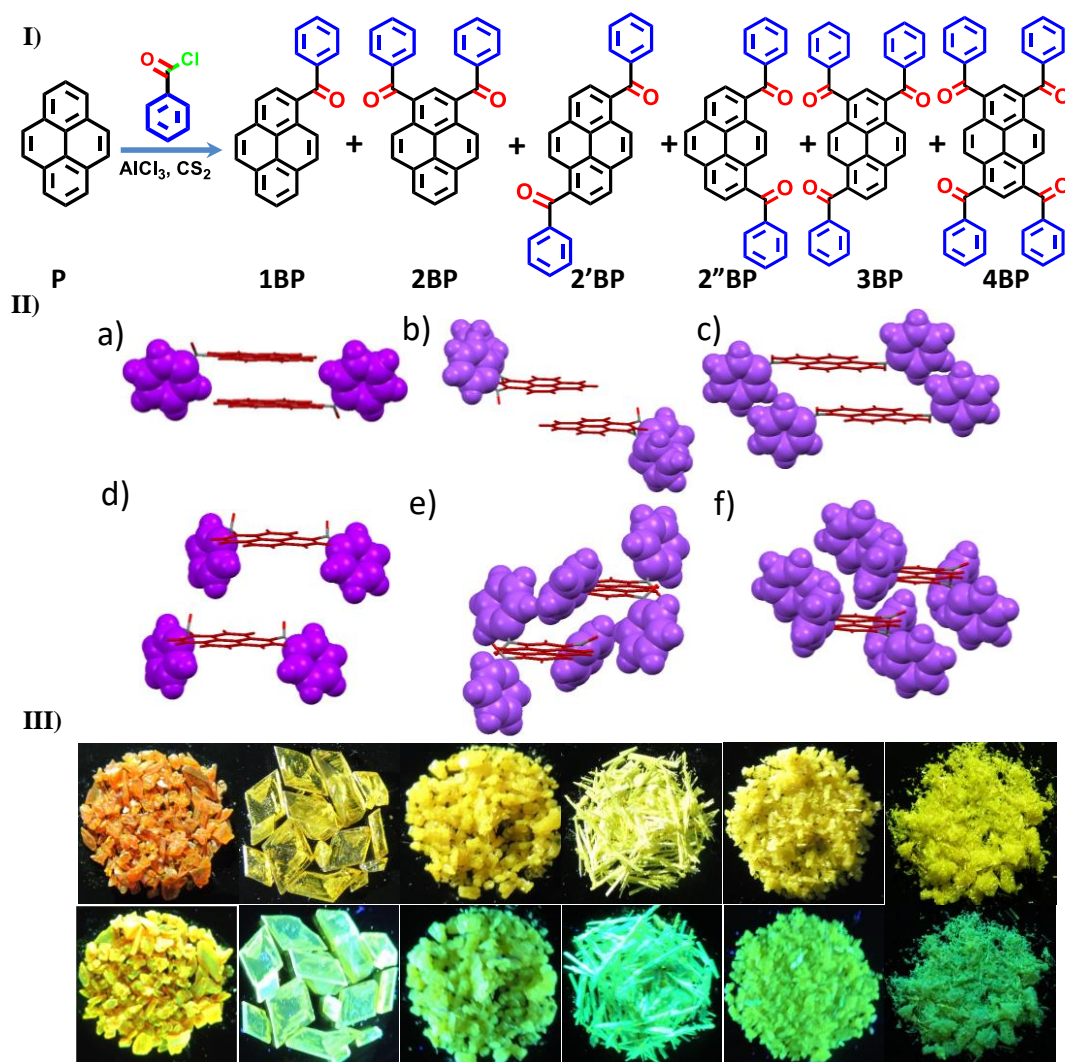


Figure 3.17. Row I: Molecular structure of 1–4BP; Row II: close packing arrangement in the crystal (a) 1BP; (b) 2BP; (c) 2'BP; (d) 2''BP; (e) 3BP and (f) 4BP; Row III: photographic image of the crystals in daylight (above) and under UV illumination (below).

2.3.6. Frontier molecular analysis and steady state studies

Frontier molecular orbital (FMO) analysis, cyclic voltammetric, UV-Vis absorption and emission measurements were employed to investigate the extent of perturbations in pyrene imparted by incremental benzoyl groups. FMO analyses of 1-4BP shows that the electron density of HOMO (Figure 3.18A) is distributed in pyrene units while electron density of LUMO is mostly localized on pyrene chromophore

Table 3.8. Shows crystallographic data and refinement parameters for crystalline 1-4BP derivatives.

	1BP	2BP	2'BP	2''BP	3BP	4BP
Formula	C ₂₃ H ₁₄ O	C ₃₀ H ₁₈ O ₂	C ₃₀ H ₁₈ O ₂	C ₃₀ H ₁₈ O ₂	C ₃₇ H ₂₂ O ₃	C ₄₄ H ₂₆ O ₄
formula wt	306.34	410.44	410.44	410.44	514.55	618.65
colour, shape	Yellow	Yellow	Yellow	Yellow	Yellow	Orange
dimens, mm	0.20x0.2x0.15	0.20x0.15x0.10	0.25x0.20x0.15	0.20x0.15 x0.10	0.20x0.15x0.10	0.20x0.10x0.10
crystal system	Triclinic	Triclinic	Monoclinic	Monoclinic	Triclinic	Monoclinic
space group, Z	<i>P</i> -1, 2	<i>P</i> -1, 2	<i>P</i> 2 ₁ / <i>n</i> , 2	<i>C</i> 2/ <i>c</i> , 8	<i>P</i> -1, 2	<i>P</i> 2 ₁ / <i>n</i> , 2
<i>a</i> , Å	8.0024	10.0326	5.4689	25.1722	8.9515	5.6503
<i>b</i> , Å	9.6519	10.6238	8.2510	8.4269	11.9373	20.897
<i>c</i> , Å	10.0837	11.6287	22.5720	19.6579	14.2375	12.787
α , deg	102.8140	94.4890	90.00	90.00	104.703	90.00
β , deg	96.5760	99.490	95.604	99.8860	102.280	101.506
γ , deg	91.4730	117.2630	90.00	90.00	109.581	90.00
<i>V</i> , Å ³	753.40	1069.82	1013.67	4107.99	1310.36	1479.5
temp, K	296	296	296	296	296	293
<i>d</i> calcd, g/cm ⁻³	1.349	1.274	1.344	1.326	1.303	1.388
no. of reflections collected	11056	15706	7234	15377	16670	14254
no. of unique reflections	2644	3761	1732	3604	3736	3578
2 θ _{max} , deg	50	50	50	50	50	50
no. of parameters	217	289	145	290	361	217
<i>R</i> 1, <i>wR</i> 2 (<i>I</i> > 2 σ (<i>I</i>))	0.0377, 0.1208	0.0408, 0.1147	0.0337, 0.0955	0.0482, 0.1237	0.0421, 0.1140	0.0403, 0.1084
<i>R</i> 1, <i>wR</i> (all data)	0.0511, 0.1458	0.0503, 0.1292	0.0427, 0.0955	0.0711, 0.1600	0.0855, 0.1610	0.0623, 0.1253
goodness of fit	1.151	1.067	1.039	1.155	1.082	1.003
CCDC number	1440151	1440152	1440153	1440154	1440155	1440156

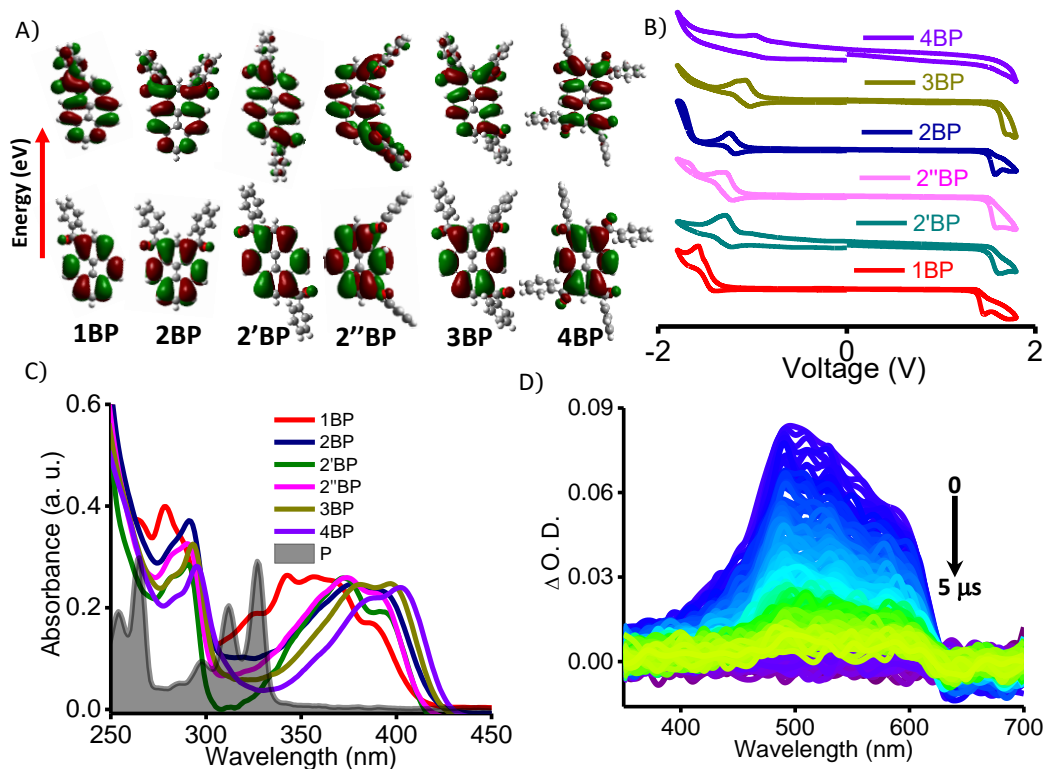


Figure 3.18. (A) Frontier molecular orbital (FMO) analysis of 1–4BP calculated from the B3LYP/6-311G**+ level of theory. Lower and upper plots represent the HOMOs and LUMOs, respectively; (B) cyclic voltammograms of 1–4BP in acetonitrile; (C) absorption spectra of 1–4BP; the area filled spectrum (grey) represents the absorption spectrum of pyrene[152] and (D) nanosecond transient absorption spectrum of 4BP in chloroform.

with a moderate extension to the carbonyl group(s). Low-lying excited electronic states mainly results from well-described π - π^* transitions with a minor contribution from n - π^* character. A decrease in the HOMO-LUMO gap from 3.59 eV (1BP) to 3.18eV (4BP) is attributed to the increase in the effective conjugation due to carbonyl groups on the pyrene unit (Table 3.9). Cyclic voltammetry (0.1 M nBu₄NPF₆ in acetonitrile) of 1BP (Figure 3.18B) exhibits oxidation peak at 1.47 V while reduction peak appear at -1.50 V. Decrease in the HOMO-LUMO gap of benzoylpyrenes (2.97eV

Table 3.9. Experimental (electrochemical) and calculated energy levels of 1-4BP.

	$E_{\text{on}}^{\text{ox}}$ (V) ^a	$E_{\text{on}}^{\text{red}}$ (V) ^a	Energy levels (eV)			Energy levels (eV)		
			E_{HOMO} (eV) ^a	E_{LUMO} (eV) ^a	E_{gap} (eV) ^a	E_{HOMO} (eV) ^b	E_{LUMO} (eV) ^b	E_{gap} (eV) ^b
1BP	1.47	-1.50	-6.27	-3.30	2.97	-5.79	-2.20	3.59
2BP	1.57	-1.20	-6.37	-3.60	2.77	-5.89	-2.42	3.47
2'BP	1.61	-1.35	-6.41	-3.50	2.91	-6.03	-2.61	3.42
2''BP	1.58	-1.33	-6.38	-3.50	2.88	-5.86	-2.30	3.56
3BP	1.67	-1.13	-6.47	-3.67	2.80	-6.06	-2.69	3.37
4BP	1.61	-1.0	-6.41	-3.80	2.61	-6.28	-3.10	3.18

^a experimental data; ^b computational data

for 1BP; 2.61eV for 4BP; Table 3.9) in comparison to P (3.37 eV) is in agreement with the FMO analysis[153].

Steady state absorption spectra of 1-4BP in chloroform exhibit two distinct bands: a band centered around 250-300 nm and another around 300-425 nm (Figure 3.18C). Time-dependent density functional theory (TDDFT)[87, 88] calculations suggest that observed bands are a combination of several electronic transitions (Table 3.10) with the longer wavelength band due to π - π^* transition. λ_{max} of long-wavelength transition of 1BP in chloroform is red-shifted by 12 nm compared to P. 2-4BP display remarkable red-shift in the long-wavelength, which could be attributed to the increase in number of benzoyl group(s). Upon excitation at 380 nm, 1BP in chloroform exhibits emission band centered around 450 nm (Figure 3.19A, Table 3.11). The emission maximum is ca. 50 nm red-shifted in comparison to P under similar conditions. However, further increase in the number of benzoyl groups, the emission maximum

Table 3.10. Excitation energy, oscillator strength, main transition orbitals and their contribution calculated for 1-4BP using TDDFT (B3LYP/6-311G^{***}).

	State	Excitation Energy (eV)	λ (nm)	Oscillator strength (f)	Main transition orbital	Contribution
1BP	T4	3.35	369.83		HOMO \rightarrow LUMO+1	0.48
	T3	3.25	381.65		HOMO-1 \rightarrow LUMO	0.58
	T2	2.96	418.89		HOMO-2 \rightarrow LUMO	0.58
	T1	2.02	614.73		HOMO \rightarrow LUMO	0.65
	S4	3.93	315.81	0.0764	HOMO \rightarrow LUMO+1	0.64
	S3	3.63	341.64	0.0162	HOMO \rightarrow LUMO+2	0.40
	S2	3.47	356.84	0.0079	HOMO-2 \rightarrow LUMO	0.60
	S1	3.20	387.36	0.3176	HOMO \rightarrow LUMO	0.67
2BP	T4	3.13	396.21		HOMO-1 \rightarrow LUMO	0.59
	T3	2.96	418.67		HOMO-3 \rightarrow LUMO	0.41
	T2	2.94	422.04		HOMO-2 \rightarrow LUMO	0.54
	T1	1.93	642.01		HOMO \rightarrow LUMO	0.67
	S4	3.59	359.84	0.0	HOMO \rightarrow LUMO+1	0.47
	S3	3.52	352.53	0.0138	HOMO-1 \rightarrow LUMO	0.55
	S2	3.23	383.43	0.0426	HOMO \rightarrow LUMO+1	0.68
	S1	3.15	393.45	0.2865	HOMO \rightarrow LUMO	0.66
2'BP	T4	3.15	393.51		HOMO-1 \rightarrow LUMO	0.67
	T3	2.96	418.40		HOMO-3 \rightarrow LUMO	0.51
	T2	2.91	425.98		HOMO-2 \rightarrow LUMO	0.49
	T1	1.93	643.61		HOMO \rightarrow LUMO	0.67
	S4	3.52	352.17	0.0	HOMO \rightarrow LUMO+1	0.69
	S3	3.45	359.48	0.0	HOMO-2 \rightarrow LUMO	0.56
	S2	3.43	361.18	0.0314	HOMO-3 \rightarrow LUMO	0.55
	S1	3.08	402.01	0.5307	HOMO \rightarrow LUMO	0.68
2''BP	T4	3.15	393.51		HOMO- 1 \rightarrow LUMO	0.67
	T3	2.96	418.40		HOMO-3 \rightarrow LUMO	0.51
	T2	2.91	425.98		HOMO-2 \rightarrow LUMO	0.49

	T1	1.93	643.61		HOMO \rightarrow LUMO	0.67
	S4	3.48	355.85	0.0065	HOMO \rightarrow LUMO+1	0.50
	S3	3.44	360.60	0.0074	HOMO-3 \rightarrow LUMO	0.58
	S2	3.41	363.81	0.0009	HOMO-2 \rightarrow LUMO	0.47
	S1	3.08	402.55	0.4693	HOMO \rightarrow LUMO	0.68
3BP	T4	2.99	413.82		HOMO-4 \rightarrow LUMO	0.42
	T3	2.93	423.53		HOMO-3 \rightarrow LUMO	0.40
	T2	2.89	428.94		HOMO-2 \rightarrow LUMO	0.42952
	T1	1.87	662.37		HOMO \rightarrow LUMO	0.68
	S4	3.45	359.22	0.0018	HOMO \rightarrow LUMO	0.42
	S3	3.39	365.66	0.0079	HOMO-3 \rightarrow LUMO	0.36
	S2	3.33	372.29	0.0006	HOMO-2 \rightarrow LUMO	0.54
	S1	3.0	413.15	0.5936	HOMO \rightarrow LUMO	0.69
4BP	T4	2.96	418.66		HOMO \rightarrow LUMO	0.31
	T3	2.91	425.48		HOMO-- 3 \rightarrow LUMO	0.44
	T2	2.91	426.32		HOMO-1 \rightarrow LUMO	0.41
	T1	1.86	667.46		HOMO \rightarrow LUMO	0.68
	S4	3.39	366.28	0.0	HOMO-3 \rightarrow LUMO	0.52
	S3	3.37	367.48	0.0059	HOMO-1 \rightarrow LUMO	0.51
	S2	3.35	369.67	0.0073	HOMO-2 \rightarrow LUMO	0.55
	S1	2.96	418.61	0.5504	HOMO \rightarrow LUMO	0.68

remains unchanged (ca. 450 nm). Very low fluorescence quantum yield was observed for 1-4BP ($\Phi_f \leq 1.0\%$, Table 3.11) in chloroform when compared to P ($\Phi_f = 65\%$)[92].

Picosecond time-resolved fluorescence measurements of 1-4BP indicate very short lifetime (<100 ps pulse width at $\lambda_{ex} = 375$ nm) when monitored at respective emission maxima (Figure 3.19B). In order to rule out the possibility of aggregates of 1-4BP in chloroform (0.1-1 μ M), we monitored the lifetime at the far red shifted emission.

Table 3.11. Shows the photophysical properties of 1-4BP derivatives.

	^a λ_{Abs} (nm)	^a λ_{Fl} (nm)	^a λ_{Ph} (nm)	^a Φ_{Fl}	^a k_r^\dagger (10^8 s ⁻¹)	^a k_{nr} (10^9 s ⁻¹)	^a τ_{Ph} (μ s)	^a Φ_T	^a τ_T (μ s)	^b λ_{Abs} (nm)	^b λ_{Fl} (nm)	^b τ_{Fl} (ns) (Amplitude) (%)	^b Φ_f	^b k_r (10^8 s ⁻¹)	^b k_{nr} (10^9 s ⁻¹)
P	337[91]	393[91]	600[154]	0.65*[81]	75	92.5	-	0.38*[81]	5.0 [¶] [4]	386[89]	472[89]	22.97 (100)	0.68[89]	0.29	0.01
1BP	349	444	510	0.01	≥ 1.56	9.84	23.2	0.48	2.1	500	620	$\tau_1=0.73$ (6.08) $\tau_2=2.49$ (81.98) $\tau_3=8.54$ (11.95)	0.261	0.59	0.17
2BP	395	434	527	0.011	≥ 1.0	9.90	26.7	0.41	1.4	426	552	$\tau_1=0.61$ (8.67) $\tau_2=2.71$ (64.67) $\tau_3=6.98$ (26.66)	0.149	0.31	0.18
2'BP	394	424	562	0.005	≥ 0.49	9.95	27.1	0.36	1.9	430	607	$\tau_1=3.33$ (59.36) $\tau_2=5.66$ (40.64)	0.177	0.39	0.18
2''BP	392	426	565	0.007	≥ 0.67	9.93	29.9	0.39	2.0	420	577	$\tau_1=3.02$ (68.75) $\tau_2=6.33$ (31.25)	0.162	0.35	0.18
3BP	397	428	633	0.005	≥ 0.49	9.95	25.2	0.35	3.3	426	524	$\tau_1=0.3$ (22.07) $\tau_2=2.40$ (57.25) $\tau_3=6.37$ (20.68)	0.032	0.16	0.22
4BP	404	429	634	0.006	≥ 0.58	9.99	21.5	0.33	2.4	446	490	$\tau_1=0.24$ (3.36) $\tau_2=2.05$ (0.22) $\tau_3=0.02$ (96.42)	0.021	0.58	2.69

*within experimental error; [¶]millisecond (ms); ^achloroform solution; ^bcrystalline state; Abs – absorption; Fl – fluorescence; Ph – phosphorescence; [†] τ_{Fl} for 1-4BP in chloroform is approximated to 100 ps (pulse duration of the excitation source) for qualitative analysis of rate of radiative and non-radiative decay. Actual rate of radiative decay (k_r) for 1-4BP in chloroform can only be faster than the estimated value, however, used exclusively for qualitative purpose. Observed decrease in the rate of radiative decay for crystalline 1-4BP when compared to 1-4BP in solution is indicative of the formation of 'H' type aggregate.

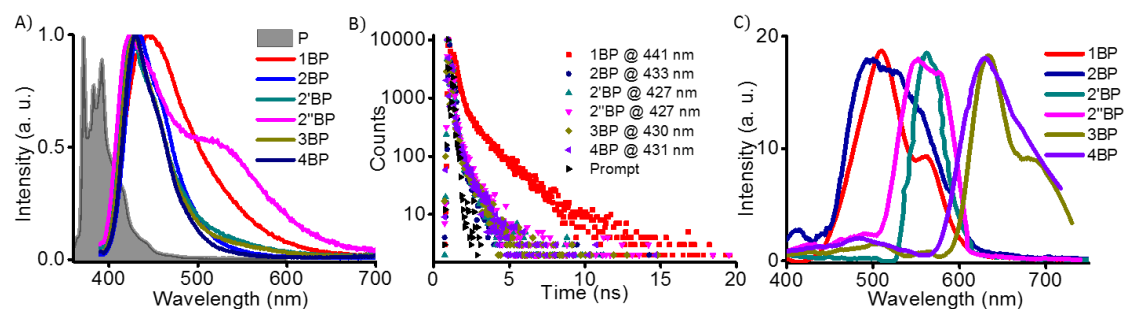


Figure 3.19. Shows the (A) fluorescence spectra; λ_{ex} = 380 nm, area filled graph (grey colour) represent the emission spectrum of pyrene in $CHCl_3$; (B) fluorescence decay; λ_{ex} = 375 nm and (C) phosphorescence spectra; λ_{ex} = 380 nm of 1-4BP derivatives in ethanol.

Time-resolved measurement at the longer emission wavelength exhibited a very short lifetime (<100 ps pulse width at λ_{ex} =375 nm) similar to that observed at the respective emission maxima. An obvious shoulder peak at around 550 nm was observed in the emission spectrum of 2''BP. Wavelength dependent time-resolved fluorescence and excitation spectra invalidates any possibility of aggregates of 2''BP in solution state under these conditions.

As stated above, low Φ_f for 1-4BP could result from an efficient intersystem crossing (ISC) induced by strong mixing of nearly-degenerate singlet and triplet states (Figure 3.18D and Table 3.11). ISC efficiency of 1-4BP was investigated by employing nanosecond time-resolved absorption spectroscopy (Table 3.11). Upon excitation at 355 nm, 1BP exhibits absorption maximum at 520 nm corresponding to triplet-triplet transition of pyrene[90] having a lifetime of 2.1 μ s. Similar features for triplet-triplet absorption were also observed for 2-4BP (Table 3.11). Estimation of triplet quantum yield (Φ_T) of 1BP based on triplet-triplet energy-transfer to β -carotene shows a value of 48% (Figure 3.18D and Table 3.11). We observed that Φ_T decreases with increase in

number of benzoyl groups (Table 3.11). Time-gated emission measurements of 1-4BP in ethanol at 77K show extremely weak phosphorescence when excited at 380 nm (Figure 3.19C and Table 3.11). With increase in number of benzoyl groups, systematic red-shift from 510 to 634 nm in the phosphorescence emission maximum was observed. In addition, non-radiative pathways could also operate to cause significantly reduced fluorescence quantum yield in 4BP in chloroform when compared to P. Bond rotations from benzoyl functional groups can contribute to energy dissipative pathways.

2.3.7. Crystal packing of 1-4BP

Having established the photophysical properties of 1-4BP in solution, further efforts were made to correlate the optical properties in the crystalline state. Detailed analyses of single crystal X-ray structure decipher the role of terminal benzoyl groups in impeding the pyrene-pyrene nearest-neighbour interactions in crystalline 1-4BP. Single crystal X-ray analysis of 1BP shows an interplanar distance (π - π) of 3.50 Å between the two nearest pyrene units having a transverse slip (along the molecular short axis of the pyrene unit) of 0.69 Å and a longitudinal slip (along the molecular long axis of the pyrene unit) of 0.93 Å. Observed transverse/longitudinal displacement complements the phenyl rings to adopt an end to face (CH... π ~2.9 Å interaction with π -electron cloud of the neighbouring pyrene unit. With increase in the number of benzoyl groups in 2-4BP, a progressive rise in the steric contribution causes an increase in the transverse/longitudinal displacement of the vicinal pyrene units in the

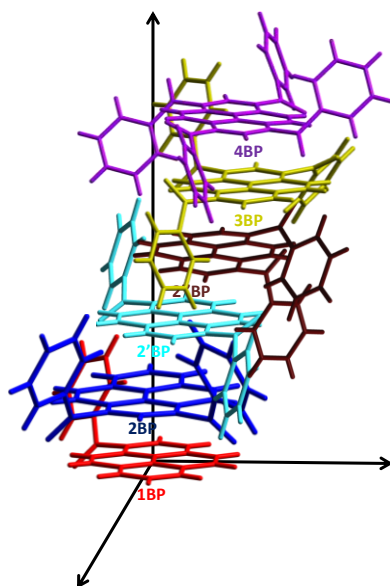


Figure 3.20. Shows the gradual increase in the traverse/longitudinal shift between nearest pyrene molecules in the crystalline 1-4BP derivatives.

crystal structure (Figure 3.20&3.21; Table 3.12). In 4BP, the bulky benzoyl hampers the strong aggregation, inducing a transverse shift (5.65 Å), prohibiting any π -contacts

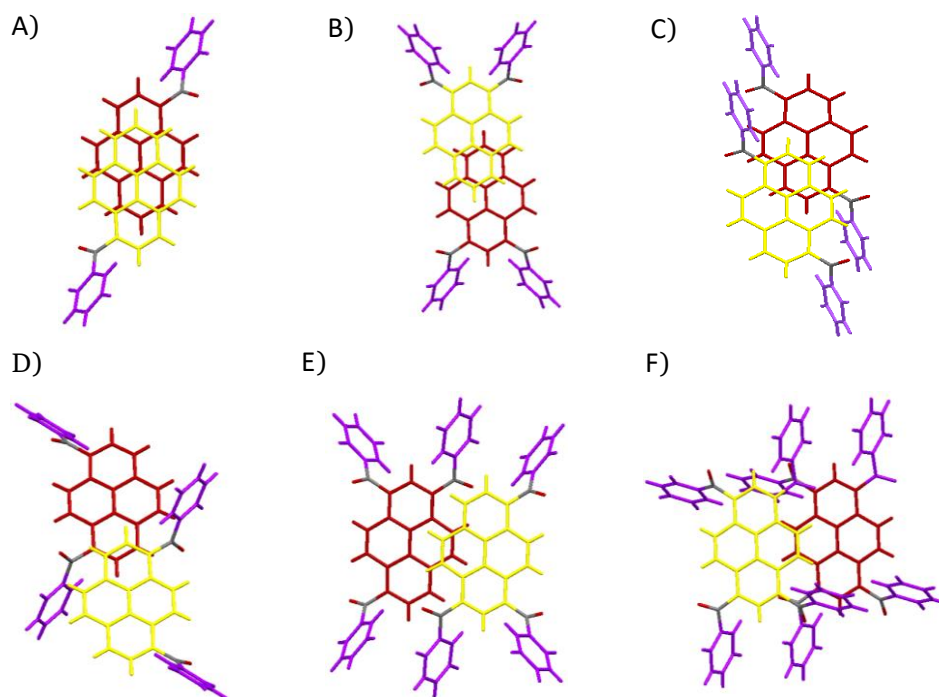


Figure 3.21. Shows the aerial overlap between adjacent pyrene units in close packing of (A) 1BP; (B) 2BP; (C) 2'BP; (D) 2''BP; (E) 3BP and (F) 4BP.

Table 3.12. Geometries in the face-to-face π -stacked arrangements in crystalline 1-4BP.

	π - π stacking	$d_{\pi-\pi}$ [\AA] ^[D]	d [\AA] ^[T]	d [\AA] ^[L]	π - π overlap [%] ^[O]
P		3.53	2.09	0.0	39.91
1BP		3.49	0.69	0.93	45.92
2BP		3.59	0.0	3.72	11.65
2'BP		3.49	1.23	3.80	7.66
2''BP		3.35	7.79	0.68	0.0†
		3.35	0.23	3.43	22.33*
3BP		3.36	5.41	0.0	1.84
4BP		3.47	5.65	0.0	0.95

[D] Separation between the mean planes of pyrene; [T] Transverse; [L] Longitudinal displacement between adjacent pyrene units; [O] Ratio of the area of overlapped units of pyrene aromatic ring in the crystal structure is calculated as the overlapped area divided by the whole area of the pyrene rings. †Lack of orbital overlap between two vicinal pyrene units indicates that the observed red-shift in emission maximum of crystalline 2''BP could arise from other possible electronic interactions, such as pyrene-benzoyl orbital interactions; *% overlap of pyrene and phenyl is calculated; the phenyl group is interdigitated between vicinal pyrene units at a stacking distance (π - π) of 3.8 \AA

between neighbouring pyrene units. The longitudinal and transverse offset imparts different degree of orbital overlap between the pyrene units that are separated at their van der Waals distances (ca. 3.35-3.59 \AA) in crystalline 1-4BP (Figure 3.17, row II, Table 3.12). This intermolecular offset of vicinal pyrene units reduces the π - π interaction that attributes to the observed decrease in the orbital overlap from 45.92% (1BP) to 0.95% (4BP). Interplanar C-H...O[155] contacts support the pyrene units for an extended interaction along all axis in the crystalline arrangement of 1-4BP (Figure 3.22).

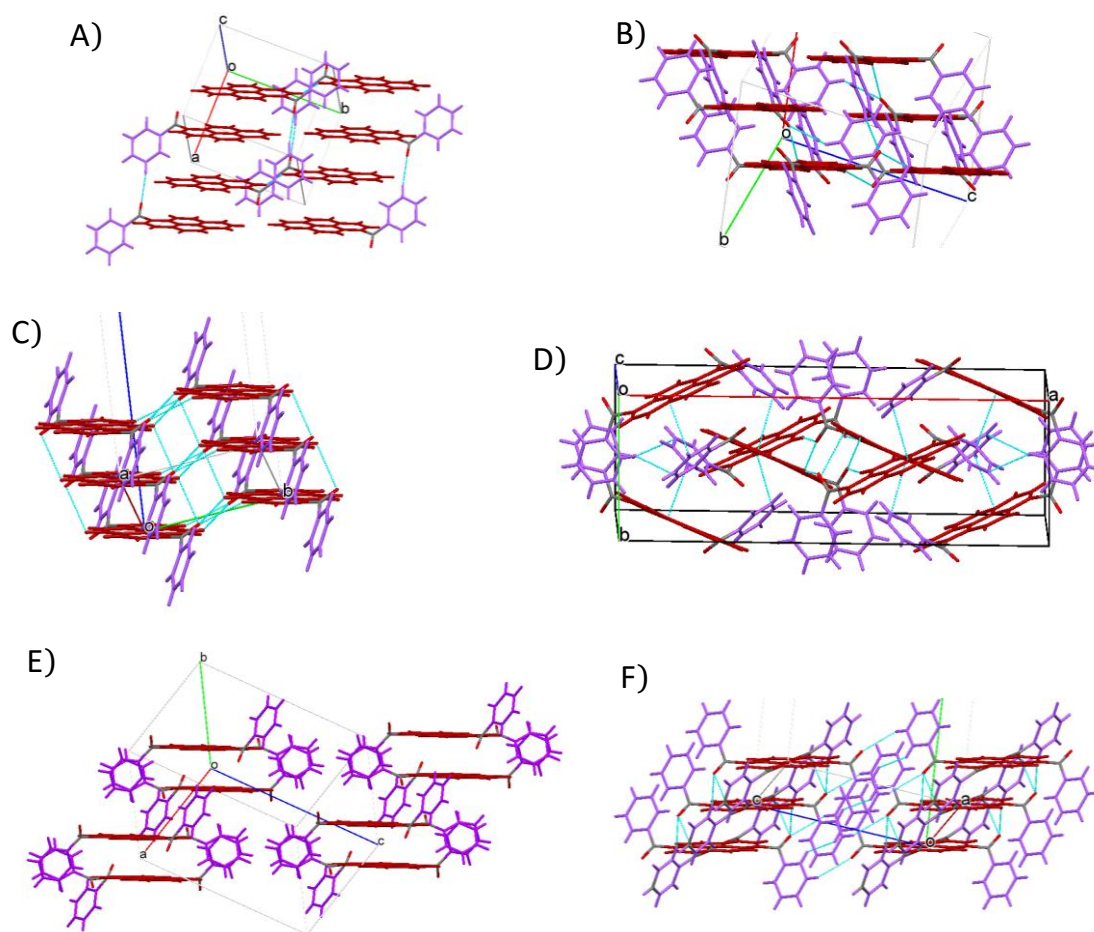


Figure 3.22. Shows the C-H...O interactions in the crystal packing of (A) 1BP; (B) 2BP; (C) 2'BP; (D) 2''BP; (E) 3BP and (F) 4BP.

2.3.8. Photophysical properties of crystalline 1-4BP

Intrigued by the sterically controlled longitudinal/transverse shift of intermolecular group vicinal pyrene units, further efforts were made to explore the photophysical properties of crystalline 1-4BP. Diverse colour in the crystalline 1-4BP ranging from pale yellow-yellow-orange red (Figure 3.17, Row III) were observed due to intermolecular offset of vicinal pyrene units in the crystalline state. Diffuse reflectance absorption spectrum of crystalline 1-4BP exhibits a broad band centered around 350-450 nm, with an additional absorption tail extending to 500 nm in 1BP

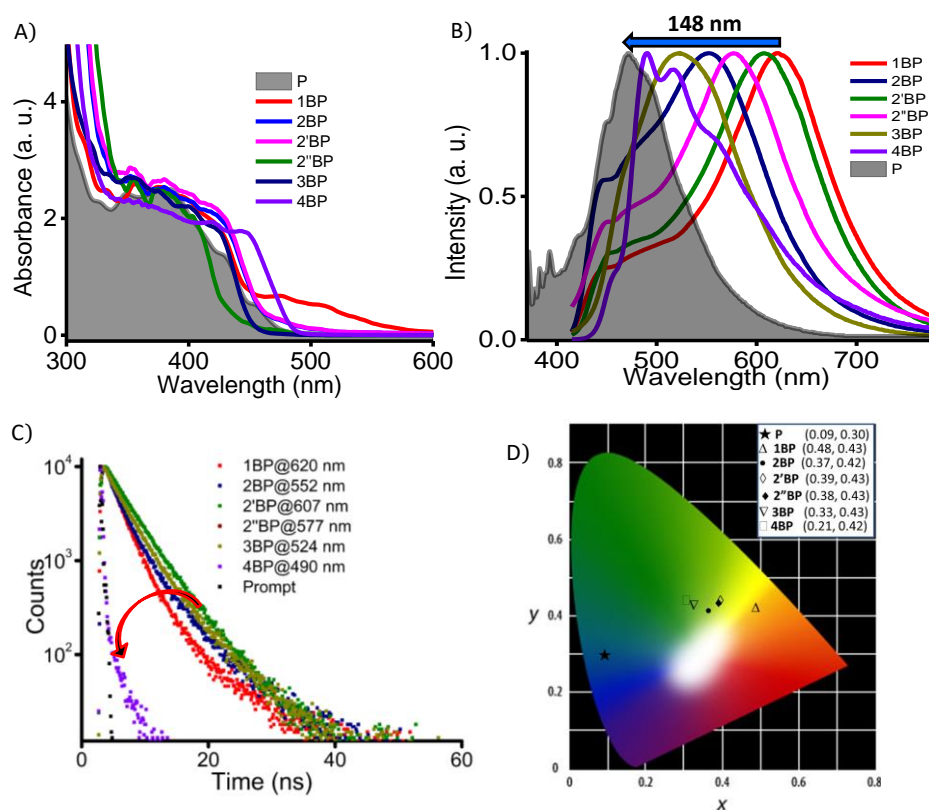


Figure 3.23. (A) Absorption; (B) fluorescence spectra of crystalline 1–4BP derivatives; $\lambda_{exc} = 380$ nm; the area filled spectrum (grey) represents the absorption and emission spectra of crystalline pyrene[156]; (C) fluorescence decay profile of crystalline 1-4BP; $\lambda_{exc} = 375$ nm and emission wavelength monitored and (D) CIE colour diagram of fluorescence emission for crystalline 1-4BP derivatives.

(Figure 3.23 and Table 3.11). Presence of benzoyl group(s) results a red-shift in the UV-Vis absorption, for example 114 nm (1BP) and 60 nm (4BP), when compared to crystalline P. Upon excitation at 380 nm, crystalline 1BP exhibits a broad emission band with the maximum centered at 620 nm red-shifted by 148 nm compared to crystalline P. A systematic blue-shift in the emission maximum was observed upon further increase in number of benzoyl groups, when compared to crystalline 1BP (Figure 3.17, Row III; Figure 3.23B&D, Table 3.11). In spite of the significant π -overlap

(π - π ; 39.91%) in absorption and emission spectra of crystalline P, a blue-shift in the emission wavelength was observed when compared to crystalline 1-4BP. A marked increase in the separation ($d_{\pi-\pi} \sim 3.53 \text{ \AA}$) between the molecular planes of vicinal pyrene units in crystalline P (Table 3.12) when compared to the crystalline BP derivatives could cause the blue-shift in the emission spectrum. Observed differences in the emission maxima for crystalline 1-4BP could be a combined consequence of different i) degree of π - π overlap and ii) distance between the molecular planes of the adjacent pyrene units. However, contributions from non-nearest neighbour can also contribute to overall electronic coupling that can influence the peak positions in emission spectra. Significant red-shift in the emission wavelength dependent excitation spectra compared to the corresponding steady-state absorption spectra of crystalline 1-4BP suggests the possible ground state interaction between the vicinal pyrene units (Figure 3.24)[117]. Substantially red-shifted dimer/excimer like emission of 1BP could arise from significant orbital overlap (π - π ; 45.92%) between the nearest pyrene units. Nearly slipped out (π - π ; 0.95%) pyrene-pyrene stack along the molecular long axis in 4BP results in a monomer-like emission possessing vibronic features.

Upon excitation at 375 nm, picosecond time-resolved fluorescence measurements of crystalline 1BP shows tri-exponential decay having the lifetime of 2.5 ns (82%), 8.5 ns (12%) and 0.7 ns (6%), when monitored at 620 nm (Figure 3.23C and Table 3.11). Long fluorescence lifetime in crystalline 1BP when compared to that in solution (<100 ps) could arise from excimer/ground state aggregate of neighbouring

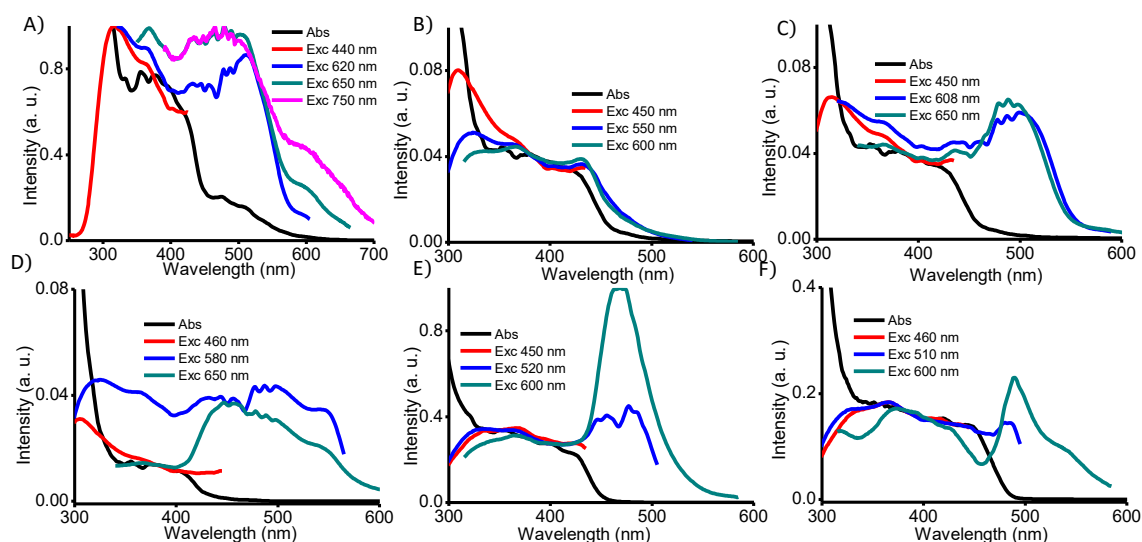


Figure 3.24. Shows fluorescence excitation spectra of crystalline (A) 1BP; (B) 2BP; (C) 2'BP; (D) 2''BP; (E) 3BP and (F) 4BP as compared to absorption spectra. Emission maxima, where the excitation spectra are monitored, are indicated in the bracket.

pyrene units possessing different orbital overlap in the crystalline state. Similarly, crystalline 2-4BP show tri-exponential fluorescence emission profile with a remarkable decrease in the lifetime of the corresponding major component (Figure 3.25A; Table 3.11). A radiative decay rate constant (k_r) of $1.56 \times 10^8 \text{ s}^{-1}$ and $0.59 \times 10^8 \text{ s}^{-1}$ in solution and crystalline state of 1BP, respectively, is estimated (Table 3.11). The faster rate of radiative decay in solution vs. crystalline state was similarly observed in 2-3BP. Observed decrease in the rate of radiative decay in crystalline 1-3BP when compared to solution state indicates the possibility of H-like aggregates and/or excimers of pyrene. Unusual formation of fluorescent H-aggregates were observed earlier in merocyanine dyes by Würthner and co-workers[147]. Notably, small π - π contact of vicinal pyrene units in 4BP imparts a monomer-like behaviour in the crystalline state (Figure 3.25A; Table 3.12), as reported earlier[157]. The twisted nature

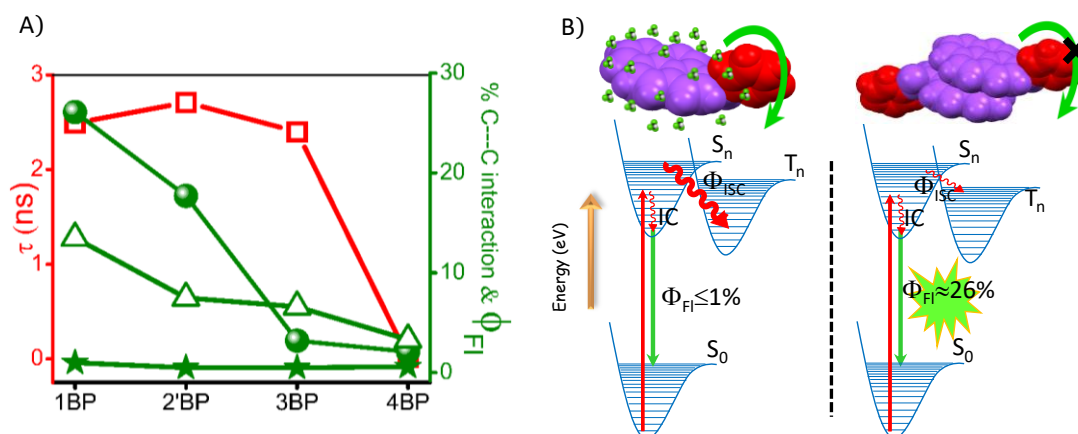


Figure 3.25. (A) Indicates τ (major component; \square); Φ_F (\bullet) of 1-4BP in the crystalline state; Φ_F ($*$) of 1-4BP in solution state and % C...C interaction (π - π , Δ) obtained from Hirshfeld analysis (Table 3.13) and B) Jablonski diagram depicting energy levels in solution (monomeric) and aggregated (crystalline) state in 1BP.

of the benzoyl group(s) with respect to the plane of pyrene chromophore drastically diminishes the aggregation of vicinal pyrene units. Observed similar rate constant in crystalline state and solution state of 4BP confirms the monomer-like behaviour in the crystalline state ($k_r \sim 0.59 \times 10^8 \text{ s}^{-1}$; Table 3.11&3.12). Unravelling the processes responsible for crystallization/ aggregation induced emission is vital for the design of new light emitting materials. Recent preliminary theoretical investigations have offered insights on the characteristics of induced CIE in a variety of organic/inorganic

Table 3.13. Percentage of intermolecular contacts of a molecule in crystalline 1-4AP.

Interaction	1BP	2BP	2'BP	2''BP	3BP	4BP
H...H %	49.9	39.3	43.9	46.3	44.4	44.3
C...H %	28.3	39.2	34.7	30.3	29.9	32.6
O...H %	7.8	13.8	13.7	12.5	13.8	12.0
C...C %	13.5	4.9	7.5	9.9	6.6	3.3
C...O %	0.0	0.5	0.2	1.4	2.2	7.2

^atotal percentage of intermolecular contacts ca. 99.5% (1BP), 97.7% (2BP), 100% (2'AP), 100% (2''AP), 96.6% (3AP), 99.4% (4AP).

chromophores[158-160]. CIE could arise as a consequence of i) electronic (dipolar/excitonic) interactions[147, 161-164] ii) arrested vibrational/rotational motions[165]; and/or iii) reduced solvation[166] in crystalline state. To investigate the extent of vibrationally promoted ISC in monomer vs. dimer states, low-lying excited electronic states of 1BP and 4BP were calculated employing TDDFT method (Figure 3.27). The energy difference between S₁ and T₁ states in monomeric and dimeric 1BP found to be 1.18 and 0.94 eV, respectively. Notable lowering of T₂ energy state was also observed from monomeric (2.95 eV) vs. dimeric (2.13 eV) 1BP. Similar observations were made in monomeric vs. dimeric 4BP. Non-significant differences in energy gap between the close-lying singlet and triplet energy levels of dimeric vs. monomeric 1BP and 4BP excludes the contribution of vibrational processes in CIE. Restriction of intramolecular rotations offered to the pendent benzoyl groups in the

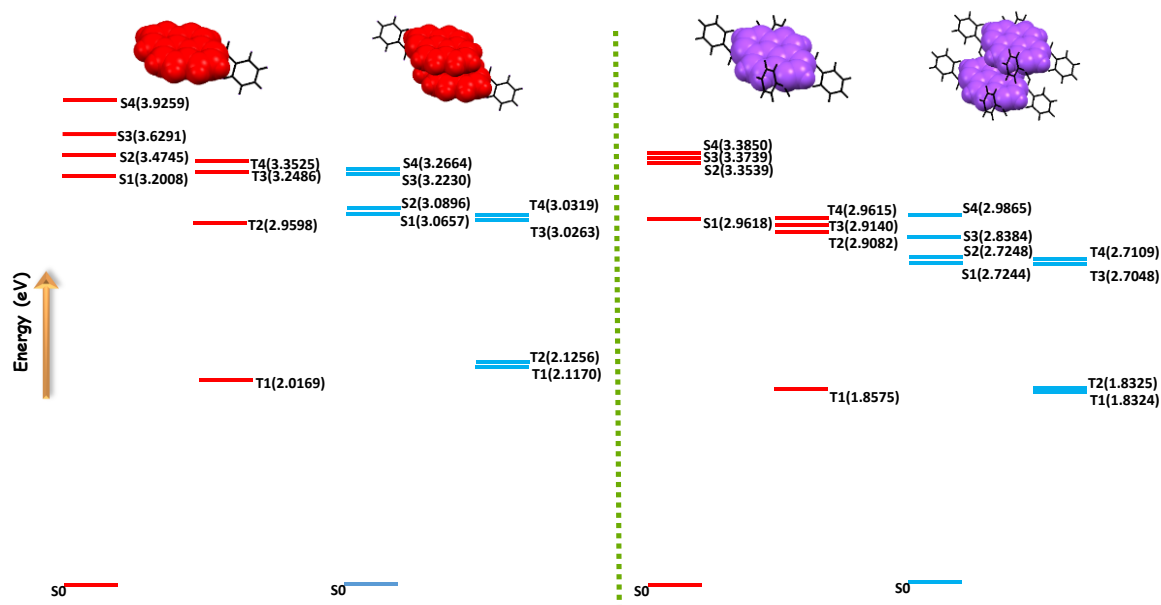


Figure 3.26. Energy levels diagram of monomer and dimer of 1BP and 4BP calculated from B3LYP/6-311G^{**++} level of theory.

crystalline (dimeric) state of 1-4BP may facilitate enhancement in the fluorescence, consistent with the earlier reports[148]. Hence, CIE in 1-4BP could arise due to i) fluorescent H-like excitonic interactions; ii) arrested rotational motion of benzoyl group(s) and/or iii) lack of solvation in the crystalline state (Figure 3.26B).

2.4. Conclusion

In summary, we modulated the extent of π - π overlap between vicinal pyrene units through successive acylation/benzoylation. Unprecedented heteropolar dihydrogen contacts (sp^2 C-H...H-C sp^3) in organic crystals are established using QTAIM. Hirshfeld surface analysis is indicative of an increase in π - π interactions and a concomitant decrease in the σ - π interactions with an increase in the number of acetyl groups per pyrene unit. A combination of C-H...H-C, C-H...O and π - π interactions facilitate the transformation of sandwich herringbone packing of P to the herringbone arrangement in 1 and 2'AP, the brickwork arrangement in 2 and 2''AP and columnar stacks in 3-4AP. A systematic decrease in the interplanar angle between the vicinal pyrene units could be attributed to the dramatic shift in the emission spectra (ca. 42-174 nm) of crystalline 1-4AP when compared to pyrene. J-like aggregation and/or AIE in the crystal packing of 1-4AP corroborates the moderately emissive blue-green-orange crystals. While through the successive benzoylation, the extent of orbital overlap (π - π) between vicinal pyrene units in crystalline 1-4BP were regulated by exploiting the steric hindrance. Progressive increment in the steric hindrance causes an increase in the transverse/longitudinal displacement of the vicinal pyrene units. As

a result, a 48-fold reduction in the π -stacking between pyrene units was observed in 4BP with respect to 1BP.

Moderating the molecular stacking along with CIE through arrested intramolecular rotations of pendent benzoyl groups may facilitates green-yellow-orange solid-state emitters. Modulating the emission properties of organic crystalline materials by controlling the extent of π -overlap through chemical strategies could lead to the construction of high performance photo-functional materials and device.

2.5. Appendix

Experimental section

- **Materials and Methods**

Pyrene (98%), acetyl chloride (98%) and aluminum chloride (99.99%) were purchased from Sigma Aldrich and used as such without further purification. Carbon disulfide used as a solvent for the reaction was dried and distilled by standard procedure. TLC analysis were performed on precoated aluminum plates of silica gel 60 F254 plates (0.25 mm, Merck) and developed TLC plates were visualized under short and long wavelength UV lamps. Flash column chromatography was performed using silica gel of 200-400 mesh employing a solvent polarity correlated with the TLC mobility observed for the substance of interest. Yields refer to chromatographically and spectroscopically homogenous substances.

Melting points (mp) were obtained using a capillary melting point apparatus and are reported without correction. IR spectra were recorded on a Shimadzu IRPrestige-21 FT-IR spectrometer as neat KBr pellets for all the derivatives. ^1H and ^{13}C NMR spectra were measured on a 500 MHz and 125 MHz Bruker advanced DPX spectrometer respectively and 1,1,1,1-tetramethylsilane (TMS) is used as the internal standard for ^1H and ^{13}C NMR measurements. CHN analyses were carried out on an Elementar vario MICRO cube Elemental Analyzer. All values recorded in elemental analyses are given in percentages. High Resolution Mass Spectra (HRMS) were recorded on Agilent 6538 Ultra High Definition (UHD) Accurate-Mass Q-TOF-LC/MS system using either atmospheric pressure chemical ionization (APCI) or electrospray ionization (ESI) mode.

- **Spectral Measurements:**

Absorption spectra were recorded on Shimadzu UV-3600 UV-VIS-NIR while fluorescence and excitation spectra were performed on Horiba Jobin Yvon Fluorolog spectrometers respectively. The excitation wavelength used is 350 nm unless otherwise mentioned. Fluorescence lifetime measurements were carried out in an IBH

picosecond single photon counting system. The fluorescence decay profiles were deconvoluted using IBH data station software version 2.1, and fitted with exponential decay, minimizing the χ^2 values of the fit to 1 ± 0.05 . All spectroscopic experiments were performed by using standard quartz cuvettes of path length 1cm for solution in dried and distilled solvents. The excitation laser used is 375 nm with a pulse width of less than 100 ps. 1-4AP derivatives in chloroform were found to have lifetime significantly shorter than the excitation pulse width. The solution state fluorescence quantum yields were determined by using optically matched solutions. Quinine sulfate dissolved in 0.5 M H₂SO₄ ($\Phi_f = 0.546$) is used as the standard for 1-4AP derivatives.

Nanosecond transient absorption measurements. Nanosecond laser flash photolysis experiments of the argon purged solutions were carried out in an Applied Photophysics Model LKS-60 laser kinetic spectrometer using the third harmonic (355 nm, pulse duration ≈ 10 ns) of a Quanta Ray INDI-40-10 series pulsed Nd:YAG laser as the excitation source. Triplet states of 1-4BP in CHCl₃ were confirmed performing the experiments with oxygen purged solutions.

Triplet quantum yields upon direct photoexcitation (355 nm) were determined by using [Ru(bpy)]Cl₂ in methanol as standard ($\Phi_T = 100\%$), with nonsaturating laser intensities. Equal volume of 0.2 mM solution of β -carotene was added to optically matched solutions of reference and the sample. The equation for the triplet quantum yield is given by,

$$\Phi_T^S = \Phi_T^{Ref} \times \frac{\Delta A^S}{\Delta A^{Ref}} \times \frac{k_{obs}^S}{k_{obs}^S - k_0^S} \times \frac{k_{obs}^{Ref} - k_0^{Ref}}{k_{obs}^{Ref}}$$

Where, Φ_T^S and Φ_T^{Ref} denote the triplet quantum yield of the sample and reference respectively; ΔA^S and ΔA^{Ref} are transient absorption intensity of β -carotene in sample and reference respectively; k_{obs}^S and k_0^S are decay rate of sample transient species before and after the addition of β -carotene. k_{obs}^{Ref} and k_0^{Ref} are decay rate of reference transient species before and after the addition of β -carotene.

Cyclic Voltammetry (CV): Electrochemical measurements were performed on a BASi (Bioanalytical Systems, Inc.) C-3 cell stand controlled by Epsilon electrochemical workstation. A three electrode system is then constructed constituting a glassy carbon as the working electrode, a platinum-wire as the counter electrode, and an Ag/Ag⁺ (3 M NaCl) as the reference electrode. The electrochemical measurements were conducted under nitrogen atmosphere (5 psi, 10 minutes) in a deoxygenated anhydrous acetonitrile of tetra-n-butylammonium hexafluorophosphate (supporting electrolyte, 0.1 M) for 1-4BP derivatives in CHCl₃ with a scan rate of 50–100 mVs⁻¹. Calibration of the instrument was performed using the ferrocene/ferrocenium (Fc/Fc⁺) redox couple as an internal standard and measured under same condition before and after the measurement of samples. The energy level of Fc/Fc⁺ was assumed to be -4.8 eV with respect to vacuum. The half-wave potential of Fc/Fc⁺ was estimated to be 0.5 V with reference to the Ag/Ag⁺ electrode.

HOMO and LUMO energy levels were calculated from the following equations:

$$E_{\text{HOMO}} = -(E_{\text{ox}}^{\text{onset}} + 4.8) \text{ eV} \quad \text{and} \quad (1)$$

$$E_{\text{LUMO}} = -(E_{\text{red}}^{\text{onset}} + 4.8) \text{ eV} \quad (2)$$

respectively, where $E_{\text{ox}}^{\text{onset}}$ and $E_{\text{red}}^{\text{onset}}$ are the onset oxidation and reduction potentials relative to the Ag/Ag⁺ reference electrode.

The electrochemical energy gap (E_g) is estimated as follows:

$$E_g = (E_{\text{LUMO}} - E_{\text{HOMO}}) \text{ eV} \quad (3)$$

where E_{LUMO} and E_{HOMO} are the corresponding to HOMO and LUMO energy levels calculated after converting the values in Ag/Ag⁺ with respect to the standard calomel electrode (SCE) convention.

Determination of fluorescence quantum yield and radiative and non-radiative rate constants: Solution state fluorescence quantum yields of 1-4BP derivatives were calculated by relative quantum yield method as follows,

$$\Phi_s = \Phi_{\text{ref}} \left(\frac{I_s}{I_{\text{ref}}} \right) \left(\frac{OD_{\text{ref}}}{OD_s} \right) \left(\frac{n_s}{n_{\text{ref}}} \right)^2 \quad (4)$$

wherein, Φ_s and Φ_{ref} are the quantum yields of sample and reference respectively, I_s and I_{ref} are the area under the emission spectrum for sample and reference

respectively. OD_s and OD_{ref} are the absorbances of sample and reference respectively at the excitation wavelength. n_s and n_{ref} are the refractive index of the solvent in which sample and reference are taken.

Radiative (k_r) and non-radiative (k_{nr}) rate constants from the singlet excited states are calculated from the fluorescence quantum yields, Φ_f .

$$\Phi_f = \frac{k_r}{k_r + k_{nr}} \quad (5)$$

The rate constants k_r and k_{nr} can be evaluated by measuring fluorescence lifetimes (τ_f) from TCSPC measurements. The following equations depict relation between Φ_f , τ_f , k_r and k_{nr} .

$$k_r = \frac{\Phi_f}{\tau_f} \quad \text{and} \quad (6)$$

$$k_{nr} = \frac{1 - \Phi_f}{\tau_f} \quad (7)$$

a change in Φ_f could be attributed to the changes in either k_r/k_{nr} . The enhancement in the quantum yield (Φ_f) with increased solvent polarity is due to the stabilization of the excited states by virtue of interaction with the solvent dipoles and decrease in the non-radiative (k_{nr}) rate constant.

- **X-ray Crystallography**

X-ray Crystallography: High-quality specimens of appropriate dimensions were selected for the X-ray diffraction experiments. Crystallographic data collected are presented in the supplementary information. Single crystals were mounted using oil (Infiniteum V8512) on a glass fibre. All measurements were made on a CCD area detector with graphite monochromated Mo $K\alpha$ radiation. The data was collected using Bruker APEXII detector and processed using APEX2 from Bruker. All structures were solved by direct methods and expanded using Fourier techniques. The non-hydrogen atoms were refined anisotropically. Hydrogen atoms were included in idealized positions, but not refined. Their positions were constrained relative to their parent atom using the appropriate HFIX command in SHELXL-97. The full validation of CIFs and structure factors of 1-4AP derivatives were performed using the CheckCIF

utility and found to be free of major alert level. 3D structure visualization and the exploration of the crystal packing of 1-4BP were carried out using Mercury 3.1.

- **Computational Methods**

Quantum Theory of Atoms in Molecules (QTAIM): The wave function for XPs were obtained employing the geometries taken from the crystal structure using Gaussian set of codes at B3LYP/6-311G**++ level.1 Quantum theory of atoms in molecules (QTAIM) analysis helps to understand the description of interatomic interaction in the single crystal X-ray structure. A bond is defined along the bond line between two nuclei, called a bond path, along which electron density is concentrated. The bond critical point (BCP) is a point along the bond path at the interatomic surface, where the shared electron density reaches a minimum. The physical characteristics of the BCPs [the electron density at BCP, $\rho(r_{\text{BCP}})$, and its Laplacian, $\nabla^2\rho(r_{\text{BCP}})$] reveal the approximate measure of the amount of electron density built up in the bonding region and as such could be taken as characteristic of the bond. When $\nabla^2\rho(r_{\text{BCP}}) < 0$ and is large in magnitude, $\rho(r_{\text{BCP}})$ is also large which means that there is a concentration of electronic charge in the internuclear region. This is also an indication of a sharing of electronic charge between both nuclei that defines the covalent (polar) bond. When $\nabla^2\rho(r_{\text{BCP}}) > 0$ there is a depletion of electronic charge in the internuclear region. Using the AIM 2000 software package, the electron density was integrated over atomic basins according to the quantum theory of atoms in molecules using PROAIM, and thus the BCP data and the molecular graphs were obtained.

Computational methods used for calculating singlet and triplet energy levels of 1-4BP derivatives: Ground state optimized energies and harmonic oscillator frequencies were computed using density functional theory (DFT) employing B3LYP functional with 6-311G**+ basis set. Vertical excitation energies were determined performing time-dependent DFT (TDDFT) calculations at the B3LYP/6-311**+ level of theory with Gaussian 09 program suite.

Hirshfeld analysis: Important intermolecular interactions within the crystal structure of 1-4BP/AP were identified through Hirshfeld surface analysis using Crystal Explorer

3.1. The Hirshfeld surface is defined as a set of points in 3D space where the ratio of promolecule and procrystal electron densities is equal to 0.5. The exploration of intermolecular contacts is provided by mapping normalized contact distances (d_{norm}), which is a function of a closest distance from the point to the nuclei interior (d_i) and exterior (d_e) to the surface as well as on the van der Waals radii (r^{vdw}). 2D fingerprint which were generated by deriving from the Hirshfeld surface by plotting the fraction of points on the surface as the function of d_i and d_e which provide a visual summary of intermolecular contacts within the crystal.

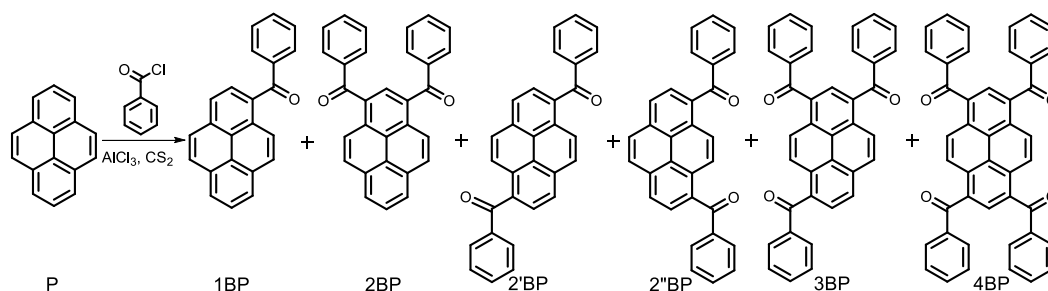
Analysis of Chromaticity Index: Coordinates (x, y, z) for chromaticity are acquired by calculating the fractional component of the tristimulus values: $x = X/(X+Y+Z)$, $y = Y/(X+Y+Z)$, $z = Z/(X+Y+Z)$. X, Y, Z are the CIE 1931 tristimulus values. By convention, chromaticity coordinates (x, y) denote the two dimensional plot CIE 1931 colour space chromaticity diagram.

Calculation of percentage overlap: The % overlap of closest dimer of vicinal pyrene units in the crystalline 1-4BP is calculated using ImageJ 1.4. It can calculate area and pixel value statistics of user-defined selections. The input geometries for the closest dimer (.bmp file) were arranged, conforming to crystal packing thereby preserving the relative positions and orientations of vicinal pyrene units. The ratio of the area of overlapped moieties of pyrene aromatic rings in the crystal structures is calculated as the overlapped area divided by the whole area of the pyrene rings.

$$\% \text{ Overlap} = \left[\frac{\text{Overlaped Area}}{\text{Overlaped Area} + \text{Non overlaped Area}} \right] \times 100$$

- **Synthesis Details**

Synthesis and characterization of 1-4AP derivatives were reported in Chapter 2.



Scheme 3.1. Shows the synthesis of benzoylpyrene (1-4BP) derivatives.

Preparation of benzoylpyrene (1-4BP) derivatives: Pyrene (10 g; 0.049 mols) dissolved in CS₂ (yellow solution, 250 mL) was maintained at ambient temperature and subsequently anhydrous AlCl₃ was added. Benzoyl chloride (27.80 g; 0.198 mols) was then slowly syringed to the suspension. Subsequently, hydrogen chloride was liberated. After 3 hrs the mixture was added slowly to a vigorously stirred mixture of ice and concentrated HCl. The resulting suspension was filtered and vacuum dried and purified through column chromatography (silica gel) to give benzoylpyrene (1-4BP) derivatives.

1BP (yield= 5.1%) M.p. 102-105 °C. ¹H NMR [500 MHz, DMSO(*d*₆), δ]: 8.40 (m, 4H), 8.43 (q, J = 9.66 Hz, 2H), 8.17 (m, 3H), 7.82 (d, J = 7.7 Hz, 2H), 7.73 (t, J = 7.2 Hz, 1H), 7.58 (d, J = 7.8 Hz, 2H). ¹³C NMR [125 MHz, DMSO(*d*₆), δ]: 197.56, 138.0, 133.60, 132.82, 132.46, 130.70, 130.08, 129.07, 128.90, 128.83, 128.66, 127.25, 126.83, 126.68, 126.35, 126.04, 124.20, 124.10, 123.84, 123.55. IR (KBr, cm⁻¹): 3037, 1651, 1595, 1506, 1446. Elemental analysis: calcd. value for C₂₃H₁₄O: 90.17% C, 4.61% H; found: 90.31% C, 4.56% H. HRMS (ESI) m/z calculated for C₂₃H₁₄O [M]⁺: 306.1045, found: 306.1037.

2BP (yield= 9.4%) M.p. 164-167 °C. ¹H NMR [500 MHz, DMSO(*d*₆), δ]: 8.50 (d, J = 7.7, 2H), 8.43 (d, J = 9.3 Hz, 2H), 8.32 (d, J = 9.2 Hz, 2H), 8.25 (t, J = 7.7 Hz, 1H), 8.13 (s, 1H), 7.88 (d, J = 8.2, 4H), 7.71 (t, J = 7.5, 2H), 7.57 (t, J = 7.8, 4H). ¹³C NMR [125 MHz, DMSO(*d*₆), δ]: 201.94, 131.41, 131.21, 130.37, 129.87, 128.03, 127.43, 127.20, 124.39, 124.18, 123.19, 30.71. IR (KBr, cm⁻¹): 3053, 1656, 1585, 1516, 1446. Elemental analysis: calcd. value for C₃₀H₁₈O₂: 87.78% C, 4.42% H; found: 87.63% C, 4.61% H. HRMS (ESI) m/z calculated for C₃₀H₁₈O₂ [M]⁺: 410.1307, found: 410.1305.

2'BP (yield= 9.6%) M.p 233-238 °C. ¹H NMR [500 MHz, DMSO(*d*₆), δ]: 8.38 (d, J = 8 Hz, 2H), 8.25 (d, J = 9.5 Hz, 2H), 8.18 (d, J = 9.5 Hz, 2H), 8.10 (d, J = 7.5 Hz, 2H), 7.73 (d, J = 7.7 Hz, 4 H), 7.64 (t, J = 7.1, 2H), 7.49 (t, J = 7.7, 4H). ¹³C NMR [125 MHz, DMSO(*d*₆), δ]: 202.20, 133.33, 132.31, 129.07, 128.20, 127.73, 126.39, 125.35, 123.73, 30.64. IR (KBr, cm⁻¹): 3051, 1649, 1571, 1490, 1442. Elemental analysis: calcd. value for C₃₀H₁₈O₂: 87.78% C,

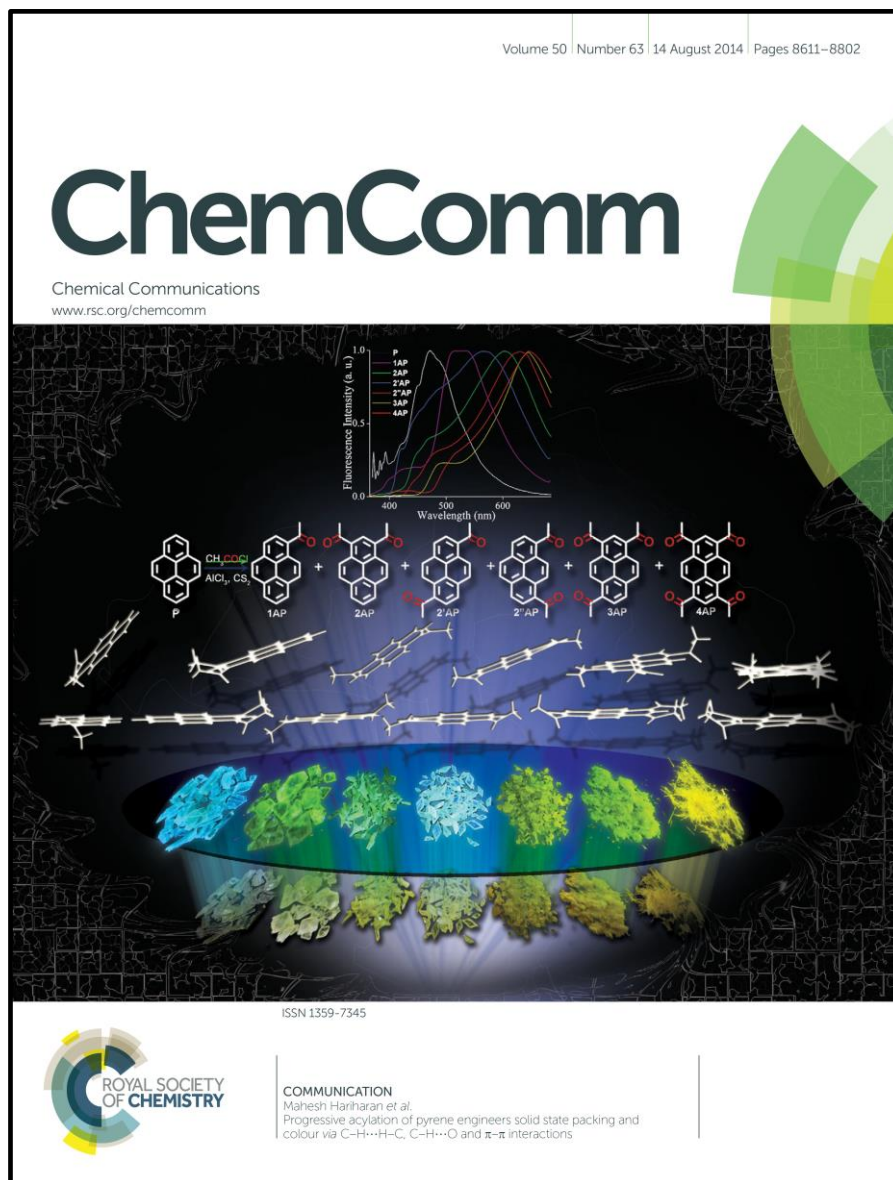
4.42% H; found: 87.71% C, 4.69% H. HRMS (ESI) m/z calculated for C₃₀H₁₈O₂ [M]⁺: 410.1307, found: 410.1301.

2''BP (yield= 37.5%) M.p. 155-158 °C. ¹H NMR [500 MHz, DMSO(*d*₆), δ]: 8.42 (d, J = 7.5 Hz, 2H), 8.35 (s, 2H), 8.11= (d, J = 3 Hz, 2H), 8.09 (s, 2H), 7.71 (d, J = 8.25, 4H), 7.61 (t, J = 8.5, 2H), 7.47 (t, J = 7.25, 4H). ¹³C NMR [125 MHz, DMSO(*d*₆), δ]: 197.82, 138.27, 134.29, 134.25, 132.99, 130.63, 129.43, 129.36, 128.57, 127.54, 126.14, 125.97, 126.14, 124.22. IR (KBr, cm⁻¹) 3051, 1654, 1595, 1446, 1446. Elemental analysis: calcd. value for C₃₀H₁₈O₂: 87.78% C, 4.42% H; found: 87.68% C, 4.59% H. HRMS (ESI) m/z calculated for C₃₀H₁₈O₂ [M]⁺: 410.1307, found: 410.1298.

3BP (yield= 18.9%) M.p. 183-187 °C. ¹H NMR [500 MHz, DMSO(*d*₆), δ]: 8.63 (d, J = 9.7 Hz, 1H), 8.54 (d, J = 9.3 Hz, 1H), 8.42 (d, J = 9.2 Hz, 1H), 8.35 (s, 2H), 8.30 (d, J = 7.8 Hz, 1H), 8.23 (s, 1H), 8.89 (m, 4H), 7.85 (d, J = 7.7 Hz, 2H), 7.75 (m, 3H), 7.63 (m, 6H). ¹³C NMR [125 MHz, DMSO(*d*₆), δ]: 197.18, 196.63, 196.52, 137.60, 137.48, 137.43, 135, 133.93, 133.90, 132.89, 132.65, 131.81, 130.42, 130.27, 130.26, 130.17, 129.77, 128.90, 128.88, 128.85, 128.06, 127.34, 127.22, 127.17, 126.44, 125.50, 124.50, 124.15, 123.64. IR (KBr, cm⁻¹): 3055, 1654, 1593, 1568, 1446. Elemental analysis: calcd. value for C₃₇H₂₂O₃: 86.36% C, 4.31% H; found: 87.41% C, 4.45% H. HRMS (ESI) m/z calculated for C₃₇H₂₂O₃ [M]⁺: 514.1569, found: 516.1552.

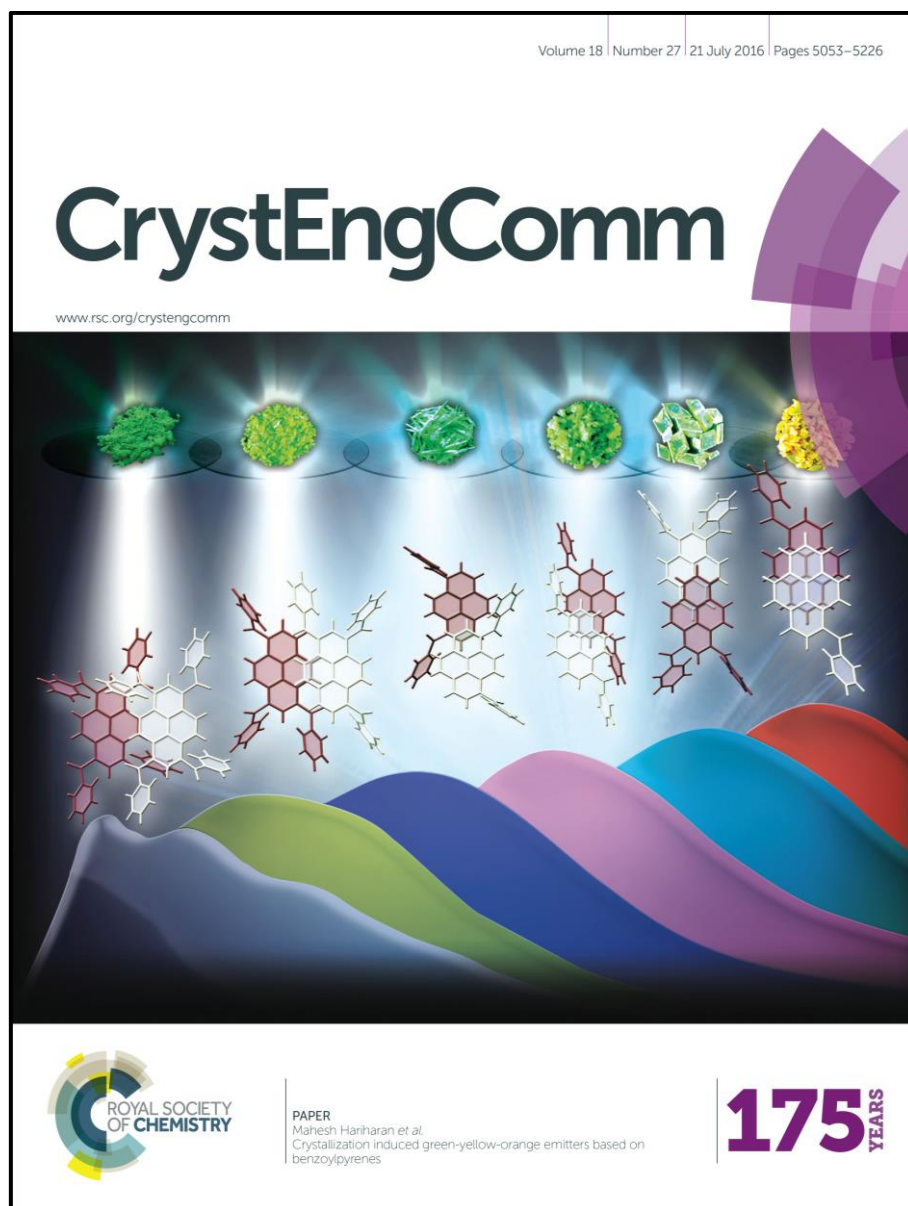
4BP (yield= 1.9%) M.p. 283-285 °C. ¹H NMR [500 MHz, DMSO(*d*₆), δ]: 8.33 (s, 4H), 8.20 (s, 2H), 7.81 (d, J = 9.25 Hz, 8H), 7.65 (t, J = 7.85 Hz, 4H), 7.50 (t, J = 7.85 Hz, 8H). ¹³C NMR [125MHz, DMSO(*d*₆), δ]: 196.93, 137.82, 134.56, 134.39, 130.80, 130.19, 129.41, 127.75, 127.46, 124.62. IR (KBr, cm⁻¹): 3055, 1654, 1593, 1568, 1446. Elemental analysis: calcd. value for C₄₄H₂₆O₄: 85.42% C, 4.24% H; found: 85.63% C, 4.31% H. HRMS (ESI) m/z calculated for C₄₄H₂₆O₄[M]⁺: 618.1831 found: 618.1820.

Progressive acylation of pyrene engineers solid-state packing and colour via C-H...H-C, C-H...O and π - π interactions



Quantum theory of atoms-in-molecules and Hirshfeld surface analyses indicated an increase in the extent of (i) C-H...H-C; (ii) C-H...O, (iii) π - π interactions and a decrease in the extent of (i) σ - π interaction, (ii) an interplanar angle between the vicinal pyrene units in a series of acetylpyrene derivatives offering blue-green-orange emissive crystals.

Crystallization induced green-yellow-orange emitters based on benzoylpyrenes



Steric hindrance due to incremental benzoyl groups causes a systematic reduction in the orbital overlap (π - π) between vicinal pyrene units affording green-yellow-orange solid-state emitters. Crystallization induced emission could arise from: i) electronic (dipolar/excitonic) interactions, ii) arrested bond rotations, and/or iii) lack of solvation in crystalline 1-4BP ($\Phi_{\text{FI}} \sim 2$ –26%) when compared to that in solution ($\Phi_{\text{FI}} \leq 1\%$).

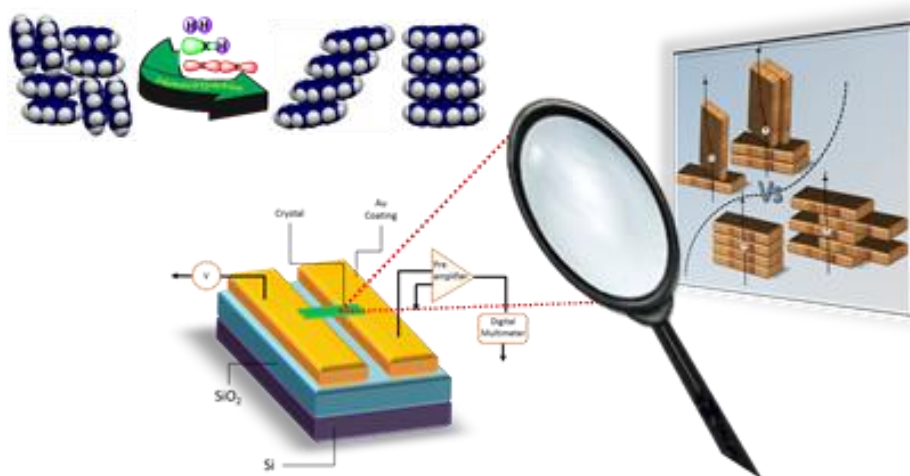
Chapter 4

Solid-state ordering of pyrene based single crystalline materials for high-performance organic field-effect transistors

Abstract

Pyrene-based materials possessing one-dimensional cofacial π - π stacked structural motifs with short inter-planar distances can have favorable charge transport properties. In this work, we have realized the switching of sandwichherringbone to lamellar/columnar arrangement by introducing α -haloacetyl substituents in pyrene.

Though various chemical and physical strategies were employed to self-assemble the molecules in an impressive array in the crystal structure, a direct understanding of such molecular ordering to enhance the device performance, still remains unexplored. We evaluate the intrinsic molecular packing on charge-transport properties of acetylpirene (AP) based materials. The adverse edge-to-face packing of pyrene units minimize the π - π overlap between the adjacent molecules leading to high resistance to charge transfer in 1AP (847 M Ω) and 2'AP (332 M Ω) when compared to the stacked face-to-face (π - π) interaction observed in the brickwork [2AP (21 M Ω) and 2''AP (18 M Ω)] and columnar [3AP (77 M Ω) and 4AP (27 M Ω)] arrangement. Hence the observed decrease in the resistance by an order of one magnitude seems that the crystals with π -stacked packing (brickwork and columnar) are better than those with herringbone packing. Field-effect measurement has been done on 4AP crystals, since these are rod-like in appearance and are easy to place on the substrate-silicon wafer with 200 nm of thermally grown oxide layer. At increasingly negative gate voltages, the mobility was found to monotonously increasing from 0.03 to 0.18 cm² V⁻¹ s⁻¹.



4.1. Introduction

Polyaromatic hydrocarbons (PAHs) have attracted a great deal of interest as semiconductor materials over the past few years due to their unique processing characteristics and improved electronic mobility[167-170]. Control of spatial arrangement of constituent molecules in functional organic materials is of paramount importance because face-to-face arrangement of arenes is a key attribute in the field of organic optical and semiconductor materials[171-174]. In general, face-to-face (π - π) stacking competes with edge-to-face (C-H $\cdots\pi$) interactions and the latter interactions usually dominate the packing arrangement of PAHs. Consequently, PAHs tend to form herringbone arrangements with negligible π -orbital overlap in the crystalline state[107, 175-178]. Switching the herringbone arrangement (C-H $\cdots\pi$) of PAHs to face-to-face lamellar/columnar arrangement by modulating molecular packing through covalent[179, 180]/non-covalent[98] routes is a burgeoning topic of interest.

Among the PAHs, pyrene based systems are a promising class of organic materials for optoelectronic devices[5, 181, 182]. Pyrene, because of the sandwich herringbone arrangement, minimizes the extent of orbital overlap through π - π interactions[183]. Albeit several approaches have been reported for constructing π -stacked arrangements of linear polyacenes such as anthracene[184], tetracene[103, 185] and pentacene[104, 186]; constructing π -stacked columnar/lamellar arrangements of pyrene received less attention. Major challenge is to regulate the non-covalent interactions through rational molecular design, thereby reorganizing the

supramolecular architecture[95, 149, 187]. Among these, hydrogen bonding[188] is the most explored, while other interactions such as the dihydrogen contacts[122] and the halogen interactions[189, 190] have been the recent topic of interest. Our ongoing interest to regulate the arene-arene interactions in crystalline state[113, 132, 133] and vesicular gels[115] prompted us to explore the role of halogen interactions in modulating the packing arrangement of pyrene. We recently tuned the extent of π - π overlap between vicinal pyrene units through progressive acylation and achieved a gradual transformation of sandwich herringbone to herringbone, then to lamellar and finally to columnar arrangement[191]. However, successive benzylation of pyrene causes a systematic reduction in the orbital overlap (π - π) between vicinal pyrene units owing to the steric hindrance offered by the benzoyl groups[192]. We have also demonstrated the diverse orbital overlap between vicinal pyrene units in a group of three regioisomeric thiazolylpyrenes where 1,3- and 1,8-substitution led to columnar arrangement while 1,6-substitution resulted in herringbone arrangement of pyrene units[193]. Herein, we present our efforts on haloacylation promoted switching of sandwich herringbone to lamellar/columnar arrangement of pyrene utilizing hydrogen bonding, halogen interactions and dihydrogen contacts.

It is generally believed that π - π stacking would be much more efficient than herringbone stacking for the transporting of charge carriers. Lots of research has been accomplished to prevent the C-H $\cdots\pi$ intermolecular interactions in order to obtain π - π stacking (lamellar structure) in the crystals through substituting at the peri-positions of acenes. Anthony and co-workers[104] introduced triisopropylsilylethynyl

(TIPS) groups to pentacene core which helps to stacks in a two dimensional columnar array with significant overlap of the pentacene rings in adjacent molecules, and demonstrated significant conductivity enhancements. Pei and co-workers[194] have realized systematic fine-tuning of the single-crystal molecular packing of five benzodifurandione-based oligo(p-phenylenevinylene) (BDOPV) through incorporation of electronegative fluorine atoms on the BDOPV backbone. Consequently, the electronic couplings for electron transfer vary from 71 meV in a slipped stack to 201 meV in a nearly cofacial antiparallel stack, leading to an increase in the electron mobility of the BDOPV derivatives from 2.6 to 12.6 cm² V⁻¹ s⁻¹.

High transportation capabilities of charge carriers in pyrene based semiconductors has attracted its application in p-type and ambipolar OFETs[181, 195]. The recent interests in pyrene based semiconductors is due to control over molecular architecture that can be achieved by modifying the structure by varying the position of substitution on the pyrene ring. Herein, we report on comparative investigation of conductivity in systematically synthesized acyl pyrene derivatives. In our approach, we first study the morphology of the derivatives by scanning electron microscopy (SEM), atomic force microscopy (AFM), and tunneling electron microscopy (TEM). Further, we determine the I-V profiles of the derivatives and use field-effect transistor (FET) measurements to obtain the charge carrier mobility which corroborate with theoretically predicted trend.

4.2. Results and Discussions

4.2.1. Synthesis, characterization and crystallization of bis-haloacetyl pyrene derivatives (XPs)

1,3- and 1,8-CP were synthesized by the Friedel-Crafts reaction[116] of pyrene with chloroacetyl chloride and are obtained in 33 and 38 % yield, respectively (Scheme 4.1). 1,3- and 1,8-BP[196]/IP[197] were obtained in moderate yields by the bromination/iodination of the corresponding acetylpyrene derivatives (AP)[85] (Schemes 4.2&4.4). The nucleophilic substitution reaction of bromoacetylpyrene with CsF resulted in corresponding 1,3- and 1,8-FP[198] in 7 and 10 % yield, respectively (Scheme 4.3). Though the syntheses of α -chloroacetylpyrenes (1,3 and 1,8-CP) and 1,8-bromoacetylpyrene (1,8-BP) were reported by Vollmann[13] and Harvey[151] respectively, 1,3-BP, 1,3- and 1,8-FP/IP were not explored in the literature. Single crystal X-ray analyses of bis(haloacetyl)pyrenes (XPs) were not reported earlier. XPs were characterized by spectroscopic and analytical techniques and their structure was confirmed by single crystal X-ray diffraction analysis (Figure 4.1 and Table 4.1). Single crystals of XPs except 1,8-C'P, suitable for X-ray diffraction, were obtained through slow evaporation of chloroform:hexane mixtures while that of 1,8-C'P, a polymorph of 1,8-CP, were obtained from dimethyl sulfoxide[199]. 1,3-BP/CP/IP yielded solvent free triclinic crystal system with space group P-1 while 1,3-FP and 1,8- FP/CP/C'P/BP exhibited solvent free orthorhombic crystal system with space group *Pbca*, *Pnma*, *P2₁2₁2₁*, *Pnma*, *Pccn*, respectively (Figure 4.1 and Table 4.1).

4.2.2. Crystal structure analyses of XPs

Qualitative analyses of the single crystal X-ray structure of XPs indicate

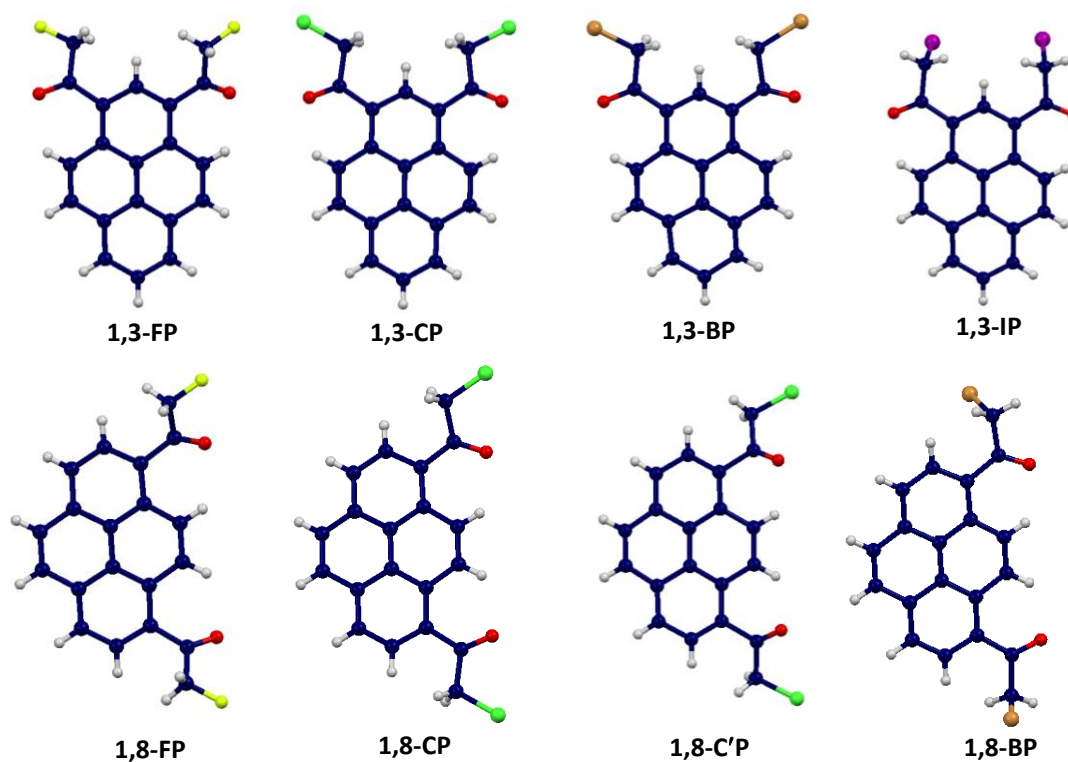


Figure 4.1. Single crystal X-ray structure of XPs.

intramolecular dihydrogen contacts and intramolecular C-H...O hydrogen bonding interaction in the range within their van der Waal's radii. Dihydrogen contacts in XPs were observed between methylenyl hydrogens and pyrenyl hydrogen within the distance of 2.4 Å (Table 4.2.). The shortest H...H interaction distance in 1,3-XP decreases from 2.1 Å in 1,3-AP to 2.02 Å in 1,3-IP (Figure 4.2.A). Similar trend was observed in 1,8-XP in which the shortest H...H interaction distance ranges from 2.32 Å in 1,8-AP to 2.06 Å in 1,8-BP. Quantum theory of atoms in molecules analyses (QTAIM)[139, 140] of the crystalline 1,3-BP revealed bifurcated dihydrogen contacts with distance of 1.96 Å and 2.01 Å, respectively (Figure 4.2.B). The accumulation of electron charge density at the (3, -1) bond critical point [BCP; $\rho_b(r)$]: 0.11 eÅ⁻³ and 0.09 eÅ⁻³, and positive value of Laplacian [$\nabla^2\rho_b(r)$] of 1.78 eÅ⁻⁵ and 1.58 eÅ⁻⁵ with the

Table 4.1. Crystal data and structure refinement for 1,3 and 1,8-XP.

	1,3-FP	1,3-CP	1,3-BP	1,3-IP	1,8-FP	1,8-CP	1,8-C'P	1,8-BP
formula	C ₂₀ H ₁₂ F ₂ O ₂	C ₂₀ H ₁₂ C ₁₂ O ₂	C ₂₀ H ₁₂ Br ₂ O ₂	C ₂₀ H ₁₂ I ₂ O ₂	C ₂₀ H ₁₂ F ₂ O ₂	C ₂₀ H ₁₂ C ₁₂ O ₂	C ₂₀ H ₁₂ C ₁₂ O ₂	C ₂₀ H ₁₂ Br ₂ O ₂
formula wt	322.30	355.20	444.12	538.10	322.30	355.20	355.20	444.12
crystal system	orthorhombic	triclinic	triclinic	triclinic	orthorhombic	orthorhombic	orthorhombic	orthorhombic
space group, Z	<i>Pbca</i> , 8	<i>P</i> -1, 2	<i>P</i> -1, 2	<i>P</i> -1, 2	<i>Pnma</i> , 4	<i>P2₁2₁2₁</i> , 4	<i>Pnma</i> , 4	<i>Pccn</i> , 4
a, Å	7.4848	7.7841	7.5885	8.638	8.114	5.225	7.1129	20.8673
b, Å	15.768	8.5413	8.0425	9.748	22.950	11.280	25.621	4.5301
c, Å	24.344	12.0066	13.943	10.406	7.598	26.310	8.5925	16.8114
α, deg	90	98.129	74.493	103.296	90	90	90	90
β, deg	90	101.832	75.258	94.979	90	90	90	90
γ, deg	90	94.942	89.916	100.159	90	90	90	90
V, Å ³	2873.1	768.0	791.0	831.9	1414.9	1550.7	1565.9	1589.20
temp, K	296	293	296	296	293	296	296	296
dcalcd,g/cm ⁻³	1.489	1.536	1.864	2.146	1.513	1.520	1.506	1.854
no. of reflections collected	39586	11665	6110	11287	6245	6510	6241	11586
no. of unique reflections	2534	2718	2978	2927	1423	2730	1571	1407
no. of parameters	217	217	217	217	109	217	109	109
R1, wR2 (I > 2σ(I))	0.0634, 0.1869	0.0382, 0.1046	0.0982, 0.2920	0.0442, 0.1474	0.0392, 0.1081	0.0522, 0.1224	0.0851, 0.1944	0.0428, 0.1203
R1, wR2 (all data)	0.1107, 0.2459	0.0538, 0.1253	0.1295, 0.3104	0.0511, 0.1626	0.0502, 0.1190	0.0989, 0.1688	0.1815, 0.2538	0.0599, 0.1366
goodness of fit	1.069	1.136	1.079	1.091	1.071	1.044	1.033	1.057

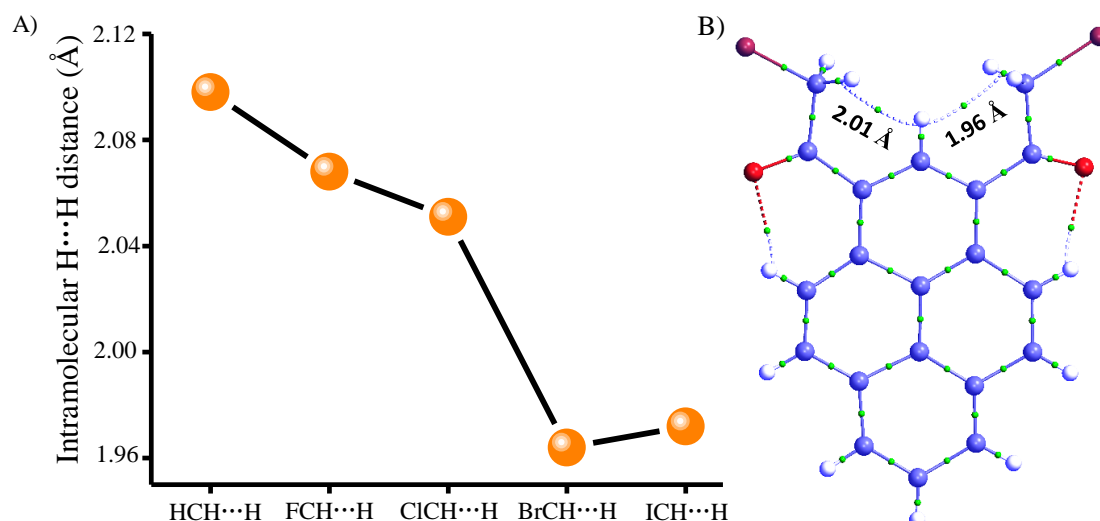
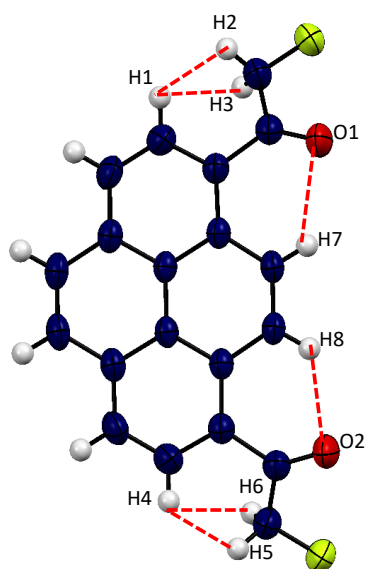
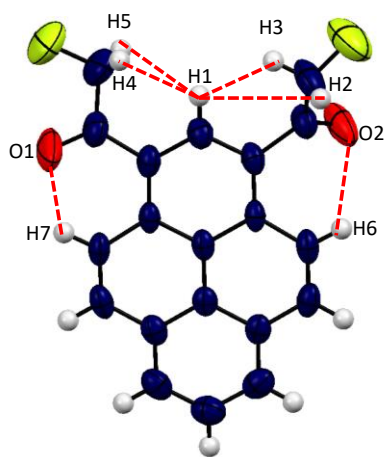


Figure 4.2. (A) Decrease in the intramolecular dihydrogen distance in 1,3-XP compared to 1,3-AP and (B) QTAIM electron density map of 1,3-BP indicating intramolecular dihydrogen and C-H...O interactions.

interaction distance of 1.96 Å and 2.01 Å, respectively, confirms the presence of intramolecular bifurcated H...H interaction in 1,3-BP. QTAIM of other XPs offered no characteristics supporting the intramolecular dihydrogen interactions at distances less than 2.4 Å. In addition to intramolecular dihydrogen contacts, intramolecular C-H...O hydrogen bonding interaction was observed in XPs between carbonyl oxygen and pyrenyl hydrogen with distance ranging from 2.17 Å to 2.88 Å (Table 4.2.). Crystal packing arrangement of XPs is shown in Figures 4.3A&B where lamellar and columnar assembly was observed. π - π stacking, halogen interactions, dihydrogen contacts and C(pyrene)-H...O (carbonyl) hydrogen bonds act as the principal driving forces for the molecular packing. In 1,3-XP, face-to-face lamellar/columnar arrangement was obtained with strong π - π stacking interactions between neighboring pyrene units with an interplanar distance of 3.52 Å (1,3-FP), 3.55 Å (1,3-

Table 4.2. Shows the intramolecular interactions in 1,3-XP and 1,8-XP as visualized through Mercury CSD 3.8.



	Interaction	d (Å)
	H1...H2	2.068
	H1...H4	2.208
13-FP	H1...H2	2.268
	O1...H7	2.205
	O2...H6	2.505
	H1...H2	2.362
	H1...H3	2.051
13-CP	H1...H4	2.208
	H1...H5	2.162
	O1...H7	2.160
	O2...H6	2.179
	H1...H3	1.964
13-BP	H1...H4	2.011
	O1...H7	2.185
	O2...H6	2.189
	H1...H2	1.972
13-IP	H1...H4	2.017
	O1...H7	2.182
	O2...H6	2.190
	Interaction	d (Å)
18-FP	H1...H2	2.091
	O1...H7	2.639
	O2...H8	
	H1...H2	2.362
	H1...H3	2.088
18-CP	H1...H4	2.218
	H1...H5	2.205
	O1...H7	2.881
	O2...H8	2.872
	H1...H3 / H1...H4	2.137
18-C'P	O1...H7 / O2...H8	2.886
	H1...H2 / H1...H4	2.061
18-BP	O1...H7 / O2...H8	2.174

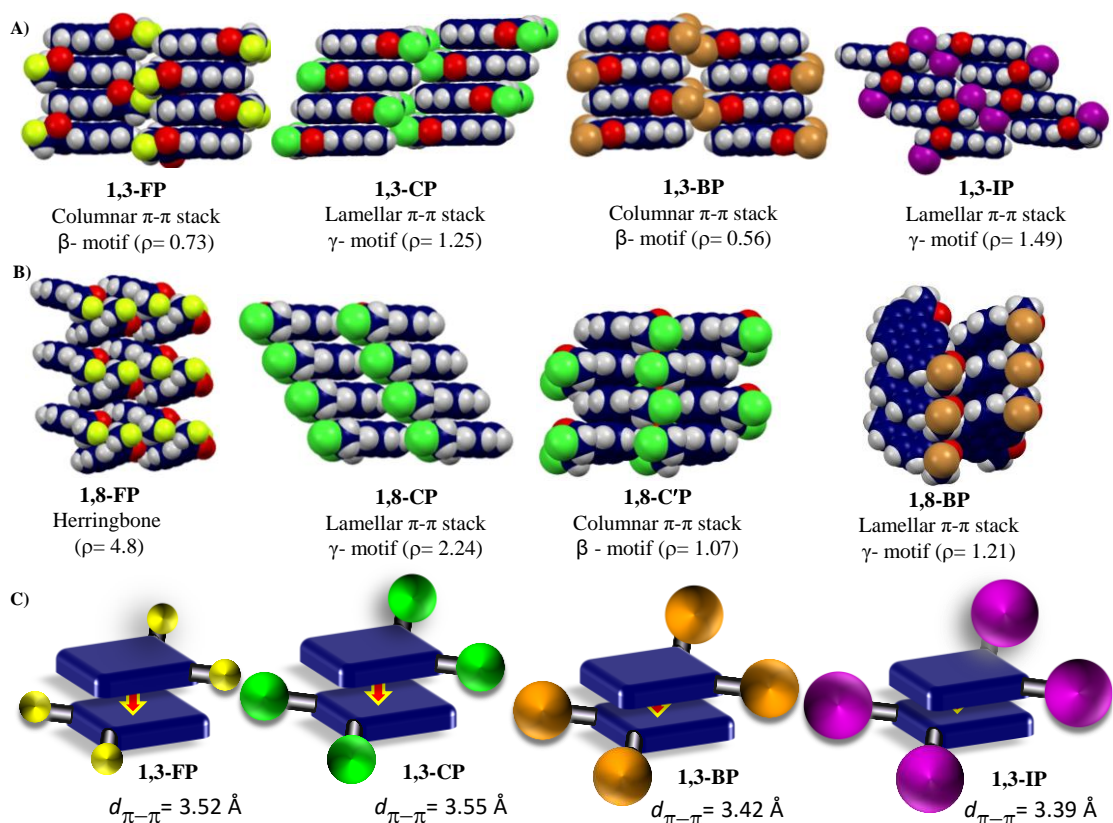


Figure 4.3. Close packing arrangement in (A) 1,3-XPs and (B) 1,8-XPs indicating the values of ρ [(%C...H)/(%C...C)]. Herringbone ($\rho > 4.5$), sandwichherringbone ($3.2 < \rho < 4.0$), γ ($1.2 < \rho < 2.7$), β ($0.46 < \rho < 1.0$) and (C) schematic representation showing the decrease in the interplanar distance between pyrene units in 1, 3-XPs.

CP), 3.42 Å (1,3-BP) and 3.39 Å (1,3-IP) respectively (Figure 4.3C&4.4). It is pertinent to point out that introduction of haloacetyl group in 1,3-XP resulted in the π - π stacked lamellar/columnar arrangement compared to the sandwich herringbone arrangement of pyrene. Similarly as the polarizability of the halogen increases, a gradual decrease

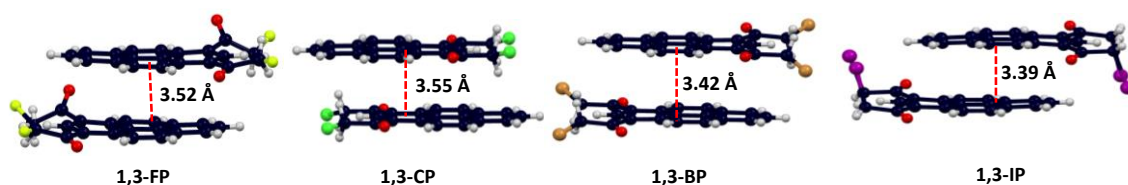


Figure 4.4. Shows the decrease in the interplanar distance between pyrene units in 1,3-XP.

in the interplanar distance was observed suggesting favorable molecular overlap. To explore the effects of haloacetylation on the crystal packing, we have generated electrostatic potential (ESP) maps to demonstrate the difference in charge distribution of XPs (Figure 4.5). Within the series of haloacetylpyrenes, there is a significant difference in charge distribution as we move from FP to IP owing to the increasing polarizability of halogens[200]. With more polarizable halogen such as iodine, the surface charge is more unevenly distributed on the molecular surface. Such reorganization of surface charge distribution create an opportunity to pack in a way to maximize the electrostatic interactions, implying that this is the weak dominant interaction in these systems. As a result, within the series, the strength of π - π stacking interaction increases as we move from FP to IP (Figure 4.5). A closer inspection of the packing of 1,3-XP revealed two type of H...X interactions including C(sp³)-H...X and C(sp²)-H...X (Figures 4.6A,B,C&D) where C(sp³)-H...X interaction in 1,3-FP ($d_{H...F}$: 2.50 Å and $\theta_{C-H...F}$: 147°), 1,3-BP ($d_{H...Br}$: 3.08 Å and $\theta_{C-H...Br}$: 149°), and 1,3-IP ($d_{H...I}$: 3.13 Å and $\theta_{C-H...I}$: 136°) leads to corresponding dimer formation in the crystalline state while C(sp²)-H...X in 1,3-FP ($d_{H...F}$: 2.55 Å and $\theta_{C-H...F}$: 140°) and 1,3-CP ($d_{H...Cl}$: 2.94 Å and $\theta_{C-H...Cl}$: 129°) and 1,3-BP ($d_{H...Br}$: 3.07 Å and $\theta_{C-H...Br}$: 138°) leads to one dimensional (1-D) chain along the *c*-axis (Figure 4.6). In addition to the C-H...X interaction and π - π stacking interaction, 1,3-XP revealed strong C-H...O interaction between (1,3-FP: $d_{H...O}$: 2.64 Å and $\theta_{C-H...O}$: 156°, 1,3-CP: $d_{H...O}$: 2.41 Å and $\theta_{C-H...O}$: 149°, 1,3-BP: $d_{H...O}$: 2.43 Å and $\theta_{C-H...O}$: 162°), carbonyl oxygen and pyrenyl hydrogen forming a 1-D chain

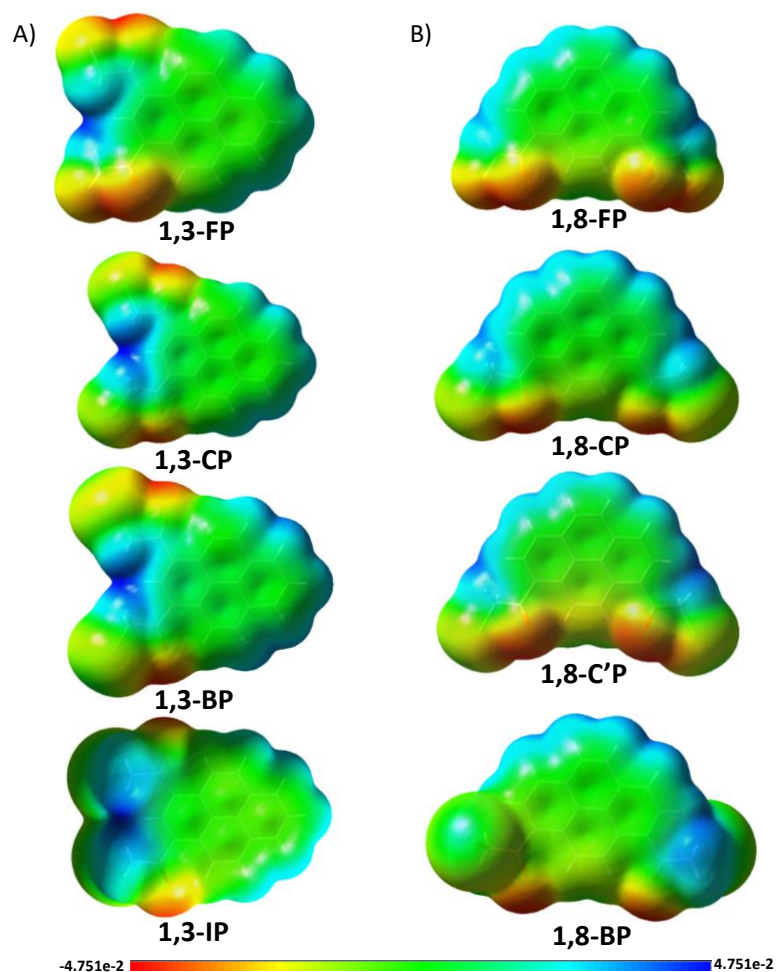


Figure 4.5. Calculated ESP maps of representative monomers of A) 1,3-XP and B) 1,8-XP from crystal structure. All maps used consistent surface potential ranges $[-4.75e-2$ au (red) to $4.75e-2$ au (blue)] and an isovalue of 0.000400 au.

along b , a , b , and a -axis respectively (Figures 4.6A,B,C&D). The C-H \cdots X and C-H \cdots O intermolecular interactions act as steering for extending adjacent lamellae/columns and generate a 3-D supramolecular assembly in the crystalline state. Intriguingly, in 1,3-IP, unusual I \cdots π interaction between iodine and π -electron cloud of neighboring pyrene moiety mediated 1D- array was observed ($d_{I\cdots\pi}$: 3.67 Å) along the c -axis (Figure 4.6D). QTAIM analysis offered characteristic electron density ($\rho_b(r)$): 0.066 eÅ $^{-3}$; 7.38 kJ mol $^{-1}$) supporting the intermolecular interaction between the iodine moiety and π -

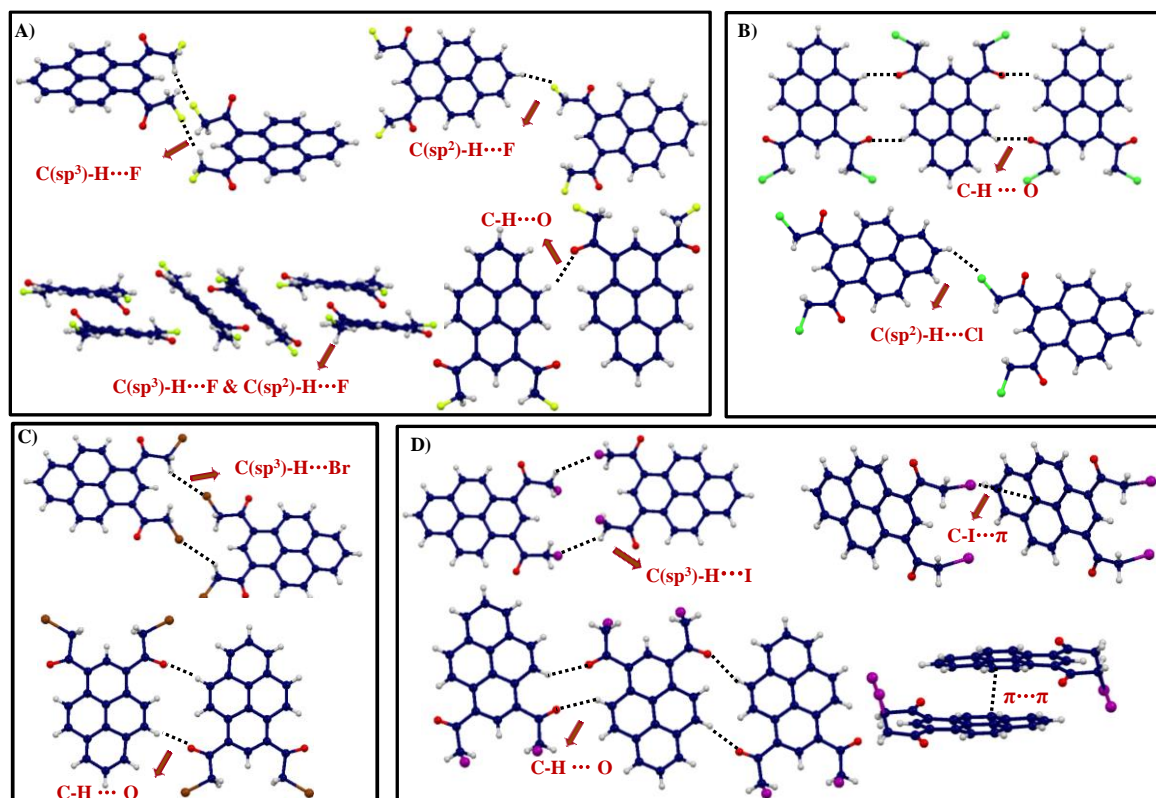


Figure 4.6. Intermolecular interactions in 1,3-XPs. (A) intermolecular C-H...F and C-H...O interactions in 1,3-FP; (B) C-H...O and C-H...Cl interactions in 1,3-CP; (C) C-H...Br and C-H...O interactions in 1,3-BP and (D) C-H...I, C-I...π C-H...O and π-π interactions in 1,3-IP.

electron cloud of neighboring pyrene moiety (Figure 4.7 and Table 4.3).

Analysis of the intermolecular contacts show that except 1,8-FP, all the other 1,8-XP derivatives make π-π contacts and generate lamellar/columnar packing. In the crystal packing of 1,8-FP, C-H...π interactions ($d_{\text{H}\dots\pi}$: 2.97 Å) involving C-H of pyrene moiety with the π electron cloud of the neighboring pyrene moiety generate a herringbone arrangement. The interplanar tilt angle between two neighboring pyrene rings is 34° and the close intermolecular C...C contacts are 3.5 Å. In addition, fluorine moiety in 1,8-FP undergoes tetrafurcated interaction including (i) F...π interaction

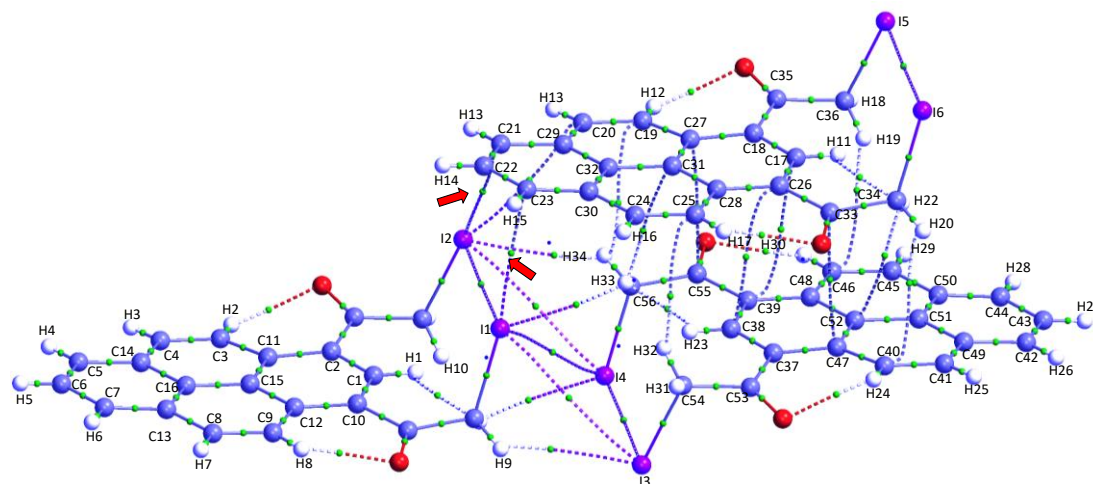


Figure 4.7. Shows QTAIM electron density map of 1,3-IP, arrows indicate the existence of intermolecular $I\cdots\pi$ contacts.

($d_{F\cdots\pi}$: 3.14 Å) between fluorine atom and π -orbitals of the C=O bond generating a self-assembled dimer; (ii) two types of C-H \cdots F interactions between fluorine and methylenyl hydrogens ($d_{H\cdots F}$: 2.58 Å and 2.66 Å, $\theta_{C-H\cdots F}$: 111° and 106° respectively) and (iii) C-F \cdots C interaction between fluorine and C of the alkyl group ($d_{F\cdots C}$: 3.15 Å) (Figure 4.8A). QTAIM analysis offered characteristic electron density ($\rho_b(r)$): 0.035 eÅ⁻³

Table 4.3. Calculated topological properties of the electron density for the intermolecular interaction in XPs.

	Interactions	^a d, (Å)	^b $\rho_b(r)$, (eÅ ⁻³)	^c $\nabla^2\rho_b(r)$, (eÅ ⁻⁵)	^d DE, (kJmol ⁻¹)
1,8-FP	F1 \cdots C38/F2 \cdots C18	3.145	0.035	0.538	4.27
1,3-IP	I2 \cdots C21/I2 \cdots C23	3.405	0.066	0.675	7.38
1,8-C'P	H7 \cdots H16/H8 \cdots H15	2.165	0.042	0.504	4.25
	H10 \cdots H17/H9 \cdots H18	2.389	0.035	0.469	3.71
1,8-BP	H10 \cdots H18/H9 \cdots H17	2.524	0.029	0.418	3.30
	Br2 \cdots C20	3.476	0.039	0.446	3.43

^ad=distance, ^b $\rho_b(r)$ =electron density at the BCP, ^c $\nabla^2\rho_b(r)$ =Laplacian of $\rho_b(r)$ and ^dDE=dissociation energy.

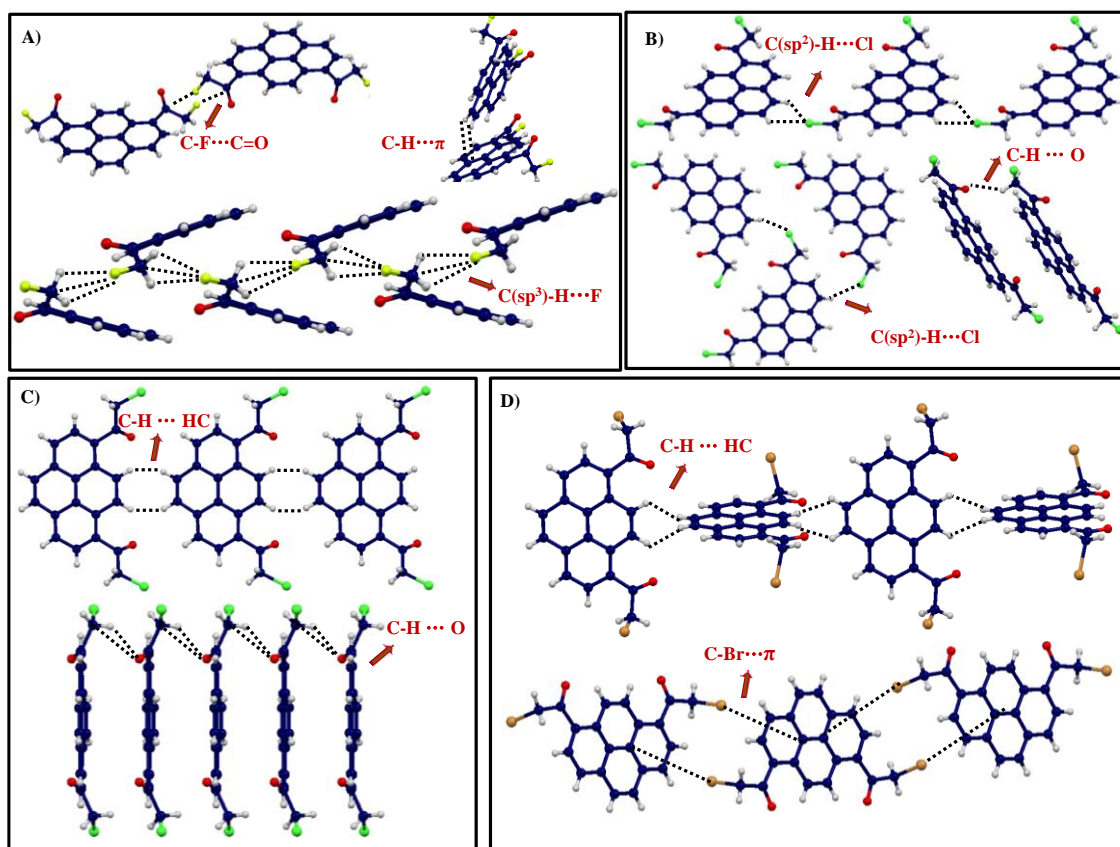


Figure 4.8. Intermolecular interactions in 1,8-XPs. (A) intermolecular $C-F\cdots C$, $C-H\cdots\pi$ and $C-H\cdots F$ interactions in 1,8-FP; (B) $C-H\cdots Cl$ and $C-H\cdots O$ interactions in 1,8-CP; (C) $C-H\cdots H-C$, and $C-H\cdots O$ interactions in 1,8-C'P and (D) $C-H\cdots H-C$ and $C-Br\cdots\pi$ interactions in 1,8-BP.

3; 4.26 kJ mol⁻¹) supporting the intermolecular interaction between the fluorine and π -orbitals of the $C=O$ bond generating a self-assembled dimer (Figure 4.10 and Table 4.3).

In 1,8-CP, 1,8-C'P and 1,8-BP, cofacial lamellar/columnar arrangement was observed with strong π - π stacking interactions between neighboring pyrene units with an

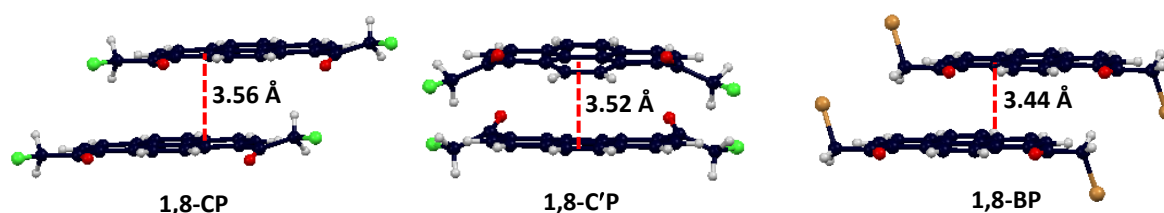


Figure 4.9. Shows the decrease in the interplanar distance between pyrene units in 1,8-XP.

interplanar distance of 3.56 Å (1,8-CP), 3.52 Å (1,8-C'P) and 3.44 Å (1,8-BP) respectively (Figure 4.9). Similar to 1,3-XP, a gradual decrease in the interplanar distance was observed with increasing the polarizability of halogens. Detailed analysis of the single crystal X-ray structure of 1,8-CP revealed the presence of two types of contacts including C-H...Cl interaction and C-H...O interaction which propagates the lamellar arrangement in 3-D. Chlorine atom of one molecule undergoes trifurcated interaction with two pyrenyl hydrogens ($d_{\text{H}\dots\text{Cl}}$: 2.78 Å and 2.85 Å, $\theta_{\text{C-H}\dots\text{Cl}}$: 129° and 125° respectively) and pyrenyl carbon ($d_{\text{F}\dots\pi}$: 3.45 Å) generating a 1-D array along *b*-axis. The C-H...O interaction mediated another 1-D array is generated along the *a*-axis ($d_{\text{H}\dots\text{O}}$: 2.40 Å and $\theta_{\text{C-H}\dots\text{O}}$: 144°) (Figure 4.8B). In 1,8-C'P, dihydrogen contacts between two pyrenyl hydrogens with the distance of 2.16 Å plays a major role in extending the columnar/lamellar arrangement in 2-D. Another 1-D array is generated along the *a*-axis by the bifurcated interaction of the carbonyl oxygen with the hydrogen ($d_{\text{H}\dots\text{O}}$:

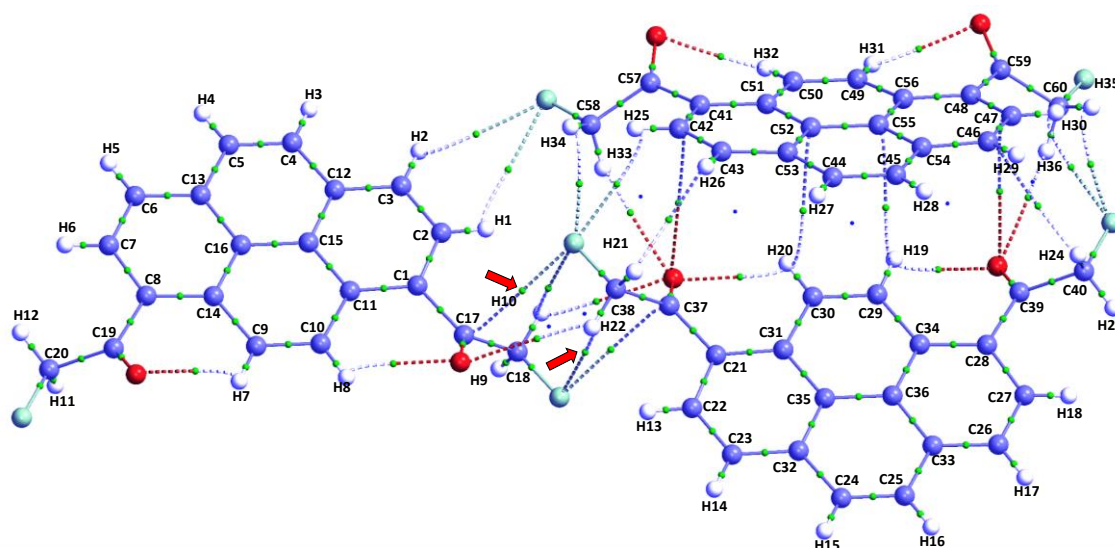


Figure 4.10. Shows QTAIM electron density map of 1,8-FP, arrows indicate the existence of intermolecular C...F interactions.

2.63 Å and $\theta_{\text{C-H}\cdots\text{O}}$: 117°) and carbon of the alkyl moiety with the distance of 3.17 Å which further supports the stacking interaction (Figure 4.8C). In 1,8-BP, pyrenyl dihydrogen interaction ($d_{\text{C-H}\cdots\text{H-C}}$: 2.39 Å) mediated 1-D array was observed along the *c*-axis. In addition, another 1-D array was observed along the *a*-axis *via* Br $\cdots\pi$ interaction ($d_{\text{Br}\cdots\pi}$: 3.48 Å) (Figure 4.8D). These two interactions extend the lamellar arrangement and generate a 3-D supramolecular assembly in the solid-state. QTAIM

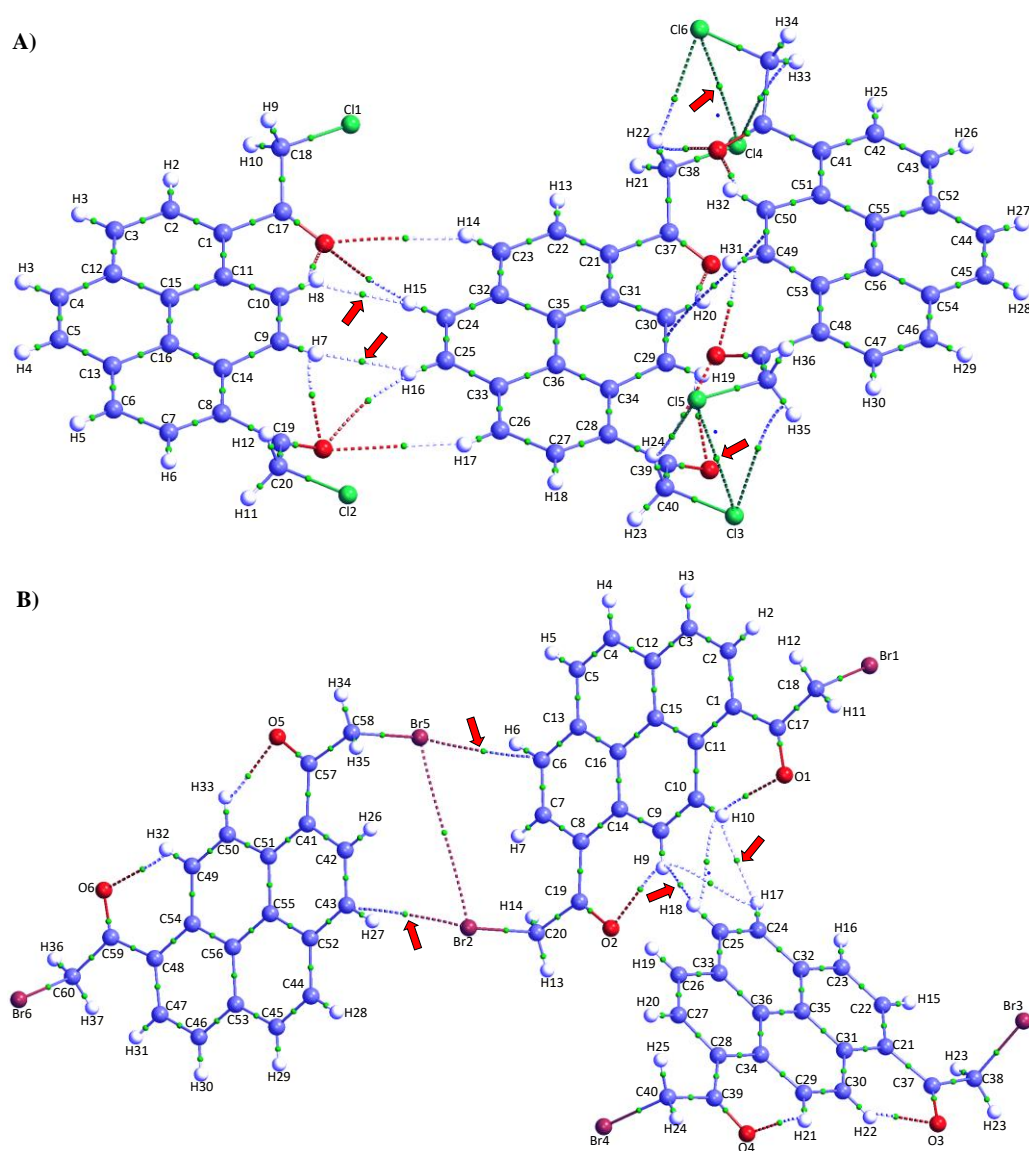


Figure 4.11. QTAIM electron density map of (A) 1,8-CP and (B) 1,8-BP indicating intermolecular interactions.

analysis further corroborate the dihydrogen contacts in 1,8-C'P where C–H...H–C interaction ($\rho_b(r)$): $0.042 \text{ e}\text{\AA}^{-3}$; 4.25 kJ mol^{-1} ; Figure 4.11A, Table 4.3) aids in extending linear arrangement of pyrene units along *a*-axis. In 1,8-BP, C–H...H–C ($\rho_b(r)$): $0.029\text{--}0.035 \text{ e}\text{\AA}^{-3}$; $3.30\text{--}3.71 \text{ kJ mol}^{-1}$; Figure 4.11B, Table 4.3) contact promotes orthogonal arrangement[201] of pyrene units along the *c*-axis. QTAIM calculations also confirmed the existence of Br... π interactions in the crystalline 1,8-BP ($\rho_b(r)$): $0.039 \text{ e}\text{\AA}^{-3}$; 3.43 kJ mol^{-1}), apart from the C–H...H–C contacts (Figure 4.11B, Table 4.3). Among the unusual interactions analyzed in XPs, I... π ($DE=7.38 \text{ kJmol}^{-1}$) represents the strongest stabilizing interaction compared to F... π ($DE=4.27 \text{ kJ mol}^{-1}$), Br... π ($DE=3.45 \text{ kJ mol}^{-1}$) and dihydrogen contact ($DE=3.30\text{--}3.71 \text{ kJ mol}^{-1}$) (Table 4.3).

4.2.3. Hirshfeld surface analysis

Hirshfeld surface analysis[134] of the crystal structures of 1,3- and 1,8-XP give insight into the nature of intermolecular interaction and packing motifs in the solid

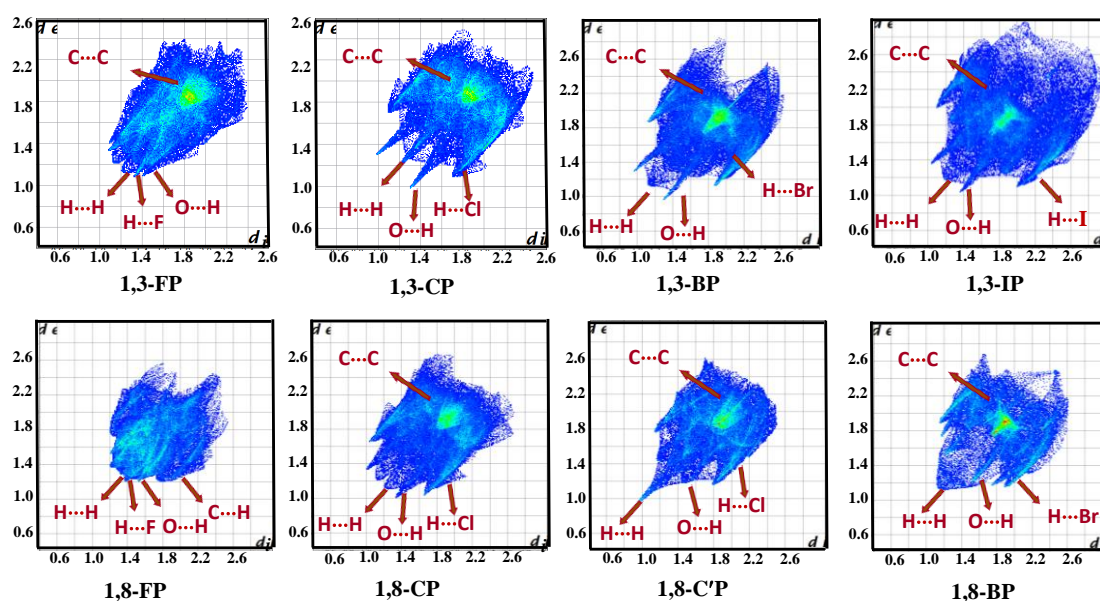


Figure 4.12. Hirshfeld 2D fingerprint plot of 1,3 and 1,8-XPs.

Table 4.4. Shows the percentage of intermolecular contacts of a molecule in crystalline XPs.

	C•••C	H•••X	O•••H	C•••H	H•••H	C•••X	C•••O	^a ρ
1,3-FP	17.4	22.3	17.3	12.7	27.9	-	-	0.73
1,3-CP	12.6	28.8	11.6	15.8	23.9	1.4	-	1.25
1,3-BP	16.7	30.1	13.2	9.4	25	-	3.2	0.56
1,3-IP	11.2	30	15.2	16.7	19.6	4.7	1.6	1.49
1,8-FP	6	21.2	17.8	28.8	20.6	1.8	-	4.8
1,8-CP	9.4	24.4	15.7	21.1	21	4	2.3	2.24
1,8-C'P	13.4	26.1	14.3	14.4	25.1	1.2	1.7	1.07
1,8-BP	13.5	29.5	15.5	16.4	20.7	2.8	0.7	1.21

^aρ = (%C•••H)/(%C•••C); Herringbone (ρ > 4.5), Sandwichherringbone (3.2 < ρ < 4.0), Lamellar (1.2 < ρ < 2.7), Columnar (0.46 < ρ < 1.0)[30].

state (Figure 4.12). Table 4.4 contains the percentages of contributions for various contacts in XPs. It is evident from the table that H•••H, O•••H, H•••X, C•••C and C•••H interactions in XP can account for more than 90% of the Hirshfeld surface area (97.6% in 1,3-FP, 92.7 % in 1,3-CP, 94.4 % in 1,3-BP, 92.7 % in 1,3-IP, 94.4 % 1,8-FP, 91.6 % in 1,8-CP, 93.3 % in 1,8-C'P and 95.6 % in 1,8-BP). In the 2D fingerprint plots, two sharp spikes of almost equal length are characteristic of C–H•••O interactions. The central spikes extending to (d_i, d_e) region of (1.2 Å, 1.2 Å) in 1,3-XP reveal relatively high percentages of H•••H contacts whereas the central spike corresponding to H•••H interaction of 1,8-XP extend up to (d_i, d_e) region of (1.3 Å, 1.3 Å) in 1,8-FP, (1.2 Å, 1.2 Å) in 1,8-CP, (1 Å, 1 Å) in 1,8-C'P and (1.1 Å, 1.1 Å) in 1,8- BP. The sharpness of central spike in 1,8- is a consequence of close H•••H contacts (~2.16 Å) in C'P that can be seen in the Hirshfeld surface as bright red spots. A significant C–H•••π interaction has been observed for 1,8-FP as indicated by the wings in the upper left and lower right of the 2D fingerprint plot extending up to (d_i, d_e) region of (1.7 Å, 1.7 Å) and contributes

28.8 % of the total contacts. It can be seen that the C...C contacts, associated with π - π stacking interactions in the (di, de) \approx 1.8 Å, 1.8 Å) region, are strong for XPs except 1,8-FP where it is minimal (only 6 % of the surface is due to C...C interactions) suggesting minimum π - π stacking interactions. Occurrence of such weak intermolecular interactions dictates the molecular packing that results in ideal face-to-face columnar 1-D π stacks (β - motif) in 1,3-FP ($\rho = 0.73$), 1,3-BP ($\rho = 0.56$) and 1,8-C'P ($\rho = 1.07$) whereas the ρ values suggest face-to-face lamellar 1D π stacking arrangement (γ -motif) in 1,3-CP ($\rho = 1.25$), 1,3-IP ($\rho = 1.49$), 1,8-CP ($\rho = 2.24$) and 1,8-BP ($\rho = 1.21$). A value of $\rho = 4.8$ in 1,8-FP indicates the formation of edge-to-face herringbone arrangement in the crystalline lattice when compared to other XPs[30]. Thus, we have realized the switching of sandwich herringbone to lamellar/columnar arrangement by introducing α -haloacetyl substituents in pyrene.

High transportation capabilities of charge carriers in pyrene based semiconductors has attracted its application in p-type and ambipolar OFETs[16-17]. The recent interests in pyrene based semiconductors is due to control over molecular architecture that can be achieved by modifying the structure by varying the position of substitution on the pyrene ring. Herein, we report on comparative investigation of conductivity in systematically synthesized acetylpyrene (AP) derivatives. In our approach, we first study the morphology of the derivatives by scanning electron microscopy (SEM), atomic force microscopy (AFM), and tunneling electron microscopy (TEM). Further, we determine the I-V profiles of the derivatives and use

field-effect transistor (FET) measurements to obtain the charge carrier mobility which corroborate with theoretically predicted trend.

Previously, we reported the synthesis of acetyl pyrenes derivatives (1-4AP) by treating a required amount of acetyl chloride to a solution of pyrene in carbon disulphide (Figure 4.13, Row I). The derivatives were analytically and spectroscopy characterized along with the X-ray molecular structure. Acetyl derivatives (1, 2', 2'', 3, 4AP) exhibit a monoclinic system, a crystal system described by vectors of unequal lengths, while 2AP exhibits an orthorhombic system (Figure 4.13, Row II). The derivatives 1AP and 2'AP tend to crystallize following a herringbone pattern, wherein the molecules interact face-to-edge through C-H... π interactions and minimize the

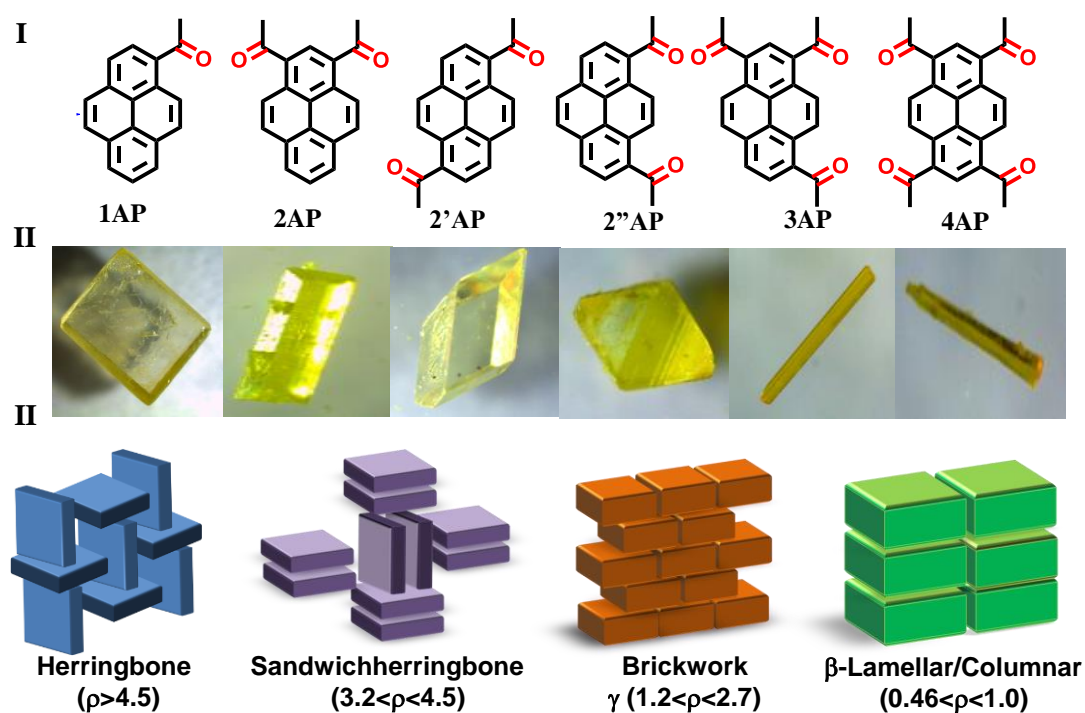


Figure 4.13. Row I: chemical structure of 1–4 AP; Row II: stereo microscopic images of corresponding single crystal and Row III: schematic drawing that depicts the possible crystal packing pattern and the range of $\rho = (\%C\cdots H)/(\%C\cdots C)$ contact ratio for each packing.

electrostatic π -orbital repulsion (Figure 4.13, Row III). A similar crystallographic analysis on 2AP and 2''AP classify the crystallization pattern to be brickwork, which is very promising for high charge carrier mobility and less sensitive to charge traps (Figure 4.13, Row III). 3AP and 4AP has completely planar geometry where the torsion angle between the pyrene rings is 0° . The molecules 3AP and 4AP form a unique two-dimensional columnar structure, wherein the molecules stack with a short intermolecular separation of 3.4–3.5 Å (Figure 4.13, Row III).

4.2.4. Morphological Analysis

Effect on increasing the acetyl group substitutions on pyrene unit brings different morphological characterization on the self-assembly of AP derivatives. These morphologies in aggregate were extensively studied by a variety of microscopic including SEM, AFM and laser scanning confocal microscopy. SEM images of the molecular aggregate in 1AP, drop-casted in benzene solution on silicon wafer, reveals

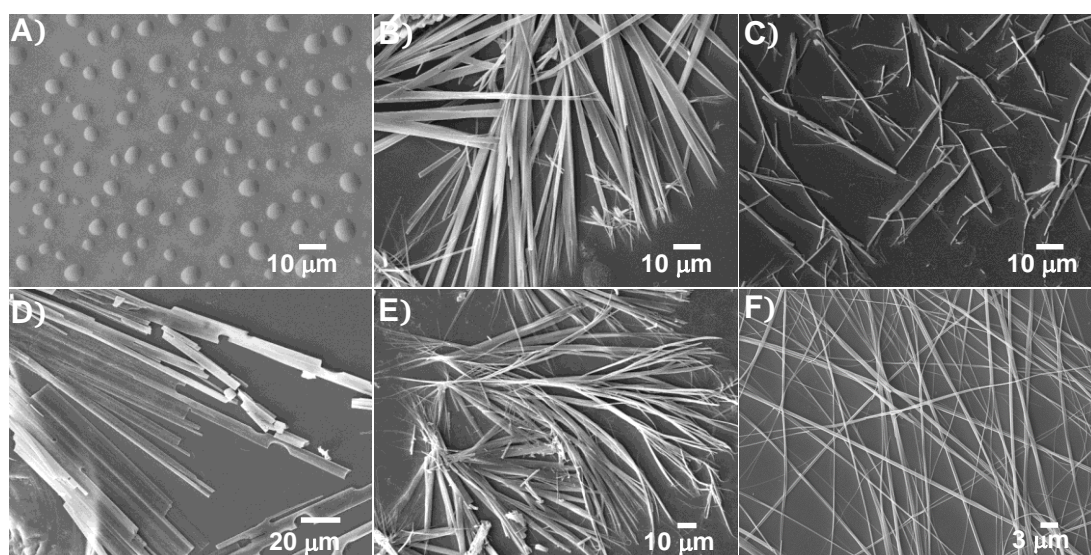


Figure 4.14. SEM images of A) 1AP B) 2AP C) 2'AP D) 2''AP E) 3AP and F) 4AP, drop casted in benzene.

nearly mono dispersed micro spheres, with an average diameter of 8.17 nm (Figure 4.14A). The spherical morphology of molecular aggregate strongly attributes to the it has a herringbone packing. The micro wires have average width of 1.05 μm and average length of 43.59 μm which corresponds to an aspect ratio of 41.24 herringbone packing (absence of π - π stacking) which prevents one dimensional assembly of the molecules. The formation of micro wires of low aspect ratio in 2'AP may be due to increased CH \cdots O interaction between the adjacent molecules, though (Figure 4.14C). Favourable π - π stacking of pyrene core in 2AP and 2''AP shows a lamellar molecular assembly resulting in micro belts (Figure 4.14B&D) with an average width of 2.40 μm and 7.72 μm respectively. These micro belts are few tens of micrometre in length, as evident from the laser confocal imaging (which is discussed latter) which leads to high aspect ratio. This high aspect ratio accounts for more organized molecular stacking and one dimensional extended growth along the long axis in the belts. Increased CH \cdots O interaction in 3AP and 4AP induces co-planarity in the pyrene units which in turn promotes π - π stacking that leads to the formation of long single crystalline self-assembled micro structures (Figure 4.14E&F).

AFM image of AP derivatives in benzene drop-casted on mica sheet captures the cross-sectional width and height of the distinct morphology of the self-assembly. The self-assembled structures so formed are in good agreement with SEM data. The morphology of 1AP was resolved for small sphere like assembly with a cross-sectional height of 1.67 nm (Figure 4.15A). In 2AP and 2''AP, a cross section perpendicular to the axis of the belts shows an average belt height of about 286.11 nm and 268.55 nm

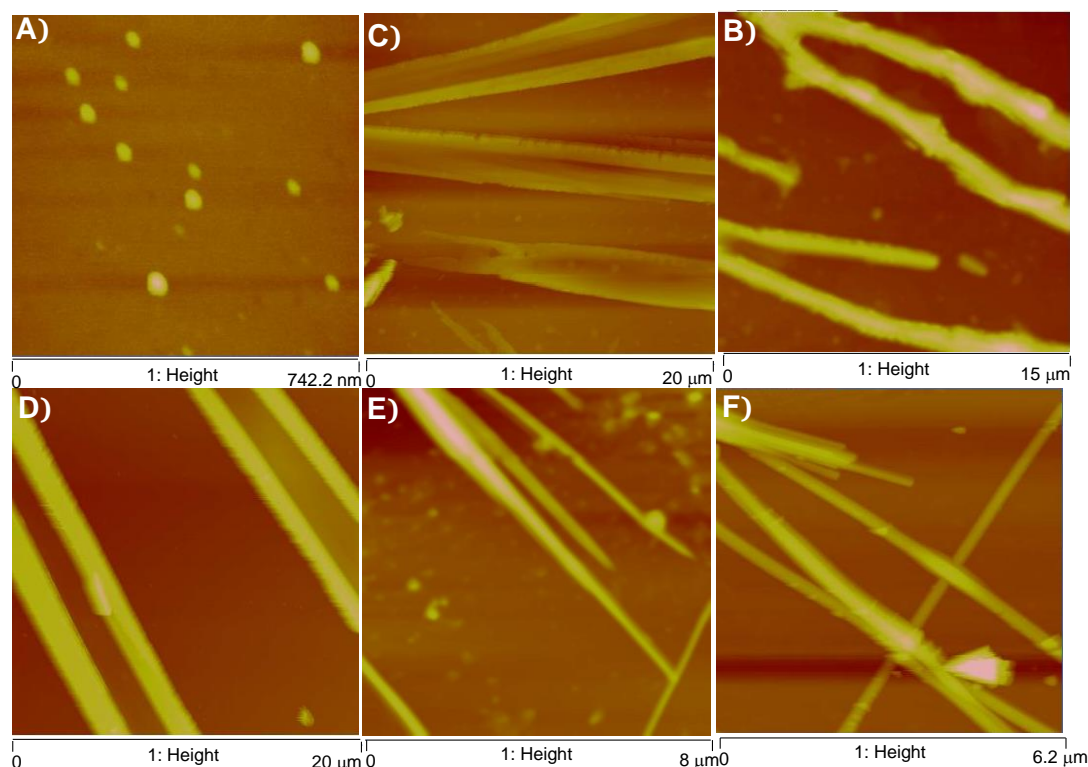


Figure 4.15. Show the AFM images of A) 1AP; B) 2AP; C) 2'AP; D) 2''AP; E) 3AP and F) 4AP, drop casted in benzene.

respectively (Figure 4.15B&D). Detailed examination of these micro belts along their length reveals that they are uniform in cross-sectional width of 1.47 μm and 2.37 μm respectively which corroborate with the SEM analysis.

The role of substrate were again nullified when silicon wafer and mica sheet used for SEM and AFM respectively, was replaced with glass coverslips to investigate the laser confocal imaging in order to understand the surface assisted self-assembling of AP derivatives. Confocal imaging of the molecular assembly of 1AP drop-casted on glass coverslips showed particulate aggregate in an approximately spherical shape, with average size of 2.50 μm (Figure 4.16A). The spherical morphology of molecular aggregate is consistent with the distorted π - π stacking which is in good accord with

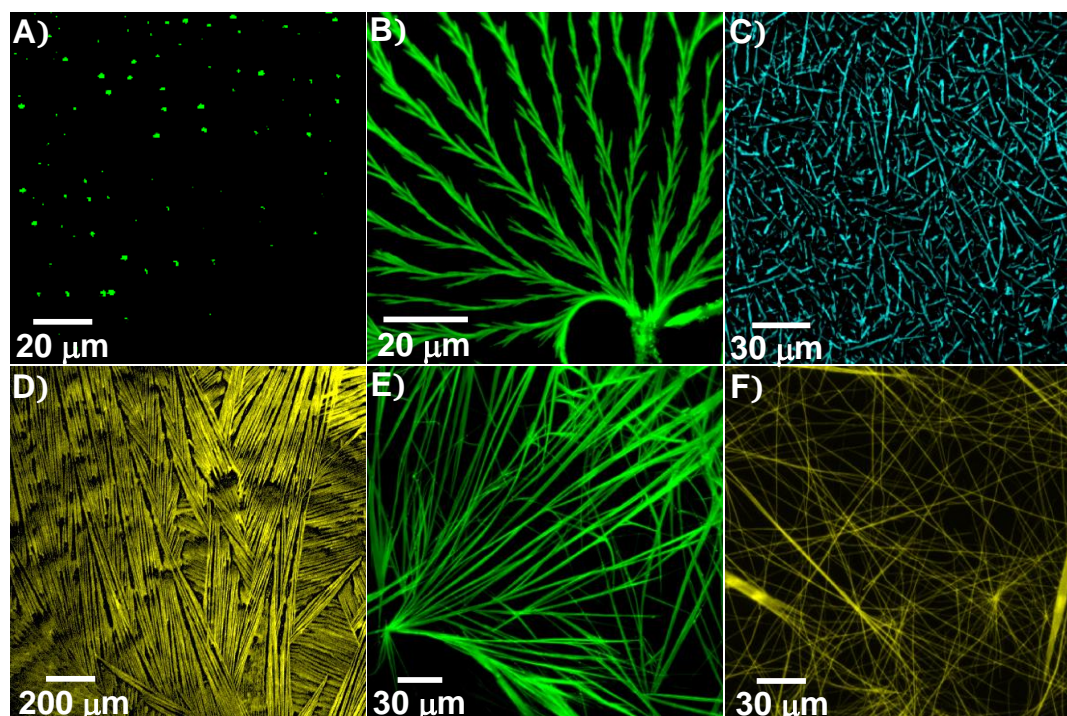


Figure 4.16. Show the laser confocal images of A) 1AP; B) 2AP; C) 2'AP; D) 2''AP E) 3AP and F) 4AP, drop casted in benzene.

the SEM and AFM data. The establishment of herringbone packing in 2'AP were identified through the formation of low aspect ratio micro wires of having an average width of 2 μm and average length of 30 μm (Figure 4.16C). The characteristic flat morphological feature remained unperturbed in drop-casted 2AP and 2''AP though the formation of microstructures with high aspect ratio (Figure 4.16B&D). The self-assembled microstructures forms fairly uniform microbelts with length ranging from tens to hundreds of micrometres. The morphology of self-assembled structures attained in 3AP and 4AP, leads to the formation of microfibril, consistent with the extended molecular stacking within the long microfibrils determined by the collective interaction between the large numbers of co-facially stacked pyrene units (Figure 4.16E&F). As revealed through the SEM analysis, 3AP and 4AP were composed of

micro-sized fibrils with high aspect ratio. The extended 1D self-assembly is likely dominated by the strong π - π interaction between the pyrene scaffolds, as indicated by the X-ray diffraction, for which the typical π - π stacking of 3.57 and 3.45 Å was observed respectively.

To further correlate the observed morphology of the molecular self-organization of AP derivatives with the crystal structure, we performed electron diffraction studies by drop-casting on carbon (copper grid; Figure 4.17). Bright field transmission electron microscopy (TEM) observations, demonstrate that 1AP ends up in highly dispersed micro spherical aggregates which corroborates with the SEM analysis. While 2AP, 2''AP, 3AP and 4AP exhibits high aspect ratio self-assembled structures, ensuring the involvement in π - π stacking along different axis.

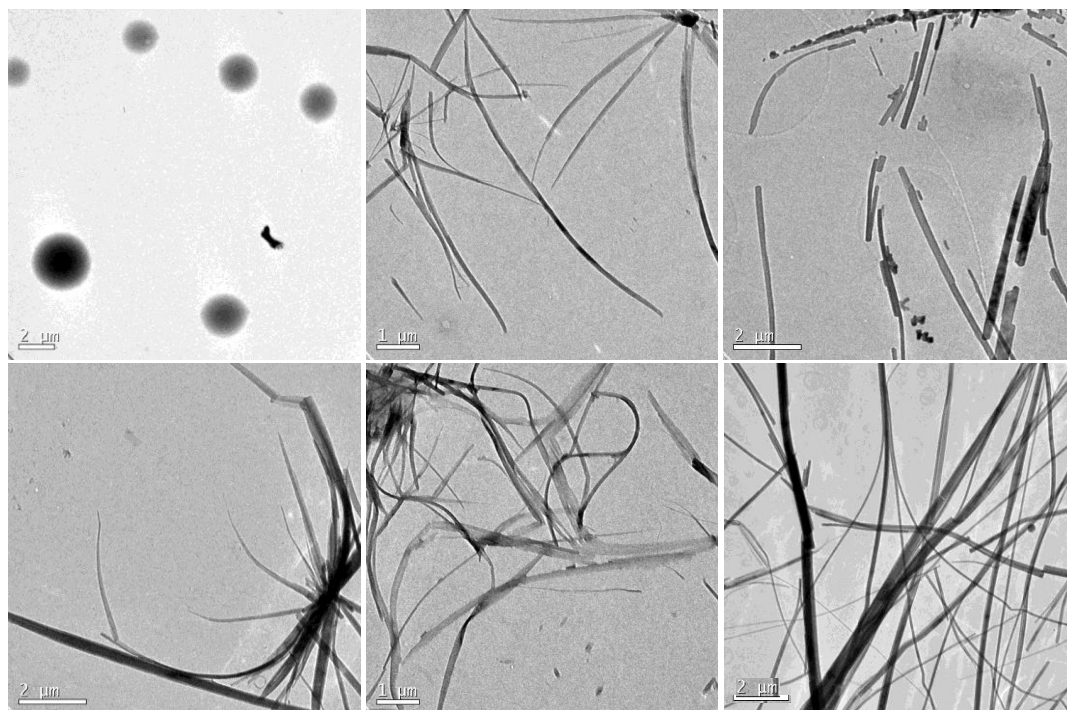


Figure 4.17. Show the TEM images of a) 1AP; b) 2AP; c) 2''AP; d) 2''AP; e) 3AP and f) 4AP, drop casted in benzene.

4.2.5. Conductivity measurements and theoretical calculations

To evaluate the intrinsic molecular packing on charge-transport properties, microcrystals suitable for device fabrication were prepared through drop-casting AP derivatives in benzene (1 mM) on a glass slide (1 cm×1 cm). The current-voltage (I–V) characteristics were investigated by two probe method by scanning the voltage from 0 to 10 V with a sweeping rate of 1.0 V s⁻¹ (Figure 4.18A). The linear dependence of the applied voltage under positive biases suggests an Ohmic carrier-transporting process inside the organic semiconductor. Under similar conditions, for the given area on the glass slide (1 cm×1 cm) and the concentration of the sample (AP) drop-casted (1mM), we extracted the electrical resistance (R) for the drop casted samples. The slope calculated from the linear fit of the I-V characteristics for the applied positive bias voltage range gave the resistance for the drop casted samples. A high resistance was offered to the charge transfer in 1AP (847 MΩ) and 2'AP (332 MΩ) while 2AP (21 MΩ),

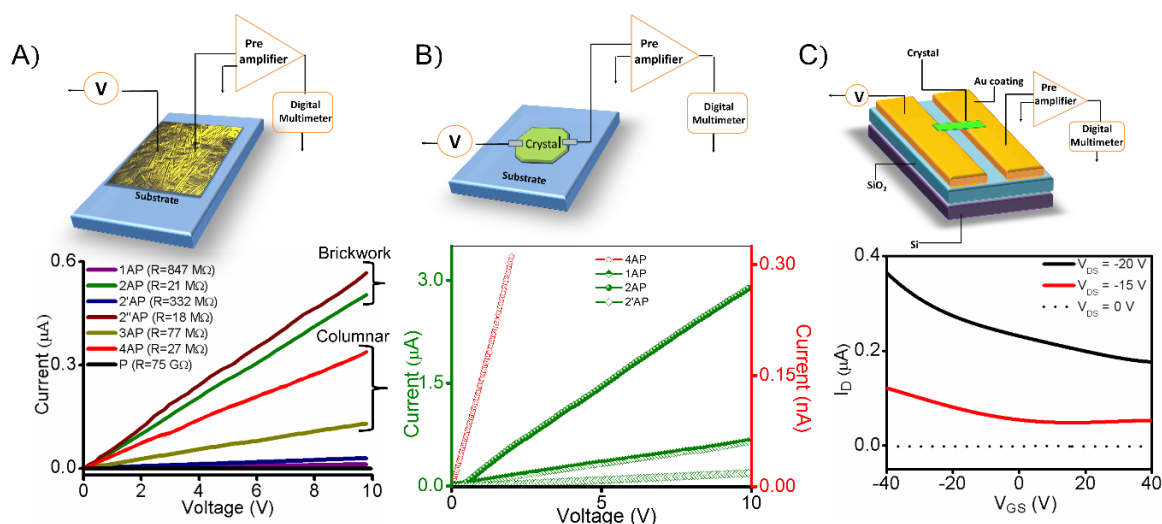


Figure 4.18. I-V profile determination by A) drop-casting in benzene; B) single crystal and C) single crystal organic field-effect transistor (OFET) measurement on 4AP.

2''AP (18 M Ω), 3AP (77 M Ω) and 4AP (27 M Ω) allows an easy accessibility to the charge transfer. The crystal structural analysis of 1AP and 2'AP affords the packing of pyrene units in so called herringbone packing in which the molecules are packed through edge-to-face in two-dimensional. This adverse edge-to-face packing of pyrene units minimize the π - π between the adjacent molecules while the stacked face-to-face observed in brickwork (2AP and 2''AP) and columnar (3AP and 4AP) lead to higher charge transfer. Hence the observed decrease by an order of one magnitude in the resistance seems that the crystals with π -stacked packing (brickwork and columnar) better than those with herringbone packing. The unsubstituted pyrene (P) showed a high resistance in magnitude of giga ohms.

To establish a direct correlation between solid-state packing and charge transport properties, we measured the resistance through the single crystals which allows us to study the corresponding electrical resistivity properties (ρ). By taking representative examples from herringbone, brickwork and columnar, illustrated through the crystal packing in 1AP, 2AP and 4AP respectively we demonstrated the relationship of charge transport properties and the packing modes of single crystals. We observed a linear relationship for the current-voltage (I-V) characteristics measured for bias voltages in the range of 0 V to 10 V (Figure 4.18B). The electrical resistance (R) for 1AP was calculated from the slope of linear plot of I-V to be $R \approx 3.29 \times 10^9 \Omega$. By measuring the dimension of the single crystal (1AP) of length (L) ≈ 122 mm and area cross-section (A), \approx calculated as $218.22 \mu\text{m}$ (width) $\times 250 \mu\text{m}$ (height), we can determine the single crystal resistivity $\rho = R A/L \approx 1.89 \times 10^7 \Omega\text{m}$. Similarly the

resistivity (ρ) for 2AP and 4AP were calculated as $1.25 \times 10^4 \text{ } \Omega\text{m}$ and $0.72 \times 10^4 \text{ } \Omega\text{m}$ respectively. The comparison of resistivity between 1AP crystal with 2AP and 4AP indicates that the charge transporting ability differ by three order, suggesting that the two dimensional orbital overlap in brickwork (2AP) and columnar (4AP) are more effective for carrier transport than herringbone (1AP) packing.

Having successfully investigated the effect of molecular packing in single crystals on charge transport, we further explored the mobility measurement on single-crystal transistors on 4AP. Single crystal FETs (SC-FETs) were fabricated using the top-contact, bottom-gate geometry on highly doped p-type silicon wafers with 300 nm thick thermally grown silica as the gate dielectric material. Figure 4.18C shows drain current (I_{DS}) vs. source voltage (V_{DS}) for various gate voltage (V_G). The inset gives the transfer characteristics I_{DS} vs V_G at $V_{DS} = -20 \text{ V}$. In both the output and transfer characteristics, the drain current is found to increase at negative gate voltages due to injection of holes in the conduction channel confirming p-channel electrical characteristics of the single-crystal device. The linear nature of the output characteristics assures that a good Ohmic contact with the gold electrode has been achieved. Since the device operation is in the linear regime, we have used the following equation in the calculations;

$$I_{DS} = (W/L)\mu C_i(V_G - V_T)V_{DS}$$

where $W = 10 \text{ } \mu\text{m}$ and $L = 60 \text{ } \mu\text{m}$ are the width and the length of the channel and $C_i = 11.5 \text{ nF/cm}^2$ is the gate capacitance per unit area. The hole mobility is extracted for various gate voltage by calculating $\partial I_{DS} / \partial V_G$ in the I_{DS} versus V_G plot. At increasingly

negative gate voltages, the mobility was found to monotonously increase from 0.03 to 0.18 cm² V⁻¹ s⁻¹, a value which is in good agreement with the theoretically predicted value of 0.2 cm² V⁻¹ s⁻¹.

4.3. Conclusion

A series of α -haloacetyl pyrene derivatives are reported and the effect of halogen interaction and dihydrogen contacts in bringing lamellar and columnar arrangement of pyrene is evaluated in the crystalline state. Incorporation of α -haloacetyl group to pyrene skeleton switched the sandwich herringbone to lamellar/columnar packing motifs. High degree of control over the π -stacking through the strategy of tuning the charge distribution by the incorporation of different halogen atom decreased the interplanar distances between pyrene moieties from 3.52 Å in 1,3-FP to 3.49 Å in 1,3-IP and 3.58 Å in 1,8-CP to 3.44 Å in 1,8-BP in lamellar/columnar motifs. QTAIM analysis confirmed the homopolar dihydrogen contacts in 1,8-C'P/BP where the accumulation of electron density promotes linear arrangement of pyrene units in 1,8-C'P while orthogonal arrangement in 1,8-BP. Apart from the dihydrogen contacts and hydrogen bonding, halogen interactions including Br $\cdots\pi$ and I $\cdots\pi$ interaction play pivotal role in extending the columnar/lamellar arrangement in a 3D manner. Hirshfeld surface analysis displayed $\rho [(\%C\cdots H)/(\%C\cdots C)]$ values suggesting the increased face-to-face lamellar/columnar arrangement in the crystalline α -haloacetyl pyrenes. This strong tendency to form self-assembled, well-defined lamellar/columnar stacks marks α -haloacetyl pyrene as promising candidates

application in opto-electronic devices.

High charge mobility was observed in single crystalline brickwork/ columnar (2 and 2''AP/ 3 and 4AP) when compared to the herringbone structure (1AP) suggesting that the two dimensional orbital overlap are more effective for carrier transport. These findings reveal the control over morphology that can be achieved in acetylpyrene to form microscale conducting materials. The OFET devices fabricated with single crystals of 4AP, displayed the hole mobility of $0.18 \text{ cm}^2 \text{ V}^{-1} \text{ s}^{-1}$, a value which is in good agreement with the theoretically predicted value of $0.2 \text{ cm}^2 \text{ V}^{-1} \text{ s}^{-1}$.

4.4. Appendix

Experimental section

- **Materials and Methods**

All chemicals were obtained from commercial suppliers and used as received without further purification. All reactions were carried out in oven-dried glassware prior to use and wherever necessary, were performed under dry nitrogen in dried, anhydrous solvents using standard gastight syringes, cannulae, and septa. Solvents were dried and distilled by standard procedures. TLC analysis were performed on precoated aluminum plates of silica gel 60 F254 plates (0.25 mm, Merck) and developed TLC plates were visualized under short and long wavelength UV lamps. Flash column chromatography was performed using silica gel of 200-400 mesh employing a solvent polarity correlated with the TLC mobility observed for the substance of interest.

X-ray Crystallography

The single crystal X-ray (SC-XRD) method is discussed in Chapter 2 (Appendix 2.)

Computational methods

Quantum Theory of Atoms in Molecules (QTAIM): The wave function for XPs were obtained employing the geometries taken from the crystal structure using Gaussian set of codes at B3LYP/6-311G**++ level.¹ Quantum theory of atoms in molecules (QTAIM) analysis helps to understand the description of interatomic interaction in the single crystal X-ray structure. A bond is defined along the bond line between two nuclei, called a bond path, along which electron density is concentrated. The bond critical point (BCP) is a point along the bond path at the interatomic surface, where the shared electron density reaches a minimum. The physical characteristics of the BCPs [the electron density at BCP, $\rho(r_{BCP})$, and its Laplacian, $\nabla^2\rho(r_{BCP})$] reveal the approximate measure of the amount of electron density built up in the bonding region and as such could be taken as characteristic of the bond. When $\nabla^2\rho(r_{BCP}) < 0$ and is large in magnitude, $\rho(r_{BCP})$ is also large which means that there is a concentration of

electronic charge in the internuclear region. This is also an indication of a sharing of electronic charge between both nuclei that defines the covalent (polar) bond. When $\nabla^2\rho(r_{\text{BCP}}) < 0$ there is a depletion of electronic charge in the internuclear region. Using the AIM 2000 software package, the electron density was integrated over atomic basins according to the quantum theory of atoms in molecules using PROAIM, and thus the BCP data and the molecular graphs were obtained.

Hirshfeld analysis: Important intermolecular interactions within the crystal structure of XPs were identified through Hirshfeld surface analysis using Crystal Explorer 3.1. The Hirshfeld surface is defined as a set of points in 3D space where the ratio of promolecule and procrystal electron densities is equal to 0.5. The exploration of intermolecular contacts is provided by mapping normalized contact distances (d_{norm}), which is a function of a closest distance from the point to the nuclei interior (d_i) and exterior (d_e) to the surface as well as on the van der Waals radii (r^{vdw}). 2D fingerprint which were generated by deriving from the Hirshfeld surface by plotting the fraction of points on the surface as the function of d_i and d_e which provide a visual summary of intermolecular contacts within the crystal.

Electrostatic surface potential: Electrostatic surface potential map illustrate the charge distributions of molecules three dimensionally. These maps allow us to visualize variably charged regions of a molecule. Knowledge of the charge distributions can be used to determine how molecules interact with one another. Gaussian supports the cube keyword to generate the cubes separately from the formatted checkpoint file using the cubegen utility program. This allows for the generation of electrostatic surface potential mapping of the molecule.

Schrödinger materials science suite: Theoretical calculations of charge carrier mobility were performed on the crystal structures in Schrödinger Materials Science Suite 2015-1 using Jaguar DFT engine. The hopping model was used for the predictions of charge carrier mobility. Geometry optimization and single point energy calculations of monomer for neutral ground state and radical ions were performed at B3LYP/LACVP**+ level of theory. Same level of theory was used for cluster

calculations. Electron reorganization energy (λ_e) and hole reorganization energy (λ_h) were calculated using the adiabatic potential energy surfaces method. To compute charge carrier transfer rates, spherical nanoparticle clusters of 10 Å were built for 1-4AP using the Nanoparticle builder in Schrödinger Materials Science Suite. The packing was carefully visualized to select only the immediate neighbor of the chosen central molecule. Average charge carrier mobility rates were determined using Marcus theory, while ignoring the anisotropy effects.

Atomic force microscopy (AFM): AFM analyses were carried out on multimode scanning probe microscope (Veeco Nanoscope V, digital instruments). Samples for analyses were prepared by drop casting 1mM solutions of the samples (1-4AP) in benzene on a freshly cleaved mica surface and dried under air. To exclude any artefacts, blank experiments were performed with solvent alone evaporated on mica. Imaging was done under ambient conditions in tapping mode regime. Micro-fabricated antimony doped silicon cantilever (MPP-11100-10, resonance frequency- 279–379 KHz, spring constant- 20–80 Nm⁻¹) tip was used to probe the sample surface. The scan rates were varied from 0.5 Hz to 1.5 Hz and AFM section analyses were carried out offline. The average dimension of the self-assembly of 1-4AP were estimated from the Lorentzian fit of the histogram of the particle size distribution curves obtained after correcting for the tip-broadening effect.

Transmission electron microscopy (TEM): TEM measurements were carried out on FEI Tecnai 30 G2 high resolution transmission electron microscope and JEOL 2010 with an accelerating voltage of 100 kV. The samples were prepared by drop casting 1mM 1-4AP in benzene solution of on a 400 mesh carbon-coated copper grid (Ted Pella, Inc.) at ambient conditions and allowing the excess solvent to evaporate under air in dust free conditions. TEM images were obtained without staining. The average dimension of the self-assembly of 1-4AP were estimated from the Lorentzian fit of the histogram of the particle size distribution curves

Scanning electron microscopy (SEM): FE-SEM measurements of NIN was carried out on FEI Nova NanoSEM 450 (FEG type), drop casting 1 mM 1-4AP in benzene on silicon

wafer and allowing to evaporate the excess solvent under air in dust free conditions. The sample was further subjected to thin chromium sputtering using JEOL JFC-1100 fine coater to increase the signal/noise ratio. The probing side was inserted into JEOL JSM-5600 LV scanning electron microscope for obtaining the images. The average diameter of the particles was determined from the Lorentzian fit of the size distribution curve.

Confocal optical microscopy: Fluorescent microscopic images of the 1-4AP sample was obtained from inverted optical microscope (LeicaSP5-DMRX Optical Microscope) equipped with a wide range of objective lenses, the sample was excited under the illumination of UV light ($\lambda_{\text{ex}} = 405 \text{ nm}$, continuous laser, $\geq 10 \text{ mW}$, pulse width $< 100 \text{ ps}$) and the emission was monitored at 480 nm . The samples (1 mM AP in benzene) were drop casted on a freshly cleaned glass coverslip, and allowed to dry under air. The coverslip was sealed on a glass slide avoiding the air bubbles and kept undisturbed. Further, slides were imaged at 63X magnification in the presence of immersion oil.

Device Fabrication:

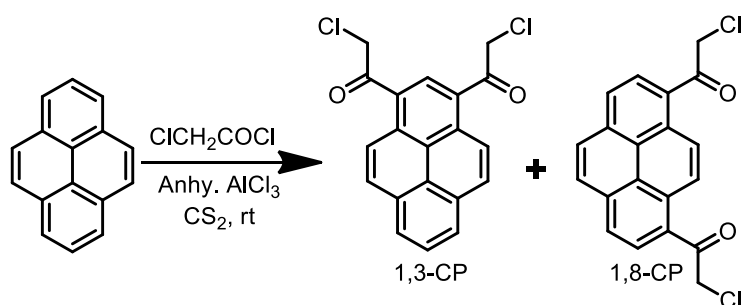
- a) **I-V measurement on drop-cased sample:** I-V measurements were carried out by drop-casting the solution of 1-4AP in benzene (1ml of 1mM solution) on a glass slide of dimension 1x1cm. Once the solution on the glass is dry, silver paint is put at the edge of the glass plate to connect the copper wire and the crystals.
- b) **I-V measurement on single crystal:** The crystals 1AP, 2AP and 2'AP are reasonably large about 3-4mm were selected and arranged on a glass substrate and conductive silver paint was used to put electrical contact on the crystal and the copper wire. The measurement setup included a voltage source which is supplied to the device under test. The current is measured through a preamplifier to Digital Multimeter.
- c) **FET measurement on single crystalline 4AP:** For field-effect mobility measurements, high-purity single crystals of 4AP were grown from solution. Single crystal FETs (SC-FETs) were fabricated using the top-contact, bottom-gate

geometry on highly doped p-type silicon wafers with 300 nm thick thermally grown silica as the gate dielectric material. Gold electrodes were thermally evaporated with a shadow mask for the channel. For surface functionalization, benzyl mercaptan was drop-casted before placing the crystal. It should be noted that the thiol was found to enhance the conduction of these SC-FETs by almost two orders of magnitude but by itself plays negligible role in the transfer characteristics. The 4AP crystals on average were 600 μm along *a*-axis and 15 μm along *b*-axis, giving the device W/L ratio of around 0.25.

Synthesis Details

The synthesis, purification and characterization of 1,3- and 1,8-Bis(acetyl)pyrenes (1,3-AP and 1,8-AP) were reported in Chapter 2 (Appendix 2.5).

Scheme 4.1. Synthesis of 1,3- and 1,8-Bis(chloroacetyl)pyrene (1,3-CP and 1,8-CP).



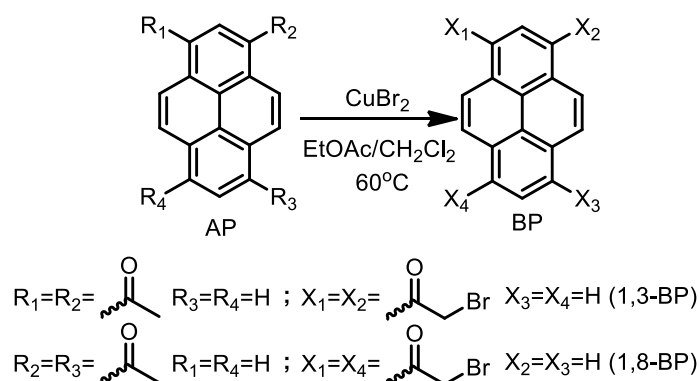
Synthesis of 1,3- and 1,8-Bis(chloroacetyl)pyrene (1,3-CP and 1,8-CP): Pyrene (1.0 g; 4.9 mmol) dissolved in CS_2 (yellow solution; 250 mL) was cooled to 0 °C (ice bath) and subsequently anhydrous AlCl_3 was added. Chloroacetyl chloride (2.49 g; 0.198 mols) was then syringed slowly to the suspension and the ice bath was removed. Hydrogen chloride was liberated upon warming to room temperature. After 3 h, the mixture was added slowly to a vigorously stirred mixture of ice and concentrated HCl . The resulting suspension was filtered and vacuum dried and further purified by column chromatography (chloroform:hexane 1:2) to give Bis(chloroacetyl)pyrene.

1,3-CP (yield= 32.8%) M.p. 143-146 °C. ^1H NMR [500 MHz, $\text{DMSO}(d_6)$, δ]: 9.09 (s, 1H), 8.69 (d, $J = 9.35$ Hz, 2H), 8.49 (d, $J = 8.05$ Hz, 2H), 8.46 (d, $J = 8.05$ Hz, 2H), 8.26 (m, 1H), 5.07 (s, 4H). ^{13}C NMR [125 MHz, $\text{DMSO}(d_6)$, δ]: 192.21, 131.54, 131.12, 130.15, 129.28,

128.73, 128.27, 127.78, 124.55, 124.31, 123.52, 32.04. IR (KBr, cm^{-1}) 3027.51, 2945.30, 1595.13, 1690.21, 850.61. Elemental analysis: calcd. value for $\text{C}_{20}\text{H}_{12}\text{Cl}_2\text{O}_2$: 67.63% C, 3.41% H; found: 67.98% C, 3.61% H. HRMS (EI) m/z calculated for $\text{C}_{20}\text{H}_{12}\text{Cl}_2\text{O}_2$ $[\text{M}]^+$: 354.0214, found: 354.0298.

1,8-CP (yield= 37.5%) M.p. 155-158 °C. ^1H NMR [500 MHz, DMSO (d_6), δ]: 8.65 (s, 2H) 8.54 (d, $J = 7.5$, 2H), , 8.32 (d, $J = 3$ Hz, 2H), 8.09 (s, 2H), 5.07 (s, 4H). ^{13}C NMR [125 MHz, DMSO (d_6), δ]: 197.82, 134.25, 130.63, 129.43, 129.36, 128.57, 127.54, 126.14, 125.14, 38.18. IR (KBr, cm^{-1}) 3057.54, 2965.31, 1587.13, 1692.51, 852.56. Elemental analysis: calcd. value for $\text{C}_{20}\text{H}_{12}\text{Cl}_2\text{O}_2$: 67.63% C, 3.41% H; found: 67.88% C, 3.48% H. HRMS (EI) m/z calculated for $\text{C}_{20}\text{H}_{12}\text{Cl}_2\text{O}_2$ $[\text{M}]^+$: 354.0214, found: 354.0292.

Scheme 4.2. Synthesis of 1,3- and 1,8-Bis(bromoacetyl)pyrene (1,3-BP and 1,8-BP).



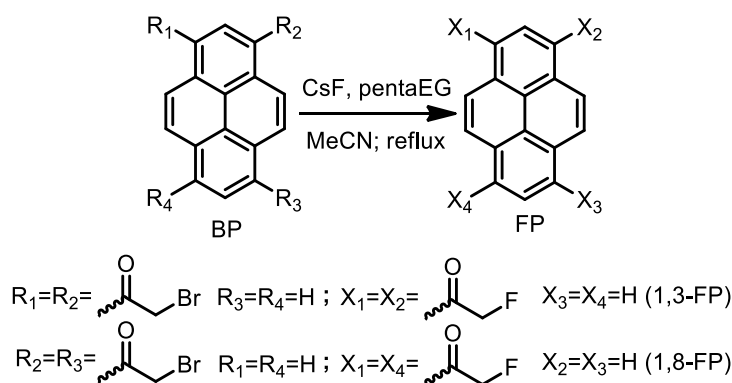
Synthesis of 1,3- and 1,8-Bis(bromoacetyl)pyrene (1,3-BP and 1,8-BP): A solution of acetylpyrene (AP) (1.0 g; 5 mmol) in EtOAc (20 mL) and CHCl_3 (20 mL) was heated to reflux with finely powdered CuBr_2 with vigorous stirring for 3.5 h. The yellow precipitate was filtered off, washed with CH_2Cl_2 , dried, and combined with the residue obtained from evaporation of the filtrate. This material was extracted with boiling benzene (5×125 mL), filtered and concentrated and further purified through column chromatography (1,3-BP, chloroform:hexane 1:2 and 1,8-BP chloroform:hexane 1:1).

1,3-BP (yield= 66%). M.p. 158-161 °C. ^1H NMR [500 MHz, DMSO(d_6), δ]: 9.16 (s, 1H), 8.79 (d, $J = 9.35$ Hz, 2H), 8.60 (d, $J = 8.05$ Hz, 2H), 8.59 (d, $J = 8.05$ Hz, 2H), 8.35 (m, 1H), 5.13 (s, 4H). ^{13}C NMR [125 MHz, DMSO(d_6), δ]: 195.19, 132.56, 132.12, 130.35, 128.88,

128.53, 128.07, 127.87, 124.95, 124.31, 123.42, 31.14. IR (KBr, cm^{-1}): 3095.75, 2920.23, 1664.57, 862.18. Elemental analysis: calcd. value for $\text{C}_{20}\text{H}_{12}\text{Br}_2\text{O}_2$: 54.08% C, 2.72% H; found: 54.32% C, 2.77% H. HRMS (EI) m/z calculated for $\text{C}_{20}\text{H}_{12}\text{Br}_2\text{O}_2$ $[\text{M}]^+$: 441.9204, found: 441.9230.

1,8-BP (yield= 83%). M.p. 193.5-195.0 °C. ^1H NMR [500 MHz, $\text{DMSO}(d_6)$, δ]: 8.76 (s, 2H), 8.64 (d, $J = 8.05$ Hz, 2H), 8.44 (d, $J = 8.05$ Hz, 2H), 8.33 (s, 2H), 5.14 (s, 4H). ^{13}C NMR [125 MHz, DMSO , δ]: 195.60, 134.07, 130.66, 129.99, 128.72, 128.18, 126.88, 126.43, 124.11, 37.46. IR (KBr, cm^{-1}): 3095.75, 2978.09, 1664.57, 1506.41, 860.25. Elemental analysis: calcd. value for $\text{C}_{20}\text{H}_{12}\text{Br}_2\text{O}_2$: 54.08% C, 2.72% H; found: 54.25% C, 2.88% H. HRMS (EI) m/z calculated for $\text{C}_{20}\text{H}_{12}\text{Br}_2\text{O}_2$ $[\text{M}]^+$: 441.9204, found: 441.9223.

Scheme 4.3. Synthesis of 1,3- and 1,8-Bis(fluoroacetyl)pyrene (1,3-FP and 1,8-FP).

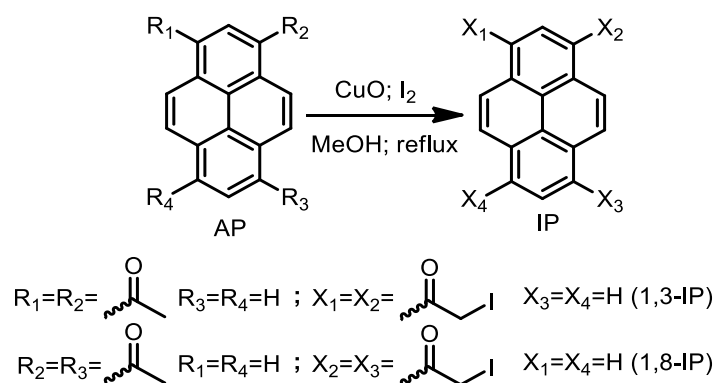


Synthesis of 1,3- and 1,8-Bis(fluoroacetyl)pyrene (1,3- and 1,8-FP): CsF (515.51 mg; 3.39 mmol) was added to a mixture of bromoacetylpyrene (BP) (250 mg; 0.57 mmol), pentaEG (119 mg; 0.5 mmol), and MeCN (4 mL) in a vial. The mixture was heated for 1.5 h at 100 °C. The reaction time was determined by checking TLC. The mixture was filtered and washed with Et_2O , and the filtrate was evaporated under reduced pressure. Column chromatography on silica gel (10% EtOAc /hexane) afforded 195 mg. 1,3-FP (yield= 7%). M.p. 133-135 °C. ^1H NMR [500 MHz, $\text{DMSO}(d_6)$, δ]: 9.10 (s, 1H), 8.78 (d, $J = 9.35$ Hz, 2H), 8.50 (d, $J = 8.05$ Hz, 2H), 8.45 (d, $J = 8.05$ Hz, 2H), 8.28 (m, 1H), 5.17 (s, 4H). ^{13}C NMR [125 MHz, $\text{DMSO}(d_6)$, δ]: 196.32, 133.34, 132.67, 132.01, 129.69, 128.43, 128.05, 127.78, 125.05, 124.45, 123.76, 31.45. IR (KBr, cm^{-1}): 3105.7, 2987.4, 1662.0, 956.6. Elemental analysis: calcd. value for $\text{C}_{20}\text{H}_{12}\text{F}_2\text{O}_2$: 74.53% C, 3.75% H; found:

74.65% C, 3.82% H. HRMS (EI) m/z calculated for $C_{20}H_{12}F_2O_2$ $[M]^+$: 322.0805, found: 322.0856.

1,8-FP (yield= 10%). M.p. 193.5-195.0 °C. 1H NMR [500 MHz, $DMSO(d_6)$, δ]: 8.57 (s, 2H), 8.55 (d, $J = 8.05$ Hz, 2H), 8.37 (d, $J = 8.05$ Hz, 2H), 8.28 (s, 2H), 5.24 (s, 4H). ^{13}C NMR [125 MHz, $DMSO$, δ]: 194.70, 133.98, 131.06, 129.57, 128.52, 128.08, 126.78, 126.33, 124.23, 36.86. IR (KBr, cm^{-1}): 3112.0, 2995.1, 1662.3, 966.2. Elemental analysis: calcd. value for $C_{20}H_{12}F_2O_2$: 74.53% C, 3.75% H; found: 74.72% C, 3.62% H. HRMS (EI) m/z calculated for $C_{20}H_{12}F_2O_2$ $[M]^+$: 322.0805, found: 322.0892.

Scheme 4.4. Synthesis of 1,3- and 1,8-Bis(iodoacetyl)pyrene (1,3- and 1,8-IP).



Synthesis of 1,3- and 1,8-Bis(iodoacetyl)pyrene (1,3- and 1,8-IP): Finely powdered CuO (0.40 g; 5.0 mmol) and I_2 (1.27 g; 5.0 mmol) were added to a well-stirred solution of the acetylpyrene (AP) (5.0 mmol) in anhyd. methanol (20 mL). The mixture was stirred for 5 min and then refluxed. After disappearance of the reactant (1–12 h, monitored by TLC), the mixture was filtered and the solvent was removed under reduced pressure. The residue was poured into 10% $Na_2S_2O_3$ solution (50 mL), the mixture was extracted with EtOAc (3×30 mL), and the organic layer was dried (Na_2SO_4). Removal of the solvent and purification of the residue by column chromatography yielded 1,3- (chloroform) and 1,8-IP (chloroform:hexane 1:1).

1,3-IP (yield= 65.0%) M.p. 178-181 °C. 1H NMR [500 MHz, $DMSO(d_6)$, δ]: 9.21 (s, 1H), 8.84 (d, $J = 9.35$ Hz, 2H), 8.65 (d, $J = 8.05$ Hz, 2H), 8.63 (d, $J = 8.05$ Hz, 2H), 8.39 (m, 1H), 5.15 (s, 4H). ^{13}C NMR [125 MHz, $DMSO(d_6)$, δ]: 196.11, 133.96, 132.86, 131.85, 129.29, 128.73, 128.01, 127.95, 125.01, 124.25, 123.65, 30.45. IR (KBr, cm^{-1}) 3039.33, 2977.61,

1650.58, 1251.32, 594.08. Elemental analysis: calcd. value for $C_{20}H_{12}I_2O_2$: 44.64% C, 2.25% H; found: 44.94% C, 2.52% H. HRMS (EI) m/z calculated for $C_{20}H_{12}I_2O_2$ $[M]^+$: 537.8927, found: 537.8979.

1,8-IP (yield= 37.5%) M.p. 155-158 °C. 1H NMR [500 MHz, $DMSO(d_6)$, δ]: 8.69 (s, 2H), 8.63 (d, $J = 9.35$ Hz, 2H), 8.42 (d, $J = 8.05$ Hz, 2H), 8.31 (s, 2H), 5.14 (s, 4H). ^{13}C NMR [125 MHz, $DMSO(d_6)$, δ]: 196.60, 134.11, 130.95, 129.67, 128.57, 128.09, 126.79, 126.60, 125.01, 37.59. IR (KBr, cm^{-1}) 31341.3, 2898.6, 1668.6, 1240.9, 591.9. Elemental analysis: calcd. value for $C_{20}H_{12}I_2O_2$: 44.64% C, 2.25% H; found: 44.89% C, 2.62% H. HRMS (EI) m/z calculated for $C_{20}H_{12}I_2O_2$ $[M]^+$: 537.8927, found: 537.8990

Bibliography

- [1] Laurent, A. Note sur l'État Actuel de la Chimique Organique. *Ann. Chim. Phys.* **66**, 136 (1837).
- [2] Graebe, C. Ueber Pyren. *Justus Liebigs Ann. Chem.* **158**, 285-299 (1871).
- [3] Bamberger, E. G.; Philip, M. Untersuchungen über hochmolekulare Kohlenwasserstoffe; Ueber das Pyren. *Justus Liebigs Ann. Chem.* **240**, 147-192 (1887).
- [4] Zou, L.; Wang, X.-Y.; Shi, K.; Wang, J.-Y.; Pei, J. Fusion at the Non-K-Region of Pyrene: An Alternative Strategy To Extend the π -Conjugated Plane of Pyrene. *Org. Lett.* **15**, 4378-4381 (2013).
- [5] Figueira-Duarte, T. M.; Müllen, K. Pyrene-Based Materials for Organic Electronics. *Chem. Rev.* **111**, 7260-7314 (2011).
- [6] Birks, J. B.; Dyson, D. J.; Munro, I. H. 'Excimer' Fluorescence. II. Lifetime Studies of Pyrene Solutions. *Proc. Roy. Soc. Lond. A Math Phys. Sci.* **275**, 575-588 (1963).
- [7] Bohne, C.; Abuin, E. B.; Scaiano, J. C. Characterization of the triplet-triplet annihilation process of pyrene and several derivatives under laser excitation. *J. Am. Chem. Soc.* **112**, 4226-4231 (1990).
- [8] Hauke, F.; Hirsch, A.; Atalick, S.; Guldi, D. Quantitative Transduction of Excited-State Energy in Fluorophore-Heterofullerene Conjugates. *Eur. J. Org. Chem.* **2005**, 1741-1751 (2005).
- [9] Duhamel, J. Polymer Chain Dynamics in Solution Probed with a Fluorescence Blob Model. *Acc. Chem. Res.* **39**, 953-960 (2006).
- [10] Mathew, A. K.; Siu, H.; Duhamel, J. A Blob Model To Study Chain Folding by Fluorescence. *Macromolecules* **32**, 7100-7108 (1999).
- [11] Jackson, G. S.; Staniforth, R. A.; Halsall, D. J.; Atkinson, T.; Holbrook, J. J.; Clarke, A. R.; Burston, S. G. Binding and hydrolysis of nucleotides in the chaperonin catalytic cycle: Implications for the mechanism of assisted protein folding. *Biochemistry* **32**, 2554-2563 (1993).
- [12] Jung, K.; Jung, H.; Wu, J.; Prive, G. G.; Kaback, H. R. Use of site-directed fluorescence labeling to study proximity relationships in the lactose permease of *Escherichia coli*. *Biochemistry* **32**, 12273-12278 (1993).
- [13] Vollmann, H.; Becker, H.; Corell, M.; Streeck, H. Beiträge zur Kenntnis des Pyrens und Seiner Derivate. *Justus Liebigs Ann. Chem.* **531**, 1-159 (1937).
- [14] Winnik, F. M. Photophysics of preassociated pyrenes in aqueous polymer solutions and in other organized media. *Chem. Rev.* **93**, 587-614 (1993).
- [15] V. I. Vullev, H. J., G. Jones. Topics in Fluorescence Spectroscopy. *Springer*, (2005).
- [16] Forster, T. K., K. Z. *Elektrochem.* **59**, 976 (1955).

- [17] Birks, J. B. *Photophysics of Aromatic Molecules*; Wiley-Interscience: London. (1970).
- [18] Kalyanasundaram, K.; Thomas, J. K. Environmental effects on vibronic band intensities in pyrene monomer fluorescence and their application in studies of micellar systems. *J. Am. Chem. Soc.* **99**, 2039-2044 (1977).
- [19] Baba, M.; Saitoh, M.; Kowaka, Y.; Taguma, K.; Yoshida, K.; Semba, Y.; Kasahara, S.; Yamanaka, T.; Ohshima, Y.; Hsu, Y.-C.; Lin, S. H. Vibrational and rotational structure and excited-state dynamics of pyrene. *J. Chem. Phys.* **131**, 224318 (2009).
- [20] Numata, Y.; Suzuki, Y.; Suzuka, I. Anomalous fluorescence from the second excited singlet state upon excitation to the S₄ state of pyrene in a supersonic jet. *J. Photochem. Photobiol., A* **237**, 49-52 (2012).
- [21] Karpovich, D. S.; Blanchard, G. J. Relating the polarity-dependent fluorescence response of pyrene to vibronic coupling. Achieving a fundamental understanding of the py polarity scale. *J. Phys. Chem.* **99**, 3951-3958 (1995).
- [22] Neuwahl, F. V. R.; Foggi, P. Direct Observation of S₂-S₁ Internal Conversion in Pyrene by Femtosecond Transient Absorption. *Laser Chem.* **19**, 375-379 (1999).
- [23] Varghese, S.; Das, S. Role of Molecular Packing in Determining Solid-State Optical Properties of π -Conjugated Materials. *J. Phys. Chem. Lett.* **2**, 863-873 (2011).
- [24] Yan, D.; Evans, D. G. Molecular crystalline materials with tunable luminescent properties: from polymorphs to multi-component solids. *Mater. Horiz.* **1**, 46-57 (2014).
- [25] Wang, C.; Chen, D.; Chen, W.; Chen, S.; Ye, K.; Zhang, H.; Zhang, J.; Wang, Y. Polymorph, assembly, luminescence and semiconductor properties of a quinacridone derivative with extended [small pi]-conjugated framework. *J. Mater. Chem. C* **1**, 5548-5556 (2013).
- [26] Shen, X. Y.; Wang, Y. J.; Zhao, E.; Yuan, W. Z.; Liu, Y.; Lu, P.; Qin, A.; Ma, Y.; Sun, J. Z.; Tang, B. Z. Effects of Substitution with Donor-Acceptor Groups on the Properties of Tetraphenylethene Trimer: Aggregation-Induced Emission, Solvatochromism, and Mechanochromism. *J. Phys. Chem. C* **117**, 7334-7347 (2013).
- [27] Desiraju, G. R.; Gavezzotti, A. Crystal structures of polynuclear aromatic hydrocarbons. Classification, rationalization and prediction from molecular structure. *Acta Cryst. B* **45**, 473-482 (1989).
- [28] Desiraju, G. R.; Gavezzotti, A. From molecular to crystal structure; polynuclear aromatic hydrocarbons. *J. Chem. Soc., Chem. Commun.*, 621-623 (1989).
- [29] Desiraju, G. R. Designing organic crystals. *Prog. Solid State Chem.* **17**, 295-353 (1987).
- [30] Loots, L.; Barbour, L. J. A simple and robust method for the identification of [small pi]-[small pi] packing motifs of aromatic compounds. *CrystEngComm* **14**, 300-304 (2012).
- [31] Davis, R.; Saleesh Kumar, N. S.; Abraham, S.; Suresh, C. H.; Rath, N. P.; Tamaoki, N.; Das, S. Molecular Packing and Solid-State Fluorescence of Alkoxy-Cyano Substituted

- Diphenylbutadienes: Structure of the Luminescent Aggregates. *J. Phys. Chem. C* **112**, 2137-2146 (2008).
- [32] W. C. McCrone. *Physics and Chemistry of the Organic Solid State*, ed. D. Fox, M. M. Labes and A. Weissberger, Wiley Interscience, New York, USA. 725-767 (1965).
- [33] Gavezzotti, A. Are Crystal Structures Predictable? *Acc. Chem. Res.* **27**, 309-314 (1994).
- [34] Brittain, H. G. *Polymorphism in Pharmaceutical Solids*, ed. Marcel Dekker, Inc., New York, (1999).
- [35] Bernstein, J. *Polymorphism in Molecular Crystals*. Oxford Univ. Press, New York, (2002).
- [36] Kitamura, C.; Ohara, T.; Kawatsuki, N.; Yoneda, A.; Kobayashi, T.; Naito, H.; Komatsu, T.; Kitamura, T. Conformational polymorphism and optical properties in the solid state of 1,4,7,10-tetra(n-butyl)tetracene. *CrystEngComm* **9**, 644-647 (2007).
- [37] Hisaki, I.; Kometani, E.; Shigemitsu, H.; Saeki, A.; Seki, S.; Tohnai, N.; Miyata, M. Polymorphism of Dehydrobenzo[14]annulene Possessing Two Methyl Ester Groups in Noncentrosymmetric Positions. *Cryst. Growth Des.* **11**, 5488-5497 (2011).
- [38] Zhang, H. Y.; Zhang, Z. L.; Ye, K. Q.; Zhang, J. Y.; Wang, Y. Organic Crystals with Tunable Emission Colors Based on a Single Organic Molecule and Different Molecular Packing Structures. *Adv. Mater.* **18**, 2369-2372 (2006).
- [39] Zhang, Z.; Zhang, Y.; Yao, D.; Bi, H.; Javed, I.; Fan, Y.; Zhang, H.; Wang, Y. Anthracene-Arrangement-Dependent Emissions of Crystals of 9-Anthrylpyrazole Derivatives. *Cryst. Growth Des.* **9**, 5069-5076 (2009).
- [40] Hsieh, C.-C.; Jiang, C.-M.; Chou, P.-T. Recent Experimental Advances on Excited-State Intramolecular Proton Coupled Electron Transfer Reaction. *Acc. Chem. Res.* **43**, 1364-1374 (2010).
- [41] Mutai, T.; Tomoda, H.; Ohkawa, T.; Yabe, Y.; Araki, K. Switching of Polymorph-Dependent ESIPT Luminescence of an Imidazo[1,2-a]pyridine Derivative. *Angew. Chem. Int. Ed.* **47**, 9522-9524 (2008).
- [42] Anthony, S. P. Polymorph-Dependent Solid-State Fluorescence and Selective Metal-Ion-Sensor Properties of 2-(2-Hydroxyphenyl)-4(3H)-quinazolinone. *Chem. Asian J.* **7**, 374-379 (2012).
- [43] Roberts, D. R. T.; Holder, S. J. Mechanochromic systems for the detection of stress, strain and deformation in polymeric materials. *J. Mater. Chem.* **21**, 8256-8268 (2011).
- [44] Zhao, Y.; Gao, H.; Fan, Y.; Zhou, T.; Su, Z.; Liu, Y.; Wang, Y. Thermally Induced Reversible Phase Transformations Accompanied by Emission Switching Between Different Colors of Two Aromatic-Amine Compounds. *Adv. Mater.* **21**, 3165-3169 (2009).
- [45] Sagara, Y.; Kato, T. Mechanically induced luminescence changes in molecular assemblies. *Nat Chem* **1**, 605-610 (2009).

- [46] Abe, Y.; Karasawa, S.; Koga, N. Crystal Structures and Emitting Properties of Trifluoromethylaminoquinoline Derivatives: Thermal Single-Crystal-to-Single-Crystal Transformation of Polymorphic Crystals That Emit Different Colors. *Chem. Eur. J.* **18**, 15038-15048 (2012).
- [47] Zhao, C.-H.; Wakamiya, A.; Inukai, Y.; Yamaguchi, S. Highly Emissive Organic Solids Containing 2,5-Diboryl-1,4-phenylene Unit. *J. Am. Chem. Soc.* **128**, 15934-15935 (2006).
- [48] Takahashi, E.; Takaya, H.; Naota, T. Dynamic Vapochromic Behaviors of Organic Crystals Based on the Open–Close Motions of S-Shaped Donor–Acceptor Folding Units. *Chem. Eur. J.* **16**, 4793-4802 (2010).
- [49] Davis, R.; Rath, N. P.; Das, S. Thermally reversible fluorescent polymorphs of alkoxy-cyano-substituted diphenylbutadienes: role of crystal packing in solid state fluorescence. *Chem. Commun.*, 74-75 (2004).
- [50] Luo, X.; Li, J.; Li, C.; Heng, L.; Dong, Y. Q.; Liu, Z.; Bo, Z.; Tang, B. Z. Reversible Switching of the Emission of Diphenyldibenzofulvenes by Thermal and Mechanical Stimuli. *Adv. Mater.* **23**, 3261-3265 (2011).
- [51] Yoon, S.-J.; Park, S. Polymorphic and mechanochromic luminescence modulation in the highly emissive dicyanodistyrylbenzene crystal: secondary bonding interaction in molecular stacking assembly. *J. Mater. Chem.* **21**, 8338-8346 (2011).
- [52] Dou, C.; Chen, D.; Iqbal, J.; Yuan, Y.; Zhang, H.; Wang, Y. Multistimuli-Responsive Benzothiadiazole-Cored Phenylene Vinylene Derivative with Nanoassembly Properties. *Langmuir* **27**, 6323-6329 (2011).
- [53] Chung, J. W.; You, Y.; Huh, H. S.; An, B.-K.; Yoon, S.-J.; Kim, S. H.; Lee, S. W.; Park, S. Y. Shear- and UV-Induced Fluorescence Switching in Stilbenic π -Dimer Crystals Powered by Reversible [2 + 2] Cycloaddition. *J. Am. Chem. Soc.* **131**, 8163-8172 (2009).
- [54] Yoon, S.-J.; Chung, J. W.; Gierschner, J.; Kim, K. S.; Choi, M.-G.; Kim, D.; Park, S. Y. Multistimuli Two-Color Luminescence Switching via Different Slip-Stacking of Highly Fluorescent Molecular Sheets. *J. Am. Chem. Soc.* **132**, 13675-13683 (2010).
- [55] Parrott, E. L. *Encyclopedia of Pharmaceutical Technology*, ed. J. Swarbrick and J. C. Boylan, Marcel Dekker, New York. 101-121 (1990).
- [56] Boldyreva, E. Mechanochemistry of inorganic and organic systems: what is similar, what is different? *Chem. Soc. Rev.* **42**, 7719-7738 (2013).
- [57] Crowley, K. J.; Zografi, G. Cryogenic grinding of indomethacin polymorphs and solvates: Assessment of amorphous phase formation and amorphous phase physical stability. *J. Pharm. Sci.* **91**, 492-507 (2002).
- [58] Sheth, A. R.; Lubach, J. W.; Munson, E. J.; Muller, F. X.; Grant, D. J. W. Mechanochromism of Piroxicam Accompanied by Intermolecular Proton Transfer

- Probed by Spectroscopic Methods and Solid-Phase Changes. *J. Am. Chem. Soc.* **127**, 6641-6651 (2005).
- [59] Zhao, N.; Li, M.; Yan, Y.; Lam, J. W. Y.; Zhang, Y. L.; Zhao, Y. S.; Wong, K. S.; Tang, B. Z. A tetraphenylethene-substituted pyridinium salt with multiple functionalities: synthesis, stimuli-responsive emission, optical waveguide and specific mitochondrion imaging. *J. Mater. Chem. C* **1**, 4640-4646 (2013).
- [60] Zhao, N.; Yang, Z.; Lam, J. W. Y.; Sung, H. H. Y.; Xie, N.; Chen, S.; Su, H.; Gao, M.; Williams, I. D.; Wong, K. S.; Tang, B. Z. Benzothiazolium-functionalized tetraphenylethene: an AIE luminogen with tunable solid-state emission. *Chem. Commun.* **48**, 8637-8639 (2012).
- [61] Gong, Y.; Tan, Y.; Liu, J.; Lu, P.; Feng, C.; Yuan, W. Z.; Lu, Y.; Sun, J. Z.; He, G.; Zhang, Y. Twisted D- π -A solid emitters: efficient emission and high contrast mechanochromism. *Chem. Commun.* **49**, 4009-4011 (2013).
- [62] Wuest, J. D. Molecular solids: Co-crystals give light a tune-up. *Nat Chem* **4**, 74-75 (2012).
- [63] Yan, D.; Patel, B.; Delori, A.; Jones, W.; Duan, X. The Formation of Hydrogen-Bond Facilitated Salts with Tunable Optical Properties: An Experimental and Theoretical Study of 2,4,5-Triphenylimidazole. *Cryst. Growth Des.* **13**, 333-340 (2013).
- [64] Yan, D.; Delori, A.; Lloyd, G. O.; Frišćić, T.; Day, G. M.; Jones, W.; Lu, J.; Wei, M.; Evans, D. G.; Duan, X. A Cocrystal Strategy to Tune the Luminescent Properties of Stilbene-Type Organic Solid-State Materials. *Angew. Chem. Int. Ed.* **50**, 12483-12486 (2011).
- [65] Anthony, S. P.; Varughese, S.; Draper, S. M. Switching and tuning organic solid-state luminescence via a supramolecular approach. *Chem. Commun.*, 7500-7502 (2009).
- [66] Kasha, M. Energy Transfer Mechanisms and the Molecular Exciton Model for Molecular Aggregates. *Radiat. Res.* **20**, 55-70 (1963).
- [67] Shimizu, M.; Hiyama, T. Organic Fluorophores Exhibiting Highly Efficient Photoluminescence in the Solid State. *Chem. Asian J.* **5**, 1516-1531 (2010).
- [68] Curtis, M. D.; Cao, J.; Kampf, J. W. Solid-State Packing of Conjugated Oligomers: From π -Stacks to the Herringbone Structure. *J. Am. Chem. Soc.* **126**, 4318-4328 (2004).
- [69] Ji, L.; Edkins, R. M.; Lorbach, A.; Krummenacher, I.; Brückner, C.; Eichhorn, A.; Braunschweig, H.; Engels, B.; Low, P. J.; Marder, T. B. Electron Delocalization in Reduced Forms of 2-(BMes₂)pyrene and 2,7-Bis(BMes₂)pyrene. *J. Am. Chem. Soc.* **137**, 6750-6753 (2015).
- [70] Brumfield, B. E.; Stewart, J. T.; McCall, B. J. Extending the Limits of Rotationally Resolved Absorption Spectroscopy: Pyrene. *J. Phys. Chem. Lett.* **3**, 1985-1988 (2012).
- [71] Niko, Y.; Sasaki, S.; Narushima, K.; Sharma, D. K.; Vacha, M.; Konishi, G.-i. 1-, 3-, 6-, and 8-Tetrasubstituted Asymmetric Pyrene Derivatives with Electron Donors and

- Acceptors: High Photostability and Regioisomer-Specific Photophysical Properties. *J. Org. Chem.* **80**, 10794-10805 (2015).
- [72] Zöphel, L.; Enkelmann, V.; Müllen, K. Tuning the HOMO–LUMO Gap of Pyrene Effectively via Donor–Acceptor Substitution: Positions 4,5 Versus 9,10. *Org. Lett.* **15**, 804-807 (2013).
- [73] Uchimura, M.; Watanabe, Y.; Araoka, F.; Watanabe, J.; Takezoe, H.; Konishi, G.-i. Development of Laser Dyes to Realize Low Threshold in Dye-Doped Cholesteric Liquid Crystal Lasers. *Adv. Mater.* **22**, 4473-4478 (2010).
- [74] Xu, Z.; Singh, N. J.; Lim, J.; Pan, J.; Kim, H. N.; Park, S.; Kim, K. S.; Yoon, J. Unique Sandwich Stacking of Pyrene-Adenine-Pyrene for Selective and Ratiometric Fluorescent Sensing of ATP at Physiological pH. *J. Am. Chem. Soc.* **131**, 15528-15533 (2009).
- [75] Conlon, P.; Yang, C. J.; Wu, Y.; Chen, Y.; Martinez, K.; Kim, Y.; Stevens, N.; Marti, A. A.; Jockusch, S.; Turro, N. J.; Tan, W. Pyrene Excimer Signaling Molecular Beacons for Probing Nucleic Acids. *J. Am. Chem. Soc.* **130**, 336-342 (2008).
- [76] Locritani, M.; Yu, Y.; Bergamini, G.; Baroncini, M.; Molloy, J. K.; Korgel, B. A.; Ceroni, P. Silicon Nanocrystals Functionalized with Pyrene Units: Efficient Light-Harvesting Antennae with Bright Near-Infrared Emission. *J. Phys. Chem. Lett.* **5**, 3325-3329 (2014).
- [77] van Ramesdonk, H. J.; Bakker, B. H.; Groeneveld, M. M.; Verhoeven, J. W.; Allen, B. D.; Rostron, J. P.; Harriman, A. Ultrafast Intersystem Crossing in 9,10-Anthraquinones and Intramolecular Charge Separation in an Anthraquinone-Based Dyad. *J. Phys. Chem. A* **110**, 13145-13150 (2006).
- [78] Kusumoto, T.; Kosumi, D.; Uragami, C.; Frank, H. A.; Birge, R. R.; Cogdell, R. J.; Hashimoto, H. Femtosecond Transient Absorption Spectroscopic Study of a Carbonyl-Containing Carotenoid Analogue, 2-(all-trans-Retinylidene)-indan-1,3-dione. *J. Phys. Chem. A* **115**, 2110-2119 (2011).
- [79] Rubtsov, I. V.; Kang, Y. K.; Redmore, N. P.; Allen, R. M.; Zheng, J.; Beratan, D. N.; Therien, M. J. The Degree of Charge Transfer in Ground and Charge-Separated States Revealed by Ultrafast Visible Pump/Mid-IR Probe Spectroscopy. *J. Am. Chem. Soc.* **126**, 5022-5023 (2004).
- [80] Vogt, R. A.; Peay, M. A.; Gray, T. G.; Crespo-Hernández, C. E. Excited-State Dynamics of (Organophosphine)gold(I) Pyrenyl Isomers. *J. Phys. Chem. Lett.* **1**, 1205-1211 (2010).
- [81] Plaza-Medina, E. F.; Rodríguez-Córdoba, W.; Peon, J. Role of Upper Triplet States on the Photophysics of Nitrated Polyaromatic Compounds: S1 Lifetimes of Singly Nitrated Pyrenes. *J. Phys. Chem. A* **115**, 9782-9789 (2011).
- [82] Niko, Y.; Hiroshige, Y.; Kawauchi, S.; Konishi, G. Additional Insights into Luminescence Process of Polycyclic Aromatic Hydrocarbons with Carbonyl Groups: Photophysical Properties of Secondary N-Alkyl and Tertiary N,N-Dialkyl Carboxamides of Naphthalene, Anthracene, and Pyrene. *J. Org. Chem.* **77**, 3986-3996 (2012).

- [83] Niko, Y.; Hiroshige, Y.; Kawauchi, S.; Konishi, G.-i. Additional Insights into Luminescence Process of Polycyclic Aromatic Hydrocarbons with Carbonyl Groups: Photophysical Properties of Secondary N-Alkyl and Tertiary N,N-Dialkyl Carboxamides of Naphthalene, Anthracene, and Pyrene. *J. Org. Chem.* **77**, 3986-3996 (2012).
- [84] Niko, Y.; Hiroshige, Y.; Kawauchi, S.; Konishi, G.-i. Fundamental photoluminescence properties of pyrene carbonyl compounds through absolute fluorescence quantum yield measurement and density functional theory. *Tetrahedron* **68**, 6177-6185 (2012).
- [85] Rajagopal, S. K.; Philip, A. M.; Nagarajan, K.; Hariharan, M. Progressive acylation of pyrene engineers solid state packing and colour via C-H[three dots, centered]H-C, C-H[three dots, centered]O and [small pi]-[small pi] interactions. *Chem. Commun.* **50**, 8644-8647 (2014).
- [86] Lai, R. Y.; Fleming, J. J.; Merner, B. L.; Vermeij, R. J.; Bodwell, G. J.; Bard, A. J. Electrogenenerated Chemiluminescence. 74. Photophysical, Electrochemical, and Electrogenenerated Chemiluminescent Studies of Selected Nonplanar Pyrenophanes. *J. Phys. Chem. A* **108**, 376-383 (2004).
- [87] Lee, C.; Yang, W.; Parr, R. G. Development of the Colle-Salvetti correlation-energy formula into a functional of the electron density. *Phys. Rev. B* **37**, 785-789 (1988).
- [88] Becke, A. D. Density-functional thermochemistry. III. The role of exact exchange. *J. Chem. Phys.* **98**, 5648-5652 (1993).
- [89] Katoh, R.; Suzuki, K.; Furube, A.; Kotani, M.; Tokumaru, K. Fluorescence Quantum Yield of Aromatic Hydrocarbon Crystals. *J. Phys. Chem. C* **113**, 2961-2965 (2009).
- [90] Thomas, J. K.; Richards, J. T.; West, G. Formation of ions and excited states in the laser photolysis of solutions of pyrene. *J. Phys. Chem.* **74**, 4137-4141 (1970).
- [91] Kumar, C. V.; Qin, L.; Das, P. K. Aromatic thioketone triplets and their quenching behaviour towards oxygen and di-t-butyl nitroxy radical. A laser-flash-photolysis study. *J. Chem. Soc., Faraday Trans. 2* **80**, 783-793 (1984).
- [92] Medinger, T.; Wilkinson, F. Concentration dependence of quantum yield of triplet-state production of pyrene in ethanol. *J. Chem. Soc. Faraday Trans.* **62**, 1785-1792 (1966).
- [93] Hollingsworth, M. D. Crystal Engineering: from Structure to Function. *Science* **295**, 2410-2413 (2002).
- [94] Servaites, J. D.; Savoie, B. M.; Brink, J. B.; Marks, T. J.; Ratner, M. A. Modeling geminate pair dissociation in organic solar cells: high power conversion efficiencies achieved with moderate optical bandgaps. *Energy Environ. Sci.* **5**, 8343-8350 (2012).
- [95] Raffy, G.; Ray, D.; Chu, C.-C.; Del Guerzo, A.; Bassani, D. M. Controlling the Emission Polarization from Single Crystals Using Light: Towards Photopolic Materials. *Angew. Chem. Int. Ed.* **50**, 9584-9588 (2011).
- [96] Kahr, B.; Freudenthal, J.; Gunn, E. Crystals in Light†. *Acc. Chem. Res.* **43**, 684-692 (2010).

- [97] Lipomi, D. J.; Bao, Z. Stretchable, elastic materials and devices for solar energy conversion. *Energy Environ. Sci.* **4**, 3314-3328 (2011).
- [98] Varughese, S. Non-covalent routes to tune the optical properties of molecular materials. *J. Mater. Chem. C* **2**, 3499-3516 (2014).
- [99] Anthony, J. E. Functionalized Acenes and Heteroacenes for Organic Electronics. *Chem. Rev.* **106**, 5028-5048 (2006).
- [100] Kawai, T.; Nakashima, Y.; Irie, M. A Novel Photoresponsive π -Conjugated Polymer Based on Diarylethene and its Photoswitching Effect in Electrical Conductivity. *Adv. Mater.* **17**, 309-314 (2005).
- [101] Kippelen, B.; Bredas, J.-L. Organic photovoltaics. *Energy Environ. Sci.* **2**, 251-261 (2009).
- [102] Hutchison, G. R.; Ratner, M. A.; Marks, T. J. Intermolecular Charge Transfer between Heterocyclic Oligomers. Effects of Heteroatom and Molecular Packing on Hopping Transport in Organic Semiconductors. *J. Am. Chem. Soc.* **127**, 16866-16881 (2005).
- [103] Moon, H.; Zeis, R.; Borkent, E.-J.; Besnard, C.; Lovinger, A. J.; Siegrist, T.; Kloc, C.; Bao, Z. Synthesis, Crystal Structure, and Transistor Performance of Tetracene Derivatives. *J. Am. Chem. Soc.* **126**, 15322-15323 (2004).
- [104] Anthony, J. E.; Brooks, J. S.; Eaton, D. L.; Parkin, S. R. Functionalized Pentacene: Improved Electronic Properties from Control of Solid-State Order. *J. Am. Chem. Soc.* **123**, 9482-9483 (2001).
- [105] Feng, Q.; Wang, M.; Dong, B.; Xu, C.; Zhao, J.; Zhang, H. Tuning solid-state fluorescence of pyrene derivatives via a cocrystal strategy. *CrystEngComm* **15**, 3623-3629 (2013).
- [106] Chang, Y.-C.; Chen, Y.-D.; Chen, C.-H.; Wen, Y.-S.; Lin, J. T.; Chen, H.-Y.; Kuo, M.-Y.; Chao, I. Crystal Engineering for π - π Stacking via Interaction between Electron-Rich and Electron-Deficient Heteroaromatics. *J. Org. Chem.* **73**, 4608-4614 (2008).
- [107] Feng, Q.; Wang, M.; Dong, B.; He, J.; Xu, C. Regulation of Arrangements of Pyrene Fluorophores via Solvates and Cocrystals for Fluorescence Modulation. *Cryst. Growth Des.* **13**, 4418-4427 (2013).
- [108] Mutai, T.; Satou, H.; Araki, K. Reproducible on-off switching of solid-state luminescence by controlling molecular packing through heat-mode interconversion. *Nat. Mater.* **4**, 685-687 (2005).
- [109] Nagura, K.; Saito, S.; Yusa, H.; Yamawaki, H.; Fujihisa, H.; Sato, H.; Shimoikeda, Y.; Yamaguchi, S. Distinct Responses to Mechanical Grinding and Hydrostatic Pressure in Luminescent Chromism of Tetrathiazolylthiophene. *J. Am. Chem. Soc.* **135**, 10322-10325 (2013).

- [110] Sun, X.; Zhang, X.; Li, X.; Liu, S.; Zhang, G. A mechanistic investigation of mechanochromic luminescent organoboron materials. *J. Mater. Chem.* **22**, 17332-17339 (2012).
- [111] Ito, H.; Muromoto, M.; Kurenuma, S.; Ishizaka, S.; Kitamura, N.; Sato, H.; Seki, T. Mechanical stimulation and solid seeding trigger single-crystal-to-single-crystal molecular domino transformations. *Nat. Commun.* **4**, (2013).
- [112] Lakowicz, J. R., *Principles of Fluorescence Spectroscopy*. In 3rd ed. Springer: New York, 2006.
- [113] Cheriya, R. T.; Nagarajan, K.; Hariharan, M. Single-Component Organic Light-Harvesting Red Luminescent Crystal. *J. Phys. Chem. C* **117**, 3240-3248 (2013).
- [114] Cheriya, R. T.; Joy, J.; Alex, A. P.; Shaji, A.; Hariharan, M. Energy Transfer in Near-Orthogonally Arranged Chromophores Separated through a Single Bond. *J. Phys. Chem. C* **116**, 12489-12498 (2012).
- [115] Cheriya, R. T.; Mallia, A. R.; Hariharan, M. Light harvesting vesicular donor-acceptor scaffold limits the rate of charge recombination in the presence of an electron donor. *Energy Environ. Sci.* **7**, 1661-1669 (2014).
- [116] Friedel, C.; Crafts, J. M. Organic chemistry. *J. Chem. Soc.* **32**, 725-791 (1877).
- [117] Lewis, F. D.; Yang, J.-S. Solid-State Fluorescence of Aromatic Dicarboxamides. Dependence upon Crystal Packing. *The Journal of Physical Chemistry B* **101**, 1775-1781 (1997).
- [118] Hassheider, T.; Benning, S. A.; Kitzerow, H.-S.; Achard, M.-F.; Bock, H. Color-Tuned Electroluminescence from Columnar Liquid Crystalline Alkyl Arenecarboxylates. *Angew. Chem. Int. Ed.* **40**, 2060-2063 (2001).
- [119] Hayer, A.; de Halleux, V.; Kölher, A.; El-Garouhy, A.; Meijer, E. W.; Barbera, J.; Tant, J.; Lein, J.; Lehmann, M.; Gierschner, J.; Cornil, J.; Geerts, Y. H. *J. Am. Chem. Soc.* **110**, 7653 (2006).
- [120] Desiraju, G. R. The C-H...O Hydrogen Bond: Structural Implications and Supramolecular Design. *Acc. Chem. Res.* **29**, 441-449 (1996).
- [121] Paliwal, S.; Geib, S.; Wilcox, C. S. Molecular Torsion Balance for Weak Molecular Recognition Forces. Effects of "Tilted-T" Edge-to-Face Aromatic Interactions on Conformational Selection and Solid-State Structure. *J. Am. Chem. Soc.* **116**, 4497-4498 (1994).
- [122] Echeverría, J.; Aullón, G.; Danovich, D.; Shaik, S.; Alvarez, S. Dihydrogen contacts in alkanes are subtle but not faint. *Nat Chem* **3**, 323-330 (2011).
- [123] Anslyn, E. V.; Dougherty, D. A., *Modern Physical Organic Chemistry*. University Science Books: Sausalito, CA, 2006.

- [124] Chercka, D.; Yoo, S.-J.; Baumgarten, M.; Kim, J.-J.; Mullen, K. Pyrene based materials for exceptionally deep blue OLEDs. *J. Mater. Chem. C* **2**, 9083-9086 (2014).
- [125] Figueira-Duarte, T. M.; Del Rosso, P. G.; Trattnig, R.; Sax, S.; List, E. J. W.; Müllen, K. Designed Suppression of Aggregation in Polypyrene: Toward High-Performance Blue-Light-Emitting Diodes. *Adv. Mater.* **22**, 990-993 (2010).
- [126] Feng, X.; Hu, J.-Y.; Iwanaga, F.; Seto, N.; Redshaw, C.; Elsegood, M. R. J.; Yamato, T. Blue-Emitting Butterfly-Shaped 1,3,5,9-Tetraarylpyrenes: Synthesis, Crystal Structures, and Photophysical Properties. *Org. Lett.* **15**, 1318-1321 (2013).
- [127] Moorthy, J. N.; Natarajan, P.; Venkatakrisnan, P.; Huang, D.-F.; Chow, T. J. Steric Inhibition of π -Stacking: 1,3,6,8-Tetraarylpyrenes as Efficient Blue Emitters in Organic Light Emitting Diodes (OLEDs). *Org. Lett.* **9**, 5215-5218 (2007).
- [128] Figueira-Duarte, T. M.; Simon, S. C.; Wagner, M.; Druzhinin, S. I.; Zachariasse, K. A.; Müllen, K. Polypyrene Dendrimers. *Angew. Chem. Int. Ed.* **47**, 10175-10178 (2008).
- [129] Feng, X.; Hu, J.-Y.; Yi, L.; Seto, N.; Tao, Z.; Redshaw, C.; Elsegood, M. R. J.; Yamato, T. Pyrene-Based Y-shaped Solid-State Blue Emitters: Synthesis, Characterization, and Photoluminescence. *Chem. Asian J.* **7**, 2854-2863 (2012).
- [130] Wu, K. C.; Ku, P. J.; Lin, C. S.; Shih, H. T.; Wu, F. I.; Huang, M. J.; Lin, J. J.; Chen, I. C.; Cheng, C. H. The Photophysical Properties of Dipyrenylbenzenes and Their Application as Exceedingly Efficient Blue Emitters for Electroluminescent Devices. *Adv. Funct. Mater.* **18**, 67-75 (2008).
- [131] Mallia, A. R.; Sethy, R.; Bhat, V.; Hariharan, M. Crystallization induced enhanced emission in conformational polymorphs of a rotationally flexible molecule. *J. Mater. Chem. C* **4**, 2931-2935 (2016).
- [132] Mallia, A. R.; Salini, P. S.; Hariharan, M. Nonparallel Stacks of Donor and Acceptor Chromophores Evade Geminate Charge Recombination. *J. Am. Chem. Soc.* **137**, 15604-15607 (2015).
- [133] Nagarajan, K.; Rajagopal, S. K.; Hariharan, M. C-H \cdots H-C and C-H \cdots π contacts aid transformation of dimeric to monomeric anthracene in the solid state. *CrystEngComm* **16**, 8946-8949 (2014).
- [134] Wolff, S. K.; Grinwood, D. J.; McKinnon, J. J.; Turner, M. J.; Jayatilaka, D.; Spackman, M. A. *CrystalExplorer 3.0*: University of Western Australia, Perth, Australia, 2012.
- [135] Macrae, C. F.; Edgington, P. R.; McCabe, P.; Pidcock, E.; Shields, G. P.; Taylor, R.; Towler, M.; van de Streek, J. Mercury: visualization and analysis of crystal structures. *J. Appl. Crystallogr.* **39**, 453-457 (2006).
- [136] Camerman, A.; Trotter, J. The crystal and molecular structure of pyrene. *Acta Crystallographica* **18**, 636-643 (1965).
- [137] Birks, J. B.; Kazzaz, A. A.; King, T. A. 'Excimer' Fluorescence. IX. Lifetime Studies of Pyrene Crystals. *Proc. Roy. Soc. Lond. A Math Phys. Sci.* **291**, 556-569 (1966).

- [138] Bakmutov, V. I., *Dihydrogen Bond: Principles, Experiments, and Applications*. John Wiley & Sons, Inc.: Hoboken, New Jersey, 2008.
- [139] Bader, R. F. W., *Atoms in Molecules: A Quantum Theory*. Oxford University Press: Oxford, U.K., 1990.
- [140] Volkov, A.; Macchi, P.; Farrugia, L. J.; Gatti, C.; Mallinson, P. R.; Richter, T.; Koritsanszky, T. *XD2006, a computer program package for multipole refinement, topological analysis of charge densities and evaluation of intermolecular energies from experimental or theoretical structure factors*, User Manual, 2006.
- [141] Wolstenholme, D. J.; Flogeras, J.; Che, F. N.; Decken, A.; McGrady, G. S. Homopolar Dihydrogen Bonding in Alkali Metal Amidoboranes: Crystal Engineering of Low-Dimensional Molecular Materials. *J. Am. Chem. Soc.* **135**, 2439-2442 (2013).
- [142] de Halleux, V.; Calbert, J. P.; Brocorens, P.; Cornil, J.; Declercq, J. P.; Brédas, J. L.; Geerts, Y. 1,3,6,8-Tetraphenylpyrene Derivatives: Towards Fluorescent Liquid-Crystalline Columns? *Adv. Funct. Mater.* **14**, 649-659 (2004).
- [143] Katoh, R.; Sinha, S.; Murata, S.; Tachiya, M. Origin of the stabilization energy of perylene excimer as studied by fluorescence and near-IR transient absorption spectroscopy. *J. Photochem. Photobiol., A* **145**, 23-34 (2001).
- [144] Kollár, J.; Hrdlovič, P.; Chmela, Š. Spectral properties of bichromophoric pyrene derivatives: Monomer vs. excimer fluorescence. *J. Photochem. Photobiol., A* **214**, 33-39 (2010).
- [145] Spano, F. C. The Spectral Signatures of Frenkel Polarons in H- and J-Aggregates. *Acc. Chem. Res.* **43**, 429-439 (2009).
- [146] Gierschner, J.; Lüer, L.; Milián-Medina, B.; Oelkrug, D.; Egelhaaf, H.-J. Highly Emissive H-Aggregates or Aggregation-Induced Emission Quenching? The Photophysics of All-Trans para-Distyrylbenzene. *J. Phys. Chem. Lett.* **4**, 2686-2697 (2013).
- [147] Rösch, U.; Yao, S.; Wortmann, R.; Würthner, F. Fluorescent H-Aggregates of Merocyanine Dyes. *Angew. Chem. Int. Ed.* **45**, 7026-7030 (2006).
- [148] Hong, Y.; Lam, J. W. Y.; Tang, B. Z. Aggregation-induced emission. *Chem. Soc. Rev.* **40**, 5361-5388 (2011).
- [149] Tou, S.-L.; Huang, G.-J.; Chen, P.-C.; Chang, H.-T.; Tsai, J.-Y.; Yang, J.-S. Aggregation-induced emission of GFP-like chromophores via exclusion of solvent-solute hydrogen bonding. *Chem. Commun.* **50**, 620-622 (2014).
- [150] Xie, Z.; Yang, B.; Li, F.; Cheng, G.; Liu, L.; Yang, G.; Xu, H.; Ye, L.; Hanif, M.; Liu, S.; Ma, D.; Ma, Y. Cross Dipole Stacking in the Crystal of Distyrylbenzene Derivative: The Approach toward High Solid-State Luminescence Efficiency. *J. Am. Chem. Soc.* **127**, 14152-14153 (2005).

- [151] Harvey, R. G.; Pataki, J.; Lee, H. The Friedel-Crafts Acylation and Benzoylation of pyrene. *Org. Prep. Proced. Int.* **16**, 144-148 (1984).
- [152] Akira, N. Solvent Effect on the Vibrational Structures of the Fluorescence and Absorption Spectra of Pyrene. *Bull. Chem. Soc. Jpn.* **44**, 3272-3277 (1971).
- [153] Hariharan, M.; Joseph, J.; Ramaiah, D. Novel Bifunctional Viologen-Linked Pyrene Conjugates: Synthesis and Study of Their Interactions with Nucleosides and DNA. *The Journal of Physical Chemistry B* **110**, 24678-24686 (2006).
- [154] Keller, S. N.; Veltri, N. L.; Sutherland, T. C. Tuning Light Absorption in Pyrene: Synthesis and Substitution Effects of Regioisomeric Donor-Acceptor Chromophores. *Org. Lett.* **15**, 4798-4801 (2013).
- [155] Jena, H. S. Effect of non-covalent interaction on the diastereoselective self-assembly of Cu(ii) complexes containing a racemic Schiff base in a chiral self-discriminating process. *New J. Chem.* **38**, 2486-2499 (2014).
- [156] Birks, J. B.; Kazzaz, A. A. Excimer Fluorescence. XII. The Pyrene Crystal Excimer Interaction Potential. *Proc. Roy. Soc. Lond. A Math Phys. Sci.* **304**, 291-301 (1968).
- [157] Sonoda, Y.; Goto, M.; Tsuzuki, S.; Tamaoki, N. Fluorinated Diphenylpolyenes: Crystal Structures and Emission Properties. *J. Phys. Chem. A* **111**, 13441-13451 (2007).
- [158] Li, Q.; Blancafort, L. A conical intersection model to explain aggregation induced emission in diphenyl dibenzofulvene. *Chem. Commun.* **49**, 5966-5968 (2013).
- [159] Gao, X.; Peng, Q.; Niu, Y.; Wang, D.; Shuai, Z. Theoretical insight into the aggregation induced emission phenomena of diphenyldibenzofulvene: a nonadiabatic molecular dynamics study. *Phys. Chem. Chem. Phys.* **14**, 14207-14216 (2012).
- [160] Hong, Y.; Lam, J. W. Y.; Tang, B. Z. Aggregation-induced emission: phenomenon, mechanism and applications. *Chem. Commun.*, 4332-4353 (2009).
- [161] McRae, E. G.; Kasha, M. Enhancement of Phosphorescence Ability upon Aggregation of Dye Molecules. *J. Chem. Phys.* **28**, 721-722 (1958).
- [162] M. Kasha, H. R. R. a. M. A. E.-B. The exciton model in molecular spectroscopy. *Pure Appl. Chem.*, 371-392 (1965).
- [163] Jelley, E. E. Spectral absorption and fluorescence of dyes in the molecular state. *Nature* **138**, 1009-1010 (1936).
- [164] Li, F.; Gao, N.; Xu, H.; Liu, W.; Shang, H.; Yang, W.; Zhang, M. Relationship between Molecular Stacking and Optical Properties of 9,10-Bis((4-N,N-dialkylamino)styryl) Anthracene Crystals: The Cooperation of Excitonic and Dipolar Coupling. *Chem. Eur. J.* **20**, 9991-9997 (2014).
- [165] Zhao, Z.; He, B.; Tang, B. Z. Aggregation-induced emission of siloles. *Chem. Sci.* **6**, 5347-5365 (2015).

- [166] Hu, R.; Leung, N. L. C.; Tang, B. Z. AIE macromolecules: syntheses, structures and functionalities. *Chem. Soc. Rev.* **43**, 4494-4562 (2014).
- [167] Coropceanu, V.; Cornil, J.; da Silva Filho, D. A.; Olivier, Y.; Silbey, R.; Brédas, J.-L. Charge Transport in Organic Semiconductors. *Chem. Rev.* **107**, 926-952 (2007).
- [168] Giri, G.; Verploegen, E.; Mannsfeld, S. C. B.; Atahan-Evrenk, S.; Kim, D. H.; Lee, S. Y.; Becerril, H. A.; Aspuru-Guzik, A.; Toney, M. F.; Bao, Z. Tuning charge transport in solution-sheared organic semiconductors using lattice strain. *Nature* **480**, 504-508 (2011).
- [169] Wang, C.; Dong, H.; Hu, W.; Liu, Y.; Zhu, D. Semiconducting π -Conjugated Systems in Field-Effect Transistors: A Material Odyssey of Organic Electronics. *Chem. Rev.* **112**, 2208-2267 (2012).
- [170] Mei, J.; Diao, Y.; Appleton, A. L.; Fang, L.; Bao, Z. Integrated Materials Design of Organic Semiconductors for Field-Effect Transistors. *J. Am. Chem. Soc.* **135**, 6724-6746 (2013).
- [171] Hinoue, T.; Shigenoi, Y.; Sugino, M.; Mizobe, Y.; Hisaki, I.; Miyata, M.; Tohnai, N. Regulation of π -Stacked Anthracene Arrangement for Fluorescence Modulation of Organic Solid from Monomer to Excited Oligomer Emission. *Chem. Eur. J.* **18**, 4634-4643 (2012).
- [172] Sun, H.; Tottempudi, U. K.; Mottishaw, J. D.; Basa, P. N.; Putta, A.; Sykes, A. G. Strengthening π - π Interactions While Suppressing Csp²-H \cdots π (T-Shaped) Interactions via Perfluoroalkylation: A Crystallographic and Computational Study That Supports the Beneficial Formation of 1-D π - π Stacked Aromatic Materials. *Cryst. Growth Des.* **12**, 5655-5662 (2012).
- [173] Calvo-Castro, J.; Warzecha, M.; Oswald, I. D. H.; Kennedy, A. R.; Morris, G.; McLean, A. J.; McHugh, C. J. Intermolecular Interactions and Energetics in the Crystalline π - π Stacks and Associated Model Dimer Systems of Asymmetric Halogenated Diketopyrrolopyrroles. *Cryst. Growth Des.* **16**, 1531-1542 (2016).
- [174] Hisaki, I.; Osaka, K.; Ikenaka, N.; Saeki, A.; Tohnai, N.; Seki, S.; Miyata, M. Arrangement Modulation of π -Stacked Columnar Assemblies of Octadecyrodibenzo[12]annulene: Substituent Effects of Peripheral Thienyl and Phenyl Rings. *Cryst. Growth Des.* **16**, 714-721 (2016).
- [175] Wang, C.; Dong, H.; Li, H.; Zhao, H.; Meng, Q.; Hu, W. Dibenzothiophene Derivatives: From Herringbone to Lamellar Packing Motif. *Cryst. Growth Des.* **10**, 4155-4160 (2010).
- [176] Putta, A.; Mottishaw, J. D.; Wang, Z.; Sun, H. Rational Design of Lamellar π - π Stacked Organic Crystalline Materials with Short Interplanar Distance. *Cryst. Growth Des.* **14**, 350-356 (2014).
- [177] Sutton, C.; Risko, C.; Brédas, J.-L. Noncovalent Intermolecular Interactions in Organic Electronic Materials: Implications for the Molecular Packing vs Electronic Properties of Acenes. *Chem. Mater.* **28**, 3-16 (2016).

- [178] Batsanov, A. S.; Howard, J. A. K.; Albesa-Jove, D.; Collings, J. C.; Liu, Z. Q.; Mkhaldid, I. A. I.; Thibault, M. H.; Marder, T. B. Structural Versatility of Pyrene-2-(4,4,5,5-tetramethyl-[1,3,2]dioxaborolane) and Pyrene-2,7-bis(4,4,5,5-tetramethyl-[1,3,2]dioxaborolane). *Cryst. Growth Des.* **12**, 2794-2802 (2012).
- [179] BaniKhaled, M. O.; Mottishaw, J. D.; Sun, H. Steering Power of Perfluoroalkyl Substituents in Crystal Engineering: Tuning the π - π Distance While Maintaining the Lamellar Packing Motif for Aromatics with Various Sizes of π -Conjugation. *Cryst. Growth Des.* **15**, 2235-2242 (2015).
- [180] BaniKhaled, M. O.; Becker, J. D.; Koppang, M.; Sun, H. Perfluoroalkylation of Square-Planar Transition Metal Complexes: A Strategy To Assemble Them into Solid State Materials with a π - π Stacked Lamellar Structure. *Cryst. Growth Des.* **16**, 1869-1878 (2016).
- [181] Zhang, H.; Wang, Y.; Shao, K.; Liu, Y.; Chen, S.; Qiu, W.; Sun, X.; Qi, T.; Ma, Y.; Yu, G.; Su, Z.; Zhu, D. Novel butterfly pyrene-based organic semiconductors for field effect transistors. *Chem. Commun.*, 755-757 (2006).
- [182] Chan, K. L.; Lim, J. P. F.; Yang, X.; Dodabalapur, A.; Jabbour, G. E.; Sellinger, A. High-efficiency pyrene-based blue light emitting diodes: aggregation suppression using a calixarene 3D-scaffold. *Chem. Commun.* **48**, 5106-5108 (2012).
- [183] Robertson, J. M.; White, J. G. 72. The crystal structure of pyrene. A quantitative X-ray investigation. *J. Chem. Soc.*, 358-368 (1947).
- [184] Kobayashi, K.; Masu, H.; Shuto, A.; Yamaguchi, K. Control of Face-to-Face π - π Stacked Packing Arrangement of Anthracene Rings via Chalcogen-Chalcogen Interaction: 9,10-Bis(methylchalcogeno)anthracenes. *Chem. Mater.* **17**, 6666-6673 (2005).
- [185] Okamoto, T.; Nakahara, K.; Saeki, A.; Seki, S.; Oh, J. H.; Akkerman, H. B.; Bao, Z.; Matsuo, Y. Aryl-Perfluoroaryl Substituted Tetracene: Induction of Face-to-Face π - π Stacking and Enhancement of Charge Carrier Properties. *Chem. Mater.* **23**, 1646-1649 (2011).
- [186] Ryno, S. M.; Risko, C.; Brédas, J.-L. Impact of Molecular Packing on Electronic Polarization in Organic Crystals: The Case of Pentacene vs TIPS-Pentacene. *J. Am. Chem. Soc.* **136**, 6421-6427 (2014).
- [187] Foster, J. A.; Piepenbrock, M.; Lloyd, G. O.; Clarke, N.; Howard, J. A. K.; Steed, J. W. Anion-switchable supramolecular gels for controlling pharmaceutical crystal growth. *Nat Chem* **2**, 1037-1043 (2010).
- [188] Desiraju, G. R. Hydrogen Bridges in Crystal Engineering: Interactions without Borders. *Acc. Chem. Res.* **35**, 565-573 (2002).
- [189] Gilday, L. C.; Robinson, S. W.; Barendt, T. A.; Langton, M. J.; Mullaney, B. R.; Beer, P. D. Halogen Bonding in Supramolecular Chemistry. *Chem. Rev.* **115**, 7118-7195 (2015).

- [190] Cavallo, G.; Metrangolo, P.; Milani, R.; Pilati, T.; Priimagi, A.; Resnati, G.; Terraneo, G. The Halogen Bond. *Chem. Rev.* **116**, 2478-2601 (2016).
- [191] Rajagopal, S. K.; Philip, A. M.; Nagarajan, K.; Hariharan, M. Progressive acylation of pyrene engineers solid state packing and colour via C-H \cdots H-C, C-H \cdots O and π - π interactions. *Chem. Commun.* **50**, 8644-8647 (2014).
- [192] Rajagopal, S. K.; Reddy, V. S.; Hariharan, M. Crystallization induced green-yellow-orange emitters based on benzoypyrenes. *CrystEngComm*, (2016).
- [193] Rajagopal, S. K.; Salini, P. S.; Hariharan, M. S \cdots π , π - π , and C-H \cdots π Contacts Regulate Solid State Fluorescence in Regioisomeric Bisthiazolypyrenes. *Cryst. Growth Des.* **16**, 4567-4573 (2016).
- [194] Dou, J.-H.; Zheng, Y.-Q.; Yao, Z.-F.; Yu, Z.-A.; Lei, T.; Shen, X.; Luo, X.-Y.; Sun, J.; Zhang, S.-D.; Ding, Y.-F.; Han, G.; Yi, Y.; Wang, J.-Y.; Pei, J. Fine-Tuning of Crystal Packing and Charge Transport Properties of BDOPV Derivatives through Fluorine Substitution. *J. Am. Chem. Soc.* **137**, 15947-15956 (2015).
- [195] Ashizawa, M.; Yamada, K.; Fukaya, A.; Kato, R.; Hara, K.; Takeya, J. Effect of Molecular Packing on Field-Effect Performance of Single Crystals of Thienyl-Substituted Pyrenes. *Chem. Mater.* **20**, 4883-4890 (2008).
- [196] Harvey, R. G.; Konieczny, M.; Pataki, J. Synthesis of the isomeric mono- and bisoxiranylpyrenes. *J. Org. Chem.* **48**, 2930-2932 (1983).
- [197] Yin, G.; Gao, M.; She, N.; Hu, S.; Wu, A.; Pan, Y. Highly Efficient and Clean Method for Direct α -Iodination of Aromatic Ketones. *Synthesis* **2007**, 3113-3116 (2007).
- [198] Jadhav, V. H.; Jang, S. H.; Jeong, H.-J.; Lim, S. T.; Sohn, M.-H.; Kim, J.-Y.; Lee, S.; Lee, J. W.; Song, C. E.; Kim, D. W. Oligoethylene Glycols as Highly Efficient Multifunctional Promoters for Nucleophilic-Substitution Reactions. *Chem. Eur. J.* **18**, 3918-3924 (2012).
- [199] *The sparingly soluble nature of 1,8-IP in various solvents prevented it from forming diffractable crystals, and thereby it is not included in the discussion.*
- [200] Mottishaw, J. D.; Erck, A. R.; Kramer, J. H.; Sun, H.; Koppang, M. Electrostatic Potential Maps and Natural Bond Orbital Analysis: Visualization and Conceptualization of Reactivity in Sanger's Reagent. *J. Chem. Educ.* **92**, 1846-1852 (2015).
- [201] Joy, J.; Cheriya, R. T.; Nagarajan, K.; Shaji, A.; Hariharan, M. Breakdown of Exciton Splitting through Electron Donor-Acceptor Interaction: A Caveat for the Application of Exciton Chirality Method in Macromolecules. *J. Phys. Chem. C* **117**, 17927-17939 (2013).

List of publications

1. Haloacetylation Driven Transformation Haloacetylation Driven Transformation of Herringbone to Lamellar/Columnar Packing in Pyrene
Salini P. S.;[†] **Rajagopal, S. K.**;[†] Hariharan, M*
Cryst. Growth Des. [10.1021/acs.cgd.6b00919].
2. S••• π , π - π and C-H••• π Contacts Regulate Solid-State Fluorescence in Regioisomeric Bisthiazolylpyrenes
Rajagopal, S. K.; Salini P. S.; Hariharan, M*
Cryst. Growth Des. **2016**, 16, 4567-4573 (**Most Read Article**).
3. Crystallization Induced Green-Yellow-Orange Emitters Based on Benzoylpyrenes
Rajagopal, S. K.; Reddy, V. S.; Hariharan, M*
CrystEngComm. **2016**, 18, 5089-5094 (**Outside Frontispiece**).
4. Progressive Acylation of Pyrene Engineers Solid State Packing and Colour via C-H•••H-C, C-H•••O and π - π Interactions
Rajagopal, S. K.; Philip, A. M.; Nagarajan, K.; Hariharan, M*
Chem. Commun. **2014**, 50, 8644-8647. (**Inside Frontispiece**).
5. C-H•••H-C and C-H••• π Contacts Aid Transformation of Dimeric to Monomeric Anthracene in the Solid State
Nagarajan, K.; **Rajagopal, S. K.**; Hariharan, M*
CrystEngComm. **2014**, 16, 8946-8949.
6. Non-Natural G-quadruplex in a Non-Natural Environment
Rajagopal, S. K.; Hariharan, M*
Photochem. Photobiol. Sci. **2014**, 16, 8946-8949.
7. DNA-Enforced Conformational Restriction of an Atropisomer
Cheriya, R. T.; Joy, J.; **Rajagopal, S. K.**; Nagarajan, K.; Hariharan, M*
J. Phy. Chem. C **2012**, 116, 22631-22636.

([†]Both the authors contributed equally)

Presentations and Conferences

- Received best poster presentation award in 5th Inter-IISER Chemistry Meet 2015 (IICM-2015) held in Indian Institute of Science Education and Research Thiruvananthapuram, December 11-13, 2015.
- Poster Presentation: "Tuning the Solid State Optical Properties of Pyrene using C–H•••H–C, C–H•••O and π – π Interactions" during '8th Asian Photochemistry Conference-APC2014' held at Taj Vivanta, Thiruvananthapuram, India, November 10-13, 2014.
- Poster Presentation: Progressive Acylation of Pyrene Engineers Solid State Packing and Colour via. C–H•••H–C, C–H•••O and π – π Interactions" during 11th JNC Research Conference on "Chemistry of Materials", Thiruvananthapuram, India, Oct 02-04, 2015.
- Poster Presentation: "DNA-Enforced Conformational Restriction of an Atropisomer" at Organic Devices: the Future Ahead (ODeFA) held at Bhabha Atomic Research Centre, Mumbai, India, March 3-6, 2014.
- Attended one day conference "ACS on Campus" an initiative from American Chemical Society held at NIIST-Thiruvananthapuram, India, November 23, 2013.
- Attended Inter-IISER Chemistry Meet-2011 held at IISER-Thiruvananthapuram, India, December, 2011.

Copyright and permission

9/10/2016

Rightslink® by Copyright Clearance Center

**RightsLink**®[Home](#)[Account Info](#)[Help](#)**ACS Publications**
Most Trusted. Most Cited. Most Read.**Title:** Fusion at the Non-K-Region of Pyrene: An Alternative Strategy To Extend the π -Conjugated Plane of Pyrene**Author:** Lin Zou, Xiao-Ye Wang, Ke Shi, et al**Publication:** Organic Letters**Publisher:** American Chemical Society**Date:** Sep 1, 2013

Copyright © 2013, American Chemical Society

Logged in as:
Shinaj R
Account #:
3001060710[LOGOUT](#)

PERMISSION/LICENSE IS GRANTED FOR YOUR ORDER AT NO CHARGE

This type of permission/license, instead of the standard Terms & Conditions, is sent to you because no fee is being charged for your order. Please note the following:

- Permission is granted for your request in both print and electronic formats, and translations.
- If figures and/or tables were requested, they may be adapted or used in part.
- Please print this page for your records and send a copy of it to your publisher/graduate school.
- Appropriate credit for the requested material should be given as follows: "Reprinted (adapted) with permission from (COMPLETE REFERENCE CITATION). Copyright (YEAR) American Chemical Society." Insert appropriate information in place of the capitalized words.
- One-time permission is granted only for the use specified in your request. No additional uses are granted (such as derivative works or other editions). For any other uses, please submit a new request.

If credit is given to another source for the material you requested, permission must be obtained from that source.

[BACK](#)[CLOSE WINDOW](#)

Copyright © 2016 [Copyright Clearance Center, Inc.](#) All Rights Reserved. [Privacy statement](#). [Terms and Conditions](#).
Comments? We would like to hear from you. E-mail us at customercare@copyright.com

9/20/2016

Rightslink® by Copyright Clearance Center

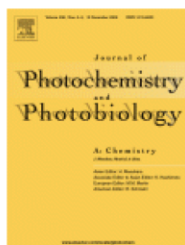


RightsLink®

Home

Account
Info

Help



Title: Anomalous fluorescence from the second excited singlet state upon excitation to the S4 state of pyrene in a supersonic jet

Author: Yasushi Numata, Yasuhiro Suzuki, Isamu Suzuka

Publication: Journal of Photochemistry and Photobiology A: Chemistry

Publisher: Elsevier

Date: 1 June 2012

Copyright © 2012 Elsevier B.V. All rights reserved.

Logged in as:
Shinaj R
Account #:
3001060710

LOGOUT

Review Order

Please review the order details and the associated [terms and conditions](#).

No royalties will be charged for this reuse request although you are required to obtain a license and comply with the license terms and conditions. To obtain the license, click the Accept button below.

Licensed Content Publisher	Elsevier
Licensed Content Publication	Journal of Photochemistry and Photobiology A: Chemistry
Licensed Content Title	Anomalous fluorescence from the second excited singlet state upon excitation to the S4 state of pyrene in a supersonic jet
Licensed Content Author	Yasushi Numata, Yasuhiro Suzuki, Isamu Suzuka
Licensed Content Date	1 June 2012
Licensed Content Volume	237
Licensed Content Issue	n/a
Licensed Content Pages	4
Type of Use	reuse in a thesis/dissertation
Portion	figures/tables/illustrations
Number of figures/tables/illustrations	1
Format	print
Are you the author of this Elsevier article?	No
Will you be translating?	No
Order reference number	
Original figure numbers	figure 1
Title of your thesis/dissertation	Photoinduced Excited State Processes in Carbonylpyrenes: A Comparison between Solution and Solid-State Properties
Expected completion date	Sep 2016
Estimated size (number of pages)	200
Elsevier VAT number	GB 494 6272 12
Requestor Location	Shinaj R IISER-TVM CET campus Sreekaryam Thiruvananthapuram, 695016 India Attn: Shinaj R
Total	0.00 USD

9/10/2016

Rightslink® by Copyright Clearance Center



RightsLink®

[Home](#)[Account Info](#)[Help](#)**Title:**

Molecular Packing and Solid-State Fluorescence of Alkoxy-Cyano Substituted Diphenylbutadienes: Structure of the Luminescent Aggregates

Logged in as:

Shinaj R

Account #:

3001060710

[LOGOUT](#)**Author:**

Riju Davis, N. S. Saleesh Kumar, Shibu Abraham, et al

Publication:

The Journal of Physical Chemistry C

Publisher:

American Chemical Society

Date:

Feb 1, 2008

Copyright © 2008, American Chemical Society

PERMISSION/LICENSE IS GRANTED FOR YOUR ORDER AT NO CHARGE

This type of permission/license, instead of the standard Terms & Conditions, is sent to you because no fee is being charged for your order. Please note the following:

- Permission is granted for your request in both print and electronic formats, and translations.
- If figures and/or tables were requested, they may be adapted or used in part.
- Please print this page for your records and send a copy of it to your publisher/graduate school.
- Appropriate credit for the requested material should be given as follows: "Reprinted (adapted) with permission from (COMPLETE REFERENCE CITATION). Copyright (YEAR) American Chemical Society." Insert appropriate information in place of the capitalized words.
- One-time permission is granted only for the use specified in your request. No additional uses are granted (such as derivative works or other editions). For any other uses, please submit a new request.

If credit is given to another source for the material you requested, permission must be obtained from that source.

[BACK](#)[CLOSE WINDOW](#)

Copyright © 2016 [Copyright Clearance Center, Inc.](#) All Rights Reserved. [Privacy statement](#). [Terms and Conditions](#).
Comments? We would like to hear from you. E-mail us at customercare@copyright.com

9/10/2016

Rightslink® by Copyright Clearance Center

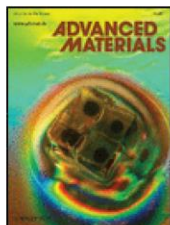


RightsLink®

Home

Account Info

Help



Title: Organic Crystals with Tunable Emission Colors Based on a Single Organic Molecule and Different Molecular Packing Structures

Author: H. Y. Zhang, Z. L. Zhang, K. Q. Ye, J. Y. Zhang, Y. Wang

Publication: Advanced Materials

Publisher: John Wiley and Sons

Date: Sep 12, 2006

Copyright © 2006 WILEY-VCH Verlag GmbH & Co. KGaA, Weinheim

Logged in as:

Shinaj R

Account #:

3001060710

[LOGOUT](#)

Order Completed

Thank you for your order.

This Agreement between Shinaj R ("You") and John Wiley and Sons ("John Wiley and Sons") consists of your license details and the terms and conditions provided by John Wiley and Sons and Copyright Clearance Center.

Your confirmation email will contain your order number for future reference.

[Get the printable license.](#)

License Number	3945210853206
License date	Sep 10, 2016
Licensed Content Publisher	John Wiley and Sons
Licensed Content Publication	Advanced Materials
Licensed Content Title	Organic Crystals with Tunable Emission Colors Based on a Single Organic Molecule and Different Molecular Packing Structures
Licensed Content Author	H. Y. Zhang, Z. L. Zhang, K. Q. Ye, J. Y. Zhang, Y. Wang
Licensed Content Date	Sep 12, 2006
Licensed Content Pages	4
Type of use	Dissertation/Thesis
Requestor type	University/Academic
Format	Print
Portion	Figure/table
Number of figures/tables	1
Original Wiley figure/table number(s)	Figure 2
Will you be translating?	No
Title of your thesis / dissertation	Photoinduced Excited State Processes in Carbonylpyrenes: A Comparison between Solution and Solid-State Properties
Expected completion date	Sep 2016
Expected size (number of pages)	200
Requestor Location	Shinaj R IISER-TVM CET campus Sreekaryam Thiruvananthapuram, 695016 India Attn: Shinaj R
Publisher Tax ID	EU826007151
Billing Type	Invoice
Billing address	Shinaj R IISER-TVM CET campus Sreekaryam

9/10/2016

Rightslink® by Copyright Clearance Center



RightsLink®

[Home](#)[Account Info](#)[Help](#)ACS Publications
Most Trusted. Most Cited. Most Read.**Title:** Anthracene-Arrangement-Dependent Emissions of Crystals of 9-Anthrylpyrazole Derivatives**Author:** Zuolun Zhang, Yu Zhang, Dandan Yao, et al**Publication:** Crystal Growth and Design**Publisher:** American Chemical Society**Date:** Dec 1, 2009

Copyright © 2009, American Chemical Society

Logged in as:

Shinaj R

Account #:

3001060710

[LOGOUT](#)**PERMISSION/LICENSE IS GRANTED FOR YOUR ORDER AT NO CHARGE**

This type of permission/license, instead of the standard Terms & Conditions, is sent to you because no fee is being charged for your order. Please note the following:

- Permission is granted for your request in both print and electronic formats, and translations.
- If figures and/or tables were requested, they may be adapted or used in part.
- Please print this page for your records and send a copy of it to your publisher/graduate school.
- Appropriate credit for the requested material should be given as follows: "Reprinted (adapted) with permission from (COMPLETE REFERENCE CITATION). Copyright (YEAR) American Chemical Society." Insert appropriate information in place of the capitalized words.
- One-time permission is granted only for the use specified in your request. No additional uses are granted (such as derivative works or other editions). For any other uses, please submit a new request.

If credit is given to another source for the material you requested, permission must be obtained from that source.

[BACK](#)[CLOSE WINDOW](#)

Copyright © 2016 [Copyright Clearance Center, Inc.](#) All Rights Reserved. [Privacy statement.](#) [Terms and Conditions.](#) Comments? We would like to hear from you. E-mail us at customercare@copyright.com

9/10/2016

Rightslink® by Copyright Clearance Center



RightsLink®

Home

Account
Info

Help



Title: Switching of Polymorph-Dependent ESIPT Luminescence of an Imidazo[1,2-a]pyridine Derivative

Author: Toshiki Mutai, Haruhiko Tomoda, Tatsuya Ohkawa, Yuji Yabe, Koji Araki

Publication: Angewandte Chemie International Edition

Publisher: John Wiley and Sons

Date: Oct 29, 2008

Copyright © 2008 WILEY-VCH Verlag GmbH & Co. KGaA, Weinheim

Logged in as:

Shinaj R

Account #:

3001060710

[LOGOUT](#)

Review Order

Please review the order details and the associated [terms and conditions](#).

No royalties will be charged for this reuse request although you are required to obtain a license and comply with the license terms and conditions. To obtain the license, click the Accept button below.

Licensed Content Publisher	John Wiley and Sons
Licensed Content Publication	Angewandte Chemie International Edition
Licensed Content Title	Switching of Polymorph-Dependent ESIPT Luminescence of an Imidazo[1,2-a]pyridine Derivative
Licensed Content Author	Toshiki Mutai, Haruhiko Tomoda, Tatsuya Ohkawa, Yuji Yabe, Koji Araki
Licensed Content Date	Oct 29, 2008
Licensed Content Pages	3
Type of use	Dissertation/Thesis
Requestor type	University/Academic
Format	Print
Portion	Figure/table
Number of figures/tables	1
Original Wiley figure/table number(s)	Figure 2
Will you be translating?	No
Title of your thesis / dissertation	Photoinduced Excited State Processes in Carbonylpyrenes: A Comparison between Solution and Solid-State Properties
Expected completion date	Sep 2016
Expected size (number of pages)	200
Requestor Location	Shinaj R IISER-TVM CET campus Sreekaryam Thiruvananthapuram, 695016 India Attn: Shinaj R
Publisher Tax ID	EU826007151
Total	0.00 USD

9/10/2016

Rightslink® by Copyright Clearance Center

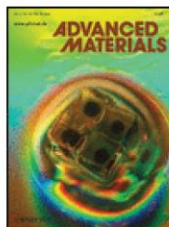


RightsLink®

Home

Account
Info

Help



Title: Thermally Induced Reversible Phase Transformations Accompanied by Emission Switching Between Different Colors of Two Aromatic-Amine Compounds

Logged in as:
Shinaj R
Account #:
3001060710

LOGOUT

Author: Yunfeng Zhao, Hongze Gao, Yan Fan, Tianlei Zhou, Zhongmin Su, Yu Liu, Yue Wang

Publication: Advanced Materials

Publisher: John Wiley and Sons

Date: Apr 14, 2009

Copyright © 2009 WILEY-VCH Verlag GmbH & Co. KGaA, Weinheim

Review Order

Please review the order details and the associated [terms and conditions](#).

No royalties will be charged for this reuse request although you are required to obtain a license and comply with the license terms and conditions. To obtain the license, click the Accept button below.

Licensed Content Publisher	John Wiley and Sons
Licensed Content Publication	Advanced Materials
Licensed Content Title	Thermally Induced Reversible Phase Transformations Accompanied by Emission Switching Between Different Colors of Two Aromatic-Amine Compounds
Licensed Content Author	Yunfeng Zhao, Hongze Gao, Yan Fan, Tianlei Zhou, Zhongmin Su, Yu Liu, Yue Wang
Licensed Content Date	Apr 14, 2009
Licensed Content Pages	5
Type of use	Dissertation/Thesis
Requestor type	University/Academic
Format	Print
Portion	Figure/table
Number of figures/tables	1
Original Wiley figure/table number(s)	Figure 3
Will you be translating?	No
Title of your thesis / dissertation	Photoinduced Excited State Processes in Carbonylpyrenes: A Comparison between Solution and Solid-State Properties
Expected completion date	Sep 2016
Expected size (number of pages)	200
Requestor Location	Shinaj R IISER-TVM CET campus Sreekaryam Thiruvananthapuram, 695016 India Attn: Shinaj R
Publisher Tax ID	EU826007151
Total	0.00 USD

9/10/2016

Rightslink® by Copyright Clearance Center



RightsLink®

[Home](#)[Account Info](#)[Help](#)ACS Publications
Most Trusted. Most Cited. Most Read.**Title:**Shear- and UV-Induced
Fluorescence Switching in
Stilbenic n-Dimer Crystals
Powered by Reversible [2 + 2]
Cycloaddition

Logged in as:

Shinaj R

Account #:

3001060710

[LOGOUT](#)**Author:**Jong Won Chung, Youngmin You,
Hyun Sue Huh, et al**Publication:**Journal of the American Chemical
Society**Publisher:**

American Chemical Society

Date:

Jun 1, 2009

Copyright © 2009, American Chemical Society

PERMISSION/LICENSE IS GRANTED FOR YOUR ORDER AT NO CHARGE

This type of permission/license, instead of the standard Terms & Conditions, is sent to you because no fee is being charged for your order. Please note the following:

- Permission is granted for your request in both print and electronic formats, and translations.
- If figures and/or tables were requested, they may be adapted or used in part.
- Please print this page for your records and send a copy of it to your publisher/graduate school.
- Appropriate credit for the requested material should be given as follows: "Reprinted (adapted) with permission from (COMPLETE REFERENCE CITATION). Copyright (YEAR) American Chemical Society." Insert appropriate information in place of the capitalized words.
- One-time permission is granted only for the use specified in your request. No additional uses are granted (such as derivative works or other editions). For any other uses, please submit a new request.

If credit is given to another source for the material you requested, permission must be obtained from that source.

[BACK](#)[CLOSE WINDOW](#)

Copyright © 2016 [Copyright Clearance Center, Inc.](#) All Rights Reserved. [Privacy statement](#). [Terms and Conditions](#).
Comments? We would like to hear from you. E-mail us at customercare@copyright.com

9/10/2016

Rightslink® by Copyright Clearance Center



RightsLink®

[Home](#)[Account Info](#)[Help](#)ACS Publications
Most Trusted. Most Cited. Most Read.**Title:** Multistimuli Two-Color
Luminescence Switching via
Different Slip-Stacking of Highly
Fluorescent Molecular SheetsLogged in as:
Shinaj R
Account #:
3001060710**Author:** Seong-Jun Yoon, Jong Won
Chung, Johannes Gierschner, et
al[LOGOUT](#)**Publication:** Journal of the American Chemical
Society**Publisher:** American Chemical Society**Date:** Oct 1, 2010

Copyright © 2010, American Chemical Society

PERMISSION/LICENSE IS GRANTED FOR YOUR ORDER AT NO CHARGE

This type of permission/license, instead of the standard Terms & Conditions, is sent to you because no fee is being charged for your order. Please note the following:

- Permission is granted for your request in both print and electronic formats, and translations.
- If figures and/or tables were requested, they may be adapted or used in part.
- Please print this page for your records and send a copy of it to your publisher/graduate school.
- Appropriate credit for the requested material should be given as follows: "Reprinted (adapted) with permission from (COMPLETE REFERENCE CITATION). Copyright (YEAR) American Chemical Society." Insert appropriate information in place of the capitalized words.
- One-time permission is granted only for the use specified in your request. No additional uses are granted (such as derivative works or other editions). For any other uses, please submit a new request.

If credit is given to another source for the material you requested, permission must be obtained from that source.

[BACK](#)[CLOSE WINDOW](#)

Copyright © 2016 [Copyright Clearance Center, Inc.](#) All Rights Reserved. [Privacy statement](#). [Terms and Conditions](#).
Comments? We would like to hear from you. E-mail us at customer@copyright.com

9/20/2016

Rightslink® by Copyright Clearance Center



RightsLink®

Home

Account
Info

Help

RSC Publishing **Title:**

A tetraphenylethene-substituted pyridinium salt with multiple functionalities: synthesis, stimuli-responsive emission, optical waveguide and specific mitochondrion imaging

Logged in as:

Shinaj R

Account #:
3001060710

LOGOUT

Author: Na Zhao, Min Li, Yongli Yan, Jacky W. Y. Lam, Yi Lin Zhang, Yong Sheng Zhao, Kam Sing Wong, Ben Zhong Tang

Publication: Journal of Materials Chemistry C

Publisher: Royal Society of Chemistry

Date: Jun 6, 2013

Copyright © 2013, Royal Society of Chemistry

Review Order

Please review the order details and the associated [terms and conditions](#).

No royalties will be charged for this reuse request although you are required to obtain a license and comply with the license terms and conditions. To obtain the license, click the Accept button below.

Licensed Content Publisher	Royal Society of Chemistry
Licensed Content Publication	Journal of Materials Chemistry C
Licensed Content Title	A tetraphenylethene-substituted pyridinium salt with multiple functionalities: synthesis, stimuli-responsive emission, optical waveguide and specific mitochondrion imaging
Licensed Content Author	Na Zhao, Min Li, Yongli Yan, Jacky W. Y. Lam, Yi Lin Zhang, Yong Sheng Zhao, Kam Sing Wong, Ben Zhong Tang
Licensed Content Date	Jun 6, 2013
Licensed Content Volume	1
Licensed Content Issue	31
Type of Use	Thesis/Dissertation
Requestor type	non-commercial (non-profit)
Portion	figures/tables/images
Number of figures/tables/images	1
Distribution quantity	1
Format	print
Will you be translating?	no
Order reference number	
Title of the thesis/dissertation	Photoinduced Excited State Processes in Carbonylpyrenes: A Comparison between Solution and Solid-State Properties
Expected completion date	Sep 2016
Estimated size	200
Requestor Location	Shinaj R IISER-TVM CET campus Sreekaryam Thiruvananthapuram, 695016 India Attn: Shinaj R
Total	0.00 USD

9/20/2016

Rightslink® by Copyright Clearance Center

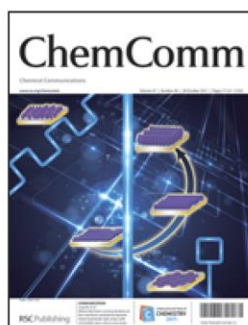


RightsLink®

Home

Account
Info

Help



Title: Benzothiazolium-functionalized tetraphenylethene: an AIE luminogen with tunable solid-state emission

Author: Na Zhao,Zhiyong Yang,Jacky W. Y. Lam,Herman H. Y. Sung,Ni Xie,Sijie Chen,Huimin Su,Meng Gao,Ian D. Williams,Kam Sing Wong,Ben Zhong Tang

Publication: Chemical Communications (Cambridge)

Publisher: Royal Society of Chemistry

Date: Jul 11, 2012

Copyright © 2012, Royal Society of Chemistry

Logged in as:

Shinaj R

Account #:

3001060710

LOGOUT

Review Order

Please review the order details and the associated [terms and conditions](#).

No royalties will be charged for this reuse request although you are required to obtain a license and comply with the license terms and conditions. To obtain the license, click the Accept button below.

Licensed Content Publisher	Royal Society of Chemistry
Licensed Content Publication	Chemical Communications (Cambridge)
Licensed Content Title	Benzothiazolium-functionalized tetraphenylethene: an AIE luminogen with tunable solid-state emission
Licensed Content Author	Na Zhao,Zhiyong Yang,Jacky W. Y. Lam,Herman H. Y. Sung,Ni Xie,Sijie Chen,Huimin Su,Meng Gao,Ian D. Williams,Kam Sing Wong,Ben Zhong Tang
Licensed Content Date	Jul 11, 2012
Licensed Content Volume	48
Licensed Content Issue	69
Type of Use	Thesis/Dissertation
Requestor type	non-commercial (non-profit)
Portion	figures/tables/images
Number of figures/tables/images	1
Distribution quantity	1
Format	print
Will you be translating?	no
Order reference number	
Title of the thesis/dissertation	Photoinduced Excited State Processes in Carbonylpyrenes: A Comparison between Solution and Solid-State Properties
Expected completion date	Sep 2016
Estimated size	200
Requestor Location	Shinaj R IISER-TVM CET campus Sreekaryam Thiruvananthapuram, 695016 India Attn: Shinaj R
Total	0.00 USD

9/20/2016

Rightslink® by Copyright Clearance Center

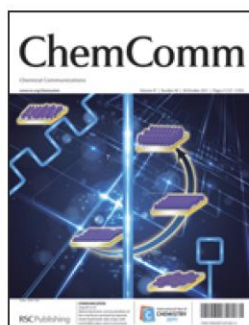


RightsLink®

Home

Account
Info

Help



Title: Twisted D–π–A solid emitters: efficient emission and high contrast mechanochromism

Author: Yongyang Gong, Yeqiang Tan, Jun Liu, Ping Lu, Cunfang Feng, Wang Zhang Yuan, Yawei Lu, Jing Zhi Sun, Gufeng He, Yongming Zhang

Logged in as:
Shinaj R
Account #:
3001060710

LOGOUT

Publication: Chemical Communications (Cambridge)

Publisher: Royal Society of Chemistry

Date: Mar 26, 2013

Copyright © 2013, Royal Society of Chemistry

Review Order

Please review the order details and the associated [terms and conditions](#).

No royalties will be charged for this reuse request although you are required to obtain a license and comply with the license terms and conditions. To obtain the license, click the Accept button below.

Licensed Content Publisher	Royal Society of Chemistry
Licensed Content Publication	Chemical Communications (Cambridge)
Licensed Content Title	Twisted D–π–A solid emitters: efficient emission and high contrast mechanochromism
Licensed Content Author	Yongyang Gong, Yeqiang Tan, Jun Liu, Ping Lu, Cunfang Feng, Wang Zhang Yuan, Yawei Lu, Jing Zhi Sun, Gufeng He, Yongming Zhang
Licensed Content Date	Mar 26, 2013
Licensed Content Volume	49
Licensed Content Issue	38
Type of Use	Thesis/Dissertation
Requestor type	non-commercial (non-profit)
Portion	figures/tables/images
Number of figures/tables/images	1
Distribution quantity	1
Format	print
Will you be translating?	no
Order reference number	
Title of the thesis/dissertation	Photoinduced Excited State Processes in Carbonylpyrenes: A Comparison between Solution and Solid-State Properties
Expected completion date	Sep 2016
Estimated size	200
Requestor Location	Shinaj R IISER-TVM CET campus Sreekaryam Thiruvananthapuram, 695016 India Attn: Shinaj R
Total	0.00 USD

9/20/2016

Rightslink® by Copyright Clearance Center

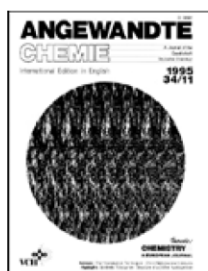


RightsLink®

Home

Account
Info

Help



Title: A Cocrystal Strategy to Tune the Luminescent Properties of Stilbene-Type Organic Solid-State Materials

Author: Dongpeng Yan, Amit Delori, Gareth O. Lloyd, Tomislav Friščić, Graeme M. Day, William Jones, Jun Lu, Min Wei, David G. Evans, Xue Duan

Publication: Angewandte Chemie International Edition

Publisher: John Wiley and Sons

Date: Nov 7, 2011

Copyright © 2011 WILEY-VCH Verlag GmbH & Co. KGaA, Weinheim

Logged in as:
Shinaj R

Account #:
3001060710

LOGOUT

Review Order

Please review the order details and the associated [terms and conditions](#).

No royalties will be charged for this reuse request although you are required to obtain a license and comply with the license terms and conditions. To obtain the license, click the Accept button below.

Licensed Content Publisher	John Wiley and Sons
Licensed Content Publication	Angewandte Chemie International Edition
Licensed Content Title	A Cocrystal Strategy to Tune the Luminescent Properties of Stilbene-Type Organic Solid-State Materials
Licensed Content Author	Dongpeng Yan, Amit Delori, Gareth O. Lloyd, Tomislav Friščić, Graeme M. Day, William Jones, Jun Lu, Min Wei, David G. Evans, Xue Duan
Licensed Content Date	Nov 7, 2011
Licensed Content Pages	4
Type of use	Dissertation/Thesis
Requestor type	University/Academic
Format	Print
Portion	Figure/table
Number of figures/tables	1
Original Wiley figure/table number(s)	Figure 1
Will you be translating?	No
Title of your thesis / dissertation	Photoinduced Excited State Processes in Carbonylpyrenes: A Comparison between Solution and Solid-State Properties
Expected completion date	Sep 2016
Expected size (number of pages)	200
Requestor Location	Shinaj R IISER-TVM CET campus Sreekaryam Thiruvananthapuram, 695016 India Attn: Shinaj R
Publisher Tax ID	EU826007151
Total	0.00 USD

9/20/2016

Rightslink® by Copyright Clearance Center

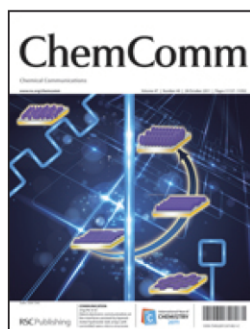


RightsLink®

Home

Account
Info

Help



Title: Switching and tuning organic solid-state luminescence via a supramolecular approach

Author: Savarimuthu Philip Anthony, Sunil Varughese, Sylvia M. Draper

Publication: Chemical Communications (Cambridge)

Publisher: Royal Society of Chemistry

Date: Nov 4, 2009

Copyright © 2009, Royal Society of Chemistry

Logged in as:
Shinaj R
Account #:
3001060710

LOGOUT

Review Order

Please review the order details and the associated [terms and conditions](#).

No royalties will be charged for this reuse request although you are required to obtain a license and comply with the license terms and conditions. To obtain the license, click the Accept button below.

Licensed Content Publisher	Royal Society of Chemistry
Licensed Content Publication	Chemical Communications (Cambridge)
Licensed Content Title	Switching and tuning organic solid-state luminescence via a supramolecular approach
Licensed Content Author	Savarimuthu Philip Anthony, Sunil Varughese, Sylvia M. Draper
Licensed Content Date	Nov 4, 2009
Licensed Content Issue	48
Type of Use	Thesis/Dissertation
Requestor type	non-commercial (non-profit)
Portion	figures/tables/images
Number of figures/tables/images	1
Distribution quantity	1
Format	print
Will you be translating?	no
Order reference number	
Title of the thesis/dissertation	Photoinduced Excited State Processes in Carbonylpyrenes: A Comparison between Solution and Solid-State Properties
Expected completion date	Sep 2016
Estimated size	200
Requestor Location	Shinaj R IISER-TVM CET campus Sreekaryam Thiruvananthapuram, 695016 India Attn: Shinaj R
Total	0.00 USD

9/10/2016

Rightslink® by Copyright Clearance Center



RightsLink®

Home

Account
Info

Help

ACS Publications
Most Trusted. Most Cited. Most Read.**Title:** Solid-State Packing of
Conjugated Oligomers: From n -
Stacks to the Herringbone
StructureLogged in as:
Shinaj R
Account #:
3001060710**Author:** M. David Curtis, Jie Cao, Jeff W.
Kampf

LOGOUT

Publication: Journal of the American Chemical
Society**Publisher:** American Chemical Society**Date:** Apr 1, 2004

Copyright © 2004, American Chemical Society

PERMISSION/LICENSE IS GRANTED FOR YOUR ORDER AT NO CHARGE

This type of permission/license, instead of the standard Terms & Conditions, is sent to you because no fee is being charged for your order. Please note the following:

- Permission is granted for your request in both print and electronic formats, and translations.
- If figures and/or tables were requested, they may be adapted or used in part.
- Please print this page for your records and send a copy of it to your publisher/graduate school.
- Appropriate credit for the requested material should be given as follows: "Reprinted (adapted) with permission from (COMPLETE REFERENCE CITATION). Copyright (YEAR) American Chemical Society." Insert appropriate information in place of the capitalized words.
- One-time permission is granted only for the use specified in your request. No additional uses are granted (such as derivative works or other editions). For any other uses, please submit a new request.

If credit is given to another source for the material you requested, permission must be obtained from that source.

BACK

CLOSE WINDOW

Copyright © 2016 [Copyright Clearance Center, Inc.](#) All Rights Reserved. [Privacy statement.](#) [Terms and Conditions.](#)
Comments? We would like to hear from you. E-mail us at customer@copyright.com